MAX PLANCK INSTITUE FOR SOLID STATE RESEARCH

Stuttgart Center for **E**lectron **M**icroscopy (StEM)

Aberration-Corrected Analytical Transmission Electron Microscopy of Light Elements in Complex Oxides: Application and Methodology

Fachbereich Material- und Geowissenschaften

Technische Universität Darmstadt

Approved dissertation to obtain the academic degree of Dr. rer. nat

By

DAN ZHOU

M. Sc. (The University of Dublin, Trinity College, Dublin, Ireland) 2012

From Jiangsu Province, China

1. Referee: Prof. Dr. Peter A. van Aken

2. Co-referee: Prof. Dr. Christoph T. Koch

Date of submission: 30/10/2015

Date of defense: 14/12/2015

Darmstadt 2016

D17

Dedication

To my beloved grandmother, parents and sisters

Declaration

I, the undersigned, declare that this work has not previously been submitted to this or any other University, and that unless otherwise stated, it is entirely my own work.

Dan Zhou

Darmstadt 2016

Acknowledgement

I am very grateful to my supervisor Prof. Dr. Peter A. van Aken, without whom none of the work presented here would be possible. Despite his busy schedule, Peter always tried his best to give guidance, support and inspiration during my Ph. D study. I am really very happy that I made a right decision to join his group at the end of 2011.

I would like to express my special thanks to Dr. Wilfried Sigle, who is my co-supervisor in Max Planck Institute for Solid State Research in Stuttgart. I often pop into Wilfried's office with questions but without appointment. Wilfried's readiness and patience to help is really appreciated. Wilfried's detailed and patient guidance and suggestions on science and on communications as a researcher is of great help to me as a young researcher. What's more, I greatly appreciate Wilfried's hard work in transforming my manuscripts, reports and thesis from messed up language and formatting to final good shape.

I would also like to thank Prof. Dr. Andreas Rosenauer and his group members Dr. Knut Müller-Caspary and Mr. Florian F. Krause from Institute of Solid State Physics, Universität Bremen. Their sharing of STEMsim and ImageEval source code, user guidance and experience, and knowledge about quantitative STEM imaging are of great inspiration to my work.

I am very grateful to Prof. Dr. Hanns-Ulrich Habermeier. His support and sharing of the knowledge on complex oxide interface structure and properties are quite inspiring.

Besides, I also want to thank the faculty and staff in Stuttgart Center for Electron Microscopy (StEM). Kersten Hahn and Peter Kopold's efforts in maintaining all the microscopes in a very nice status are quite essential for high-spatial resolution work presented in this thesis. Marion Kelsch prepared my challenging samples to meet my experiments' requirements. Ute Salzberger helped to solve my computer problems. What's more, Marion and Ute's care on personal life are also appreciated. I want thank Dr. Yi Wang for quite inspiring discussions in the office. I can't list every one's name here, in general, I would like to thank all the StEM members for their accompanies and supports personally and scientifically.

I appreciate the support and scientific input from Prof. Dr. Hans-Joachim Kleebe in TU Darmstadt. Thanks also go to Prof. Dr. Christoph T. Koch in HU Berlin for his sharing of knowledge in STEM simulation and discussions during my PhD study.

I would also like to thank the German Electron Microscopy Society (Deutsche Gesellschaft für Elektronenmikroskopie e. V., DGE), Microscopy Society of America (MSA), European Microscopy Society (EMS) for awarding young researcher scholarship to attend conferences.

I would also like to thank Max Planck Institute for Intelligent systems for providing Grassroots project funding.

Financial support by ESTEEM2 is gratefully acknowledged.

Last but not least, I would like to give my deepest gratitude and love to my family.

Thank you all.

Dan Zhou

Stuttgart, October 2015

Abstract

The advent of aberration correctors for electron optical lenses at the end of 20th century has brought atomic resolution analysis of the materials into a new era. In this thesis, the new possibilities of application and methodology on aberration-corrected analytical transmission electron microscopy (TEM) of light elements in complex oxides are explored by experiments and image simulations, with the emphasis on annular bright-field (ABF) imaging.

The arrangement and bonding of light elements, like lithium (Li) and oxygen (O), in complex oxides plays a crucial rule in the material's properties, however the characterization of the materials remains challenging. In recent years ABF imaging has become a popular imaging technique owing to its ability to map both light and heavy elements. I start from the application of ABF on qualitatively determining O's distribution in ZrO_2-$La_{2/3}Sr_{1/3}MnO_3$ (LSMO) pillar–matrix thin films, together with the application of high-angle annular dark-field (HAADF) and electron energy-loss spectroscopy (EELS) to obtain a fuller picture of the investigated complex oxide. After that, the methodology study of ABF imaging, concerning the quantitative determination of atom column position and concentration, is presented. The accuracy of atom column position determination is of great importance for investigating atomic structure defects like elastic and plastic strains.

Atomic-scale control of the synthesis of complex oxide materials envisages the atomic-scale properties and requires the knowledge of atomic-scale characterization. The ZrO_2-LSMO pillar–matrix thin films were found to show anomalous magnetic and electron transport properties controlled by the amount of ZrO_2. With the application of an aberration–corrected analytical transmission electron microscope (TEM), structure and interfacial chemistry of the system, especially of the pillar–matrix interface were revealed at atomic resolution. In addition, three types of Mn segregated antiphase boundaries (APBs) connecting ZrO_2 pillars were investigated by HAADF and ABF imaging. The local atomic structure, chemical composition, cation valence and electric field were determined at atomic-scale. These results provide detailed information for future studies of macroscopic properties of these materials.

Moreover, a consequence of aberration-correctors is the high electron dose rate in the scanning mode. This can lead to radiation-induced modifications of materials. I studied the electron-beam-induced reconstruction of three types of APBs. With the utilization of HAADF scanning transmission electron microscopy (STEM), ABF STEM and EELS, the

motion of both heavy and light element columns under moderate electron beam irradiation are revealed at atomic resolution. Besides, Mn segregated in the APBs was found to have reduced valence states, which can be directly correlated with oxygen loss. Charge states of the APBs are finally discussed based on these experimental results. This study provides support for the design of radiation engineering solid-oxide fuel cell materials.

The determination of atom positions from atomically resolved transmission electron micrographs is fundamental for the analysis of crystal defects and strain. Contrast formation in ABF is partially governed by the phase of the electron wave, which renders the technique more sensitive to the tilt of the electron beam with respect to the crystal zone axis than in high-angle annular dark-field (HAADF) imaging. I show this sensitivity experimentally and use image simulations to quantify this effect. This is essential for future quantitative ABF studies including error estimation.

Another aspect of quantification is the number of atoms in an atom column. The attempt to quantify Li concentration by ABF imaging has been done by simulations. The influences of convergence semi-angle, collection semi-angle, and defocus are explored, while direct correlation with experimental results need more theoretical investigations in this area. Semi-quantification of the Li amount was studied by EELS in case of the particle-size dependent delithiation process of $LiFePO_4$. From the core-loss region and low-loss region analysis it is found that the sample with particle size of 25 nm delithiates homogeneously over the whole particle, whereas the 70 nm and 150 nm particles form an $FePO_4$ core and a $LiFePO_4$ shell. The practical considerations, like radiation damage, delocalization, interface effects and so on are also discussed.

Zusammenfassung

Am Ende des 20. Jahrhunderts gelang es, Korrektoren für Fehler elektronenoptischer Linsen zu realisieren. Damit begann eine neue Ära der Materialanalyse mit atomarer Auflösung. In dieser Arbeit werden die neuen Möglichkeiten der aberrationskorrigierten Transmissions-Elektronenmikroskopie (TEM) für die Analyse leichter Elemente sowohl experimentell als auch anhand von Bildsimulationen untersucht.

Die chemische Bindung und die atomare Anordnung leichter Elemente, wie beispielsweise von Lithium (Li) oder Sauerstoff (O), spielen eine entscheidende Rolle für die Eigenschaften in komplexen Oxiden. Dagegen ist die Charakterisierung leichter Elemente nach wie vor eine besondere Herausforderung. Im Bereich der TEM wurde vor wenigen Jahren die „annular bright-field"-Abbildung (ABF) eingeführt mit deren Hilfe eine Abbildung sowohl schwerer als auch leichter Elemente ermöglicht wird. Hier wende ich diese Methode auf die Bestimmung der atomaren Position von O-Atomen in ZrO_2–$La_{2/3}Sr_{1/3}MnO_3$ (LSMO) an. Parallel dazu wird die Abbildung mit stark gestreuten Elektronen („high-angle annular dark-field", HAADF) sowie die Elektronen-Energieverlustspektroskopie (EELS) zur vollständigen Charakterisierung angewandt. Diese Untersuchungen werden schließlich durch die quantitative Untersuchung der atomaren Position leichter Elemente mittels Bildsimulationen komplettiert. Die Genauigkeit der Positionsbestimmung ist von großer Bedeutung um beispielsweise die atomare Struktur von Defekten oder elastische bzw. plastische Dehnungen zu untersuchen.

Das oben genannte Material ZrO_2–LSMO zeichnet sich durch säulenförmiges Wachstum von ZrO_2-Ausscheidungen in der LSMO-Matrix aus. Dieses Material zeigt anomales Verhalten der elektrischen Leitfähigkeit, für welches die atomare Struktur und die chemische Bindung bedeutend sind. Mittels HAADF, ABF und EELS wird gezeigt, dass an den Grenzflächen zwischen den Phasen ausgeprägte Interdiffusion stattfindet. Zudem liegen die Manganatome, abhängig von ihrer Position, in unterschiedlichen Valenzzuständen vor. Weiterhin wurden Antiphasengrenzen gefunden die ZrO_2-Säulen verbinden. Aus den gemessenen Daten wurden die Ladungszustände der Antiphasengrenzen bestimmt.

Nach intensiver Bestrahlung der Antiphasengrenzen in ZrO_2–LSMO wurde mittels HAADF, ABF und EELS festgestellt, dass sich die atomare Struktur und die chemische Bindung in diesen Grenzflächen verändern. Dies zeigt sich durch die Bewegung von

Atomsäulen sowie durch die Änderung des Valenzzustandes der Manganatome und einem damit einhergehenden Verlust von Sauerstoff. Mit Hilfe dieser Ergebnisse konnte auch die Änderung des Ladungszustandes der Antiphasengrenzen bestimmt werden. Diese atomaren Untersuchungen der bestrahlungsinduzierten Materialmodifikation könnten für die künftige Untersuchung von Strahlenschäden von Bedeutung sein.

Schließlich wird die Konzentration von Li-Atomen in $LiFePO_4$, einem vielversprechenden System für künftige Li-Batterien, untersucht. Hierzu wurde anhand von Bildsimulationen der Kontrast von Li-Säulen in ABF-Bildern untersucht wobei die Anzahl der Li-Atome in den Säulen variiert wurde. Außerdem wurden die Strahlkonvergenz, der Detektionswinkel des ABF-Detektors sowie der Defokus als freie Parameter zugelassen. Experimentell wird mittels EELS der Prozess der Beladung und Entladung von feinkörnigem $LiFePO_4$ untersucht. Die Ergebnisse aus dem Bereich niedriger und hoher Energieverluste zeigen, dass die Be-/Entladung bei kleinen Korngrößen (25 nm) homogen über das Kornvolumen erfolgt. Dagegen bildet sich bei größeren Körnern ein $FePO_4$-Kern mit einer umgebenden $LiFePO_4$-Schale aus. Experimentelle Grenzen wie Strahlenschädigung, Delokalisierung sowie Grenzflächeneffekte werden diskutiert.

List of Abbreviations

ABF	annular bright-field
ADF	annular dark-field
APB	antiphase boundary
BF	bright-field
CCD	charge-coupled device
EDXS	energy-dispersive X-ray spectroscopy
EELS	electron energy-loss spectroscopy
ELNES	electron energy-loss near-edge spectroscopy
EXELFS	extended energy-loss fine structure spectroscopy
FIB	focused ion beam
FOLZ	first order Laue zone
FPO	$FePO_4$
GPA	geometric phase analysis
HAADF	high-angle annular dark-field
HCI	hollow-cone illumination
HRTEM	high-resolution transmission electron microscopy
HWHM	half width at half maximum
LAADF	low-angle annular dark-field
LAO	$LaAlO_3$
LFPO	$LiFePO_4$
LSMO	$La_{2/3}Sr_{1/3}MnO_3$
MAADF	medium-angle annular dark-field
MABF	middle-angle bright-field
MSA	multivariate statistical analysis
PACBED	position-averaged convergent beam electron diffraction

SNR	signal-to-noise ratio
SOLZ	second order Laue zone
STEM	scanning transmission electron microscopy
TDS	thermal diffuse scattering
TEM	transmission electron microscopy/microscope
UHV	ultra-high vacuum
VP	volume plasmon
WPCA	weighted principle-component analysis
WPO	weak phase object
ZLP	zero-loss peak
ZOLZ	zero order Laue zone

Table of Contents

Dedication ..... *i*

Declaration ..... *ii*

Acknowledgement ..... *iii*

Abstract ..... *v*

Zusammenfassung ..... *vii*

List of Abbreviations ..... *ix*

Table of Contents ..... *xi*

Chapter 1 Introduction *1*

1.1 Introduction to aberration-corrected TEM **1**

1.2 Light element imaging by TEM **2**

1.3 Complex oxide **3**

1.4 Scope of this thesis **4**

Chapter 2 Methodology *5*

2.1 Introduction **5**

2.2 Probe formation **6**

2.3 HAADF and ABF STEM imaging **9**

2.3.1 *Z*-contrast HAADF STEM imaging 10

2.3.2 ABF STEM imaging 11

2.3.3 Detector axial alignment and sensitivity 14

2.4 EELS **18**

2.4.1 Zero-loss peak (ZLP) 18

2.4.2 Low-loss region 19

2.4.3 Core-loss region 19

2.4.4 Tackling with some practical issues 19

2.4.5 Application of EELS in this thesis 20

Chapter 3 Interfacial Chemistry and Atomic Structure of ZrO_2-$La_{2/3}Sr_{1/3}MnO_3$ Pillar-matrix Structures *21*

3.1 Introduction **22**

3.2 Experimental section **23**

3.3 Results and discussions **24**

3.4 Conclusions **36**

Chapter 4 Linking Atomic Structure and Local Chemistry at Manganese-Segregated Antiphase Boundaries in ZrO_2-$La_{2/3}Sr_{1/3}MnO_3$ Thin Films *38*

4.1 Introduction **39**

4.2 Sample preparation and TEM experimental details **40**

4.3 Results **41**

4.3.1 Geometric arrangement of the three boundary types 41

4.3.2 Elemental mapping of the APB wall 43

4.3.3 O position determination 45

4.4 Discussions **48**

4.4.1 Strain-driven formation of APBs 48

4.4.2 Atomic reconstruction: Charge neutrality by varying atomic occupation 52
4.5 Conclusions 55
Chapter 5 Electron-Beam-Induced Antiphase Boundary Reconstructions in a ZrO_2-$La_{2/3}Sr_{1/3}MnO_3$ Pillar-Matrix System 56
5.1 Introduction 57
5.2 Sample preparation and TEM details 57
5.3 Results 58
5.3.1 Geometric arrangement change under electron beam illumination 58
5.3.2 Elemental distribution and valence states 61
5.3.3 O position determination 64
5.4 Discussions 67
5.4.1 The occurrence of the electron-beam-induced reconstructions 67
5.4.2 Atomic occupation and valence discussions 69
5.5 Conclusions 72
Chapter 6 Sample Tilt Effects on Atom Column Position Determination in ABF-STEM Imaging 74
6.1 Introduction 75
6.2 Method 76
6.2.1 Experimental 76
6.2.2 Simulation 77
6.2.3 Data processing 79
6.3 Experimental results 80
6.4 Simulation results 83
6.4.1 Preliminary remarks 83
6.4.2 Correlating simulation with experimental results 84
6.4.3 Convergence and collection angles 86
6.4.4 Tilt amount 88
6.5 Discussions 90
6.5.1 Influence on the angle measurement 90
6.5.2 Summary of experimental and simulation results and suggestions to minimize errors 91
6.6 Preliminary application – mis-orientation of LSMO on two sides of APBs 92
6.7 Appendix 93
6.7.1 More data about the convergence semi-angle's influence on ABF imaging 93
6.7.2 Quick view of the tilting effect 94
6.7.3 Factors influcing the precision of the simulated deviations 95
6.7.4 Diffraction pattern rotation 98
6.7.5 Direction relationship between Laue center and diffraction pattern intensity gravity center when small tilt exists 100
6.7.6 Weak-phase object approximation at thin specimen regions 101
6.8 Outlook 103
6.8.1 Probe aberration's influences 103
6.8.2 Interface's influences 104
6.9 Conclusions 105
Chapter 7 Contrast Investigation of Annular Bright-Field Imaging in Scanning Transmission Electron Microscopy of $LiFePO_4$ 107
7.1 Introduction 108
7.2 Simulation set-up 108
7.3 Results and Discussions 109
7.3.1 Preliminary remarks 109

7.3.2 Effects of collection semi-angle 111
7.3.3 Effects of defocus 111
7.4 Conclusions and future work 112
Chapter 8 EELS Investigation of Size-dependent Delithiation Process in $LiFePO_4$ 114
8.1 Introduction 115
8.2 Experimental section 115
8.3 Results and discussions 116
8.3.1 The core-loss region 116
8.3.1.1 Delithiation related features at the O-K and Fe-L edge 116
8.3.1.2 Practical considerations 117
8.3.1.3 Experimental results 117
8.3.2 The low-loss region 119
8.3.2.1 Delithiation related features in the low-loss region 119
8.3.2.2 Practical considerations 120
8.3.2.3 Experimental results 123
8.4 Conclusions and outlook 124
Chapter 9 Conclusion and Outlook 125
List of Tables 128
List of Figures 129
Curriculum vitae 139
Bibliography 146

Chapter 1 Introduction

1.1 Introduction to aberration-corrected TEM

Since its invention [1] more than 80 years ago transmission electron microscopy (TEM) has been widely used to investigate and refine the internal structure and chemistry of materials. The implementation of schemes diagnosing and correcting the imperfections (aberrations) [2, 3] of the electron lenses pushed these analyses to the sub-angstrom and even single atom scale [3-12]. I focus on the discussions related to probe-aberration-corrected scanning transmission electron microscopy (STEM) and skip the image-corrected TEM because of its rare application in this thesis. In STEM, a sufficiently fine electron beam positioned on a specific atom column in thin specimens does not spread significantly to neighbouring columns and thus atomic resolution is achieved.

It is known that the image resolution in STEM is primarily determined by the probe size[13-15] which is limited by the probe-forming lens aberrations (spherical and chromatic) and the energy spread of the electron source [16]. A simplified view of the modification to the probe size by spherical aberration correction in STEM is illustrated in Fig. 1.1. The reduction of spherical aberration from 1.2 mm to -500 nm can reduce the minimum accessible probe size (d_{59} criteria, i.e. width of the beam where 59% of probe intensity is included) from 0.24 nm at a convergence semi-angle of 6.8 mrad to 0.09 nm at a convergence semi-angle of 25.5 mrad. For both situations, the probe size is limited by the diffraction limit at small convergence semi-angles whereas at large convergence semi-angles the limitation comes from spherical aberration for a non-corrected system and from chromatic aberration for a spherical-aberration-corrected system. Moreover, the probe size deteriorates faster in a non-corrected system than in a spherical-aberration-corrected system when the convergence angle deviates from the minimum probe size point. Thus aberration correction not only provides smaller probe size and eventually better spatial resolution but also more freedom in selecting the convergence semi-angle, which can facilitate some techniques requiring small depth of focus with high spatial resolution. Most importantly, the large convergence semi-angle goes along with a largely increased probe current which is important for analytical techniques such as EELS or energy-dispersive X-ray spectroscopy (EDXS). Apart from the spherical aberration, for practical situations one needs to include higher-order aberrations. The details of the equations used for calculating probe size can be found in [17].

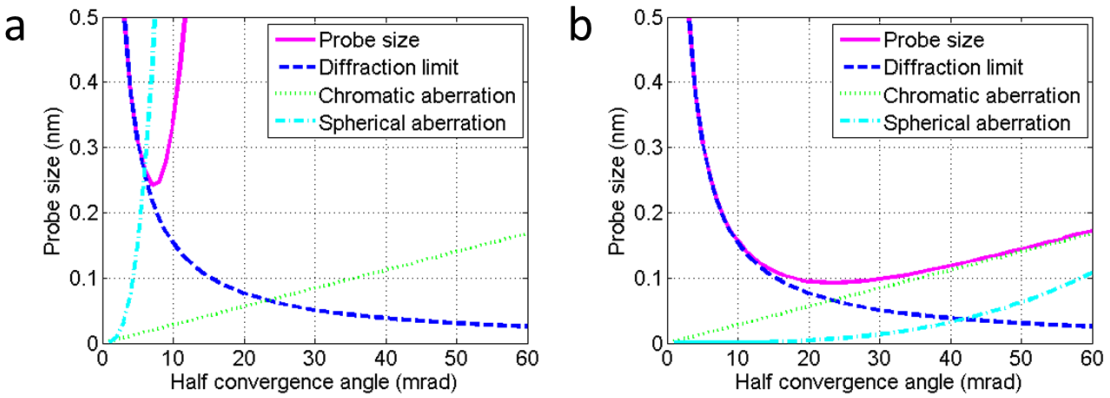

Figure 1.1 Calculated probe size with parameters (a) 200kV, 1.4 mm chromatic aberration, 1.2 mm spherical aberration, 0.4 eV energy spread; (b) 200 kV, 1.4 mm chromatic aberration, -500 nm spherical aberration, 0.4 eV energy spread.

1.2 Light element imaging by TEM

Light elements, normally considered to be the ones lighter than fluorine, are important to the structure and properties of a wide range of materials, including lithium-ion batteries, complex-oxide-based superconductors, catalysts, ZrH applied in nuclear reactor and so on. The challenges in imaging light elements lie on two points: visibility and radiation damage. Before the advent of aberration correctors, spatial resolution was the limiting factor for viewing both heavy and light elements in the TEM. At then, numerical correction for the spherical aberration based on either exit-wave focal series reconstruction [18-23] or holographic techniques [24] was widely used to push the point spatial resolution to the information limit of the microscope which is eventually limited by chromatic aberration (due to high-voltage and current instabilities) and mechanical instabilities. The application of high-angle annular dark-field (HAADF) imaging on heavy elements was also limited by the poor signal-to-noise ratio. HAADF STEM imaging soon became more widely applied due to the improved spatial resolution and signal-to-noise ratio. However, compared to heavy elements, the weak electron scattering of light elements to high angles makes HAADF unsuitable for imaging light elements. Besides, when light elements and heavy elements coexist in material, light elements are normally invisible in a HAADF image due to the extreme contrast difference.

Tackling with the challenges discussed above, TEM techniques including negative Cs high-resolution transmission electron microscopy (HRTEM) [4, 25], phase contrast imaging [26, 27], middle-angle bright-field (MABF) [28, 29] STEM imaging, differential phase-contrast imaging[30], and annular bright-field (ABF) imaging [31, 32] were developed.

Moreover, the development of segmented detectors [33] and pixelated detectors[34, 35] enables more flexible and optimized selections of the interested signal of interest. Among all these methods, ABF STEM imaging has been mostly applied to explore practical materials [36-42] due to its monotonic intensity variation with atomic number, little change of contrast with specimen thickness and defocus and strong signal.

However, qualitative visibility of light elements just starts the research in this area. The next step is to approach quantitative information, such as the atom position and the number of atoms. Findlay et. al.[43] explored the contrast mechanisms involved in ABF imaging by simulations taking into account the specimen thickness, defocus, probe convergence semi-angle, inner and outer collection semi-angles, inter-atomic column spacing and disorder. An attempt to use ABF for measuring absolute O positions was also reported[44]. These studies were all based on the assumption of perfect crystalline specimens oriented perfectly into a zone axis. In real situations this might be more complicated. The direct extracted atom positions from a single image are questionable considering the elastic coherent signal generated in the bright-field region. Moreover, quantifying the amount of light elements by ABF imaging has not yet been achieved. A simple scheme would be to apply the procedures for quantitative HAADF imaging. However, the signal for HAADF imaging is much less sensitive to strain compared with the signal in the bright-field (BF) region. Therefore, it is impossible to simply copy the strategy of HAADF. Therefore more research on the possibility and application of ABF are still needed.

In this thesis, the reliability of absolute atom position determination by ABF will be investigated combining experimental observations and simulation results taking into account specimen tilt. ABF simulations are also used to explore the quantification of the amount of light elements in case of Li in $LiFePO_4$. Besides, as an alternative technique to imaging, EELS' application will also be presented with experimental results.

1.3 Complex oxide

Technical advances in the atomic-scale synthesis of oxide heterostructures have provided a fertile new ground for creating novel phenomena at their interfaces, such as interface superconductivity, magneto-electric coupling, and the quantum Hall effect which can't be found in the bulk constituents[45-48]. A characteristic feature is the reconstruction of the charge, spin, and orbital states at interfaces which can be caused by structure, composition, and bonding change on the atomic scale. The advent of aberration-corrected TEM enables the characterization of this information at the atomic scale and thus provides evidence for further theoretical, synthesis and application work. In this thesis, a

comprehensive application of TEM techniques, including HAADF, ABF, and EELS will be applied to investigate a complex oxide material, a ZrO_2-$La_{2/3}Sr_{1/3}MnO_3$ (LSMO) pillar–matrix structures.

1.4 Scope of this thesis

In this thesis, part I (chapter 3-5) is devoted to the application of ABF on qualitatively determining O's distribution in the ZrO_2-$La_{2/3}Sr_{1/3}MnO_3$ (LSMO) pillar–matrix thin films, together with the application of high-angle annular dark-field (HAADF) and electron energy-loss spectroscopy (EELS) for the full picture of the investigated complex oxide; and part II (chapter 6-8) is focused on the methodology investigation to the quantitative determination of atom column position and concentration by ABF imaging.

Chapter 2 is a brief introduction to the experimental techniques used in my research with emphasis on ABF STEM imaging.

Chapters 3-5 focus on the application of aberration-corrected analytical TEM on the study of the structure, composition, and bonds in complex oxides.

Chapter 6 is devoted to the effects of tilt on the atom column position determination in ABF and HAADF STEM imaging.

Chapter 7 gives preliminary ABF simulation on Li concentration quantification.

Chapter 8 presents the EELS investigation of size-dependent delithiation process in $LiFePO_4$.

Conclusions and outlook of this doctorate work are summarized in chapter 9.

Chapter 2 Methodology

2.1 Introduction

Two different TEMs have been used in this study (For detailed specifications of each microscope the reader is referred to its operation manual):

Vacuum Generator (VG) HB 501UX: A dedicated STEM machine, equipped with a cold field electron gun operated at 100 kV, an ultra-high vacuum (UHV) sample pre-chamber and a parallel EELS spectrometer (Gatan Enfina).

JEOL ARM-200F: Probe-aberration corrected cold field emission (S)TEM. This is a state-of-the-art (S)TEM with exceptional stability and the capability to conduct atomic-level analysis with STEM spatial resolution better than 0.08 nm. The microscope is equipped with an advanced post-column EELS system, Gatan GIF Quantum ERS (Part number 966, with the intrinsic spectrometer resolution of 0.04 eV) with dual-EELS and fast EELS capabilities. The spectrometer comes with Gatan annular dark-field (ADF) and BF detectors. The microscope also includes an EDXS system (JEOL Centurio EDX detector) for compositional analysis. The hexapole-type DCOR (CEOS GmbH, Heidelberg, Germany) probe-corrector corrects all axial aberrations up to fourth order semi-automatically and the six-fold astigmatism 'A5' is largely reduced[49]. The experimental work presented in chapter 3 and part of chapter 4 was done with an initially installed CESCOR corrector, the other experimental work was done using the DCOR corrector. Details can be found in the experimental section of each chapter concerning the minor change of convergence and collection angles. The TEM is set up for operation voltages of 30 kV, 60 kV, 80 kV, and 200 kV. Moreover, the microscope has a series of detectors enabling various imaging modes. The detectors include: (from electron gun, top to down) JEOL HAADF detector, Gatan Orius (SC2000) diffraction charge-coupled device (CCD), JEOL bright-field (BF) detector, Gatan annular dark-field (ADF) and BF detectors, Gatan XP1000 CCD (also called pre-GIF CCD) and the CCD of the Gatan GIF Quantumn ER(S) (also called GIF CCD).

This chapter is concerned with the theory, background, practical use and some preliminary experimental results of the STEM methods applied in this thesis. Moreover, some experimental details and data processing methods will be discussed.

2.2 Probe formation

The information which can be extracted from STEM imaging critically depends on the size and the intensity distribution of the electron probe, the composition and thickness of the specimen and the angular range selected for imaging.

The electron wave after passing the specimen can be written as [50]

$$\psi_t(\boldsymbol{x}) = \psi_{inc}(\boldsymbol{x})t(\boldsymbol{x})$$

where $t(\boldsymbol{x})$ involves the effects of the specimen and the electron propagation function, $\psi_{inc}(\boldsymbol{x})$ is the electron wave function before entering the specimen, and $\boldsymbol{x}$ is a two-dimensional vector in the object plane.

For an ideal lens, the probe is simply the Airy disc, i.e. the Fourier transform of the uniformly illuminated aperture in the back-focal plane. Coherent or geometrical aberrations cause a residual phase shift of the electron wave leading to a directly observable deviation of the electron trajectories from the ideal shape of a non-aberrated beam.[51] To include the aberrations, the probe function is calculated as the inverse Fourier transform of the aperture function $A(\boldsymbol{k})$ in the back focal plane, which includes the phase change $\exp(-i\chi(\boldsymbol{k}))$ due to aberrations and an aperture shape function

$$\psi_{inc}(\boldsymbol{x}) = \int A(\boldsymbol{k}) \exp(-i\boldsymbol{x}\cdot\boldsymbol{k})\, d\boldsymbol{k} = \int H(\boldsymbol{k}) \exp(-i\chi(\boldsymbol{k})) \exp(-i\boldsymbol{x}\cdot\boldsymbol{k})\, d\boldsymbol{k}$$

where $H(\boldsymbol{k})$ is the top-hat aperture function defining the maximum illumination angle (that has a value of unity inside the aperture and zero outside), $\boldsymbol{k}$ is a two-dimensional vector in the back-focal plane of the probe-forming lens. Therefore, the calculation of the electron beam profile is equivalent to the propagation of an electron wave through a phase plate and calculating the intensity of the resulting wave[16].

$$I(\boldsymbol{x}) = \psi_{inc}(\boldsymbol{x}) * \psi_{inc}^{*}(\boldsymbol{x})$$

There is no generally accepted notation for aberration coefficients. The relation between the notations used by Krivanek *et al.*, [52] Uhlemann & Haider, [53] Saxton [54] and Hawkes & Kasper [55] has been listed in Appendix A of the book *Aberration-Corrected Analytical Transmission Electron Microscopy* [56] edited by Rik Brydson. In this thesis, the notations from Uhlemann & Haider [53] have been chosen because the TEM I used is equipped with a CEOS corrector. Since our system can measure up to S_5, our description stops at this order.

$$\chi(\boldsymbol{k}) = \frac{2\pi}{\lambda} Re\{\frac{1}{2}\boldsymbol{k}\bar{\boldsymbol{k}}C_1 + \frac{1}{2}\bar{\boldsymbol{k}}^2 A_1 + \frac{1}{3}\bar{\boldsymbol{k}}^3 A_2 + \boldsymbol{k}^2\bar{\boldsymbol{k}}B_2 + \frac{1}{4}\left(\boldsymbol{k}\bar{\boldsymbol{k}}\right)^2 C_3 + \frac{1}{4}\bar{\boldsymbol{k}}^4 A_3 + \boldsymbol{k}^3\bar{\boldsymbol{k}}S_3 + \frac{1}{5}\bar{\boldsymbol{k}}^5 A_4 + \boldsymbol{k}^3\bar{\boldsymbol{k}}^2 B_4 + \boldsymbol{k}^4\bar{\boldsymbol{k}}D_4 + \frac{1}{6}\left(\boldsymbol{k}\bar{\boldsymbol{k}}\right)^3 C_5 + \frac{1}{6}\bar{\boldsymbol{k}}^6 A_5 + \boldsymbol{k}^5\bar{\boldsymbol{k}}R_5 + \boldsymbol{k}^4\bar{\boldsymbol{k}}^2 S_5\}$$

where λ is the electron wavelength, $\bar{\boldsymbol{k}}$ as the conjugate complex of $\boldsymbol{k}$. The variation of the defocus caused by the variation of the electron energy due to the finite energy width of the electron source has to be taken into account. The defocus C_1 is modified by $C_{1C} = C_1 + C_c \frac{E-E_0}{E_0}$.

Therefore, the final phase factor of the incident electron wave can be written as

$$\chi(\boldsymbol{k}) = \frac{2\pi}{\lambda} Re\{\frac{1}{2}\boldsymbol{k}\bar{\boldsymbol{k}}C_1 + \frac{1}{2}\bar{\boldsymbol{k}}^2 A_1 + \frac{1}{3}\bar{\boldsymbol{k}}^3 A_2 + \boldsymbol{k}^2\bar{\boldsymbol{k}}B_2 + \frac{1}{4}\left(\boldsymbol{k}\bar{\boldsymbol{k}}\right)^2 C_3 + \frac{1}{4}\bar{\boldsymbol{k}}^4 A_3 + \boldsymbol{k}^3\bar{\boldsymbol{k}}S_3 + \frac{1}{5}\bar{\boldsymbol{k}}^5 A_4 + \boldsymbol{k}^3\bar{\boldsymbol{k}}^2 B_4 + \boldsymbol{k}^4\bar{\boldsymbol{k}}D_4 + \frac{1}{6}\left(\boldsymbol{k}\bar{\boldsymbol{k}}\right)^3 C_5 + \frac{1}{6}\bar{\boldsymbol{k}}^6 A_5 + \boldsymbol{k}^5\bar{\boldsymbol{k}}R_5 + \boldsymbol{k}^4\bar{\boldsymbol{k}}^2 S_5 + \frac{1}{2}\boldsymbol{k}\bar{\boldsymbol{k}}C_c\frac{E-E_0}{E}\}$$

From these calculations, we can have a look at the effects of aberrations with spherical aberration as an illustration on the size and intensity distribution of the electron probe. C_1, A_1, A_2 and B_2 are assumed to be 0, which is approximately the case in the experiment. The other aberrations are listed in Table 2.1, which are taken from one of my experimental measurements, except the values of C_3, C_c, and the energy spread of the electron gun $E–E_0$.

Table 2.1 The experimentally measured aberration coefficients (except C_3, C_C, and $E–E_0$).

Aberration coefficients	Value	Angle (degree)
C_3/mm	1.2 or 0.0001	Not applicable
A_3/nm	89.17	-138
S_3/nm	12.96	-117.8
A_4/um	0.3397	125.2
D_4/um	0.4004	-61.8
B_4/um	0.1996	-154.3
C_5/mm	0.2444	Not applicable
A_5/um	32.41	157
R_5/um	3.046	-104.5
S_5/um	5.772	174.8
C_C/mm	1.4	Not applicable
E-E_0 /eV	0.4	Not applicable

Fig. 2.1 displays a comparison of the phase plate in the back-focal plane and the beam intensity in the incident plane with C_3 = 100 nm and 1.2 mm, respectively. One can see a tremendous increase in the beam intensity in a smaller probe size when C_3 is small.

Moreover, the large angular range in the back focal plane with almost constant phase facilitates techniques like phase imaging.

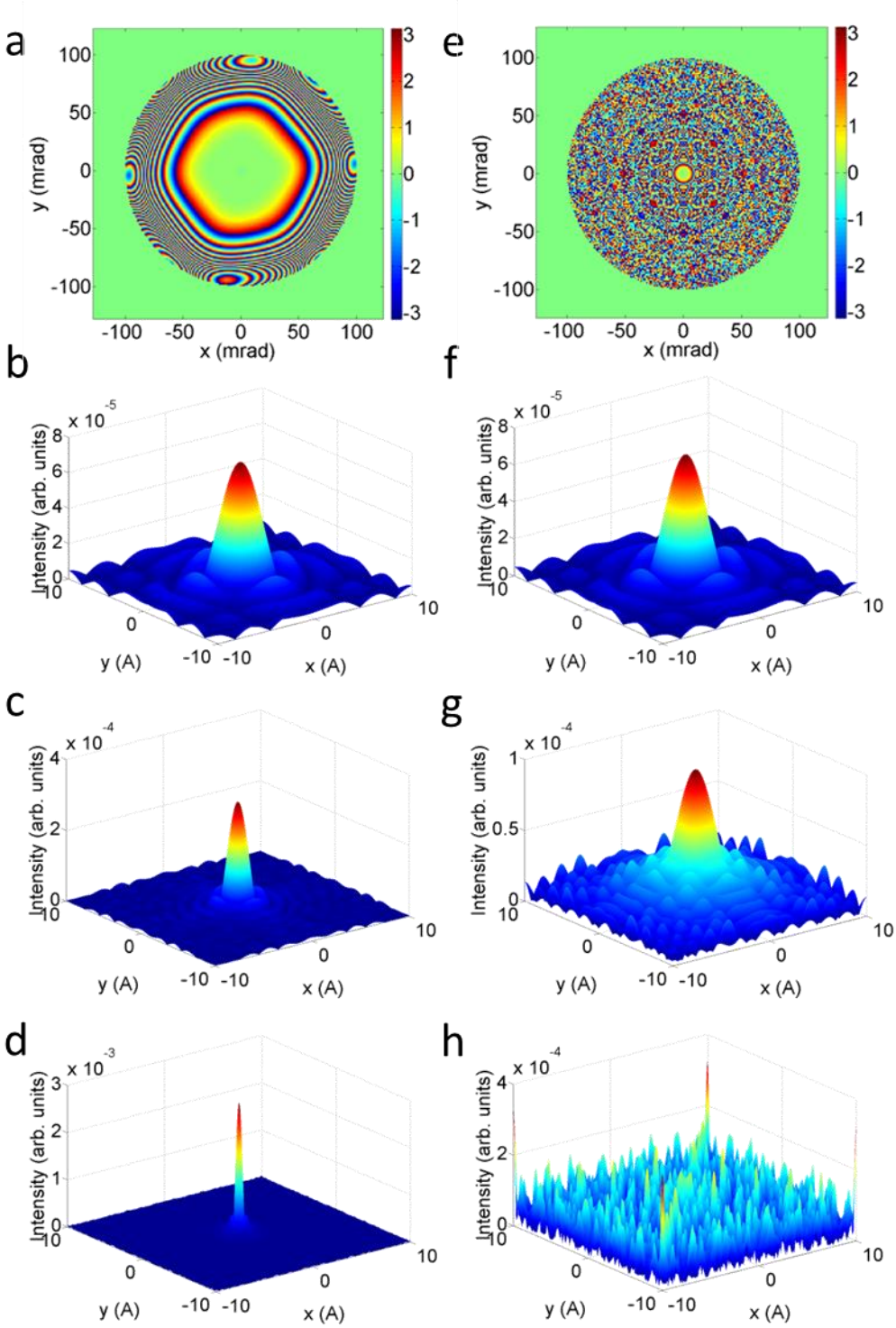

Figure 2.1 Phase plate of the electron probe in the back focal plane when C_3 is (a) 100 nm and (e) 1.2 mm. Electron probe intensity in the incident plane when C_3 is 100 nm and the convergence semi-angle is (b) 5 mrad, (c) 10 mrad, and (d) 30 mrad. Electron probe intensity in the incident plane when C_3 is 1.2 mm and the convergence semi-angle is (f) 5 mrad, (g) 10 mrad, and (h) 30 mrad.

Precise alignment of the aberration corrector includes three steps: rough manual alignment, auto continuous measurement for correction of aberrations up to second order and acquisition of Zemlin tableaus for measuring higher-order aberrations and fine-correction of second-order aberrations. In each step a certain level of correction must be achieved before continuing with the next step. In principle, a larger magnification of the HAADF image used for alignment and a larger value of maximum beam tilt for Zemlin tableaus give higher correction precision. However, the HAADF images need to include enough features for diffractometry. Therefore, I used an Ir sample which has smaller particles than the standard Au sample and thus leads to higher precision and thus better alignment status. The maximum beam tilt of Zemlin tableaus for improving the alignment precision is limited by the stability caused by dynamic tilting of the electron beam during Zemlin tableau acquisition. For more details, the readers are referred to the corresponding corrector manual.

2.3 HAADF and ABF STEM imaging

Among the variety of imaging modes applicable in STEM, only HAADF and ABF, which are applied in this thesis, will be discussed in detail, with emphasis on ABF. By the principle of reciprocity [57], both HAADF and ABF imaging are equivalent to hollow-cone illumination (HCI) in conventional TEM, but with many differences due to the signals coming from different angular range. As shown in Fig. 2.2, the electrons scattered to high angles outside the illumination cone are the signal source of HAADF imaging, while the ABF signal lies inside the illumination cone with the collection semi-angle (β) angular range of about half the convergence semi-angle α (practically the convergence semi-angle can be varied by the selection of condenser aperture size and the collection semi-angle can be varied by the camera length).

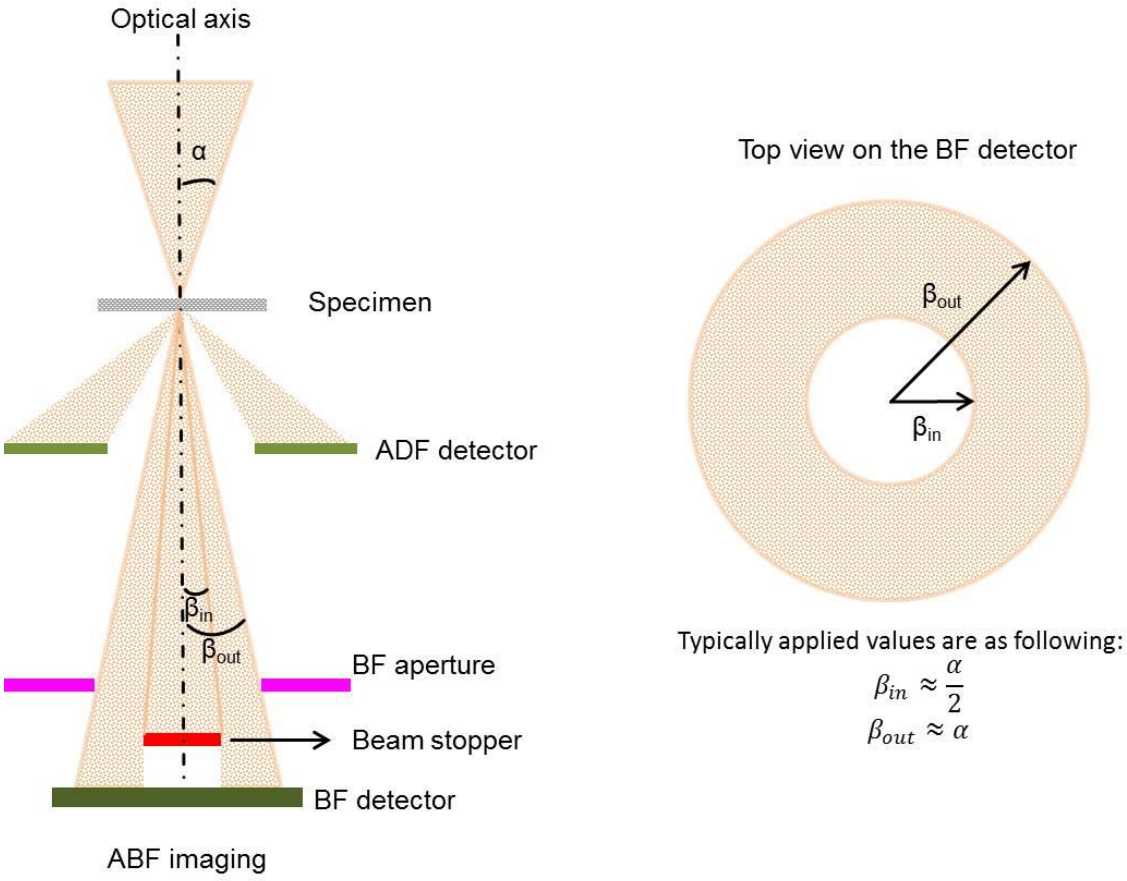

Figure 2.2 Schematic illustration of ABF imaging and HAADF imaging in STEM.

2.3.1 *Z*-contrast HAADF STEM imaging

In general, the electrons scattered outside the illumination cone are used for dark-field imaging and can be generally called ADF. Both thermal diffuse scattering (TDS) and Bragg scattering make important contributions to the ADF images. The lower angular range of the ADF signal includes considerable contributions of elastic Bragg scattering, the dependence of which on atomic number is not simple due to the strong coherent interference. Therefore, as a rough guide, the inner collection semi-angle should be at least three times the convergence semi-angle for incoherent imaging, and ideally amounts to five times to eliminate effects of thickness oscillations in crystals[58]. Imaging with electrons scattered at such large angles is called HAADF STEM imaging, which is dominated by localized TDS favoring a simple interpretation in terms of an incoherent imaging mode and shows atomic number contrast owing to predominant electron scattering at the potential of the nucleus, similar to Rutherford scattering[13, 59-61]. It is known that the intensity in HAADF STEM images is proportional to $t \cdot Z^a$, where t is the sample thickness, Z is the atomic number of the element and a is a parameter between 1.5 and 2 (often quoted as being around 1.7 for most experimental setups) depending on the exact sample

composition and detector geometry[14]. For qualitative determination of atom species and calculations of atomic column distances, HAADF STEM imaging is widely used due to the simple interpretation and the absence of contrast reversal. However, quantitative information needs simulations for comparison. In this thesis, I only apply HAADF STEM for atom position determination; therefore, the quantitative part won't be explained in detail.

The large central hole of the HAADF detector allows convenient integration with EELS, lower angular range ADF (medium-angle ADF (MAADF) and low-angle ADF (LAADF)) and BF techniques (BF, ABF, phase imaging, MABF). This allows atomic-resolution images to be obtained simultaneously with chemical analysis, strain analysis, light element imaging, electrical field analysis, and so on, from individual columns of atoms.

Currently, HAADF STEM images are also used for strain analysis although distortions in STEM images due to sample drift and scan distortions make the measurement of local strain often difficult. This can be approximately solved by post-acquisition data processing, e.g using the Jitterbug package by Lewys Jones[62], which is however time-consuming and difficult to apply to a bunch of data currently. To minimize these difficulties minimizing the sample drift is essential. One reason is the charging caused by hydrocarbon contamination introduced during sample preparation or exposure in the air for long time. The approaches to eliminate contamination include heating the sample over 100 $^{\circ}$C, plasma cleaning, and intense broad electron beam irradiation (i.e. beam shower). The other reason is the stability of the sample holder, which can originate from environmental factors, like mechanical vibrations, electromagnetic fields, or simply from the delay of mechanical stability after moving the sample holder. The former (charging effect) need to find out the exact reason and are normally solved in daily use. The latter one can be solved by waiting (at low magnification in case of radiation damage) and acquiring the image under high magnification without holder movement afterwards.

2.3.2 ABF STEM imaging

ABF STEM imaging has attracted research interest since the first report in 2009 by Okunishi et. al.[32] because of the robust capability of imaging of both heavy and light elements. Despite of the simple interpretation of HAADF STEM images over a wide thickness range, the signal scales strongly with atomic number which is beneficial when intending to distinguish between elements with close atomic numbers but is a disadvantage when heavy and light elements coexist. In ABF imaging electrons scattered to relatively

small angles are collected. This low-angle scattering is caused by the atom potential remote from the very core region where the potential difference among atoms of different Z is less pronounced. Therefore, collecting electrons scattered at low angles results in similar sensitivity to both heavy and light elements. The reduced dependence of image intensity on atomic number, approximately $\sim Z^{1/3}$ [43], compared with that of HAADF STEM imaging, and the large thickness range allowance makes it the most applicable TEM technique in recent years for studying light elements.

As an illustration of the capability of this technique, I present experimental results on $LiFePO_4$. Fig. 2.3 shows an HAADF image of a focused ion beam (FIB)-prepared specimen and a thickness map. Two areas with thicknesses below 50 nm and 100 nm were selected for simultaneous HAADF and ABF imaging (Fig. 2.4). Li and pure O atomic columns are clearly visible in ABF images whereas these are invisible in HAADF images (especially for the thick specimen). Note that in ABF images, atom columns show up as dark spots on a bright background, which resembles absorptive contrast. In HAADF images, atom columns show up as bright spots on a dark background. I note that in the HAADF image from thin specimen regions bright spots are occasionally observed at Li atom columns. This might be due to some substitution of Li by Fe.

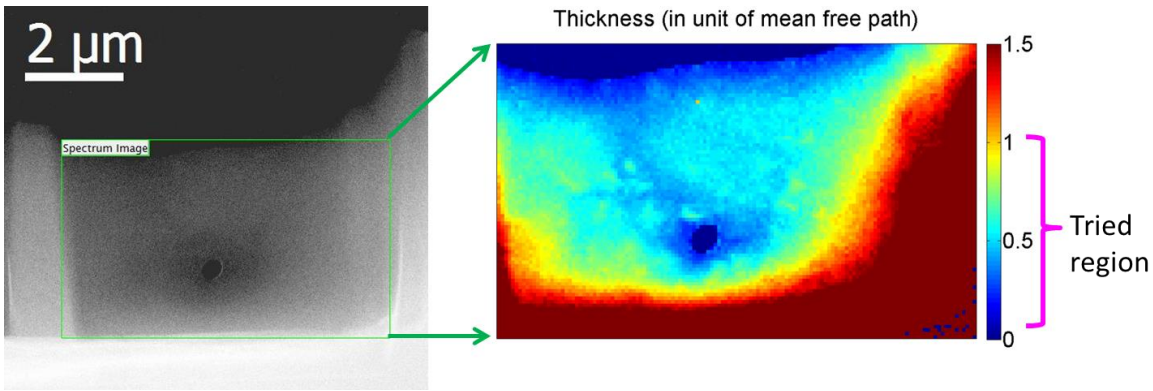

Figure 2.3 Overview of a $LiFePO_4$ TEM specimen prepared by FIB. Left: HAADF image taken with a collection semi-angle of 90–370 mrad. Right: Thickness map using an EELS collection semi-angle of 60 mrad. The thickness scale is in units of the mean free path which amounts to 101.4 nm [63, 64].

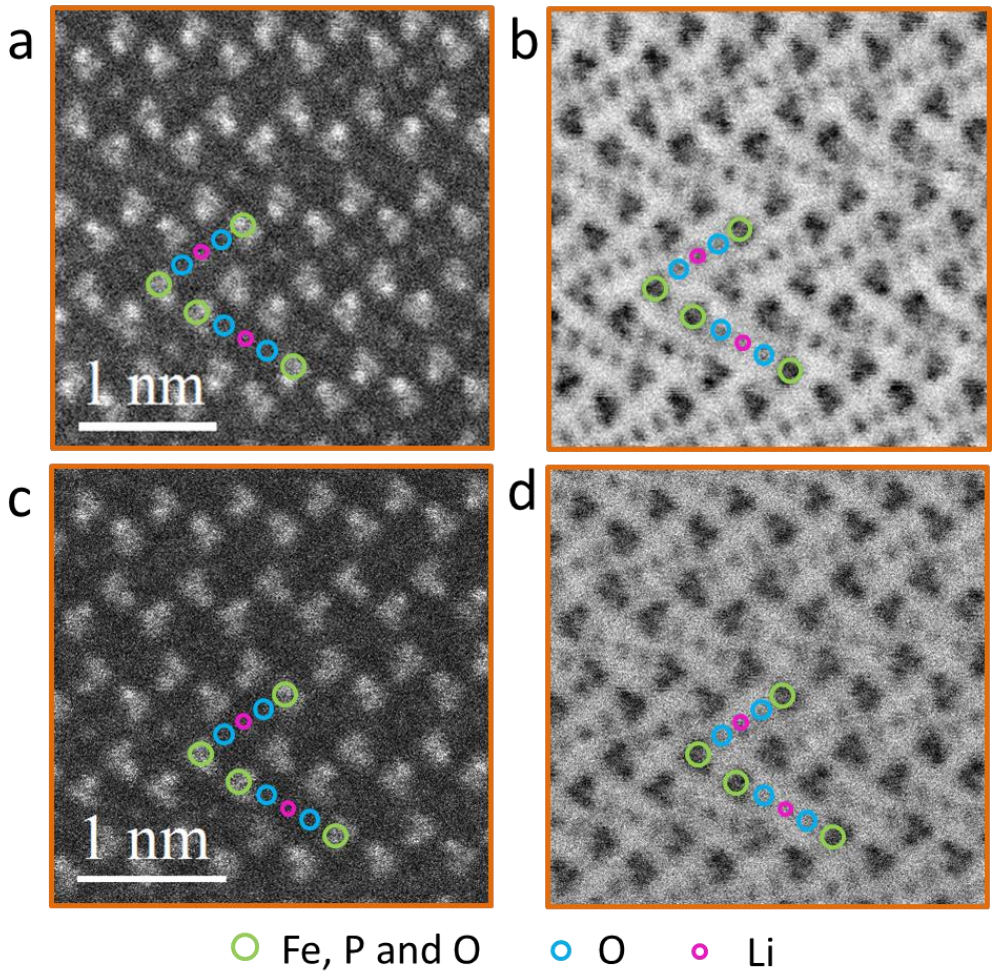

Figure 2.4 (a,c) HAADF images acquired using collection semiangles of 90–370 mrad. (b,d) ABF images using collection semi-angles of 11–22 mrad. (a) and (b) were simultaneously acquired from a sample region below 50 nm thickness. (c) and (d) were simultaneously acquired from a sample region of about 100 nm thickness. The convergence semiangle was 22 mrad and the probe size was about 0.08 nm.

Given the fact that the ABF detector is collecting diffracted electrons within the illumination cone, the contrast mechanism is more complicated than *Z*-contrast imaging. As shown in Fig. 2.5, different from the HAADF image intensity which has monotonic relationship with both atomic number and thickness, the ABF image intensity shows much less sensitivity to thickness. Furthermore, the ABF intensity fluctuates with thickness leading to possible reversed contrast ratios between heavy and light elements at different thicknesses. This makes it essential to acquire simultaneous HAADF and ABF images to combine both imaging modes capabilities, especially the monotonic behavior of HAADF and light element imaging of ABF.

The thickness dependence of the ABF signal is actually a consequence of the thickness dependence of the elastic scattering distribution in the diffraction plane[31, 43]. It is

known that incoherence in ADF is the result of both the detector geometry and the TDS that reduces the intra-column coherence, while ABF is collecting low-angle scattered electrons that interfere strongly with each other. Findlay et al. explored the reason and suggested an s-state model attributing the *z*-dependent (here *z* is the electron beam propagation distance inside the sample) phase factor contribution to the exit wave function [31, 43]. This model is based on the assumption of a specimen with well-separated atom columns while it fails for closely spaced columns and fine electron probes.

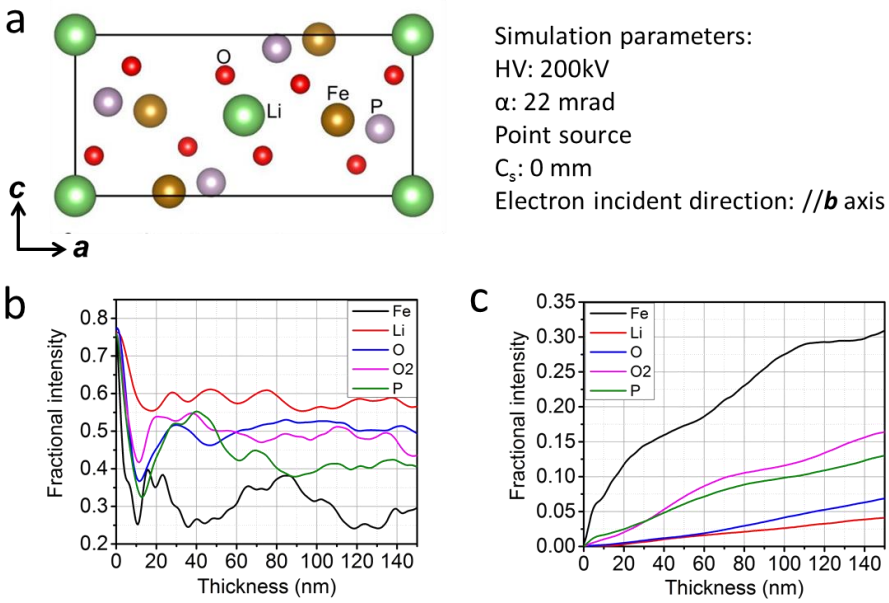

Figure 2.5 (a) Structure model of $LiFePO_4$ viewed along the [010] axis. Simulated (b) ABF (11–22 mrad) and (c) HAADF (90–370 mrad) image intensity of each atomic column as function of thickness. The convergence semi-angle is 22 mrad and HT is 200 kV.

The detailed imaging mechanisms of ABF imaging are still under investigation. Current researches on the imaging dynamics are mainly conducted by comparison between simulation and experiments. In Findlay's paper [43], the factors, like defocus, convergence and collection semi-angle as well as inter-column spacing and local disorder are presented. Here, I don't repeat this information, since it will partly be represented in my results during investigations of reliability of atomic column position determination by ABF STEM imaging.

2.3.3 Detector axial alignment and sensitivity

From the descriptions above, it is clear that the acquired signal and thus information extractable is critically dependent on the collection semi-angles, which are theoretically assumed to be centered with the optical axis. In practice the centering of the annular detectors might not be fulfilled. In the following, the reasons for this and solutions how to correct for centering in the JEOL ARM200F will be presented.

As shown in Fig. 2.6, the "ABF detector" is actually composed by three parts: a non-spherical BF detector covering a large angular range, an aperture the size of which can be selected (6 mm, 3 mm, 1 mm, and 0.3 mm) which is used to limit the outer collection angle, and a beam stopper to block the central beam and thus limiting the inner collection angle. As can be seen from Fig. 2.6b, the 1 mm and 0.3 mm BF apertures cannot be used for ABF imaging because they are smaller than the beam stopper. Only the 3 mm aperture can give the angular requirement of ABF imaging, i.e. $\beta_{out} \approx 2\beta_{in}$. All of them can be inserted to and extracted from the optical path, but only the BF aperture is adjustable by the user from the control panel. To achieve highest efficiency and to make use of the most homogeneous sensitivity region (Fig. 2.9a and Fig. 2.9b), the beam stopper has to be centered on the BF detector mechanically by a company engineer. Then the BF aperture can be adjusted to be concentric with the beam stopper, while the optical path can be easily adjusted by the projector lens.

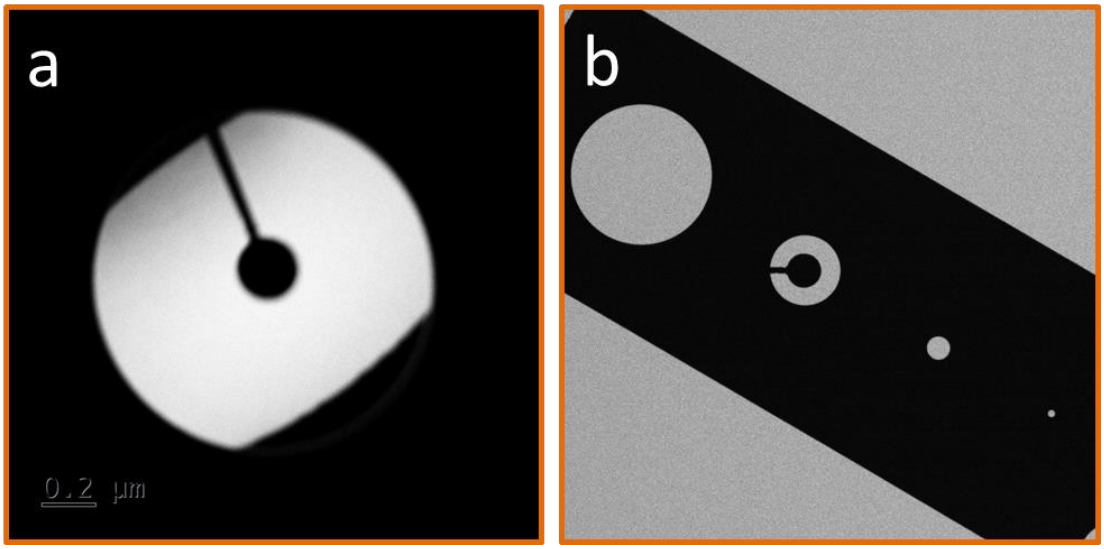

Figure 2.6 (a) Scanning image of the detector (with inserted beam stopper) showing variations in detector sensitivity. (b) Beam stopper (centered on 3 mm aperture) and BF apertures on pre-GIF Gatan XP1000 CCD.

The HAADF detector is physically simpler but more complicated to center [65]. Only the projected inner detector hole can be viewed on the CCD. Owing to manufacturing inaccuracies, the axis of the inner detector hole is not exactly parallel to the electron beam (Fig.2.7), i.e. the position of the projected image of the hole (magenta circle in Fig.2.8d) does not exactly correspond to the center of the sensitive area of the detector. Therefore, the centering of optical axis with the shadow image does not really guarantee that the detector is centered.

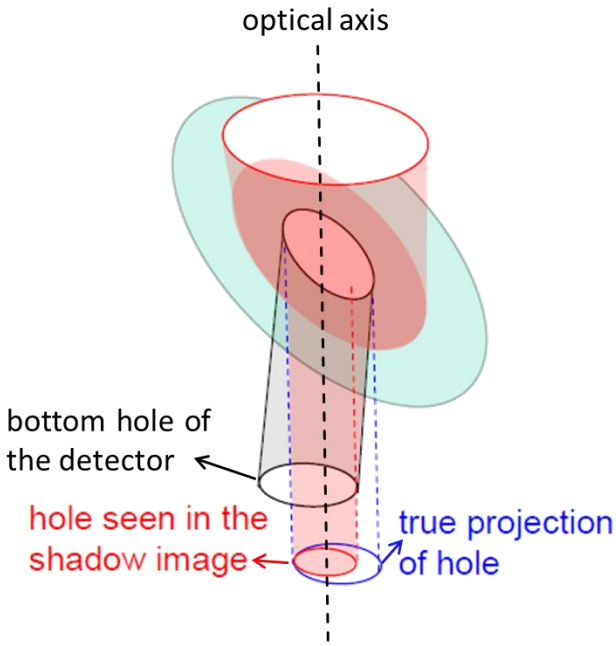

Figure 2.7 Schematic illustration of the JEOL HAADF detector.

In order to center the detector properly an electron beam with small illumination angle is scanned across the detector (Fig. 2.8a, b). Whenever this beam touches the sensitive region of the detector a signal will become visible from the HAADF detector. Detection of these signals along the circumference of the hole gives the real shape of the hole (turquoise circle in Fig. 2.8d).

To make sure that all detectors used are on the optical axis of the microscope, the beam stopper needs to be located at the center of HAADF detector, which also needs a company engineer to mechanically adjust. From the descriptions above, it is always easier to adjust the beam stopper, but if the other components are too far from the optical axis, they should also be adjusted mechanically.

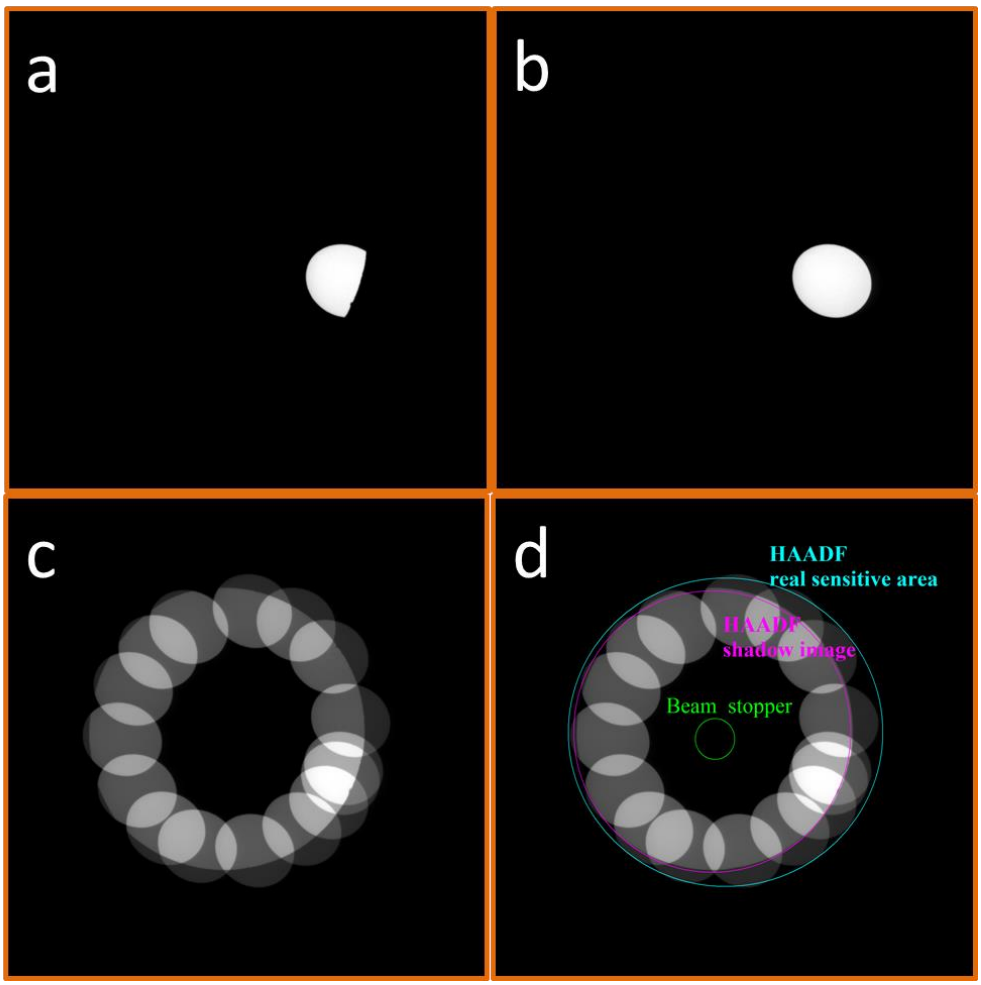

Figure 2.8 Pre-GIF CCD image of the 150 µm CL aperture at a camera length of 2 cm (a) with HAADF detector inserted (b) with HAADF detector retracted. (c,d) Superposition of all the images. In (d) the projected hole is shown in magenta color and the real hole of the beam-sensitive area in turquoise color for comparison.

The detector centering for the Gatan ADF detector was also tested. The only difference of this procedure is that the GIF CCD has to be used because the ADF detector is too close to the PreGIF CCD.

As reported[66-68], the detector sensitivity is quite important for normalization of the HAADF intensity to the incident beam current. Only by this normalization, quantitative STEM imaging becomes possible. Although I won't present any quantitative STEM imaging in this thesis, a check of the detector sensitivity is also important regarding the angular sensitivity of the signal variation in the BF region. As shown in Fig. 2.9, data for the JEOL BF (Fig. 2.9a), ABF (Fig. 2.9b), JEOL HAADF (Fig. 2.9c) and Gatan ADF (Figure 2.9d) detectors are presented. It is apparent that the ABF detector sensitivity is quite homogeneous. The HAADF detector sensitivity is more inhomogeneous which will influence the HAADF contrast.

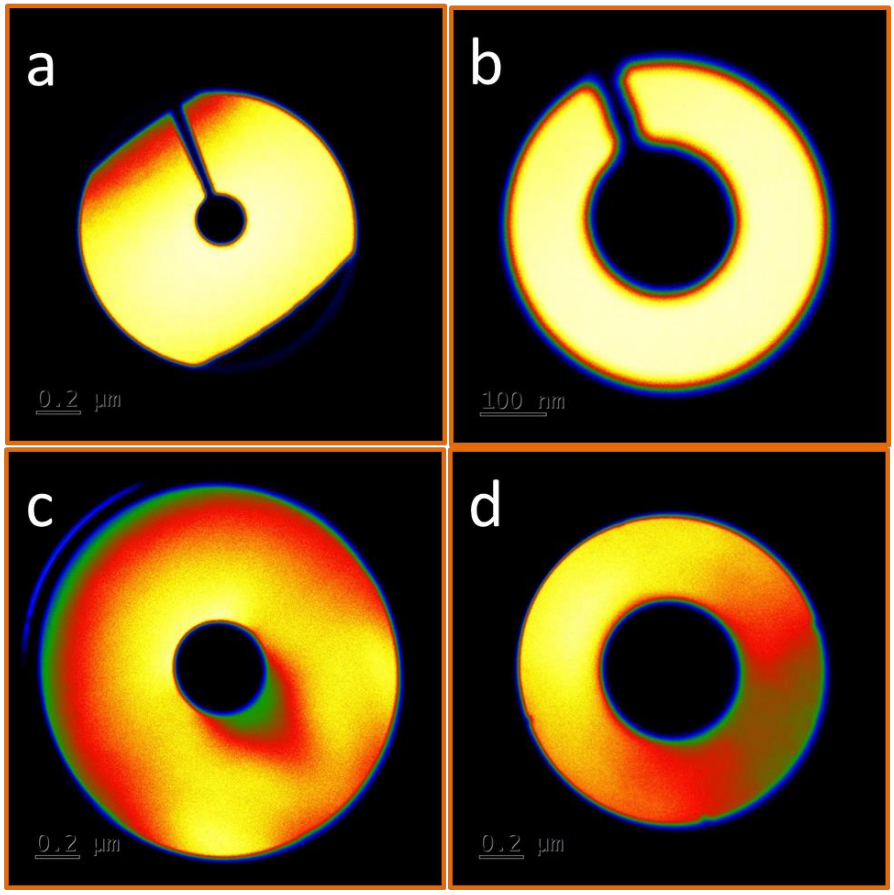

Figure 2.9 Detector sensitivity (a) JEOL BF detector with only beam stopper inserted (b) JEOL BF detector with 3 mm BF aperture inserted (ABF mode) (c) JEOL HAADF detector (d) Gatan ADF detector. In all cases a probe size 10 c and a 30 µm CL aperture were used.

2.4 EELS

EELS involves analyzing the energy distribution of the electrons after having interacted with the specimen[69]. The compositional, chemical, and bonding information extracted from such analysis makes EELS a quite useful technique in material science. There are distinct regions in an EELS spectrum, which can be related to different energy-loss mechanisms[17, 69, 70]: the zero-loss, low-loss and core-loss regions.

2.4.1 Zero-loss peak (ZLP)

The dominant feature in an EELS spectrum is the ZLP due to unscattered electrons elastically scattered electrons, and electrons which have suffered an energy loss less than the width of the ZLP (e.g. phonon excitation). The width of the ZLP reflects the energy spread of the primary electrons and the resolution of the spectrometer. It also provides the energy resolution for the final EELS spectrum, which indicates how much detail can be expected from the low-loss and core-loss region (note that in the core-loss region features are mostly smeared by lifetime broadening). With the application of a cold field-emission

gun used, the energy resolution is typically between 0.4 eV and 0.7 eV. Therefore, phonon scattering, which occurs in the range of few tens of meV[71, 72], is included in the ZLP. Only very recently further improvement of the EELS energy resolution to about 10 meV has opened the door to study phonons[73]. The ratio between inelastic and elastic scattering includes the sample thickness information. In addition, the ZLP together with the low-loss region provides the information for removing multiple scattering effects from the low loss and core-loss region.

2.4.2 Low-loss region

Inelastic scattering from outer-shell electrons leads to excitation of volume and surface plasmons, which are collective oscillations of the valence electrons, and of interband transitions of single electrons from the occupied valence-band states into the empty states of the conduction band. The low-loss region of an EELS spectrum provides information similar to optical spectroscopy, containing valuable information about the band structure and in particular about the dielectric function of a material. This low-loss region can also include parasitic losses due to the excitation of Cherenkov radiation[74, 75], which should be identified and excluded from the low-loss EELS analysis. More details will be presented in chapter 5.

2.4.3 Core-loss region

Inelastic scattering at energies above 50 eV are caused by ionization of inner-shell electrons and are therefore characteristic of the atomic elements in the specimen. It is straightforward to identify the edges by looking at their edge on-set energy and comparing it with reference tables. Bonding and electronic structure only have a marginal effect on the position of these peaks. In favorable cases, when the edges do not overlap, identification and quantification can be carried out. Moreover, the specific shape near the onset of a core-loss edge contains information about the bonding and electronic structure in the material. The fast electron can be seen to probe locally the unoccupied density of states. These studies are termed as electron energy-loss near-edge spectroscopy (ELNES) [76, 77]. Further above the edge, extended energy-loss fine structure spectroscopy (EXELFS) can be seen as a very weak oscillations around the ideal edge shape. This deviation is caused by interference of a secondary ejected electron wave which leaves the excited electron and its backscattered waves from neighbouring atoms. The technique can reveal data on the interatomic distances and the number of neighbouring atoms in the specimen [69].

2.4.4 Tackling with some practical issues

The EELS detector normally has a limited dynamic range. This is a problem if low-loss and core-loss data are to be acquired simultaneously. In this case the acquisition time will be limited by the strong ZLP and the core-loss data will be very noisy if not invisible. To circumvent this problem the dual-EELS capability of the Gatan GIF system is used. In this mode two consecutive exposures of the low-loss and the core-loss regions of the EELS spectrum are recorded with different exposure times on different areas of the CCD detector.

Another issue is radiation damage of the specimen. Especially for the core-loss region, the weak core-loss signal requires longer acquisition time to get an appropriate signal-to-noise ratio. The required high electron dose might destroy the sample. An approach to tackle with this problem is to use sub-pixel scanning, which scans the beam over a lot of sample points (pixels) and integrate the signal to one spectrum pixel. This can be done for 2D- and 1D-spectrum imaging. Instead of a measurement of a single point, one can use, as an option in DigiScan, the live imaging window to view a small local area. This not only reduces the electron dose per area, but also gives control over the area position during data acquisition, which is important in case of specimen drift.

The delocalization of inelastic scattering is the main factor determining the spatial resolution in EELS experiments, especially for the low-loss region[78]. Delocalization refers to the fact that inelastic scattering does not occur at a sharp, predictable point. Instead, it means that the incident electron can excite atomic electrons even if the overlap of the fast-electron field with the wave function of the core electron is small. This delocalization is below 1 nm above 100 eV energy loss but can be as large as 10 nm at energy losses below 5 eV. An additional factor limiting spatial resolution in the core-loss region EELS is electron beam broadening caused by the interaction between the electron beam and the specimen.

2.4.5 Application of EELS in this thesis

For the less beam-sensitive materials the core-loss near-edge structure was mainly investigated. Low-loss spectra were acquired for energy scale calibration and removal of multiple scattering effects. For light elements characterization, especially for the Li battery materials, the low-loss region was used, because the relevant signals appear in this energy-loss range. This has also the advantage of short acquisition times which reduces radiation damage.

Chapter 3 Interfacial Chemistry and Atomic Structure of ZrO_2-$La_{2/3}Sr_{1/3}MnO_3$ Pillar-matrix Structures

Abstract

I studied ZrO_2-$La_{2/3}Sr_{1/3}MnO_3$ pillar–matrix thin films which were found to show anomalous magnetic and electron transport properties. With the application of an aberration–corrected transmission electron microscope, interfacial chemistry and atomic-arrangement of the system, especially of the pillar–matrix interface were revealed at atomic resolution. Minor amounts of Zr were found to occupy Mn positions within the matrix. The Zr concentration reaches a minimum near the pillar–matrix interface accompanied by oxygen vacancies. La and Mn diffusion into the pillar was revealed at atomic resolution and a concomitant change of the Mn valence state was observed.

People involved in this part research: Dan Zhou (1), Wilfried Sigle (1), Eiji Okunishi (2), Yi Wang (1), Marion Kelsch (1), Hanns-Ulrich Habemeier (3), Peter A. van Aken (1).

(1) Max Planck Institute for Intelligent Systems, Stuttgart Center for Electron Microscopy, Heisenbergstrasse 3, 70569, Stuttgart, Germany

(2) JEOL Ltd., 1-2 Musashino, 3-Chome Akishima, 196-8558, Tokyo, Japan

(3) Max Planck Institute for Solid State Research, Heisenbergstrasse 1, 70569, Stuttgart, Germany

3.1 Introduction

In functional oxides such as superconducting cuprates and ferromagnetic manganites the investigation of electrically insulating columnar oxide defects embedded in the conducting matrix materials has experienced an increasing research activity in the past decade.[79-82] From the fundamental point of view, this activity was initiated by the exploration of the crystalline structure and elemental distribution at the interface between the columnar defects and the matrix material with the subsequent strain- and defect-induced modification of their electronic and magnetic properties. Elemental and electronic reconstructions at the interface between complex oxides with different functionalities are challenging phenomena to be explored. They give rise to interference effects between the states across interfaces with the potential to generate new properties and functionalities.[45, 83] Research on self-assembled vertically aligned nanocomposite thin films with two immiscible components hetero-epitaxially grown on single crystal substrates represents another branch of these activities.[79-81, 84] These structures have the advantage of utilizing the functionalities of both components with the possibility to tune the material properties by tailoring the interface-to-volume ratio, hetero-epitaxial strain, or modifying the cation valence state. From the application point of view, columnar non-conducting $BaZrO_3$ or $SrZrO_3$ defects in superconducting $YBa_2Cu_3O_7$ thin films have been proven to enhance the flux-line pinning properties drastically and are used in several 3rd generation commercial superconducting tape fabrication technologies.[85, 86] Additionally, the thermoelectric figure of merit $ZT = (S^2\sigma/\kappa)T$ (with S being the Seebeck-coefficient, σ and κ the electrical and thermal conductivity, respectively) can be enlarged by introducing precipitates and columnar defects, thus reducing the phonon part of the thermal conductivity in order to achieve an "electron crystal / phonon glass''–type material.[87, 88]

In ultrathin $La_{2/3}Sr_{1/3}MnO_3$ (LSMO) films (thickness ~ 45 nm) with a low density (0 – 6 mol%) of ZrO_2 precipitates an unusual low temperature resistivity increase associated with quantum interference effects of the electron waves was observed in conjunction with anomalous magnetic anisotropies.[89-91] Evidently, electronic transport of LSMO is sensitively influenced by the presence of ZrO_2 precipitates. Whereas up to now, only macroscopic properties of ZrO_2-LSMO pillar-matrix systems (charge transport and magnetism) have been studied, microscopic properties at the atomic level were not investigated at all. Here, I report the structure and interfacial chemistry of these precipitates, which are found to exist as pillars in the LSMO matrix. I use aberration-corrected scanning transmission electron microscopy (STEM) and simultaneous electron

energy-loss spectroscopy (EELS) to reveal the structure, composition, and valence state at atomic resolution[92-95] especially for the pillar–matrix interface. The work is regarded as a case study for similar pillar-matrix systems based on functional ceramics with insulating precipitates.

3.2 Experimental section

Zirconium oxide (ZrO_2) and lanthanum strontium manganese oxide ($La_{2/3}Sr_{1/3}MnO_3$, LSMO) were co-deposited epitaxially on (001) single-crystalline lanthanum aluminum oxide ($LaAlO_3$, LAO) substrate by pulsed laser deposition. Stoichiometric amounts of LSMO and ZrO_2 according to (1-x)LSMO+ $x$$ZrO_2$, with x= 0, 0.06, 0.2, and 0.3, were used. Details of the material growth process can be found in Gao *et al.*.[89]

In order to obtain 3-dimensional information, electron transparent specimens for transmission electron microscopy (TEM) studies were prepared perpendicular (cross-sectional view) and parallel (plan-view) to the substrate by grinding, dimpling, and low temperature (under liquid nitrogen) argon ion thinning with a precision ion polishing system (PIPS, Gatan, model 691).

High resolution transmission electron microscopy (HRTEM) images from cross-sectional specimens were acquired using an image-aberration-corrected JEOL ARM 200CF microscope operated at 200 keV. High-angle annular dark-field (HAADF) images, electron energy-loss spectroscopy (EELS) spectrum images from plan-view specimens were obtained using a probe-aberration-corrected JEOL ARM200CF microscope operated at 200 keV, equipped with a Gatan GIF Quantum ERS imaging filter with dual-EELS acquisition capability. The experimental convergence angle was 30 mrad for HAADF and EELS imaging. The corresponding inner and outer collection semi-angles for HAADF were set to 54-220 mrad. The inner and outer collection semi-angles for annular dark field (ADF) images acquired simultaneously during EELS spectrum imaging with Gatan ADF detector were 72−172 mrad, and the collection angle for EELS spectrum imaging was 72 mrad. Multivariate statistical analysis (MSA) was performed to reduce the noise of the EEL spectra with weighted principle-component analysis (WPCA). From HAADF images dislocations have been identified and strain distributions were calculated using geometric phase analysis (GPA) software from HREM Research Inc..

3.3 Results and discussions

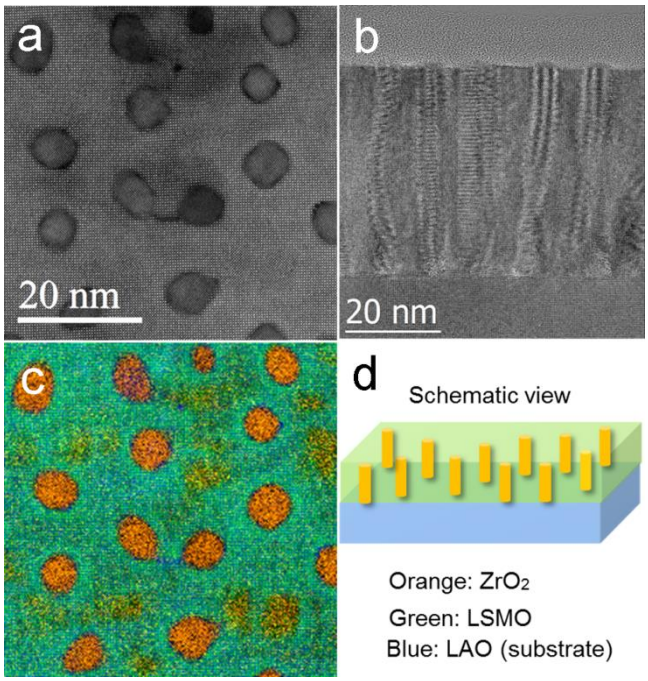

Figure 3.1 (a) Annular dark-field (ADF) image of a plan-view 70 mol%LSMO-30 mol%ZrO_2 sample. (b) HREM image of the side-view specimen with 30 mol% ZrO_2. (c) Three-color EELS spectrum image of the area shown in (a) with Zr-$L_{2,3}$ in orange, Mn-$L_{2,3}$ in blue and La-$M_{4,5}$ in green. (d) A schematic view of the sample.

The pillar structure is verified for both plan-view and side-view specimens. Fig. 3.1a shows the top-view HAADF image of the ZrO_2 (30 mol%)−LSMO thin film with clear circular precipitates. The aberration-corrected HREM image (Fig. 3.1b) of the side-view specimen reveals a columnar structure within the film and the film thickness is measured to be about 45 nm. The phase separation manifests itself in a Moiré contrast arising from the overlap of ZrO_2 and LSMO crystal lattices having different lattice parameters. It shows that the pillars extend all the way through the LSMO film until the substrate. Even though all the pillars penetrate through the film thickness, some penetrate straight with a relatively sharp edge, while other pillars are bent.

The EELS spectrum image of Fig. 3.1a is shown in Fig. 3.1c where the intensities of Zr-$L_{2,3}$, La $M_{4,5}$, and Mn-$L_{2,3}$ edges are displayed in orange, green, and blue, respectively. Oxygen is distributed everywhere and is not shown here. It is clear that pillar-shaped structures of ZrO_2 have formed. They show circular or elliptical, sometimes faceted circumferences. A schematic view of the whole specimen is presented in Fig. 3.1d.

From Fig 3.1b, but also numerous other micrographs, I believe that the vast majority of pillars extend from the bottom to the top of the film. The light orange regions close to the

pillars and in the matrix are attributed to bent pillars, small pillars or pillars ending inside the film. These regions were excluded from the following interface studies. Characteristics of such regions are shown in Fig. 3.2 (bent pillar) and Fig. 3.3 (small pillar). In the LSMO region, brighter columns correspond to heavy La/Sr (A-site) ions, and weaker columns to the lighter mixed Mn-O (B-site) ions. In the pillar region, only Zr columns are visible because oxygen columns are invisible in HAADF due to the small elastic scattering cross section. Bending of pillars will lead to a mixture of the image contrasts as shown in Fig. 3.2. In the overlapping region (upper part of the darker area), the brightness of La/Sr columns is markedly reduced compared to the neighbouring LSMO region. Small pillars (Fig. 3.3) can be identified from the lack of A/B intensity variation. Comparing the contrast and intensity of the atom positions pointed out by blue arrows and yellow arrows reveals the compositional change from LSMO (blue arrows) to ZrO_2 (yellow arrows). I excluded those regions from strain and elemental distribution studies.

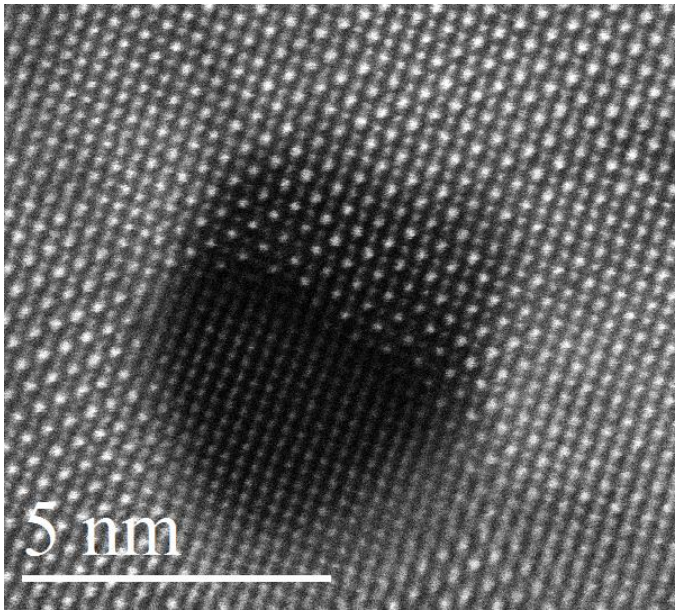

Figure 3.2 HAADF image of ZrO_2 pillar overlapping with the LSMO matrix.

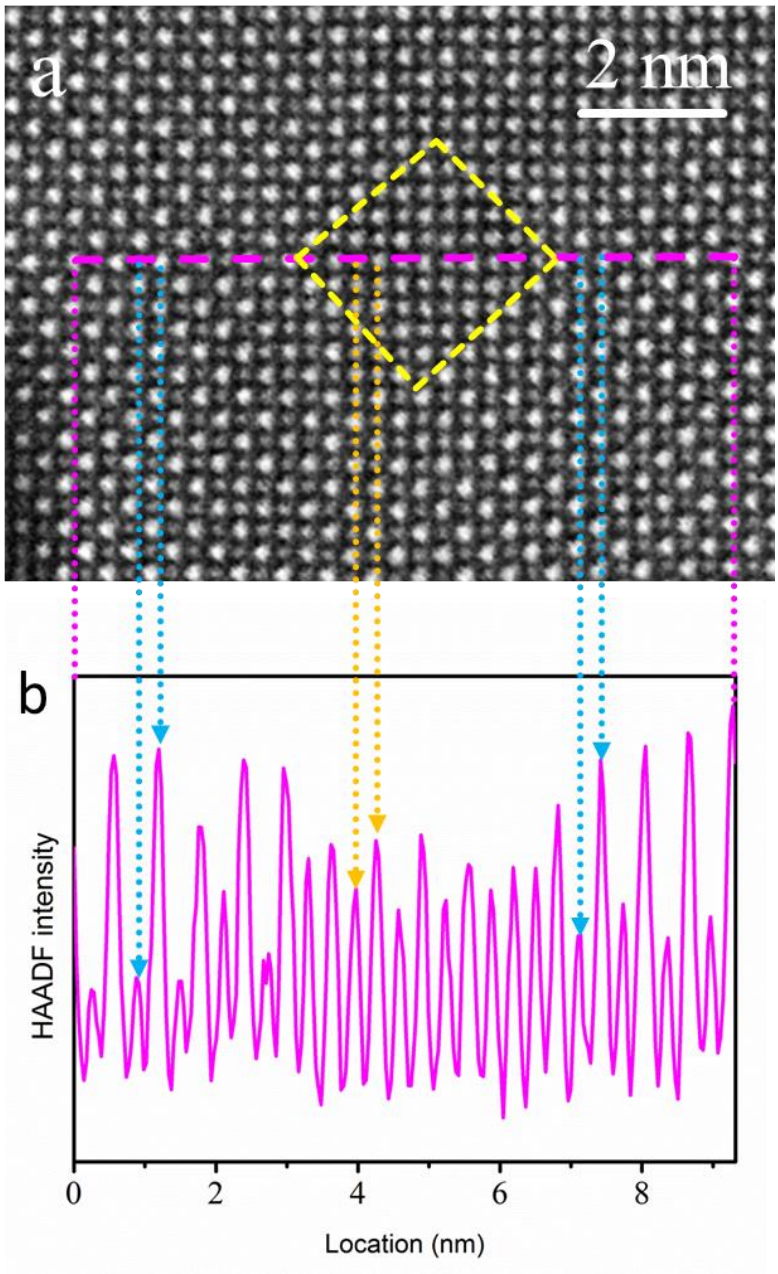

Figure 3.3 (a) HAADF image showing a matrix region with possible existence of small pillars, as indicated by the yellow frame. (b) Line profile of the intensity of the magenta line area in (a). Yellow arrows indicate reduced contrast in the yellow square area in (a), whereas blue arrows represent the contrast of LSMO.

From a statistical analysis of the pillar areas a diameter of (5.1 ± 0.8) nm was deduced for the 30 mol% ZrO_2 specimen and of (3.7 ± 0.8) nm for the 20 mol% ZrO_2 sample.

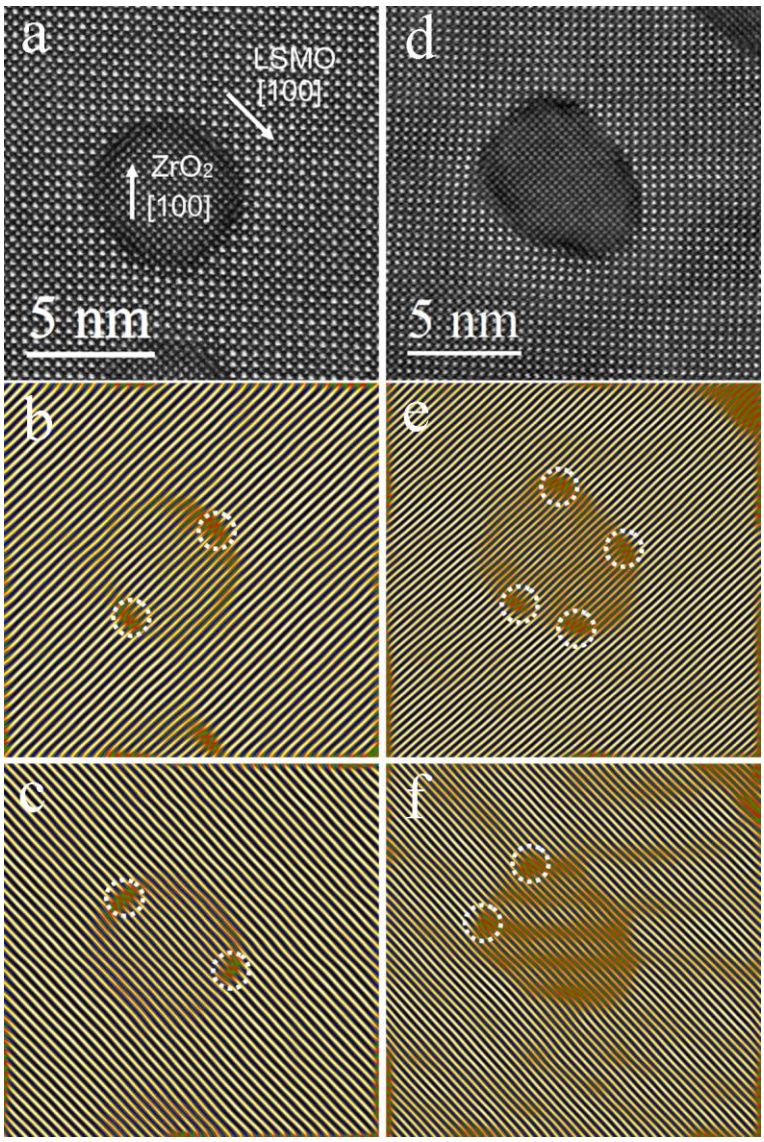

Figure 3.4 (a, d) HAADF images of a plan-view 70 mol%LSMO-30 mol%ZrO_2 sample. Fourier filtered images using (b, e) {100} reflections and (c, f) {010} reflections.

Fig. 3.4a displays a representative high magnification HAADF image of a pillar with sharp interfaces. Towards the interface to the matrix the column brightness is reduced. As will be explained later, this is most likely related to the substitution of Zr by Mn. I note that bent pillars do not exhibit this type of contrast (see Fig. 3.2 and Fig. 3.3) and were excluded from strain and elemental analysis.

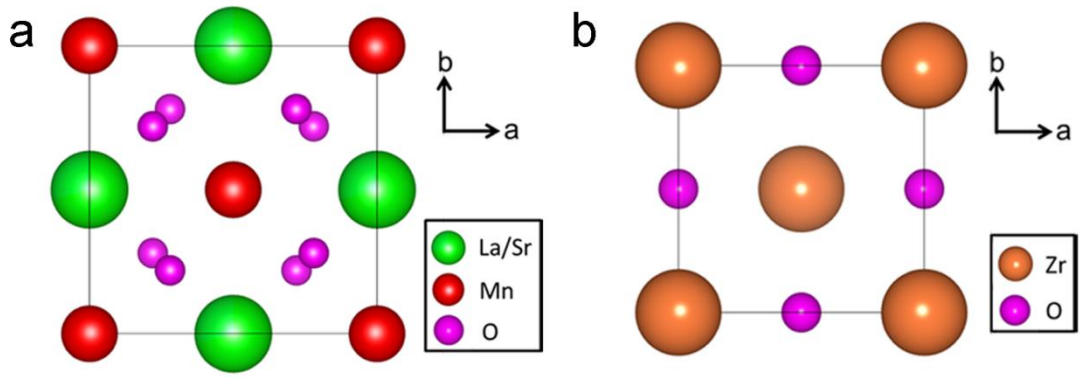

Figure 3.5 Structure model of tetragonal LSMO (a) and tetragonal ZrO_2 (b) viewing along [001] direction.

Since a [001]-oriented LAO substrate was used, the orientation relationship between the thin film and the substrate can be determined from the HAADF and HREM image of the top-view and cross-section specimens. To facilitate the correlation of crystallographic orientation between LAO, LSMO, and ZrO_2, I use here LAO[96] and LSMO[97, 98] in the tetragonal notation (Space group I4/mcm, No. 140) and ZrO_2 in the tetragonal system (space group P42/NMCS, No. 137).[99] The corresponding crystal structure can be found in Fig. 3.5. With our low sample-preparation temperature of 770 $^{\circ}$C,[89] pure ZrO_2 is expected to crystallize in the monoclinic phase[100, 101] which however doesn't match with the square atomic arrangement seen in the HAADF image (Fig. 3.4a). I believe that tetragonal or cubic ZrO_2 is formed by partial substitution of Zr by Mn atoms as will be explained in detail later. Here I describe it in the tetragonal system to facilitate our description. Thus the orientation relationships of LSMO and ZrO_2 with respect to the LAO substrate are as follows:

LSMO[100]//LAO[100], LSMO[001]//LAO[001]

ZrO_2[110]// LSMO[100], ZrO_2[001]//LSMO[001]

The presence of faceted interfaces between ZrO_2 and LSMO (Fig. 3.4a) indicates a preference towards $\{110\}_{ZrO_2}/\{100\}_{LSMO}$, and $\{100\}_{ZrO_2}/\{110\}_{LSMO}$ interfaces.

As reported in a previous paper on this group of material,[91] the *a* and *b* values of LSMO are 5.4472 Å, 5.4483 Å, 5.4624 Å, and 5.4471 Å for LSMO films with 0 mol%, 3 mol%, 6 mol%, and 20 mol% ZrO_2, respectively. This means that the LSMO crystal lattice expands by the addition of ZrO_2, but partially relaxes again at high ZrO_2 content.

I use the *a* and *b* values of LSMO with 20 mol% ZrO_2. For ZrO_2, depending on sample preparation, ***a*** values range from 3.562 Å[99] to 3.646 Å.[102] Thus LSMO and ZrO_2 is

expected to have a mismatch of about (5.3–7.5) %. For the 30 mol% ZrO_2 sample, by measuring the plane distances of ZrO_2 pillars and surrounding matrix, I found a lattice mismatch between LSMO and ZrO_2 of from 5.6 % to 9.2%. These values are large enough to initiate the nucleation of misfit dislocations at the interfaces, which are confirmed by TEM. The visibility of misfit dislocations in the *ab*-plane can be enhanced by Fourier filtering selecting {100} and {010} reflections in the GPA analysis (Fig. 3.4). For the pillar shown in Fig. 3.4a, the misfit dislocations appear in pairs along *a* and *b* planes, as shown in Fig. 3.4b, c. Fig. 3.4e, f show the dislocations along a and b planes for the pillars shown in Fig. 3.2d. It is directly visible that the dislocations along *b* planes are not paired. Choosing the x-axis parallel to [100] and y-axis parallel to [010] direction and using the matrix as reference area, I get the symmetric strain-field image in Fig. 3.6. It is obvious that the compressive strain extends into the matrix regions where non-paired misfit dislocations occur, whereas the strain is relaxed for the matrix regions with paired misfit dislocations.

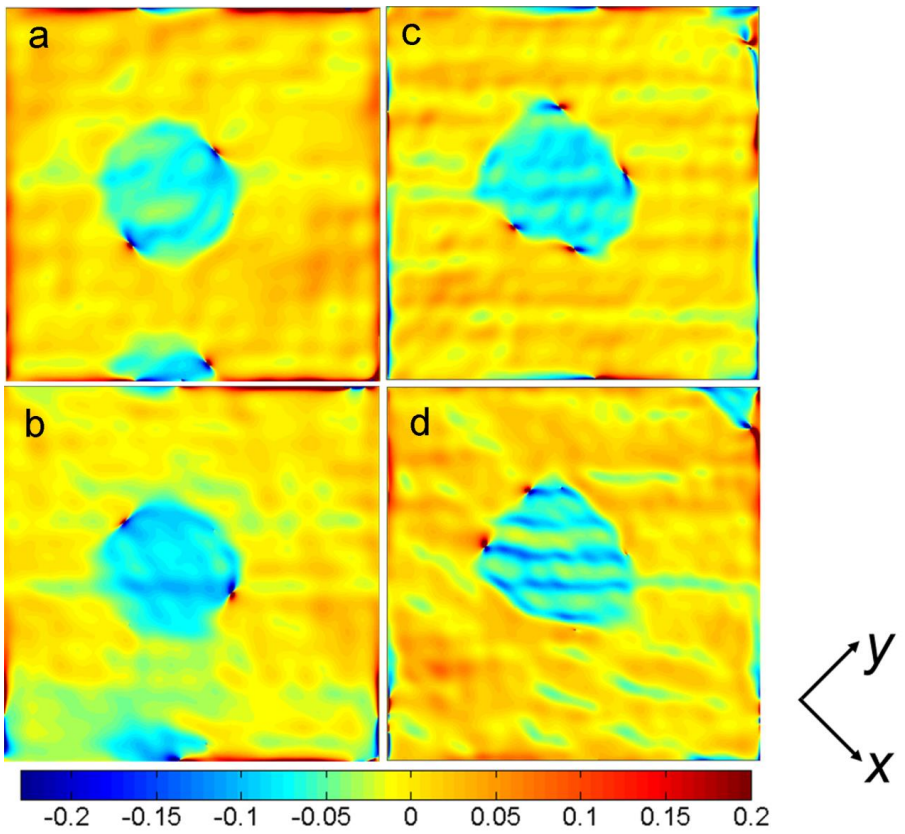

Figure 3.6 Strain field images of the area shown in Fig. 3.4 a and d. (a) ε_{xx} and (b) ε_{yy} of Fig. 3.4a showing strain relaxed for the pillar-matrix interface with paired dislocations. (c) ε_{xx} and (d) ε_{yy} of Fig. 3.4d showing that compressive strain extends into the matrix on the side where misfit dislocations are missing (Fig. 3.4d, bottom right). This is not visible in the perpendicular direction because the misfit dislocations are paired (Fig. 3.4c).

These examples show that the overall structure of the pillars has not reached elastic equilibrium yet. This is because, according to the lattice misfit, the pillar size has reached a value which only just enables nucleation of a misfit dislocation. Probably because of insufficient thermal activation (low deposition temperature, 770 $^{\circ}$C[89]) or high deposition rate, not every pillar has managed to nucleate a sufficient number of misfit dislocations and remains in a 'superstrained' state with tensile stresses on the ZrO_2 side of the interface. The formation of misfit dislocations is one way to relax the strain in a two-component system. Alternatively, strain can be accommodated by interdiffusion. This reduces the abruptness of the interfaces in terms of lattice misfit and chemical potential.[103] In the present system I found several evidences for interdiffusion which will be discussed below: (i) Zr atoms are detected in the LSMO matrix; (ii) Mn atoms are found within the ZrO_2 pillars; (iii) a third Mn-rich phase is formed connecting adjacent pillars; details of the latter will be presented in next chapter.

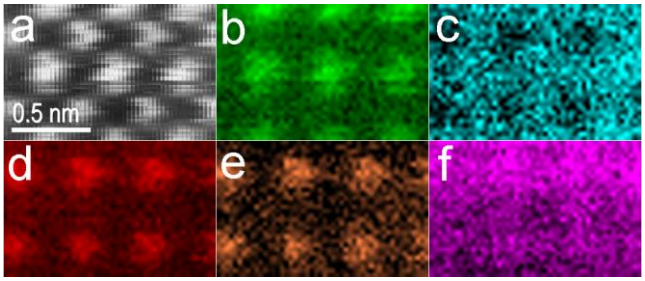

Figure 3.7 (a) ADF image of the LSMO matrix area in a plan-view 70 mol%LSMO-30 mol%ZrO_2 sample. EELS spectrum image of (b) La-$M_{4,5}$ (integration window 821–868 eV), (c) Sr-$L_{2,3}$ (1935–2066 eV), (d) Mn-$L_{2,3}$ (627–678 eV), (e) Zr-$L_{2,3}$ (2218–2404 eV), and (f) O-K (520–578 eV).

The atomic resolution EELS spectrum imaging (SI) of the matrix region in the 30 mol%-ZrO_2 sample (processed with PCA to improve the signal-to-noise ratio of spectra at each pixel) is shown in Fig. 3.7. La and Sr (Fig. 3.7b and Fig. 3.7c) occupy the same locations as expected from the LSMO structure. Mn and Zr (Fig 3.7d and Fig. 3.7e) take the same location which confirms that Zr is present in the matrix and occupies Mn/O column positions. The O map shows minimum values at La/Sr positions while being present everywhere else, which is as expected from the LSMO structure.

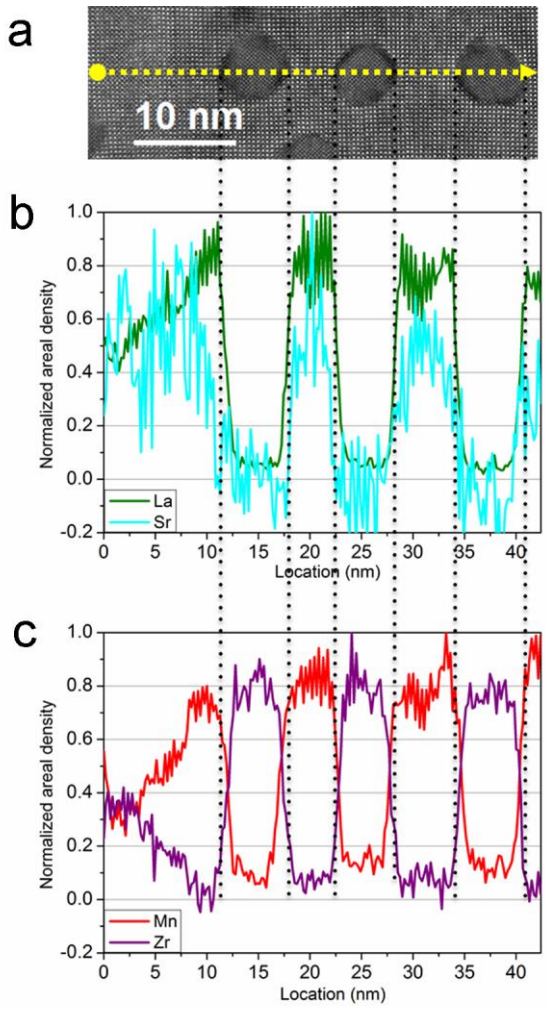

Figure 3.8 (a) ADF image of a plan-view 70 mol%LSMO-30 mol%ZrO_2 sample. EELS spectrum line profile of areal density of (b) La-$M_{4,5}$ and Sr-$L_{2,3}$, and (c) Mn-$L_{2,3}$ and Zr-$L_{2,3}$ of the line drawn with identical integration windows to Fig. 3.7. The areal densities are normalized to the maximum value for each element.

To obtain an overview of the elemental distribution, EELS line profiles across several ZrO_2/LSMO interfaces are shown in Fig. 3.8 along with an ADF image (Fig. 3.8a). The EELS line profiles are normalized to the maximum areal density for each element. The ADF image contrast in the region left of dashed lines of Fig. 3.8 is similar to that found in orange regions of Fig. 3.1 (also shown in Fig. 3.3). I therefore suppose that this area does not represent the pure LSMO matrix but is influenced by the existence of a small or inclined pillar. Neglecting this region, I find that La and Mn concentrations quickly drop within the pillar region, however not reaching zero concentration. This shows that La and Mn atoms are present in the zirconia lattice. Sr shows a less steep gradient across the interface than the other cations and is absent inside the pillar.

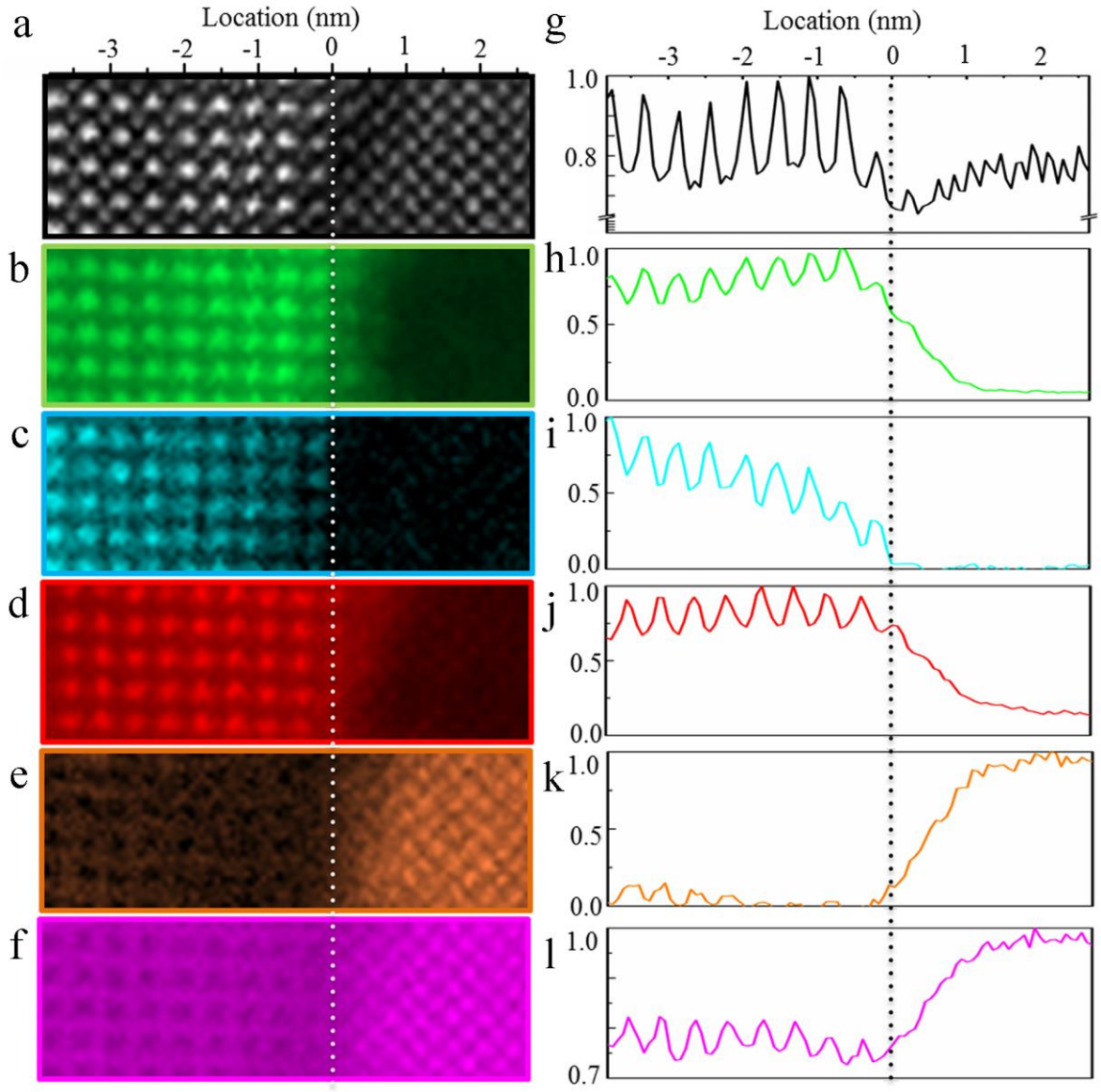

Figure 3.9 (a) ADF image of a plan-view 70 mol%LSMO-30 mol%ZrO_2 sample at the pillar-matrix interface (matrix, left of the dotted line; pillar, right of the dotted line). Atomic-resolution EELS spectrum image of areal density of (b) La-$M_{4,5}$, (c) Sr-$L_{2,3}$, (d) Mn-$L_{2,3}$, (e) Zr-$L_{2,3}$, and (f) O-K with identical integration windows to Fig. 3.7 of the pillar-matrix interface area shown in (a). The integrated line profiles of images (a) to (f) are shown in (g) to (l) respectively. The integrated areal density was normalized to the maximum value in each profile. The *x*-axis in (g) to (l) is the location axis as shown in (a), and the *y*-axis is the normalized intensity.

A detailed elemental distribution from an area free from small or inclined pillars is shown in the atomically resolved EELS maps as displayed in Fig. 3.9 along with the simultaneously acquired ADF image. In the bulk regions, the elements are distributed as expected from the structure models of LSMO and ZrO_2: Within LSMO, La (Fig. 3.9b) and Sr columns (Fig. 3.9c) take the same positions, Mn-O (Fig. 3.9d & f) columns are located in the center of four La/Sr columns, Zr columns are located at Mn-O columns, which is consistent with the results presented in Fig. 3.7, and pure oxygen (Fig. 3.9f) is located

between La/Sr positions. Mn is octahedrally surrounded by oxygen atoms. Along the <001>-projection, mixed Mn−O columns and pure O columns exist. In the Mn map the Mn−O columns are clearly resolved. Because of the limited spatial resolution of the oxygen map (Fig. 3.9f) the columns containing oxygen are not visible separately but appear as horizontal and vertical stripes in LSMO. Within ZrO_2, Mn (Fig. 3.9d), Zr (Fig. 3.9e), and O (Fig. 3.9f) columns are atomically resolved. La is found to exist within the pillar, while the concentration is too low to be atomically resolved by this analysis (Fig. 3.9b). Mn is found to be located in the Zr columns. However, the gradual increase of the Zr concentration profile (Fig. 3.9k) and the ADF image intensity (Fig. 3.9g) from the interface to the pillar center suggests that lighter Mn substitutes heavier Zr inside the pillar, which contributes to the darker contrast at the interface and the stabilization of ZrO_2 .

From the atomically resolved EELS maps and the ADF image, line profiles were obtained by integrating intensities in the direction parallel to the interface. These are displayed in Fig. 3.9g-l. I mark the interface position by a dotted line, right of which no Sr signal was detected. For the ADF image, I find an increasing intensity followed by a damping on the LSMO side when approaching the interface. Such a damping is also visible on the ZrO_2 side of the interface. This damping is obvious in every ADF or HAADF image as a dark circular region around each pillar. Since HAADF image intensity is proportional to the atomic number, the intensity damping here can be directly correlated with the elemental distribution at the interface. Oxygen vacancies were found on both LSMO and ZrO_2 sides of the interface, as can be seen from Fig. 3.9f and l.

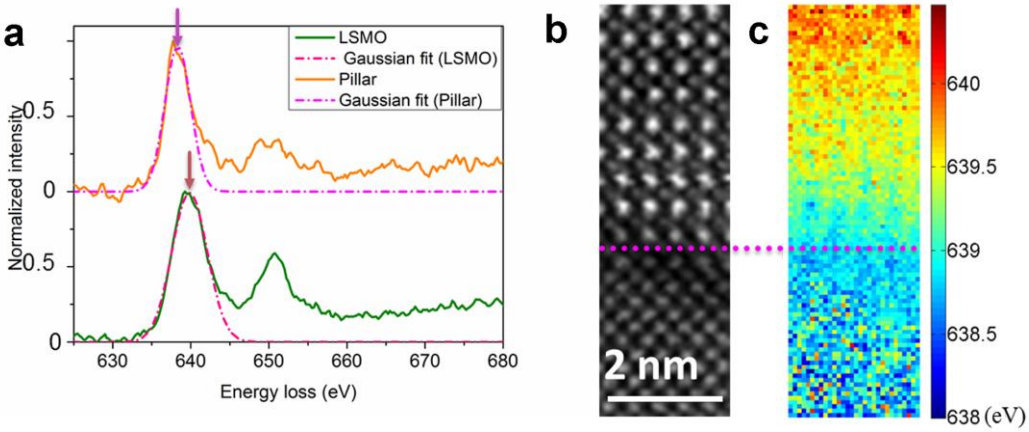

Figure 3.10 (a) Nonlinear Gaussian least square fitting on background subtracted Mn-L_3 edge of the two spectra from pillar and matrix region of the plan-view 70 mol%LSMO-30 mol%ZrO_2 sample; (b) same as Fig. 3.9a, clockwise rotated by 90°; (c) Mn-L_3 peak positions obtained from Gaussian fitting of the background subtracted Mn-L_3 spectrum image recorded from the area in (b).

The valence state of Mn was checked by doing nonlinear least square fitting of a Gaussian peak to the Mn L_3 peaks, as shown in Fig. 3.10. Spectra from the matrix region and the pillar center (Fig. 3.10a) show Mn L_3 peak positions of 639.75 eV and 638.25 eV, respectively, *i.e.* a difference of 1.5 eV. Comparison with literature data[104, 105] shows that this can be interpreted as a reduced valence state of Mn in the pillar. Applying the same procedure to the Mn spectrum image in Fig. 3.9d from the area in Fig. 3.10b, which is a replica of Fig. 3.9a, I obtain the Mn L_3 peak position map in Fig. 3.10c, showing a decrease of Mn valence state from the matrix to the pillar.

The concentration profiles shown in Fig. 3.9 show enhanced La and Mn concentrations at the pillar-matrix interface. I note here that this enhancement is hardly visible in between close pillars. Sr is slightly depleted in this interface region whereas Zr is almost absent there. It seems that La occupies Sr positions close to the interface and the overall interface composition resembles $LaMnO_{3-x}$. As shown in Fig. 3.10, the Mn valence at the interface gradually decreases as compared to the LSMO matrix, probably to a value between 2.5 and 3 for about two atomic columns before the interface line, and to a value between 2 and 2.5 in the pillar. Because the La valence is 3+, charge balance can be obtained by introducing oxygen vacancies into the interface region. A loss of oxygen in this region is indeed shown in Fig. 3.9(l). Assuming a Mn valence of 2.5+, x would be 0.25, corresponding to an oxygen vacancy concentration of 8 %.

It is known that Mn can stabilize the tetragonal or cubic structure of ZrO_2 at low temperatures by varying Mn concentrations.[106-108] Our observation of tetragonal or cubic ZrO_2 pillars and the presence of Mn within the ZrO_2 pillars indicates that this stabilization is a driving force for Mn dissolution within the pillars. This has also been observed by other groups in the past, e.g. [107, 109] For charge balance reasons oxygen vacancies have to accompany the Mn_{Zr} substitution. This fits well with our observation of a loss of oxygen in the interface region where the concentration of Mn_{Zr} is particularly high. The incorporation of oxygen vacancies permits stabilized zirconia to conduct O^{2-} ions, provided there is sufficient vacancy mobility, a property that increases with temperature.

As a consequence of the Mn_{Zr} substitution, the replaced Zr ions diffuse into the LSMO matrix. The detection of Zr in LSMO is consistent with former results,[110] where Zr-substituted $La_{0.7}Sr_{0.3}Mn_{1-x}Zr_xO_3$ with $0 < x < 0.20$ was investigated by neutron diffraction revealing that substitutional Zr^{4+} occupies the Mn site. Zr^{4+} most likely replaces Mn^{4+} ions [110], because of charge balance. However, one has to notice that the ionic radius of Zr^{4+} is 0.72 Å whereas that of Mn^{4+} is only 0.53 Å. This introduces strain and increases

the lattice parameter of LSMO.[91] This imposes an upper limit to the soluble Zr amount. At concentrations above this solubility limit ZrO_2 precipitates nucleate, leading to a reduction of strain because of the smaller lattice parameter of the ZrO_2 precipitates compared to the LSMO matrix. Strain is then mainly localized at the precipitate−matrix interface.

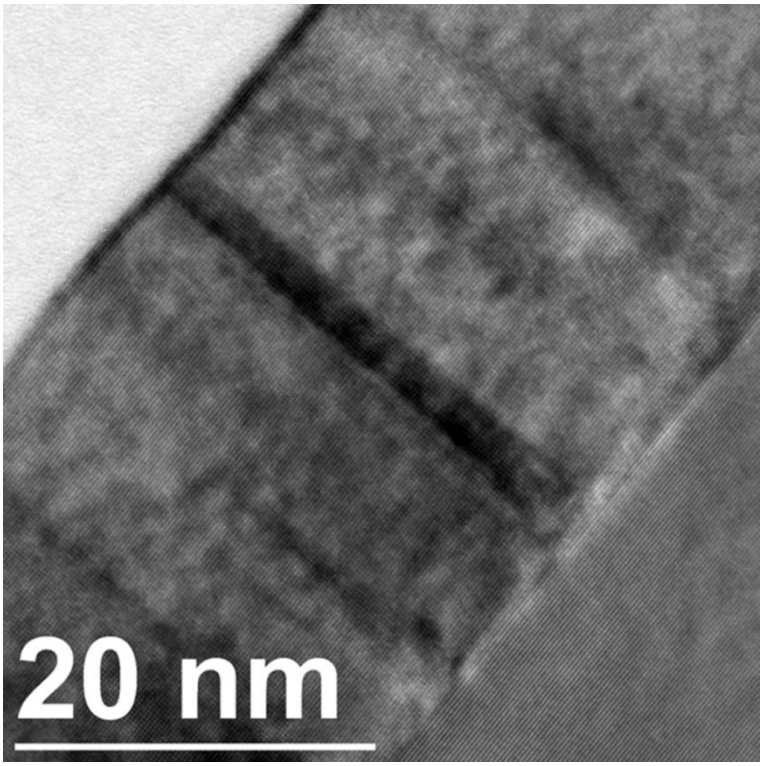

Figure 3.11 HREM image of the side-view sample of the LSMO specimen with 6 mol% ZrO_2. It already shows the formation of pillar.

Fig. 3.11 shows that ZrO_2 precipitates form even in the specimen with 6 mol% ZrO_2. This shows that the solubility of Zr in LSMO must be less than 6 mol%. There are literature data claiming higher solubility, e.g. 10% [110, 111], but this is probably due to the higher processing temperature in these studies. As noted above the limited solubility may partially be due to the strain imposed by the large Zr ions in the LSMO matrix. Moreover, as mentioned by Kim *et al.*,[110] oxygen vacancies and interdiffusion may also play an important role. Oxygen vacancies have been found and studied before in LSMO.[112, 113] The concentration of oxygen vacancies are correlated with the sample preparation temperature and oxygen pressure. The existence of oxygen vacancies would convert some Mn^{4+} to Mn^{3+}, thus reduce the number of Mn^{4+} positions that can be replaced with Zr^{4+}. This is clearly confirmed by our results shown in Fig. 3.8 and 3.9: Zr reaches a minimum in the LSMO accompanied by oxygen vacancies. Therefore, the combination of charge balance, strain, and oxygen vacancies is the possible cause for the low Zr solubility in the matrix. These results are relevant for the equilibrium constitution of the ZrO_2/Zr/LSMO system.

A discussion of the implications of the observed microstructure for electron transport properties is beyond the scope of the present article. Probably these implications are manifold due to the delicate interplay of charge-balance effects induced by the substitutional Mn-Zr exchange and the inhomogeneous oxygen vacancy distribution. It is well known that in LSMO electron transport is determined by the double-exchange mechanism between Mn atoms of different valence (Mn^{3+}-O-Mn^{4+}). The substitution of Mn with Zr can therefore be expected to influence this mechanism and thus the electronic transport in this system. Most importantly, however, the pillars act as scattering centers modifying the phase of the scattered electron wave function which can give rise to effects such as weak localization. Here, the pillar size and its densities play an important role. However, there might also be more subtle influences by the atomic substitutions mentioned above.

3.4 Conclusions

In summary, I have presented atomic-scale studies of the structure and chemistry of the ZrO_2−LSMO pillar matrix system. I showed that ZrO_2 precipitates form at concentrations as low as 6 mol%. Precipitates mainly form pillars extending the entire LSMO film. Substantial interdiffusion is found at the LSMO−ZrO_2 interface with Mn replacing Zr in ZrO_2 (thus stabilizing the cubic or tetragonal phase) and Zr replacing Mn atoms in LSMO. Charge balance requires the combination of change of the Mn valence state and oxygen vacancy formation which are observed to segregate at the interface. Strain analyses show that the system has not yet reached elastic equilibrium. It is clear that LSMO as well as pillar regions are strained because of the misfit, however, also modified by the interdiffusion. In the $La_{(1-y)}Sr_yMnO_3$ system, the magnetic properties are directly related to the y value.[114] Therefore, I believe that our results are not only relevant for the understanding the mechanisms of electron transport and magnetism in this material system, like the observed anomalous transport properties and localization transition, but also pave the way for a deeper microscopic understanding of the electronic properties of complex oxide interfaces at an atomistic level.

ACKOWLEDGEMENTS

This work has been initiated by Prof. J. Zhang (Department of Physics, Shanghai University). Samples have been prepared by Dr. Y. Gao during his PhD work at Max Planck Institue for Solid State Physcis (MPI-FKF). The research leading to these results

has received funding from the European Union Seventh Framework Program [FP/2007/2013] under grant agreement no 312483 (ESTEEM2).

Chapter 4 Linking Atomic Structure and Local Chemistry at Manganese-Segregated Antiphase Boundaries in ZrO_2-$La_{2/3}Sr_{1/3}MnO_3$ Thin Films

Abstract

This chapter presents direct experimental evidence of Mn segregation at three types of antiphase boundaries in $La_{2/3}Sr_{1/3}MnO_3$ thin films doped with ZrO_2. The local atomic structure of these antiphase boundaries was investigated by high-angle annular dark-field and annular bright-field imaging in a scanning transmission electron microscope. Chemical composition and cation valence were determined by electron energy-loss spectroscopy. I find evidence that strain relaxation and Zr_{Mn} substitution are driving forces for the formation of the antiphase boundaries. Analysis of atomic structure, image contrast, Mn valence state, and Mn occupancy shows that the antiphase boundaries are charge-neutral with minimized internal electric fields.

People involved in this part research: Dan Zhou, Wilfried Sigle, Marion Kelsch, Hanns-Ulrich Habemeier, Peter A. van Aken.

Max Planck Institute for Solid State Research, Stuttgart Center for Electron Microscopy, Heisenberstrasse 1, 70569, Stuttgart, Germany

4.1 Introduction

Emerging phenomena at oxide interfaces, such as superconductivity, magnetism, and ferroelectricity, have stimulated intense experimental and theoretical research [45, 47, 83, 115, 116]. Small structural and chemical modifications at interfaces can lead to massive changes in the electronic structure and thus giving rise to interesting and unexpected new properties. As one class of oxide interfaces, domain boundaries separating regions of uniform order parameter, show a local structure or chemical composition different from that of the domains themselves [47, 117, 118].

Perovskites, with chemical formula ABO_3, normally have heavy metal elements at A-sites and transition metal elements at B-sites. The enormous diversity of physical phenomena can be achieved by tuning atomic species at A-sites, multi-valence states of B-sites and oxygen octahedral tilt in a layer-by-layer or a solid-solution manner. In a seminal experiment, Ohtomo et.al [119] found metallic conductivity in a superlattice structure composed of two insulators $LaTi^{3+}O_3$ and $SrTi^{4+}O_3$ with maximum thickness of 5 $LaTi^{3+}O_3$ layers. Similarly, both, $LaMn^{3+}O_3$ and $SrMn^{4+}O_3$, are anti-ferromagnetic insulators at low temperatures while their solid solution $La_{1-x}Sr_xMnO_3$ shows a metallic double-exchange-mediated ferromagnetic phase over a wide compositional range as well as an insulating ferromagnetic state for a narrow window for $0.1 < x < 0.15$ accompanied by Mn valence state change between 3+ and 4+. The Mn–O–Mn bond angle varies as well, as a function of x, which modifies the magnetic properties by changing the superexchange process between Mn atoms. [120] Ultrathin $La_{2/3}Sr_{1/3}MnO_3$ (LSMO) films have been extensively studied to explore the modification of their properties as a function of thickness, substrate-induced lattice strain and details of the deposition process [121]. Alternatively, by introducing a foreign phase such as ZrO_2, anomalous magnetic and electron transport properties controlled by the amount of ZrO_2 emerge, where the foreign phase appears in the film as pillars penetrating throughout the film [89, 91, 122]. In my previous paper [122] and Chapter 3, strain, elemental segregation, interdiffusion, and Mn valence change at the ZrO_2-$La_{2/3}Sr_{1/3}MnO_3$ pillar–matrix interfaces were studied at atomic resolution using aberration-corrected transmission electron microscopy. Here, I report on Mn-rich antiphase boundaries (APBs) connecting adjacent pillars. I show that these APBs can relax the strain in a two-component system [122]. Detailed analysis of the atomic structure allows us to analyze their charge state. Increasing the x value in the $(1–x)$LSMO + $x$$ZrO_2$ system not only leads to a higher density and larger size of ZrO_2 pillars, but also to a higher number of APBs.

Three types of APBs were found in both 70 mol% LSMO + 30 mol% ZrO_2 and 80 mol% LSMO + 20 mol% ZrO_2 samples and will be discussed in detail in this paper. HAADF STEM and simultaneous EELS is used to reveal the structure, composition, and valence state at the APBs. By simultaneous HAADF and ABF STEM imaging, the oxygen atomic-column positions for different APBs inside these boundaries are visualized at the atomic scale from which the atomic arrangement for each APB is derived. Finally, I discuss the formation mechanism of the APBs in the context of strain relaxation and electrostatic coupling at the boundaries.

4.2 Sample preparation and TEM experimental details

ZrO_2 and LSMO were co-deposited epitaxially on (001) single-crystalline LAO substrate by pulsed laser deposition. Stoichiometric amounts of LSMO and ZrO_2 according to $(1–x)$LSMO + $x$$ZrO_2$, with x = 0.3 and 0.2, were used. Details of the material growing process can be found in Gao *et al.* [89].

The plan-view specimens for TEM studies were prepared by grinding and dimpling followed by low-temperature (at liquid nitrogen temperatures) argon ion thinning with a precision ion polishing system (PIPS, Gatan, model 691) to achieve electron transparency.

HAADF images, EELS spectrum images and ABF images from plan-view specimens were obtained using an aberration-corrected JEOL ARM200CF microscope operated at 200 keV, equipped with a CEOS DCOR probe corrector, and a Gatan GIF Quantum ERS imaging filter with dual-EELS acquisition capability.

The experimental convergence angle was 20.4 mrad for ABF, HAADF, and EELS imaging. The corresponding inner and outer collection semi-angles for ABF and HAADF were set to 11–23 mrad and 75–310 mrad, respectively. The inner and outer collection semi-angles for ADF images acquired simultaneously during EELS spectrum imaging with a Gatan ADF detector were 67−166 mrad, and the collection angle for EELS spectrum imaging was 67 mrad.

MSA was performed to reduce the noise of the EEL spectra with WPCA. From HAADF images dislocations and strain were calculated using GPA software from HREM Research Inc..

4.3 Results

4.3.1 Geometric arrangement of the three boundary types

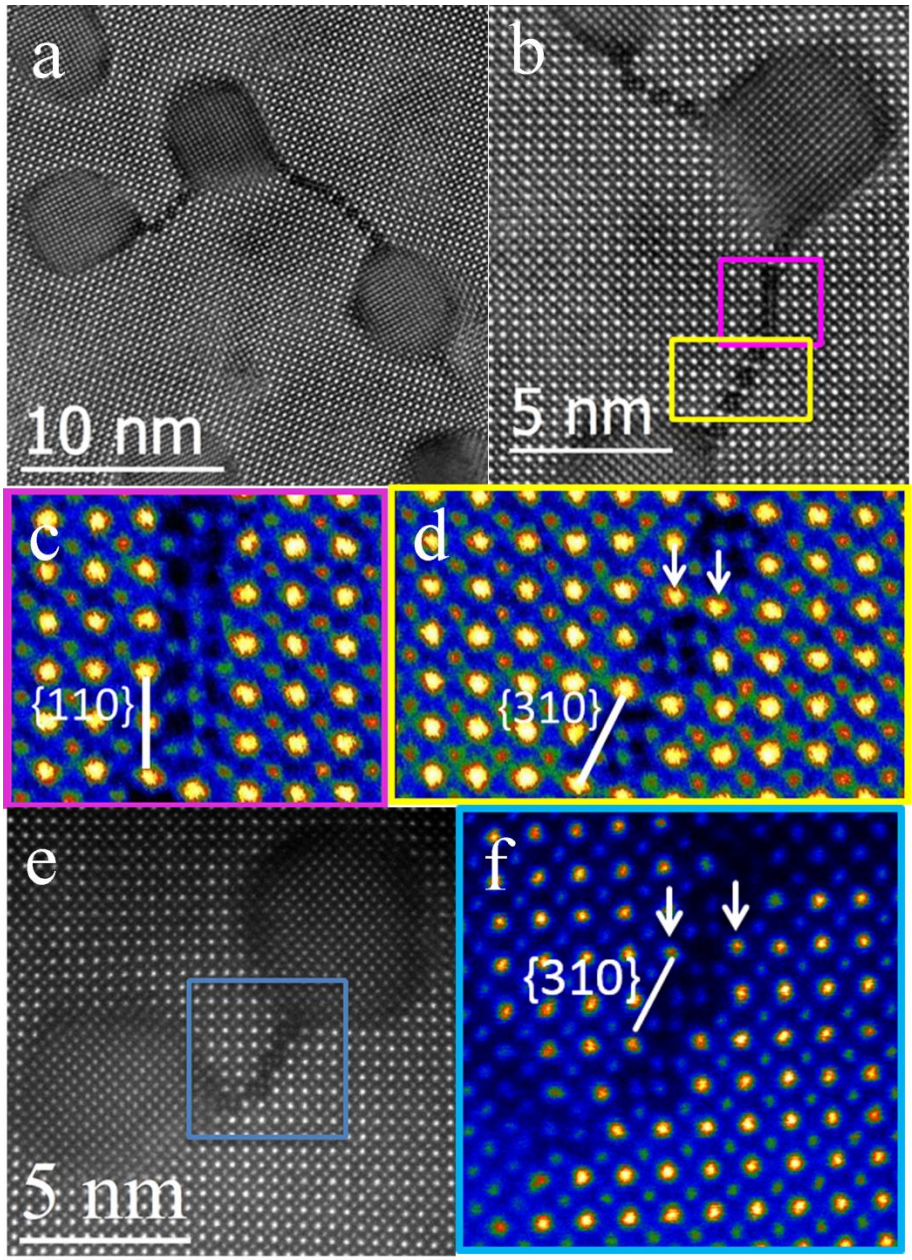

Figure 4.1 (a) HAADF image of a plan-view 70 mol% LSMO-30 mol% ZrO_2 sample showing three ZrO_2 pillars connected by boundaries. (b) Magnified image of part of the boundary region shown in (a). (c) Temperature-colour view of the magenta frame region in (b) showing APB-1. (d) Temperature-colour view of the yellow frame region in (b) showing APB-2. (e) HAADF image of a plan-view 80 mol% LSMO-20 mol% ZrO_2 sample showing three ZrO_2 pillars connected by APB-3. (f) Temperature-colour view of the blue frame region in (e) showing APB-3.

Aberration-corrected HAADF STEM images of the pillar–matrix structure along the [001] axis are shown in Fig 4.1. The details of chemistry and structure of the pillar-matrix interface were already presented in my previous paper [122] and Chapter 3. To be consistent

with our former report, I use LSMO in the tetragonal notation (space group I4/mcm, No. 140). The unit cell is shown in Fig. 4.2. I note that HAADF images of the matrix region show bright columns corresponding to the heavy A-site (La/Sr) atomic columns and weaker columns corresponding to the lighter BO-site (Mn/O) atomic columns in $La_{2/3}Sr_{1/3}MnO_3$. Due to the low elastic scattering cross section of oxygen atoms and the angular range used for HAADF imaging, the pure oxygen ion columns are invisible in HAADF images. Because of the strong *Z*-contrast, ZrO_2 pillars can be clearly distinguished from the LSMO matrix. Notably, some pillars are connected by lines exhibiting lower contrast than the surrounding LSMO matrix. On closer inspection these lines are identified as APBs. Fig. 4.1b–d and 4.1f show magnified details of APBs in Fig. 4.1a and 4.1e, respectively. The use of temperature color scale allows subtle details of the low intensity part of the image to be readily seen in a way that would be difficult in a grey-scale image.

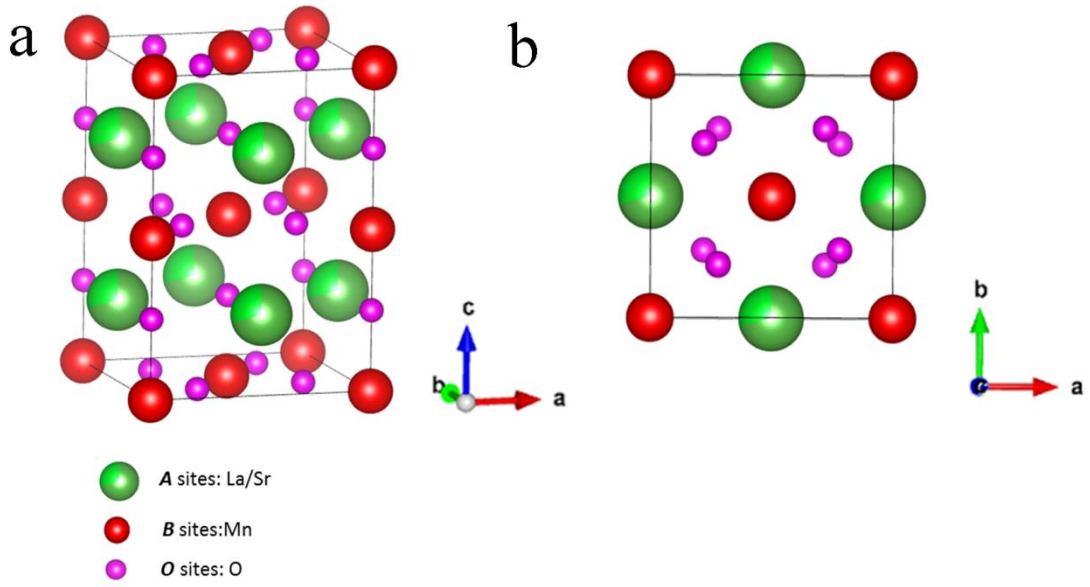

Figure 4.2 (a) Side-view and (b) plan-view of the structure model of tetragonal LSMO.

Three different types of APBs are discernible which I denote as APB-1 (Fig. 4.1c), APB-2 (Fig. 4.1d), and APB-3 (Fig. 4.1f). There is a shift of half a {110} plane distance, corresponding to $\frac{1}{4}d_{110}$, across the boundary along the [110] direction for APB-1 and APB-2 and along the [1-10] direction for APB-3, as required for an APB. The boundary planes are {110} for APB-1 and {310} for APB-2 and APB-3, respectively. Note that APB-2 and APB-3 have different atomic arrangements because the angles between APB shift direction and APB plane are different. This is visible from the different distances between A-sites in the boundary plane as pointed out by arrows in Fig. 4.1d and 4.1f. The A-site distance in APB-2 is about $d_{110}=\frac{a}{\sqrt{2}}$ while the one for APB-3 is about $d_{100} = a$. A

key feature of the HAADF image for APB-1 is the ‘’ladder’’ appearance of pairs of atomic columns in the boundary. The HAADF contrast of these columns is similar to BO-site columns in the matrix. The ladder structure also appears in APB-2 and APB-3. Survey of APBs from a large area shows that APB-3 occurs most frequently, followed by APB-2 and APB-1.

4.3.2 Elemental mapping of the APB wall

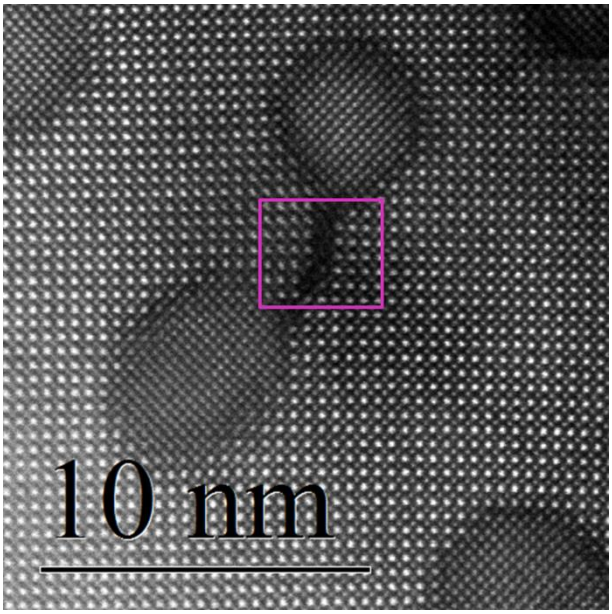

Figure 4.3 HAADF image of the area from which the EELS-SI shown in Fig. 4.4 was taken (magenta rectangle).

To investigate the elemental distribution and chemical state inside the APB walls, EELS spectrum imaging (SI) was applied to the magenta frame marked region in Fig. 4.3, as presented in Fig. 4.4. The region shown in this figure includes both APB-1 (upper part) and APB-2 (lower part). Fig. 4.4b–d show elemental maps using the La-$M_{4,5}$ edge, O-K edge, and Mn-$L_{2,3}$ edge, and a simultaneously acquired ADF image is shown in Fig. 4.4a. The low-magnification ADF image revealing the pillars connected by the APBs is given in Fig. 4.3. EELS-SI of APB-3, not presented here, gives similar conclusions as with APB-1 and APB-2. Fig. 4.4d indicates that the APBs are rich in Mn, rendering them dark in the HAADF image compared to the LSMO matrix. The O-K map in Fig. 4.4c evidences that O is present both inside the wall and in the matrix. Fig. 4.4e and 4.4f present O-K and Mn-$L_{2,3}$ edges of the matrix and APB areas, respectively. No significant difference can be found which indicates that the Mn valence is the same in the APB as in the matrix (i.e. +10/3). Different from the pillar–matrix interface [122], there is no change of La or Sr concentration when approaching the APB.

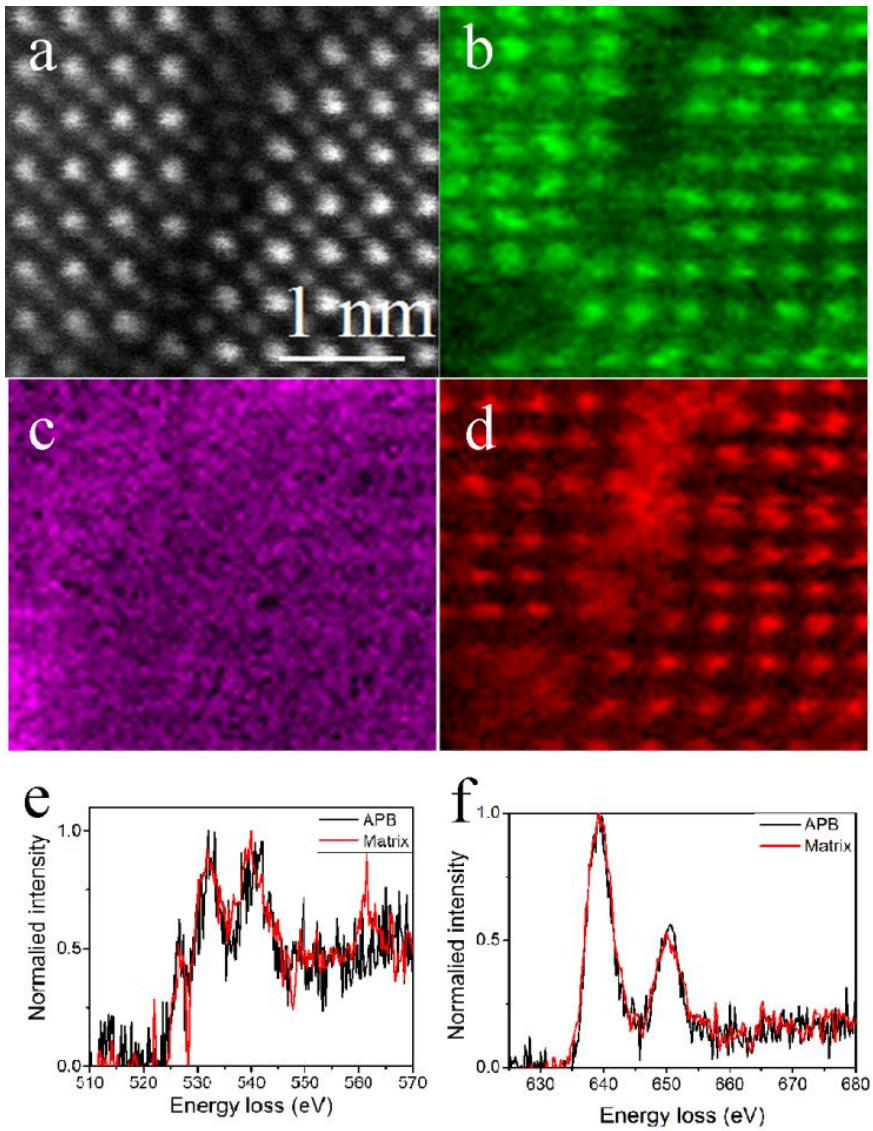

Figure 4.4 (a) ADF image of the sample area including APB-1 and APB-2 in a plan-view 80 mol% LSMO-20 mol% ZrO_2 sample. EELS spectrum image of (b) La-$M_{4,5}$, (c) O-K, and (d) Mn-$L_{2,3}$. Background-subtracted (e) O-K and (f) Mn-$L_{2,3}$ EELS spectra from the APB region and the LSMO matrix region.

4.3.3 O position determination

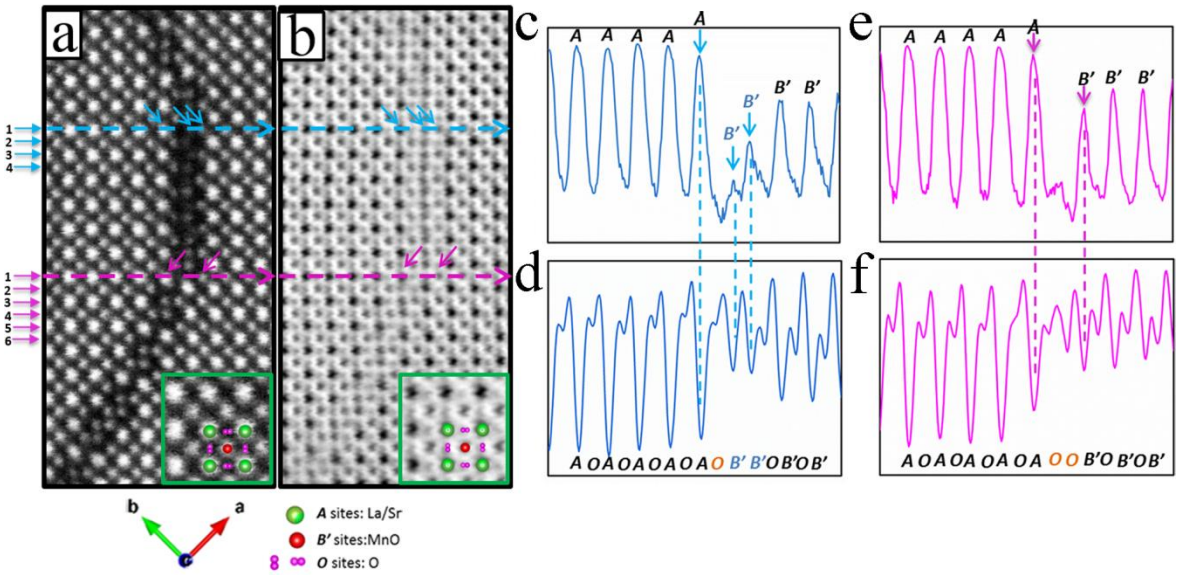

Figure 4.5 Simultaneously acquired HAADF image (a) and ABF image (b) of a region including APB-1 and APB-2 of the plan-view 80 mol% LSMO-20 mol% ZrO2 sample. Line profiles along the blue line in (c) the HAADF image and (d) the ABF image and along the magenta line in (e) the HAADF image and (f) the ABF image. The line profiles are integrated along the vertical direction over 5 pixels.

To retrieve the oxygen atomic positions in and at the APBs, ABF and HAADF images were simultaneously acquired. It should be noted that in HAADF images atoms appear bright on a dark background and the brightness scales with the atomic number, ~$Z^{1.7}$, whereas in ABF imaging atoms appear dark on a bright background with less dependence of the contrast with *Z*. Therefore, ABF imaging enables visualizing light-element columns [31, 32]. Simultaneous acquisition of HAADF and ABF images helps identifying the exact light-element position relative to the heavy-atom positions. Fig. 4.5a and 4.5b show simultaneously acquired HAADF and ABF images of an area including APB-1 and APB-2. Fig.4.5c and 4.5d show the line profiles along the blue line in Fig. 4.5a (HAADF) and 4.5b (ABF), respectively. Fig. 4.5e and 4.5f depict the corresponding line profiles along the magenta line in Fig. 4.5a and 4.5b, respectively. In the HAADF line profiles, the peaks are assigned to A columns and BO (denoted by B' in the figures and the following tables for simplification) columns, respectively. The phase shift is evident from the presence of A columns on one side and of B' columns on the other side of the APB. In the ABF line profiles, deep minima are assigned to A columns and B' columns, as marked by double arrows. The shallow minima between A and B' columns are assigned to pure oxygen columns "O". Therefore, the atom arrangement at the boundary is as follows:

Blue line: AOAOAOAOA*OB'B'*OB'OB'

Magenta line: AOAOAOAOA*OOB'*OB'OB'

This means that there exist two B'-site columns close to each other along the blue line and two oxygen columns close to each other along the magenta line.

From a similar analysis of the atomic layers below the two lines I can get the total atom arrangement of APB-1 and APB-2 as listed in Tables 4.1 and 4.2 and in Fig. 4.8 and Fig. 4.9. Atomic columns within the APBs with different atomic occupancies from those in the LSMO matrix are represented by different colors. The A-sites marked by arrows in Fig. 4.1d and 4.1f are in bold italic font and black color. For APB-1, line 1 and line 2 are the repeating unit along the vertical direction, i.e. the [110] direction, and thus constitute a building block of the APB. For APB-2, the building block comprises lines 1–4 along the [110] direction. Lines 5 and 6 resemble the atomic arrangement of lines 1 and 2, but with $\frac{1}{2}d_{110}$ shift to the left side.

Table 4.1 Atomic-column arrangement within APB-1. The direction from left to right corresponds to [1-10] and the direction from top to bottom to [-1-10].

Blue	1	2	3	4	5	6	7	8	9	10	11	12	13	14	15	16
1	A	O	A	O	A	O	A	O	A	***O***	***B'***	***B'***	O	B'	O	B'
2	O	B'	O	B'	O	B'	O	B'	O	***B'***	***B'***	***O***	A	O	A	O
3	A	O	A	O	A	O	A	O	A	***O***	***B'***	***B'***	O	B'	O	B'
4	O	B'	O	B'	O	B'	O	B'	O	***B'***	***B'***	***O***	A	O	A	O

Table 4.2 Atomic-column arrangement within APB-2. The direction from left to right corresponds to [1-10] and the direction from top to bottom to [-1-10].

Magenta	1	2	3	4	5	6	7	8	9	10	11	12	13	14	15	16
1	A	O	A	O	A	O	A	O	***A***	***O***	***O***	B'	O	B'	O	B'
2	O	B'	O	B'	O	B'	O	B'	***O***	***O***	***A***	O	A	O	A	O
3	A	O	A	O	A	O	A	O	***B'***	***B'***	O	B'	O	B'	O	B'
4	O	B'	O	B'	O	B'	O	***B'***	***B'***	O	A	O	A	O	A	O
5	A	O	A	O	A	O	***A***	***O***	***O***	B'	O	B'	O	B'	O	B'
6	O	B'	O	B'	O	B'	***O***	***O***	***A***	O	A	O	A	O	A	O

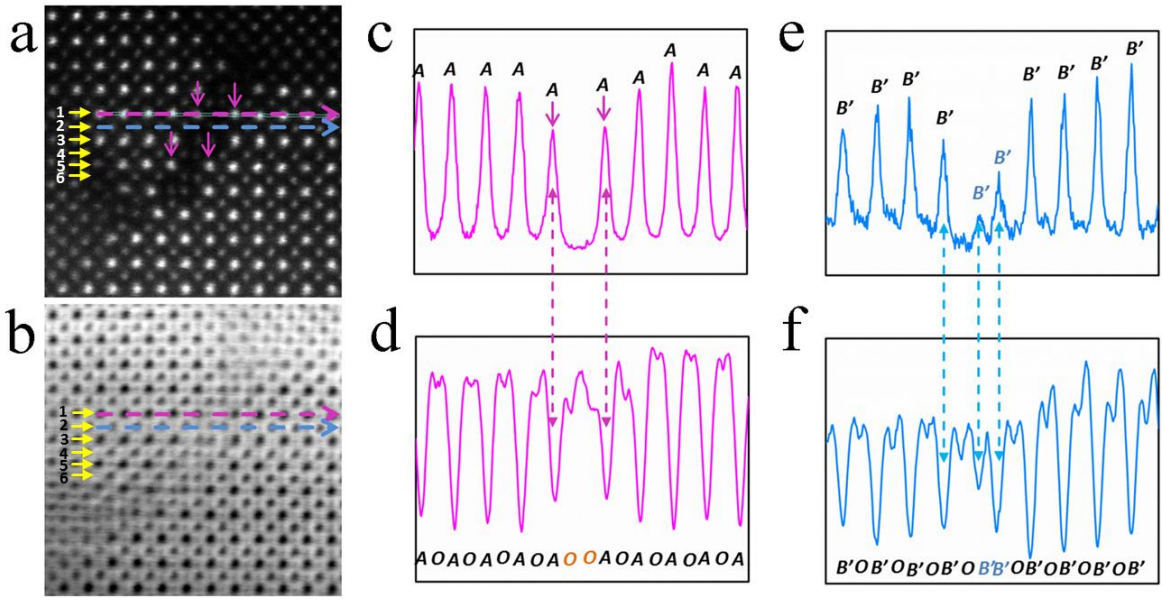

Figure 4.6 Simultaneously acquired HAADF image (a) and ABF image (b) of a region including APB-3 of a plan-view 80 mol% LSMO-20 mol% ZrO_2 sample. Line profiles along the magenta lines in the HAADF image (c) and the ABF image (d) and along the blue lines in the HAADF image (e) and the ABF image (f). The line profiles are integrated along the direction vertical to the line over 5 pixels.

Table 4.3 Atomic-column arrangement within APB-3. The direction from left to right corresponds to [1-10] and the direction from top to bottom to [-1-10].

Line	1	2	3	4	5	6	7	8	9	10	11	12	13	14	15	16
1(Blue)	A	O	A	O	A	O	A	O	***A***	***O***	***O***	***A***	O	A	O	A
2(Magenta)	O	B’	O	B’	O	B’	O	B’	O	***B’***	***B’***	O	B’	O	B’	O
3	A	O	A	O	A	O	A	O	***B’***	***B’***	O	A	O	A	O	A
4	O	B’	O	B’	O	B’	O	***B’***	***B’***	O	B’	O	B’	O	B’	O
5	A	O	A	O	A	O	***A***	***O***	***O***	***A***	O	A	O	A	O	A
6	O	B’	O	B’	O	B’	O	***B’***	***B’***	O	B’	O	B’	O	B’	O

The same analysis procedure is applied to the simultaneously acquired HAADF and ABF images (Fig. 4.6) acquired at APB-3, and the atomic arrangement is shown in Table 4.3. Different from the atomic arrangement presented in Table 4.1 and Table 4.2 for APB-1 and APB-2, the anti-phase shift of APB-3 can be seen along the vertical direction instead of the horizontal direction. Rotating the picture clockwise by 90°, I obtain the atomic arrangement shown in Table IV. Same as in the Tables presented above, different colors represent different occupation. Comparison with APB-1 (Table 4.1) shows that they have exactly the same atomic arrangement if the atomic occupation and vertical alignment are

ignored. Taking account of the different occupation and vertical alignment makes them totally different APBs.

Table 4.4 Atom-column arrangement within APB-3. The direction from left to right corresponds to [-1-10] and the direction from top to bottom to [1-10].

	1	2	3	4	5	6	7	8	9	10	11	12	13	14
1 (magenta line)	A	O	***B'***	***B'***	***O***	***B'***	O	B'	O	B'	O	B'	O	B'
2	O	B'	O	***B'***	***O***	***B'***	***B'***	O	**A**	O	A	O	A	O
3	A	O	A	O	A	O	***B'***	***B'***	***O***	***B'***	O	B'	O	B'
4	O	B'	O	B'	O	B'	O	***B'***	***O***	***B'***	***B'***	O	A	O
5	A	O	A	O	A	O	A	O	**A**	O	***B'***	***B'***	***O***	***B'***

Whereas ABF helped us to locate the position of oxygen atomic columns, quantification of oxygen content would require much more elaborate analysis which is beyond the scope of the present paper.

4.4 Discussions

4.4.1 Strain-driven formation of APBs

An ideal two-component system will be free of strain if the two components are perfectly lattice-matched, chemically stable, and have the same thermal expansion coefficients. Deviations from these conditions will lead to strain or defect formation. I showed that there is a lattice mismatch of 5.6% to 9.2% between LSMO and ZrO_2 [122]. Once the pillar size reaches a critical value, misfit dislocations form at the pillar/matrix interface. To fully relax the strain, the dislocations need to form symmetrically around the circumference of the pillar. I found that this does not happen always, i.e. some dislocations remain unpaired and the pillar is still in a strained state. This is visible in Fig. 4.7, which shows unpaired misfit dislocations for the pillars connected by APBs. This indicates that the APB formation assists strain reduction. This is possible if the APB translation vector has a component parallel to the missing misfit dislocation, which is indeed the case for the system shown in Fig. 4.7. I note that APBs form only between closely spaced pillars because otherwise the total APB energy would exceed the strain energy of the missing misfit dislocation. In fact, no extended APBs were found between remote pillars. Careful inspection of the position of different APBs shows that only APB-2 and APB-3 are directly connected to pillars while APB-1 always links APB-2 or APB-3. Furthermore, APB-1 appears between two pillars farther from each other than the ones with only APB-2 and APB-3. From these observations, I conclude that APB-1 has lower APB energy than APB-2 and APB-3.

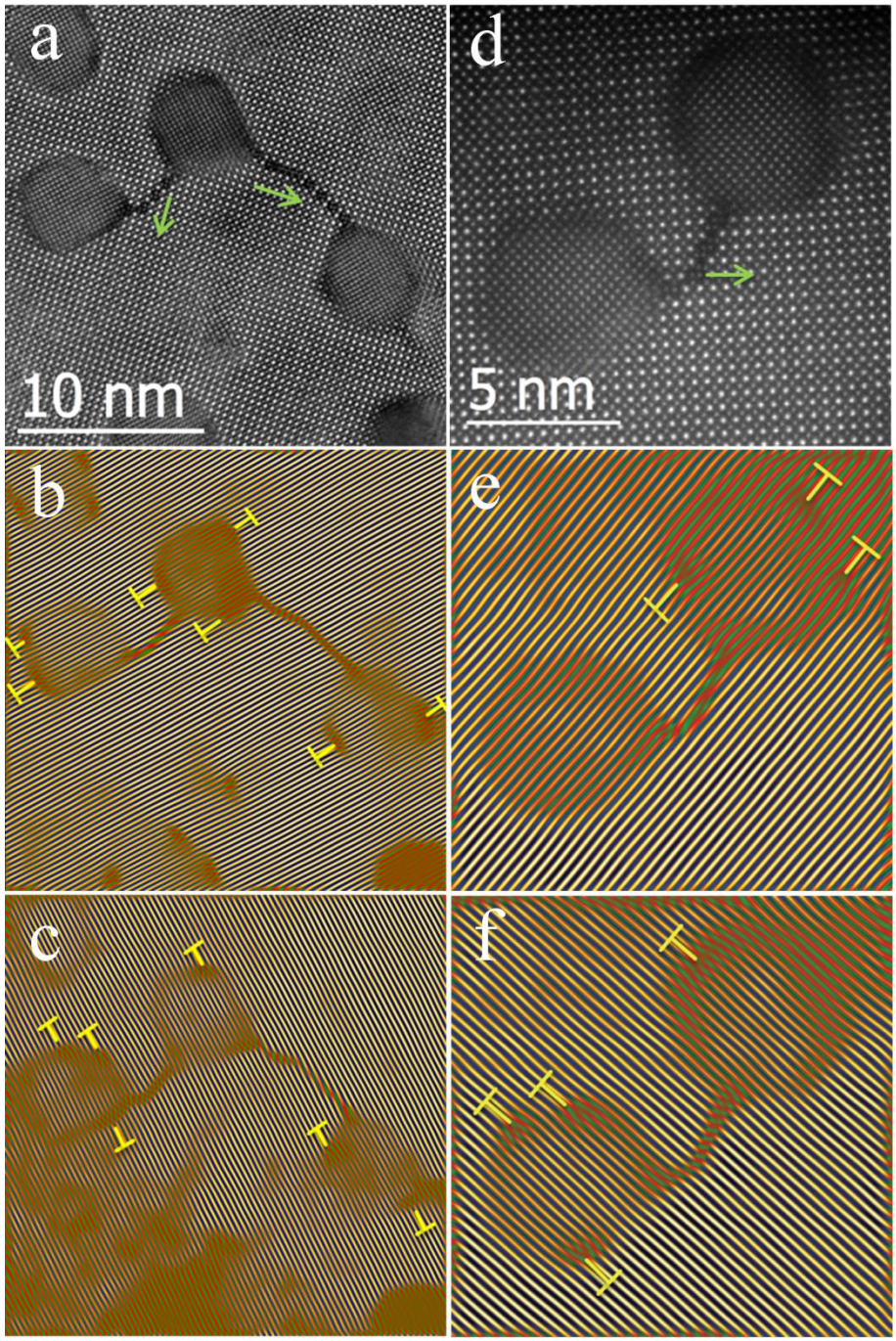

Figure 4.7 (a) HAADF image of a sample region including APB-1 and APB-2, replica of Fig. 4.1a. Fourier-filtered images using 100 reflections (b) and 010 reflections (c) of the sample region in (a). (d) HAADF image of a sample region including APB-3, replica of Fig. 4.1e. Fourier-filtered images using 100 reflections (e) and 010 reflections (f) of the sample region in (d). Arrows in (a) and (d) represent the phase shift direction of the labelled side with respect to the other side of the APBs.

The possible formation of APB-1, APB-2, and APB-3 is demonstrated in Fig. 4.8–4.10. Starting from the perfect LSMO structure, viewed along the [001] orientation, strain relaxation causes phase shift along (110) planes by ¼ [110] (Fig. 4.8b). By this

mechanism the strain caused by the missing misfit dislocation at the pillar–matrix interface is (at least partially) compensated. The antiphase shear results in closely spaced positively (or negatively) charged ions within the boundary. Even though the whole system is still charge balanced, the strong Coulomb forces and the large size of closely spaced A-site (La/Sr) ions makes this structure not energetically favorable. Therefore, additional reconstruction of the APB is required. This can be achieved by a change of the composition. From our experimental results I know that (i) both the original A-sites and the pure oxygen atomic columns inside the blue box drawn in Fig. 4.8b are changed to Mn–O columns and (ii) the occupancies of B'-sites and pure oxygen columns are lower compared to the LSMO bulk, as revealed by HAADF and ABF image intensities. Therefore I get the APB-1 structure model as shown in Fig. 4.8c. Different colors were applied to represent the same atom species but different occupancy of B' sites in the bulk (red) and in the APB (blue) and of O sites in the bulk (magenta) and in the APB (orange). The same color scheme was applied for the following APB-2 and APB-3 structure models.

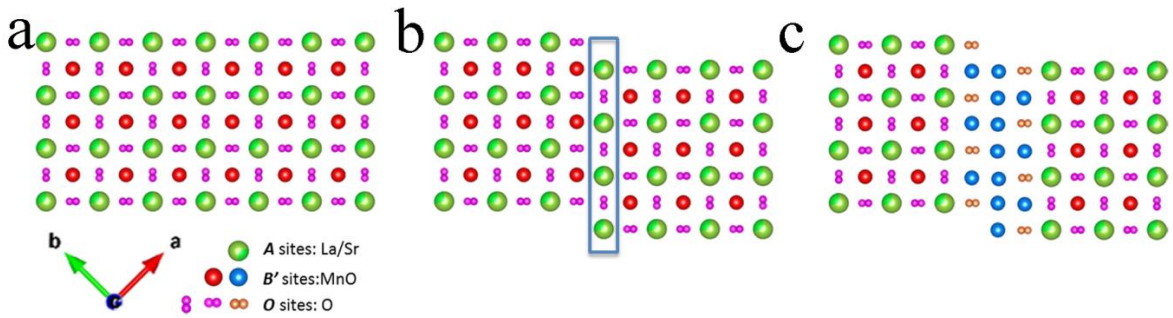

Figure 4.8 Illustration of the formation process of APB-1. (a) Starting structure model of LSMO viewing along <001> direction. (b) Phase shift of $\frac{1}{4}d_{110}$along {110} planes from (a). (c) Final structure model of APB-1 with atomic reconstructions from (b).

Fig. 4.9 shows the formation process for APB-2. To help understanding the process, I artificially divide it into steps which practically and possibly happen simultaneously. As shown in Fig. 4.9a, to realize the phase shift of $\frac{1}{4}d_{110}$ driven by strain relaxation, the B'-site atoms and oxygen columns in the dashed box must be removed firstly. Along with the required phase shift, I get two adjacent A-sites as labeled by dashed boxes in Fig. 4.9b which is not energetically favorable. As revealed by the experimental results, these A-sites will be substituted by Mn and O, which might derive from the removed ones in the first step. Then, I get the APB-2 structure as shown in Fig. 4.9c.

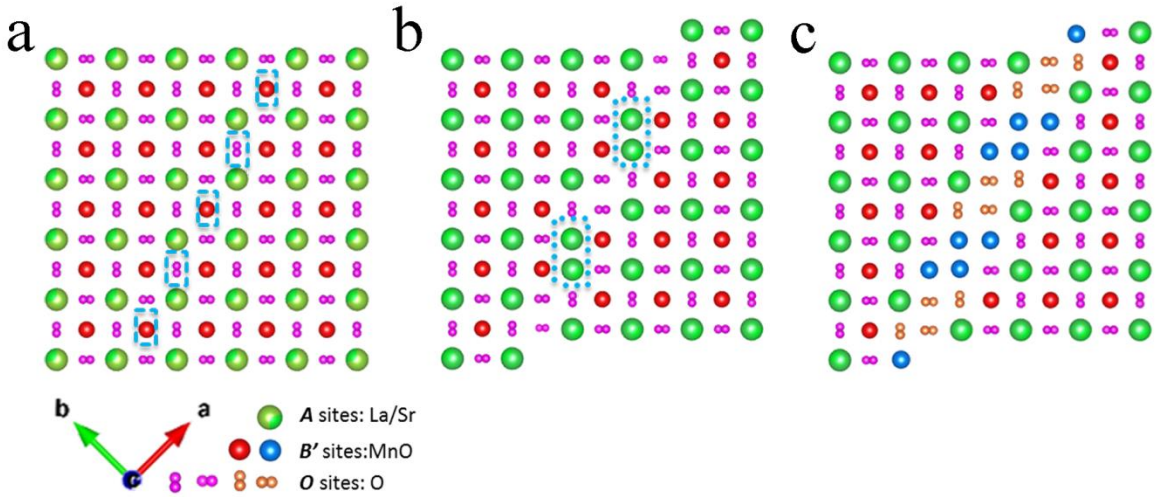

Figure 4.9 Illustration of the formation process of APB-2. (a) Starting structure model of LSMO viewing along <001> direction. (b) Phase shift of $\frac{1}{4}d_{110}$ along {310} planes from (a). (c) Final structure model of APB-2 with atomic reconstructions from (b).

The situation for APB-3 is shown in Fig. 4.10. Different from APB-2, extra oxygen and A-sites have to be removed, as shown by the long dashed box. After the phase shift of $\frac{1}{4}d_{110}$ (Fig. 4.10b) and Mn-O substitution of A-sites, I finally get the APB-3 structure (Fig. 4.10c).

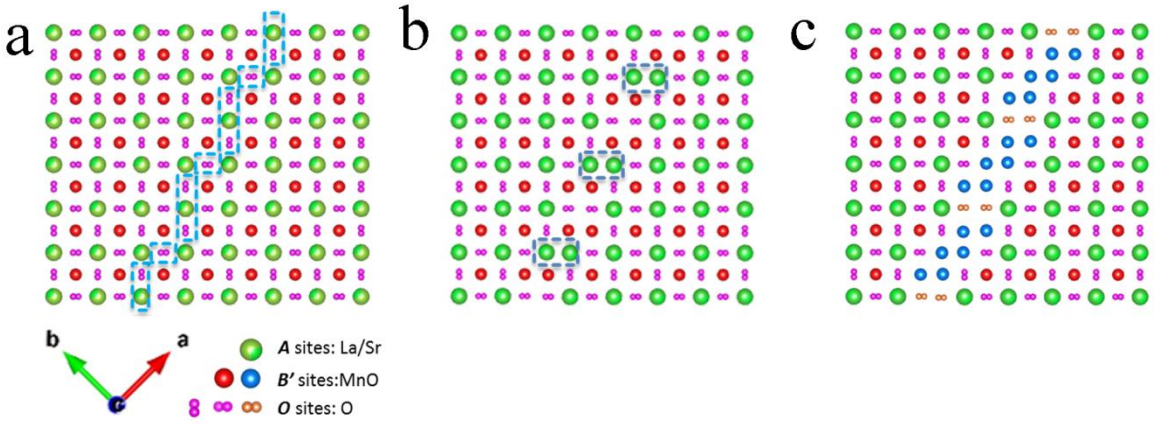

Figure 4.10 Illustration of the formation process of APB-3. (a) Starting structure model of LSMO viewing along <001> direction. (b) Phase shift of $\frac{1}{2}d_{110}$along {310} planes from (a). (c) Final structure model of APB-3 atomic reconstructions from (b).

In [13] and chapter 3 I have shown that La segregates at the pillar–matrix interface and that Zr occupies Mn sites in the LSMO matrix. It is highly conceivable that the excess Mn atoms partially segregate at the observed APBs. Therefore it is likely that the formation of the APBs is driven by multiple factors contributing to varying degrees, namely strain

relaxation and elemental segregation to minimize the total free energy of the pillar–matrix–APB system.

4.4.2 Atomic reconstruction: Charge neutrality by varying atomic occupation

I have shown that strain relaxation is a driving force for APB formation. In the following I will analyze the charge distribution across the APB walls. This will show that the APB structure is consistent with a charge-balanced state.

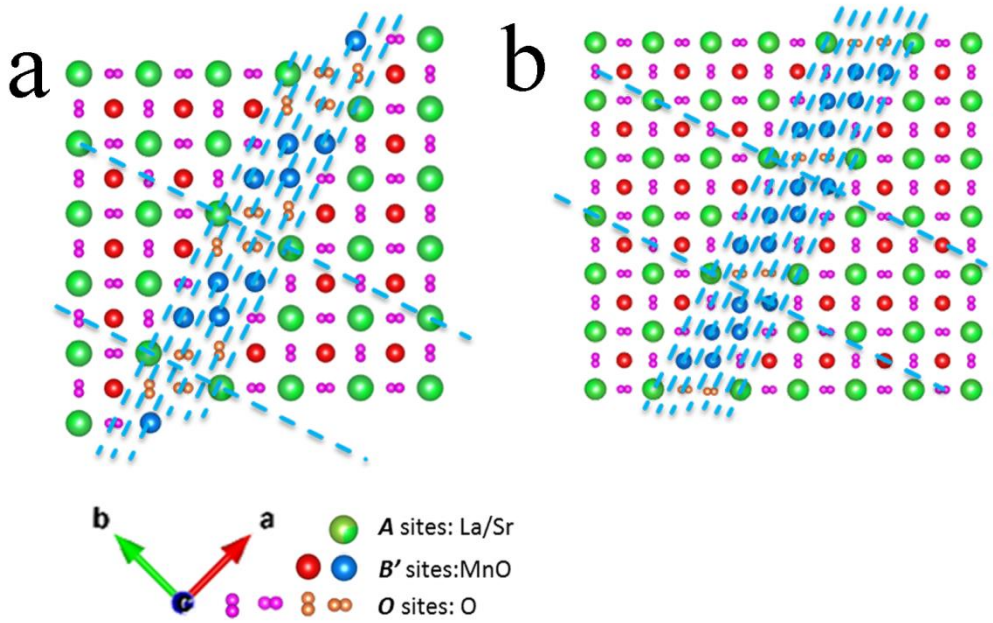

Figure 4.11 Illustration of the plane components in boundary planes in sequence of (a) APB-2 and (b) APB-3.

For extracting the charge sequence of {310} planes, which are parallel to the APB plane for APB-2 and APB-3, I identify all {310} planes within the APB and draw lines perpendicular to the {310} planes (see Fig. 4.11). The atomic arrangements along these lines are shown in Table 4 for APB-2 and APB-3.

As revealed from the $La_{2/3}Sr_{1/3}MnO_3$ structure model shown in Fig. 4.2, there are three different atomic columns along the <001> direction, i.e. A-site columns, B'-site columns, and pure oxygen column. Within one unit cell length along the <001> direction, there are two atoms of each A, B', and O. For simplicity, I ignore the common factor 2 and therefore use charge carried by A as $\frac{8}{3}(\frac{2}{3}La^{3+} + \frac{1}{3}Sr^{2+})$, B' as $\frac{4}{3}(Mn^{10/3+} + O^{2-})$ and O as –2. As presented in the previous section, Mn inside the boundaries has the same valence state as in the matrix region. HAADF intensities of the B'-sites inside the APBs, i.e. the B'-sites highlighted by blue color in Fig. 4.8–4.10, are similar but not identical. For simplification I denote O_{Mn} and O_O as *average* occupancies of Mn and O inside the APB

relative to the ones in the bulk. Assuming pure ionicity, the charge sequence of (1-10) planes of APB-1 can be obtained as shown in Table 5. For APB-2 and APB-3, I extract the charge sequence of {310} planes, parallel to the APB plane, as shown in Fig. 4.11. The atomic arrangements and charge distributions of APB-2 and APB-3 are displayed in Table 5 as well. The distance of planes along the horizontal direction is $\frac{1}{6}d_{310}$ for APB-2 and APB-3, and $\frac{1}{2}d_{110}$ for APB-1. The atom arrangement along the horizontal direction in the tables is actually not exactly planar, which I neglect here to simplify the charge calculations.

To achieve zero total charge across the APB, the following conditions have to be met:

APB-1: $\frac{2}{3} + 2 * \left(\frac{10}{3}O_{Mn} - 4O_O\right) + \left(\frac{20}{3}O_{Mn} - 4O_O\right) = 0$ (1)

APB-2: $\frac{2}{3} + 4 * \left(\frac{10}{3}O_{Mn} - 4O_O\right) = 0$ (2)

APB-3: $\frac{2}{3} + 4 * \left(\frac{10}{3}O_{Mn} - 4O_O\right) + \left(\frac{20}{3}O_{Mn} - 4O_O\right) = 0$ (3)

Therefore,

APB-1: $O_O = \frac{10}{9}O_{Mn} + \frac{1}{18}$ (4)

APB-2: $O_O = \frac{5}{6}O_{Mn} + \frac{1}{24}$ (5)

APB-3: $O_O = O_{Mn} + \frac{1}{30}$ (6)

and, by restricting O_{Mn} and O_O to positive values,

APB-1: $0 < O_{Mn} \leq \frac{17}{20}$ and $\frac{1}{18} < O_O \leq 1$ (7)

APB-2: $0 < O_{Mn} < 1$ and $\frac{1}{24} < O_O \leq \frac{7}{8}$ (8)

APB-3: $0 < O_{Mn} \leq \frac{29}{30}$ and $\frac{1}{30} < O_O \leq 1$ (9)

Table 4.5 Charge sequence across the APB walls. For APB-1, the direction from left to right corresponds to [1-10] and the direction from top to bottom to [-1-10]. For APB-2 and APB-3, the direction from left to right corresponds to [1-30] and the direction from top to bottom to [-3-10].

					In the APB walls								
APB-1	O B’	A O	O B’	A O	***O*** ***B’***	***B’*** ***B’***	***B’*** ***O***	O A	B’ O	O A	B’ O
Charge	$-\frac{2}{3}$	$\frac{2}{3}$	$-\frac{2}{3}$	$\frac{2}{3}$	$\frac{10}{3}O_{Mn}-4O_O$	$\frac{20}{3}O_{Mn}-4O_O$	$\frac{10}{3}O_{Mn}-4O_O$	$\frac{2}{3}$	$-\frac{2}{3}$	$\frac{2}{3}$	$-\frac{2}{3}$
Charge Eq. (4)	$-\frac{2}{3}$	$\frac{2}{3}$	$-\frac{2}{3}$	$\frac{2}{3}$	$-\frac{2}{9}-\frac{10}{9}O_{Mn}$	$-\frac{2}{9}-\frac{20}{9}O_{Mn}$	$-\frac{2}{9}-\frac{10}{9}O_{Mn}$	$\frac{2}{3}$	$-\frac{2}{3}$	$\frac{2}{3}$	$-\frac{2}{3}$
Charge (Electrical dipoles minimized)	$-\frac{2}{3}$	$\frac{2}{3}$	$-\frac{2}{3}$	$\frac{2}{3}$	$-\frac{2}{3}$	$\frac{2}{3}$	$-\frac{2}{3}$	$\frac{2}{3}$	$-\frac{2}{3}$	$\frac{2}{3}$	$-\frac{2}{3}$
APB-2	O B’	A O	O B’	A O	***O*** ***B’***	***B’*** ***O***	***O*** ***B’***	***B’*** ***O***	A O	O B’	A O	O B’
Charge	$-\frac{2}{3}$	$\frac{2}{3}$	$-\frac{2}{3}$	$\frac{2}{3}$	$\frac{10}{3}O_{Mn}-4O_O$	$\frac{10}{3}O_{Mn}-4O_O$	$\frac{10}{3}O_{Mn}-4O_O$	$\frac{10}{3}O_{Mn}-4O_O$	$\frac{2}{3}$	$-\frac{2}{3}$	$\frac{2}{3}$	$-\frac{2}{3}$
Charge Eq. (5)	$-\frac{2}{3}$	$\frac{2}{3}$	$-\frac{2}{3}$	$\frac{2}{3}$	$-\frac{1}{6}$	$-\frac{1}{6}$	$-\frac{1}{6}$	$-\frac{1}{6}$	$\frac{2}{3}$	$-\frac{2}{3}$	$\frac{2}{3}$	$-\frac{2}{3}$
APB-3	O B’	A O	O B’	A O	***O*** ***B’***	***B’*** ***O***	***B’*** ***B’***	***O*** ***B’***	***B’*** ***O***	A O	O B’	A O	O B’
Charge	$-\frac{2}{3}$	$\frac{2}{3}$	$-\frac{2}{3}$	$\frac{2}{3}$	$\frac{10}{3}O_{Mn}-4O_O$	$\frac{10}{3}O_{Mn}-4O_O$	$\frac{20}{3}O_{Mn}-4O_O$	$\frac{10}{3}O_{Mn}-4O_O$	$\frac{10}{3}O_{Mn}-4O_O$	$\frac{2}{3}$	$-\frac{2}{3}$	$\frac{2}{3}$	$-\frac{2}{3}$
Charge Eq. (6)	$-\frac{2}{3}$	$\frac{2}{3}$	$-\frac{2}{3}$	$\frac{2}{3}$	$-\frac{2}{3}O_{Mn}-\frac{2}{15}$	$-\frac{2}{3}O_{Mn}-\frac{2}{15}$	$\frac{8}{3}O_{Mn}-\frac{2}{15}$	$-\frac{2}{3}O_{Mn}-\frac{2}{15}$	$-\frac{2}{3}O_{Mn}-\frac{2}{15}$	$\frac{2}{3}$	$-\frac{2}{3}$	$\frac{2}{3}$	$-\frac{2}{3}$

From Equation (4–6), I can rewrite the charge sequence in the third line of each APB in Table 4.5, respectively. I note that the requirement of charge neutralization is equivalent to having no change of electrical-potential slope across the APB which is a prerequisite for preventing polar catastrophe.

I can further confine the charge state if I demand minimization of electrical dipoles across the APBs. For example, APB-1 is completely dipole-free if $O_{Mn} = 0.4$ and $O_O = 0.5$. The charge state in this case is shown in the fourth line of APB-1 in Table 4. This occupancy can be compared with the contrast in HAADF images [123]. From the contrast ratio between B' columns in the APB with those in the bulk, where the occupancy is assumed to be unity, I find $O_{Mn} = (0.4 \pm 0.08)$. This is in excellent agreement with the value derived from the charge considerations which indicates that minimization of electrostatic energy contributes to the observed APB structure. In case of APB-3 the electrical dipole moment cannot be eliminated, but continuation of the bulk charge modulation up to the central plane of the APB is possible if $O_{Mn} = 0.8$ and $O_O = 0.83$. This is in reasonable agreement with HAADF contrast which yields $O_{Mn} = (0.66 \pm 0.09)$. For APB-2 the dipole moment does not depend on O_{Mn} and O_O, i.e. condition (6) cannot be further confined. HAADF contrast gives $O_{Mn} = (0.70 \pm 0.09)$.

4.5 Conclusions

Structure, composition, and charge state of three APBs in LSMO/ZrO_2 were analysed. I observe a ladder structure of atomic columns within all APBs. All APBs are rich in Mn where the Mn valence is the same in the APB as in bulk LSMO. Lower HAADF contrast in APBs indicates lower occupancies of atomic sites within the APBs as compared to bulk LSMO. From combined HAADF and ABF imaging I obtain structure models with all positions of cation and anion atomic columns.

The formation of APBs is supposed to be driven by strain relaxation and the availability of Mn atoms due to substitution of Mn atoms by Zr. From charge analysis I conclude that the APB structure is in accordance with minimization of electrostatic energy.

Owing to their reduced occupancy numbers, the APBs might act as efficient ionic conductors. This could make such materials interesting as cathode materials in solid-oxide fuel cells.

ACKOWLEDGEMENTS

This work has been initiated by Prof. J. Zhang (Department of Physics, Shanghai University). Samples have been prepared by Dr. Y. Gao during his PhD work at Max Planck Institue for Solid State Research (MPI-FKF). The research leading to these results has received funding from the European Union Seventh Framework Program [FP/2007/2013] under grant agreement no 312483 (ESTEEM2).

Chapter 5 Electron-Beam-Induced Antiphase Boundary Reconstructions in a ZrO_2-$La_{2/3}Sr_{1/3}MnO_3$ Pillar-Matrix System

Abstract

The availability of aberration-correctors for the probe-forming lenses makes simultaneous modification and characterization of materials down to atomic-scale inside a transmission electron microscopy (TEM) realizable. In this chapter, I report on the electron-beam-induced reconstructions of three types of antiphase boundaries in a probe-aberration corrected TEM. With the utilization of HAADF STEM, ABF STEM and EELS, the motion of both heavy element Mn and light element O atomic columns under moderate electron beam irradiation are revealed at atomic resolution. Besides, Mn segregated in the antiphase boundaries (APBs) was observed to have reduced valence states, which can be directly correlated with oxygen loss. Charge states of the APBs are finally discussed based on these experimental results. This study provides support for the design of radiation-engineering solid-oxide fuel cell materials.

People involved in this part research: Dan Zhou, Wilfried Sigle, Marion Kelsch, Hanns-Ulrich Habemeier, Peter A. van Aken.

Max Planck Institute for Solid State Research, Stuttgart Center for Electron Microscopy, Heisenberstrasse 1, 70569, Stuttgart, Germany

5.1 Introduction

The radiation effects in charged particle microscopes are usually thought to introduce undesirable disorder, and thus deteriorate the material. However, with controlled dose and beam energy, these radiations may have beneficial effects on nanostructured materials, like self-organization and self-assembly. Recent reports demonstrate that they can be used to tailor the mechanical[124, 125], electronic [126], and even magnetic properties [127-129] of the material. Among these charged particles, the electrons in scanning electron microscopy [130] and TEM[131, 132] have attracted more and more interest due to the possibility of simultaneous structural and chemical modifications and characterizations down to atomic-scale.

In a recent report [133, 134] and Chapter 4, I showed that the formation of antiphase boundaries (APB) provides a means for strain relaxation in a system composed of ZrO_2 pillars in $La_{2/3}Sr_{1/3}MnO_3$ thin films. Three types of APBs were observed and studied in detail. In the course of this chapter I found that under prolonged electron irradiation a structural and chemical reconstruction of the APBs appeared. This reconstruction is studied *in situ* at atomic resolution using HAADF and ABF STEM and simultaneous EELS. Finally, I discuss the reconstruction mechanism of the APBs in the context of radiation effects and electrostatic coupling at the boundaries.

5.2 Sample preparation and TEM details

ZrO_2 and LSMO were co-deposited epitaxially on (001) single-crystalline LAO substrate by pulsed laser deposition. Stoichiometric amounts of LSMO and ZrO_2 according to $(1–x)\text{LSMO}+x\text{ZrO}_2$, with x =0.2, were used. Details of the material growth process can be found in Gao *et al.* [89].

The plan-view specimens for TEM studies were prepared by grinding and dimpling followed by low-temperature (at liquid nitrogen temperature) argon ion thinning with a precision ion polishing system (PIPS, Gatan, model 691) to achieve electron transparency.

HAADF images, EEL spectrum images and ABF images from plan-view specimens were obtained using a probe-aberration-corrected JEOL ARM200CF microscope operated at 200 keV, equipped with a Gatan GIF Quantum ERS imaging filter with dual-EELS acquisition capability.

The experimental convergence angle was 28 mrad for HAADF and EELS imaging. The corresponding inner and outer collection semi-angles for HAADF were set to 75–310

mrad. The inner and outer collection semi-angles for ADF images acquired simultaneously during EELS spectrum imaging with Gatan ADF detector were 67−166 mrad, and the collection angle for EELS spectrum imaging was 67 mrad. MSA was performed to reduce the noise of the EEL spectra with WPCA.

The time-series HAADF image stacks were acquired with 20 µs/pixel, 1000 µs flyback time, 512 by 512 pixels per frame resulting in 5.75 s total frame time. I acquired 30 frames per series. To minimize the electron illumination on the interface region, I did focusing and astigmatism alignment on nearby remote area remote from the interface to ensure the interface will be in focus during acquisition. Appropriate condenser lens settings and condenser apertures were chosen so that the time scales of structure variation and acquisition time were similar.

5.3 Results

5.3.1 Geometric arrangement change under electron beam illumination

Aberration-corrected HAADF STEM images of the three APB types before and after electron beam modification are presented in Fig. 5.1. The details of the chemistry and structure of these APBs before electron beam modification were already presented in Chapter 4. To be consistent with my former reports, I keep using the denotations of APB-1, APB-2, and APB-3 and LSMO in the tetragonal notation (space group I4/mcm, No. 140). There is a phase shift of half a {110} plane distance across the boundary along the [110] direction for APB-1 and APB-2 and along the [1-10] direction for APB-3. The boundary planes are {110} for APB-1 and {310} for APB-2 and APB-3. The ladder-like features inside these APBs are Mn/O atomic columns with smaller occupation compared to that in the matrix region. APB-1 and APB-2 before electron-beam-induced reconstructions are shown in Fig. 5.1a and APB-3 in Fig. 5.1c; APB-1 and APB-2 after electron-beam-induced reconstructions are presented in Fig. 5.1b and APB-3 in Fig. 5.1d.

The HAADF images of the matrix region show bright columns corresponding to the heavy A-site (La/Sr) atomic columns and weaker columns corresponding to the lighter B'-site (BO-site, Mn/O) atomic columns in $La_{2/3}Sr_{1/3}MnO_3$. Due to the low elastic scattering cross section of oxygen atoms and the angular range used for HAADF imaging, the pure oxygen ion columns are invisible in HAADF images.

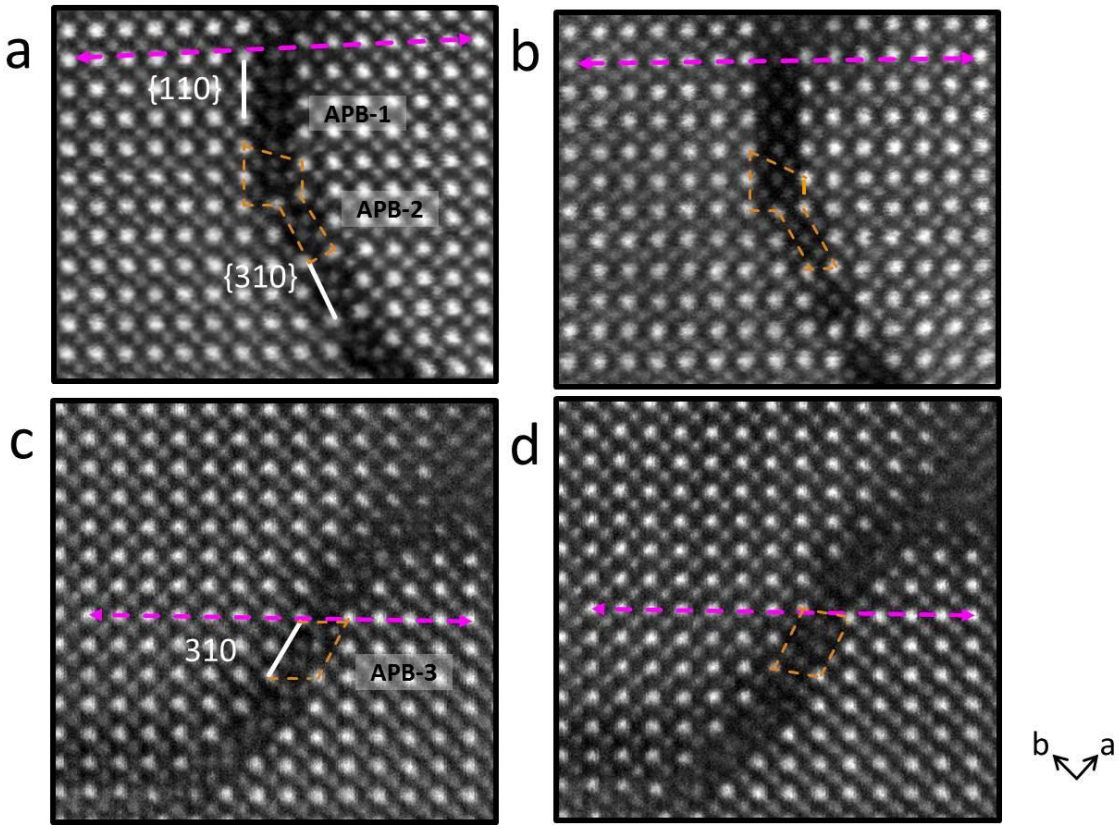

Figure 5.1 HAADF image of a plan-view 80 mol% LSMO-20 mol% ZrO_2 sample showing APB-1 and APB-2 (a) before and (b) after electron-beam-induced reconstructions, and APB-3 (c) before and (d) after electron-beam-induced reconstructions.

Comparison of these images reveals a few differences.

Firstly, the ladder-like appearance of Mn/O atomic columns inside these APBs disappears. The arrangement of these Mn/O atomic columns becomes more like in the matrix region if the difference between A-sites and B'-sites is ignored.

Secondly, local atomic plane shifts are observed. The original phase shift of half a {110} plane distance disappears for APB-1 and APB-2 while the boundary plane remains the same, as shown in Fig. 5.1a and Fig. 5.1b. Lower magnification HAADF images, as shown in Fig. 5.2, confirm the disappearance of the original phase shift. Fig. 5.2a shows an HAADF image acquired before electron-beam-modification. There are 16 and 16.5 {110} plane distances between the two yellow lines on the left and right side of APB-1, respectively. The difference of 0.5 {110} plane distance manifests the phase shift as required for an APB. In Fig. 5.2b, the HAADF image acquired after electron-beam-modification, there are 16 {110} plane distances on both sides of APB-1, which proofs the disappearance of the phase shift required by an APB.

Whereas APB-3 (Fig. 5.1c and 5.1d), another phase shift of half a {110} plane distance along the [110] direction is found in addition to the original phase shift of half a

{110} plane distance along the [1-10] direction. This leads to an overall local phase shift of half a {100} plane distance along the [100] direction for APB-3 under moderate electron beam irradiation. The shifted atomic planes are the ones perpendicular to the phase shift direction [110] for APB-1 and APB-2 and parallel to the phase shift direction [1-10] for APB-3. They are actually the same atomic planes and differentiated by their relationships to the phase shift direction of these APBs before electron-beam-induced reconstruction.

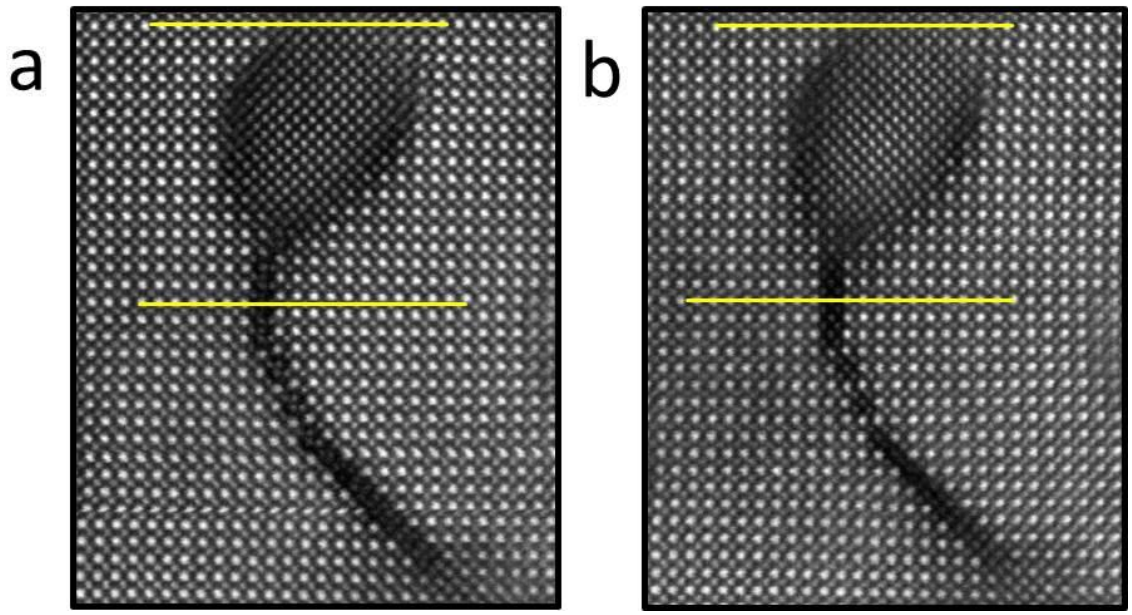

Figure 5.2 Lower magnification HAADF images of the area shown in (a) Fig. 5.1a and (b) Fig. 5.1b, respectively.

The lines drawn in magenta color connect two A-site atomic columns on two sides of these APBs before electron beam modification (Fig. 5.1a and 5.1c) and are moved without any rotation to the images acquired after electron beam modification. One end of the copied lines was located at the same A-site atomic column as before irradiation (Fig. 5.1b and 5.1d). I find that this line also ends on A-site atomic columns on the other side of the APB, indicating no change of the atomic column positions at some distance away from the APB walls for all the APBs. Close to the APBs the deviation from the magenta line is clearly different before and after irradiation. These modifications are achieved by atomic column shifts to opposite directions on the two sides of the APB walls, i.e. left side upwards and right side downward for the situations presented in Fig. 5.1. These local modifications occur in a region extending to about 1 nm away from the APB boundaries. It is worth noting that the plane spacing parallel to the APB plane are not influenced by the APB.

Thirdly, the number of B'-site atomic columns inside the APB walls reduces for APB-1 and APB-2, but not for APB-3. As demonstrated in Fig. 5.1a and 5.1b by the orange marks, there is one less B'-site column inside APB-1 walls for every 5 B'-sites columns and inside APB-2 walls for every 4 B'-site columns. Visually, the two atomic columns at the centre of APB-1 and APB-2 have merged. The 6 B'-site columns inside APB-3 walls are kept, as given in Fig. 5.1c and 5.1d.

In addition, the B'-site occupation in APB-1 and APB-2 is more uniform as judged from the more homogeneous HAADF intensity after electron-beam-reconstructions as compared to that of before. For APB-3, no visible redistribution of B'-site occupation can be observed from the HAADF images.

5.3.2 Elemental distribution and valence states

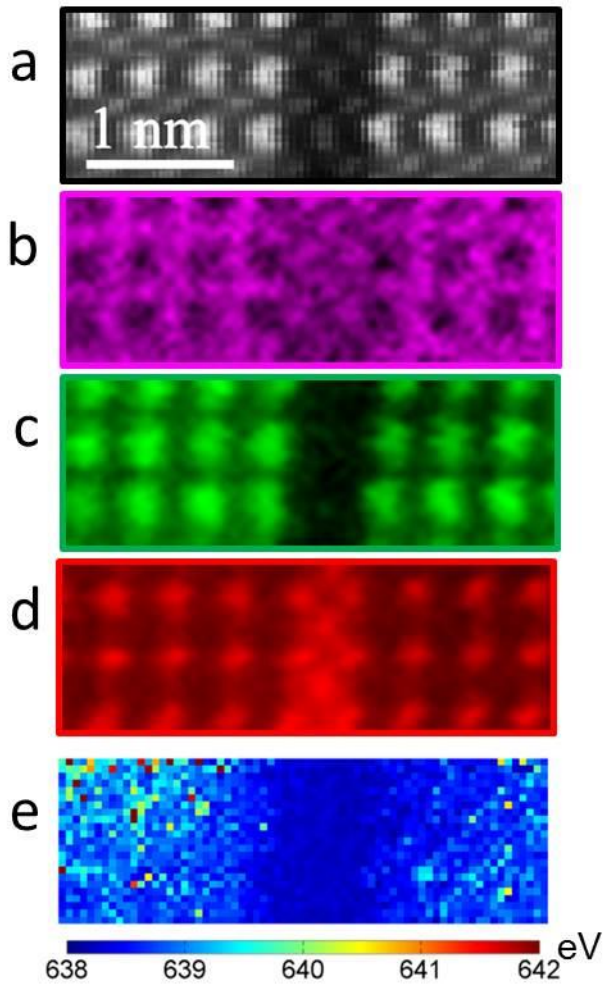

Figure 5.3 (a) ADF image of the APB-1 area in Fig. 5.1b in a plan-view 80 mol% LSMO-20 mol% ZrO_2 sample. EELS spectrum image of (b) O-K, (c) La-$M_{4,5}$, and (d) Mn-$L_{2,3}$. (e) Mn-L_3 peak positions obtained from Gaussian fitting of the background-subtracted Mn-L_3 spectrum image.

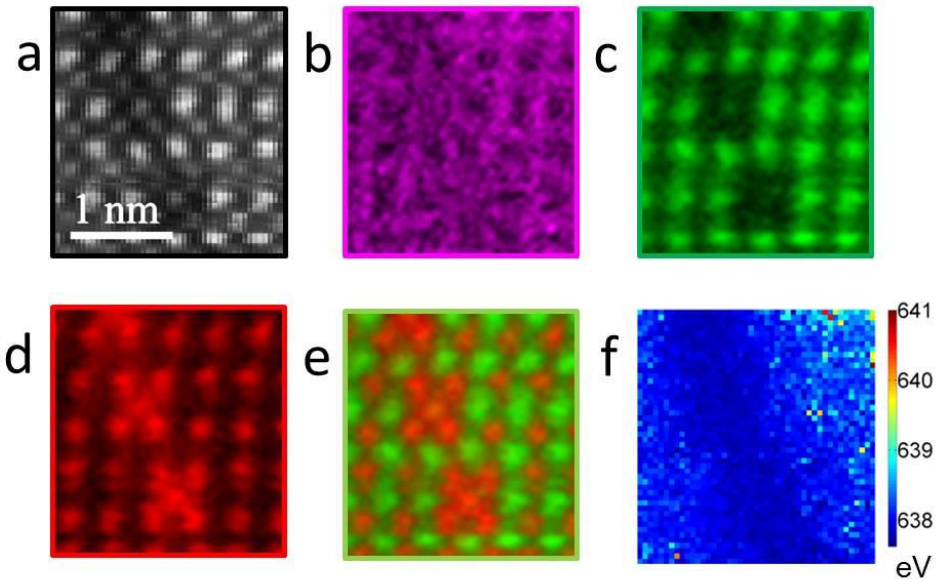

Figure 5.4 (a) ADF image of the APB-2 area in Fig. 5.1b in a plan-view 80 mol% LSMO-20 mol% ZrO_2 sample. EELS spectrum image of (b) O-K, (c) La-$M_{4,5}$, and (d) Mn-$L_{2,3}$. (e) Overlay of EELS spectrum image of La-$M_{4,5}$ in green and Mn-$L_{2,3}$ in red. (f) Mn-L_3 peak positions obtained from Gaussian fitting of the background subtracted Mn-L_3 spectrum image.

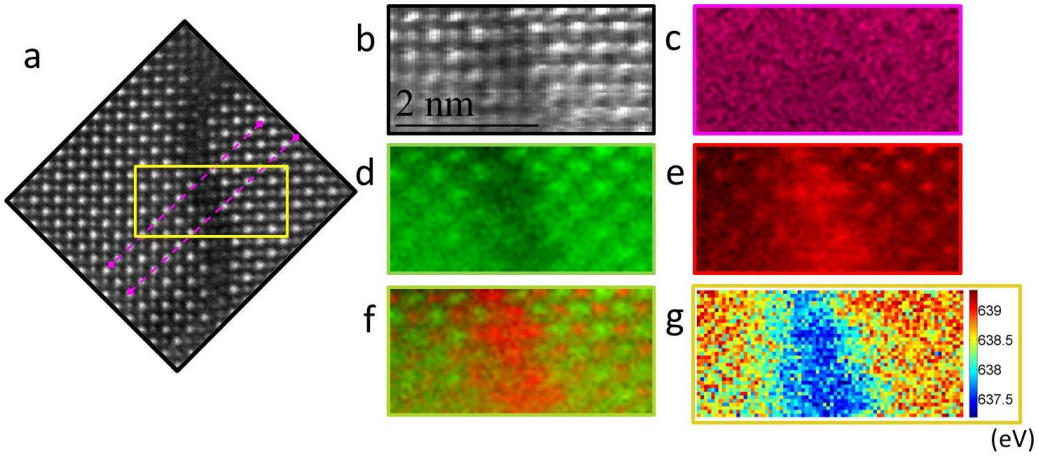

Figure 5.5 (a) HAADF image of the APB-3 area in a plan-view 80 mol% LSMO-20 mol% ZrO_2 sample, same as presented in Fig. 5.1d but rotated counterclockwise for about 45 degree. (b) ADF image of the sample area labeled by the yellow frame in (a). EELS spectrum image of (c) O-K, (d) La-$M_{4,5}$, and (e) Mn-$L_{2,3}$. (f) Overlay of EELS spectrum image of La-$M_{4,5}$ in green and Mn-$L_{2,3}$ in red. (g) Mn-L_3 peak positions obtained from Gaussian fitting of the background subtracted Mn-L_3 spectrum image.

In chapter 4, I showed that these APBs are Mn-rich. To investigate the elemental distribution and chemical states inside the APB walls after electron beam modification, EELS spectrum imaging (SI) was applied, as presented in Fig. 5.3 for APB-1, Fig. 5.4 for APB-2 and Fig. 5.5 for APB-3, respectively. These figures reveal that Mn enrichment is still present after structural modification. No diffusion of A-site atoms into the APB is

observed. The upper-left magenta line drawn in Fig. 5.5a is the same line as the magenta line drawn in Fig. 5.1d.

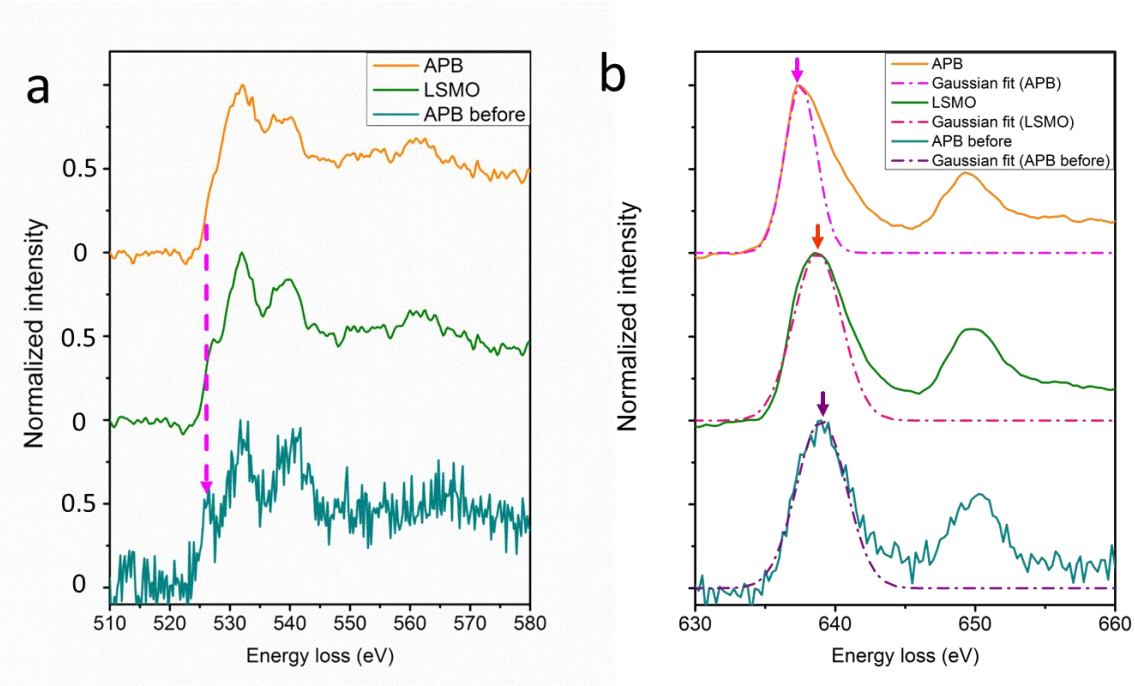

Figure 5.6 Comparison of (a) O-K and (b) Mn-$L_{2,3}$ near-edge fine structures from the APB region before electron beam modification (labeled by "APB before"), the APB region after electron beam modification (labeled by "APB") and the LSMO matrix region near the APB walls after electron beam modification (labeled by "LSMO").

Fig. 5.6a and 5.6b present the O-K and Mn-$L_{2,3}$ edges of the region inside the APB walls before and after electron-beam modification and the LSMO matrix region close to the APB walls after electron-beam modification. The O-K edges are normalized to the maximum intensity in the presented energy loss range, i.e. the peak intensity at the main peak around 535 eV. The Mn $L_{2,3}$ edges are normalized to the maximum intensity in the presented range, i.e. the Mn L_3 peak at about 640 eV.

The dominant reason for the pre-peak intensity is the number of unoccupied 3d states available for mixing or hybridizing with the O 2p states; this means that the pre-peak intensity decreases with a decreasing number of unoccupied 3d states.[135] Therefore, the pre-peak intensity reduction can be attributed to a few reasons: (i) Substitution of Mn by elements with less unoccupied 3d states, like Fe, Co or Ni,[135] or even like Ga[136], whose 3d band is fully occupied and having the same valence as Mn thus not changing Mn's valence states, which however reduces the sum of the unoccupied 3d states hybridized with O 2p orbitals, (ii) variation of the Mn valence state by changing the ratio of La and Sr. Since La has a valence of 3+ and Sr of 2+, an increase of the La concentration will decrease the Mn

valence states with reducing amount of unoccupied 3d states which will also lead to the reduction of O pre-peak intensity, (iii) formation of oxygen vacancies which hinder the mixing of O 2p with unoccupied Mn 3d states by reducing the available O 2p states. These processes can happen independently to modify the O K pre-peak intensity or in a combined way. Moreover, the energy separation between the pre-peak and the adjacent main peak was found to decrease with lowering of the Mn valence.

My experimental data of O-K edges shown in Fig. 5.6a reveal a decrease of the pre-peak intensity, a shift of the pre-peak to higher energy and a reduced separation between the pre-peak and the adjacent main peak after irradiation. No variation of the La to Sr ratio or other element substituting Mn is observed in the elemental distribution analysis. Therefore, the observed change of the O-K edge can only be attributed to the creation of oxygen vacancies, which leads to a reduction of the Mn valence state, as confirmed from the Mn-L_3 peak positions shown in Fig. 5.6b. Nonlinear least square fitting of a Gaussian peak to the background-subtracted Mn-L_3 peaks were applied to verify the valence state of Mn. Spectra from the matrix region and the APB region show Mn-L_3 peak positions of 638.73 eV and 637.53 eV, respectively, i.e. a difference of 0.19 eV and 1.39 eV respectively compared to the spectra collected before modification of 638.92 eV. Comparison with literature data shows that this left shift can be interpreted as a reduced valence state of Mn [104, 137-139]. The comparison also reveals that the APB region is faster and more influenced by electron-beam irradiation than the LSMO matrix region.

Applying the same nonlinear least square fitting of a Gaussian peak to the Mn spectrum image from these three APB regions show a consistent gradual decrease of the Mn valence state from the matrix to the boundary regions, as given in Fig. 5.3e, Fig. 5.4(f) and Fig. 5.5 (g), respectively.

5.3.3 O position determination

To retrieve the oxygen atomic positions in and at the APBs after electron-beam modifications, simultaneous HAADF and ABF images are acquired. It should be noted that in HAADF images atoms appear bright on a dark background, whereas in ABF imaging atoms appear dark on a bright background.

As shown in Fig. 5.7 for APB-1, the disappearance of a phase shift of half a {110} plane distance under electron beam illumination could give two possible structures, as shown in Fig. 5.7b or Fig. 5.7c, starting from the structure shown in Fig. 5.7a. The difference of these two structures relies on the oxygen columns between two B’-sites in the boundary. Qualitatively speaking, this difference can occur if all the oxygen atoms in the

B’-sites columns inside the APBs move together with Mn. If so, one would obtain the final structure shown in Fig. 5.7b. Otherwise, one would obtain the structure shown in Fig. 5.7c is obtained. The results from simultaneously acquired HAADF and ABF images are shown in Fig. 5.7(d-g). From the line profile drawn across 3 B’-sites inside the APB, the existence of pure oxygen columns can be recognized from the slight damping of the intensity between neighbouring B’ sites in the ABF line profile. These results confirm the structure to be as depicted in Fig. 5.7c.

A comparison of Fig. 5.8, which is a lower-magnification HAADF image of Fig. 5.7d and e, with Fig. 5.1a and 5.1b, and Fig. 5.7 confirms that the data shown in Fig. 5.7 are for an APB-1 before and after electron-beam-induced reconstructions happened.

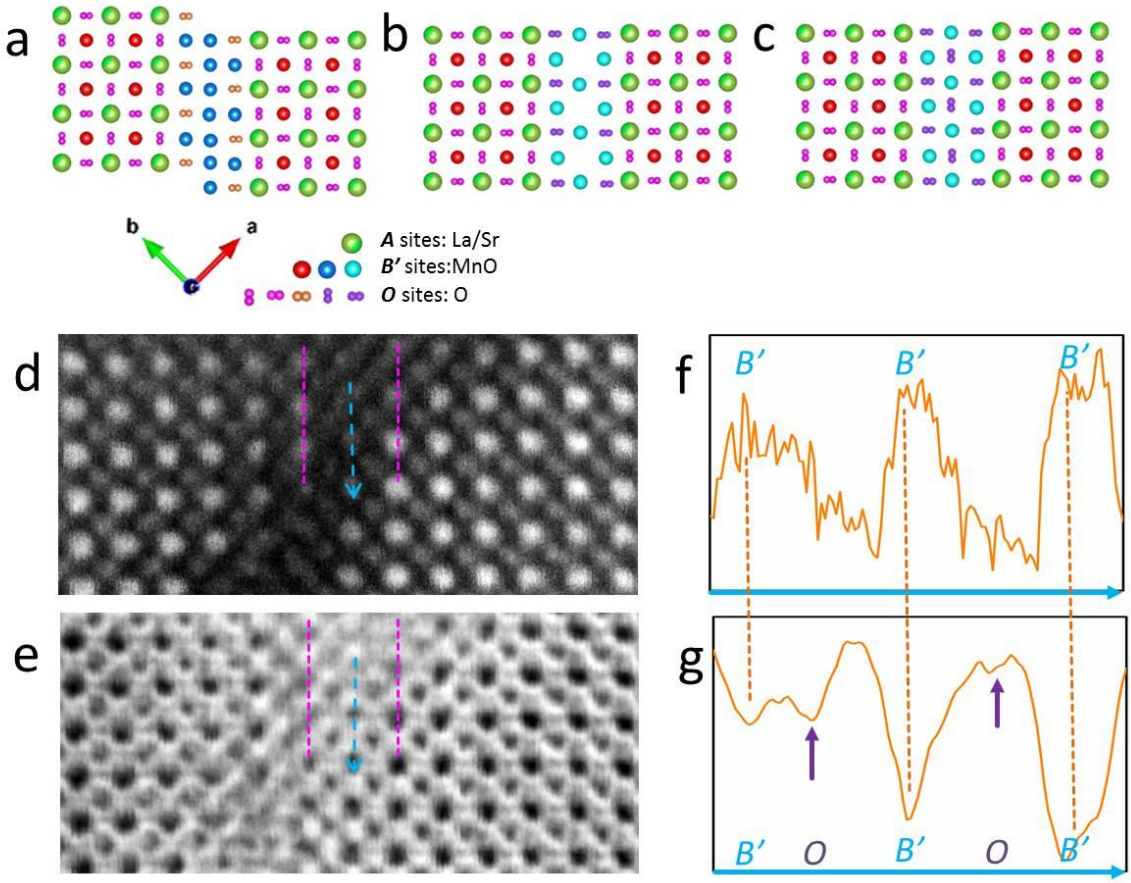

Figure 5.7 (a) Starting structure model of APB-1, as derived in chapter 4. Possible structure of APB-1 after electron beam modifications (b) non-presence and (c) presence of oxygen columns between B’-sites inside the APB. Simultaneously acquired (d) HAADF image and (e) ABF image of a region including APB-1 after electron beam illumination of the plan-view 80 mol% LSMO-20 mol% ZrO_2 sample. Line profiles along the blue line in (f) the HAADF image and (g) the ABF image. The line profiles are integrated along the horizontal direction for 3 pixels. The magenta lines are drawn to help identifying the APB walls and thus confirm the structure of APB-1 after electron-beam-modification, as shown in Fig. 5.8.

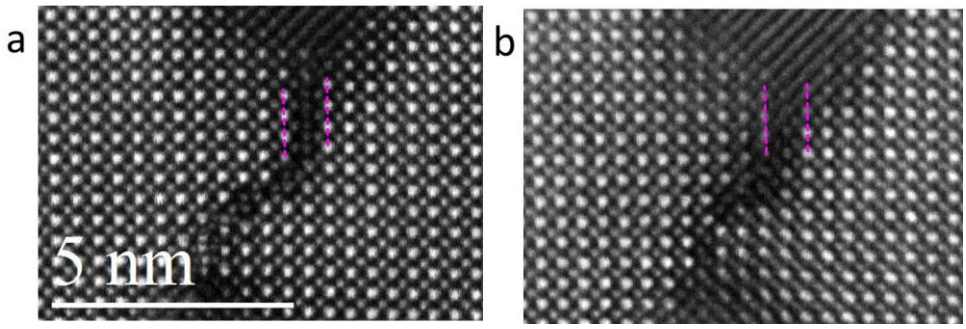

Figure 5.8 Lower-magnification HAADF image of APB-1including the sample area shown in Fig. 5.7d and 5.7e before (a) and after (b) electron-beam-induced reconstructions. The magenta lines cross the same atomic columns as the magenta lines in Fig. 5.7.

The situation for APB-2 is shown in Fig. 5.9. The simultaneously acquired HAADF and ABF images confirm the structure after electron modifications to be as shown in Fig. 5.9b. Visually, the two B' columns and the two pure O columns, marked by light blue frames in Fig. 5.9a, merge to one B' column and one pure O column, respectively. The homogeneous HAADF intensity of B' columns inside the wall, as shown in Fig. 5.1b, revealed the further redistribution of B' column inside the APB walls.

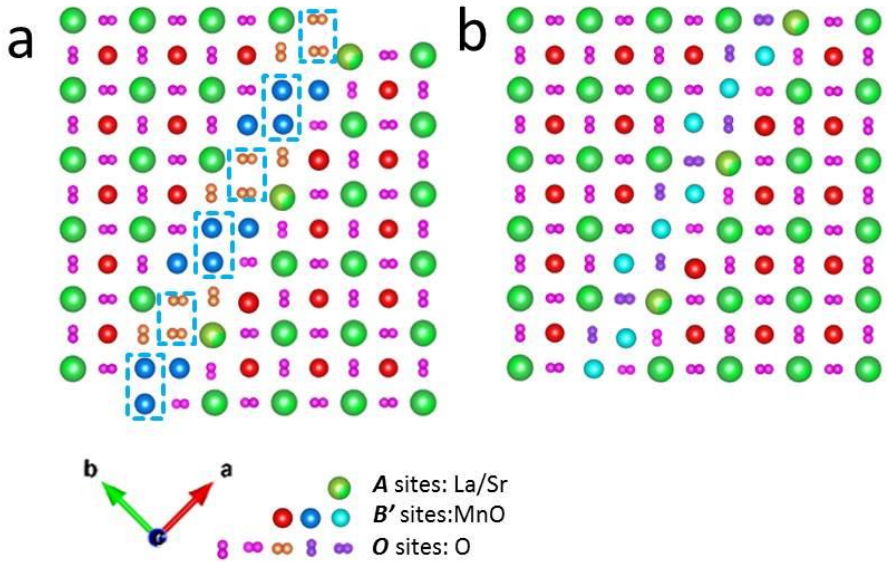

Figure 5.9 (a) Starting structure model of APB-2, as derived in Chapter 4. (b) Structure model of APB-2 after electron beam modifications.

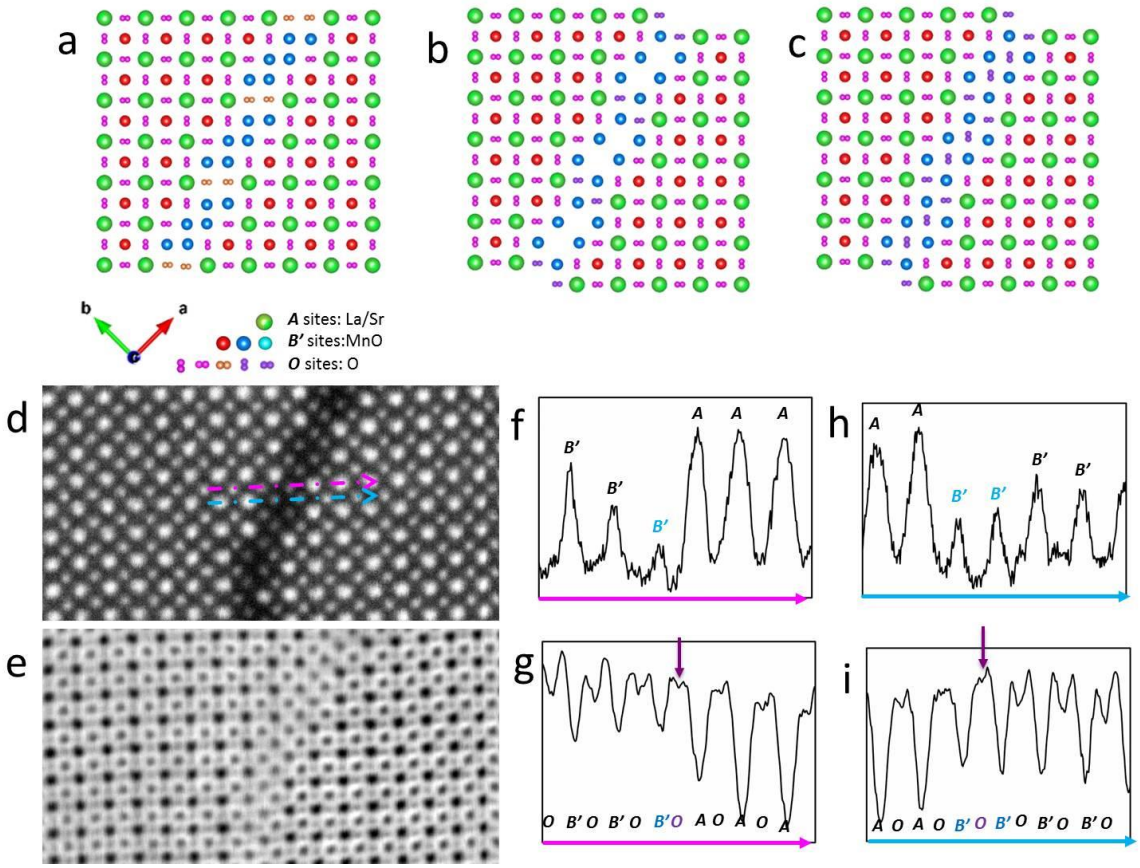

Figure 5.10 (a) Starting structure model of APB-3, as derived in chapter 4. Possible structure of APB-3 after electron beam modifications (b) non-presence and (c) presence of oxygen columns between B'-sites along the <110> direction inside the APB. Simultaneously acquired (d) HAADF image and (e) ABF image of a region including APB-3 after electron beam illumination of the plan-view 80 mol% LSMO-20 mol% ZrO_2 sample. Line profiles are shown along the magenta line in (f) the HAADF image and (g) the ABF image and along the blue line in (h) the HAADF image and (i) the ABF image. The line profiles are integrated along the vertical direction for 3 pixels.

Fig 5.10 gives details about APB-3 after electron-beam-induced reconstructions. Derived from the heavy atomic column arrangement from HAADF images, the structure of APB-3 is shown in Fig. 5.10b or Fig. 5.10c, with differences in the presence of oxygen columns between neighbouring B'sites inside the APB walls. The results from simultaneously acquired HAADF and ABF images are shown in Fig. 5.10d–i. From the line profiles, the existence of pure oxygen columns can be recognized from the arrowed slight damping of the intensity between neighbouring A and B' sites (Fig. 5.10g) or neighbouring B' sites (Fig. 5.10i) in the ABF line profile. These results confirm the structure to be as represented in Fig. 5.10c.

5.4 Discussions

5.4.1 The occurrence of the electron-beam-induced reconstructions

As reported before, Mn oxides are sensitive to electron beam illumination[140-142] especially when a focused electron beam in an aberration-corrected TEM is used. After Egerton[143], 'in the case of transitional metal-oxides, radiolysis is believed to occur via the Knotek-Feibelman mechanism: the incident electron creates an inner shell vacancy on the metal site by (interatomic) Auger decay from the oxygen. This results in a (neutral) or positive O atom which is repelled by the surrounding metal ions and ejected into the vacuum leaving a metal-rich surface with a mottled (pitted-appearance). The process continues until the material becomes sufficiently conducting to screen the positive oxygen ion'. The resulting rupture of Mn-O bonds can cause the movement of Mn atom columns.

The existence of defects, like interfaces, can speed up the process described above. Oxygen vacancy formation/ordering is found to drive the lattice mismatch accommodation/strain relief mechanism [144, 145]. A good proof of this claim is that there is more reduction of Mn valence states inside APB than the LSMO matrix region under the same electron beam illumination, as shown in Fig. 5.6. Therefore, the modifications observed in this chapter can be ascribed to the interplay between the strain imposed by the formation of unpaired misfit dislocations, changes in oxygen vacancy content and cation mobility, and the ordering of oxygen vacancies.

The process can be described as follows. Oxygen loss inside the boundaries caused by electron beam irradiation leads to the rupture of bonds between oxygen and A-sites and Mn. The resulted A-site atoms and Mn atoms have lower displacement energy and thus move under further electron beam irradiation towards a stable state. For APB-2 and APB-3, a common feature in the boundaries before irradiation is the presence of two or more pure closely spaced oxygen column. This might generate much stronger interaction to electron beam than the other oxygen atoms or columns.

The occupancy of the B' sites inside these APBs can be achieved from the background-subtracted signal in HAADF images [123]. From the background-subtracted signal ratio between B' columns in the APB with those in the LSMO matrix region, where the B' occupancy is assumed to be unity, I find Mn occupancy for APB-1 to be 0.57±0.24 before irradiation and 0.83±0.08 after irradiation, for APB-2 to be 0.65±0.26 and 0.89±0.24 before and after irradiation, and for APB-3 to be 0.73±0.17 and 0.72±0.35 before and after irradiation. As already mentioned in Chapter 5.3.1, for APB-1, 5 B'-sites are observed to 'merge' to 4 B'-sites. If only oxygen is lost during irradiation, the Mn occupancy after irradiation is 0.71 (5 times 0.57 divided by 4), which is close to but lower than the measured value of 0.83. For APB-2, considering the merge and redistribution, the

calculated Mn occupancy should be 0.87 if no Mn is lost, which also meet with the experimentally measured value. For APB-3, the value should be the same, as calculated and observed. Inspection of a time-series of HAADF images (which can be requested from me as a movie) shows that the observable A-site and B'-site atomic column movement stops at about 150 s. Quantitative analysis of this time-series of HAADF images gives the Mn occupancies shown in Fig. 5.11, showing a decrease until about 150 s, then a gradual increase until about 400 s, and kept constant within error consideration afterwards. These results could be correlated with the ordered to disordered and again to ordered atomic column arrangement under electron beam illumination.

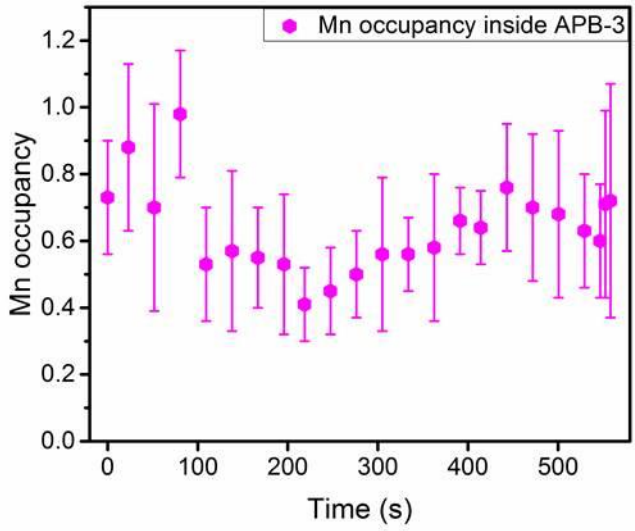

Figure 5.11 Mn occupancy of APB-3 measured from the time-series HAADF images during reconstructions.

Prolonged electron-beam irradiation without changing probe size or dwell time over 20 minutes cannot further modify the structures. However, a large increase of dose rate by increasing probe size, condenser aperture or dwell time leads to much darker contrast in the APBs indicating loss of Mn atoms and even amorphorization in the boundaries.

5.4.2 Atomic occupation and valence discussions

From the results above I can exclude heavy atom loss during irradiation. Similar to our previous report in Chapter 4, assuming pure ionicity I get the charge sequence of planes parallel to the boundary planes for these three boundaries (Fig. 5.12), as shown in Table 5.1. Columns in the boundary region are highlighted by different color. To differentiate from the original structure, where we let O_{Mn} and O_O to be the average occupancies of Mn and O inside the APBs relative to the ones in the bulk, here we let $O_{\mathrm{Mn}}{}'$

and $O_O{}'$ to be the average occupancies of Mn and O inside the boundaries relative to the ones in the bulk and $V_{Mn}{}'$ to be the average Mn valence state in the APB region.

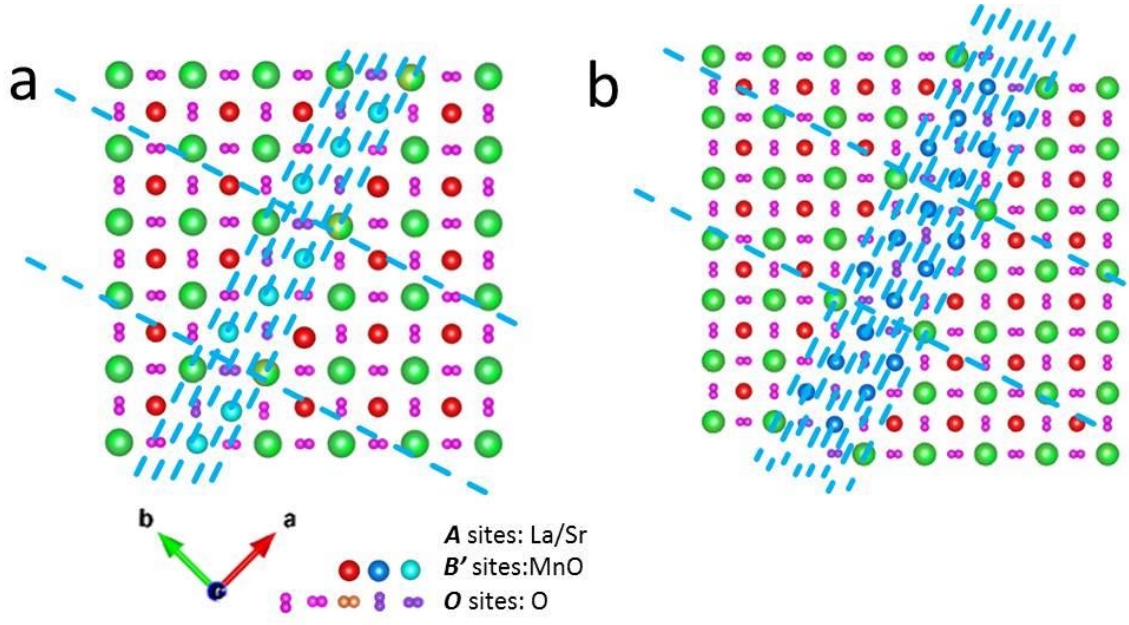

Figure 5.12 Illustration of the plane components in boundary planes in sequence of (a) APB-2 and (b) APB-3.

Table 5.1 Charge sequence across the APB walls. For APB-1, the direction from left to right corresponds to [1-10] and the direction from top to bottom to [-1-10]. For APB-2 and APB-3, the direction from left to right corresponds to [1-30] and the direction from top to bottom to [-3-10].

			In the APB walls							
APB-1	O B'	A O	***O*** ***B'***		***B'*** ***O***		***O*** ***B'***		A O	O B'
Charge	$-\frac{2}{3}$	$\frac{2}{3}$	$-4O_O{}' + O_{Mn}{}' \; V_{Mn}{}'$		$-4O_O{}' + O_{Mn}{}' \; V_{Mn}{}'$		$-4O_O{}' + O_{Mn}{}' \; V_{Mn}{}'$		$\frac{2}{3}$	$-\frac{2}{3}$
Charge neutrality	$-\frac{2}{3}$	$\frac{2}{3}$	$-\frac{2}{9}$		$-\frac{2}{9}$		$-\frac{2}{9}$		$\frac{2}{3}$	$-\frac{2}{3}$
APB-2	O B'	A O	***O*** ***B'***		***O*** ***B'***		***B'*** ***O***		A O	O B'
Charge	$-\frac{2}{3}$	$\frac{2}{3}$	$-4O_O{}' + O_{Mn}{}' \; V_{Mn}{}'$		$-4O_O{}' + O_{Mn}{}' \; V_{Mn}{}'$		$-4O_O{}' + O_{Mn}{}' \; V_{Mn}{}'$		$\frac{2}{3}$	$-\frac{2}{3}$
Charge neutrality	$-\frac{2}{3}$	$\frac{2}{3}$	$-\frac{2}{9}$		$-\frac{2}{9}$		$-\frac{2}{9}$		$\frac{2}{3}$	$-\frac{2}{3}$
APB-3	O B'	A O	***O*** ***B'***	***B'*** ***O***	***B'*** ***O***	***O*** ***B'***	***O*** ***B'***	***B'*** ***O***	A O	O B'
Charge	$-\frac{2}{3}$	$\frac{2}{3}$	$-4O_O{}' + O_{Mn}{}' \; V_{Mn}{}'$	$-4O_O{}' + O_{Mn}{}' \; V_{Mn}{}'$	$-4O_O{}' + O_{Mn}{}' \; V_{Mn}{}'$	$-4O_O{}' + O_{Mn}{}' \; V_{Mn}{}'$	$-4O_O{}' + O_{Mn}{}' \; V_{Mn}{}'$	$-4O_O{}' + O_{Mn}{}' \; V_{Mn}{}'$	$\frac{2}{3}$	$-\frac{2}{3}$
Charge neutrality	$-\frac{2}{3}$	$\frac{2}{3}$	$-\frac{1}{9}$	$-\frac{1}{9}$	$-\frac{1}{9}$	$-\frac{1}{9}$	$-\frac{1}{9}$	$-\frac{1}{9}$	$\frac{2}{3}$	$-\frac{2}{3}$

To achieve zero total charge across the APB, the following conditions have to be met:

APB-1: $\frac{2}{3}+3*(-4{O_O}'+{O_{Mn}}'{V_{Mn}}')=0$ (1)

APB-2: $\frac{2}{3}+3*(-4{O_O}'+{O_{Mn}}'{V_{Mn}}')=0$ (2)

APB-3: $\frac{2}{3}+6*(-4{O_O}'+{O_{Mn}}'{V_{Mn}}')=0$ (3)

Therefore,

APB-1: ${O_O}'=\frac{1}{4}{O_{Mn}}'{V_{Mn}}'+\frac{1}{18}$ (4)

APB-2: ${O_O}'=\frac{1}{4}{O_{Mn}}'{V_{Mn}}'+\frac{1}{18}$ (5)

APB-3: ${O_O}'=\frac{1}{4}{O_{Mn}}'{V_{Mn}}'+\frac{1}{36}$ (6)

The relationship between original occupancy and occupancy after radiation

APB-1: $3{O_{Mn}}'=4O_{Mn}$ (7)

APB-2: $3{O_{Mn}}'=4O_{Mn}$ (8)

APB-3: ${O_{Mn}}'=O_{Mn}$ (9)

And we use *x* to represent the reduced valence, i.e. ${V_{Mn}}'=V_{Mn}-x=\frac{10}{3}-x$

And I also have

APB-1: $O_O=\frac{10}{9}O_{Mn}+\frac{1}{18}$ (10)

APB-2: $O_{Mn}=\frac{6}{5}O_{\mathrm{O}}-\frac{1}{20}$ (11)

APB-3: $O_O=O_{Mn}+\frac{1}{30}$ (12)

Then I have

APB-1: ${O_O}'=O_{\mathrm{O}}-\frac{3}{10}x(O_{\mathrm{O}}-\frac{1}{18})$ (13)

APB-2: ${O_O}'=\frac{4}{3}O_{\mathrm{O}}-\frac{2}{5}x\left(O_{\mathrm{O}}-\frac{1}{24}\right)$ (14)

APB-3: ${O_O}'=\frac{5}{6}O_{\mathrm{O}}-\frac{1}{4}x(O_{\mathrm{O}}-\frac{1}{30})$ (15)

To estimate how much oxygen lost in each building block, I have:

APB-1: $\Delta O=6O_{\mathrm{O}}-6{O_O}'=\left(\frac{9}{5}O_{\mathrm{O}}-\frac{1}{10}\right)x$ (16)

APB-2: $\Delta O=8O_{\mathrm{O}}-6{O_O}'=\left(\frac{12}{5}O_{\mathrm{O}}-\frac{1}{10}\right)x$ (17)

APB-3: $\Delta O = 10O_O - 12O_O{}' = \left(3O_O - \frac{1}{10}\right)x$ (18)

Suppose $V_{Mn}{}' = 2$, i.e. $x = \frac{4}{3}$, then

APB-1: $\Delta O = \frac{12}{5}O_O - \frac{2}{15}$ (19)

APB-2: $\Delta O = \frac{16}{5}O_O - \frac{2}{15}$ (20)

APB-3: $\Delta O = 4O_O - \frac{2}{15}$ (21)

From Equation (4-6), we can rewrite the charge sequence in the third line of each APB in Table 5.1, respectively. All APBs do not depend on the occupancies. This is different from the situations before electron beam modifications, where the dipole moments of APB-1 and APB-3 depend on the atom occupancy to minimize the electric field and that of APB-2 does not.

5.5 Conclusions

Electron-beam-induced reconstructions of the structure, composition and charge state of three APBs in LSMO/ZrO_2 were observed and analyzed. For all the APBs, the Mn segregation inside the boundaries is kept, but with a reduced valence state. Atomic columns on the two sides of APBs of the LSMO matrix region move in local area, accompanying the movement of B' sites inside the APBs. From combined HAADF and ABF imaging, I obtain structure models with all positions of cation and anion atomic columns. Moreover, despite the change of number of B'-sites inside the APBs, all APBs are confirmed to lose no heavy atoms, i.e. Mn, analyzed from the background subtracted HAADF signal ratio.

The mechanism of electron-beam-induced reconstructions is supposed to be driven by the strengthened radiolysis at the interface region. Due to the loss of oxygen under electron beam irradiation and therefore rupture of bonds between oxygen and heavy atoms, the structures went from order to disorder, and to order again by local area atomic column movement to reach a new stabilized status. From charge analysis, we conclude all the APBs' electric fields do not depend on the elemental occupancies once charge neutrality is achieved.

ACKNOWLEDGEMENTS

This work has been initiated by Prof. J. Zhang (Department of Physics, Shanghai University). Samples have been prepared by Dr. Y. Gao during his PhD work at Max Planck Institute for Solid State Research (MPI-FKF). The research leading to these results has received funding from the European Union Seventh Framework Program [FP/2007/2013] under grant agreement no 312483 (ESTEEM2).

Chapter 6 Sample Tilt Effects on Atom Column Position Determination in ABF-STEM Imaging

Abstract

The determination of atom positions from atomically resolved transmission electron micrographs is fundamental for the analysis of crystal defects and strain. In recent years ABF imaging has become a popular imaging technique owing to its ability to map both light and heavy elements. Contrast formation in ABF is partially governed by the phase of the electron wave, which renders the technique more sensitive to the tilt of the electron beam with respect to the crystal zone axis than HAADF imaging. Here I show this sensitivity experimentally and use image simulations to quantify this effect. This is essential for error estimation in future quantitative ABF studies.

People involved in this part research: Dan Zhou (1), Knut Müller-Caspary (2), Wilfried Sigle (1), Florian F. Krause (2), Andreas Rosenauer (2), and Peter A. van Aken (1).

(1) Max Planck Institute for Solid State Research, Stuttgart Center for Electron Microscopy, Heisenbergstraße 1, 70569, Stuttgart, Germany

(2) Institut für Festkörperphysik, Universität Bremen, Otto-Hahn-Allee 1, D-28359, Bremen, Germany

6.1 Introduction

ABF imaging in STEM has intrigued research interest in recent years due to its ability to directly visualise light elements, such as Li, N, and O [32, 36, 38, 42, 146, 147]. Light elements give rise to weak electron scattering at high angles leading to low intensities in HAADF images, which are nowadays commonly used for atomic resolution studies. ABF contrast has been shown to be less dependent on atomic number (approximately proportional to $Z^{1/3}$ [43] in ABF imaging where Z is the atomic number, and $Z^{1.7}$ [56] in HAADF imaging), enabling it to directly visualise light elements, even in the presence of heavy elements. However, owing to the small scattering angles used in ABF imaging, coherent scattering leads to a non-monotonic intensity relationship with atomic number at all thicknesses. The reduced dependence on atomic number makes distinguishing between two atom columns with close atomic numbers more difficult. Thus it appears that simultaneous acquisition of HAADF and ABF images is a tempting approach to visualize atoms of a large range of atomic numbers. Such an approach is important in the atomic-scale study of a great number of material systems consisting of light and heavy elements. As an example, macroscopic properties of complex oxides can be critically influenced by small changes of the ligand coordination or by the exact arrangement of the oxygen sub-lattice at hetero-interfaces[44]. To extract reliable atom positions directly from the images one has to assume that intensity maxima in HAADF images (bright spots at atom column positions on a dark background), or intensity minima in ABF images (dark spots at atom column positions on a bright background) accurately correspond to the atom positions. Moreover, to extract distances and angles between different atom columns, one has to assume that in the case of deviations between intensity maxima/minima in HAADF/ABF images and real atom positions, the deviations of the compared atom columns from the real positions are the same for the different columns.

Here I investigate the reliability of the atom column position determination in ABF-STEM. I focus on the important issue of how sensitive intensity minimum positions are with regard to small tilts of the electron beam with respect to the crystal zone axis. In (S)TEM experiments, small specimen tilts from the targeted zone axis can easily be present. These can occur by inaccurate tilting by the operator, but can also have intrinsic reasons such as in the case of static tilts of crystal planes or atom columns near crystal defects, such as dislocations or small-angle grain boundaries. I perform image simulations of both HAADF and ABF and compare positions of intensity minima and maxima with real atom positions. The effect of specimen tilt on the contrast of ADF STEM imaging has

been thoroughly explored in the literature [148]. Therefore, I will pay particular attention to the atom position determination in ABF imaging.

To cover both heavy and light elements in this study, I selected a two-element material system, namely cubic ZrO_2 (space group Fm-3m, a=0.507 nm) with a heavy element Zr columns and a light element O columns along the [001] axis. Along this axis Zr and O column separations are quite large (1.8 Å), resulting in a small overlap of their projected atomic potentials. The structure model of ZrO_2 is shown in Fig. 6.1a and Fig. 6.1b along the [811] axis and the [001] axis.

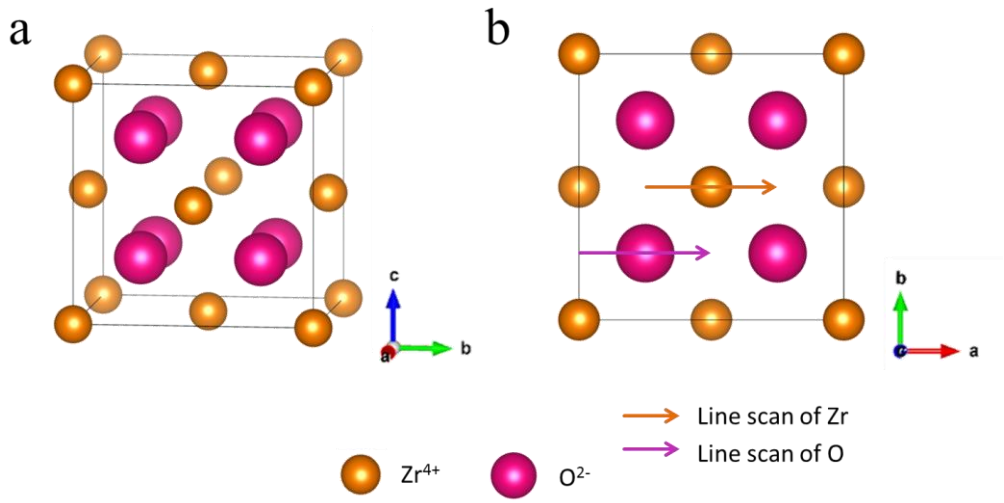

Figure 6.1 Structure models of cubic ZrO_2 viewed along (a) the [811] direction and (b) the [001] axis.

I start from the experimental observations of simultaneously acquired HAADF and ABF images with different convergence and collection angles revealing the minima/maxima position sensitivity to specimen tilts. This is followed by image simulation studies.

6.2 Method

6.2.1 Experimental

A plan-view specimen of ZrO_2-LSMO pillar–matrix structure, as described in references[122, 133] and in Chapter 3-5, was investigated. For my current purpose, I use the ZrO_2 pillar area, as indicated in Fig. 6.2 to investigate both the heavy element (Zr) and the light element (O) atom column positions. The electron beam direction is parallel to the [001] axis.

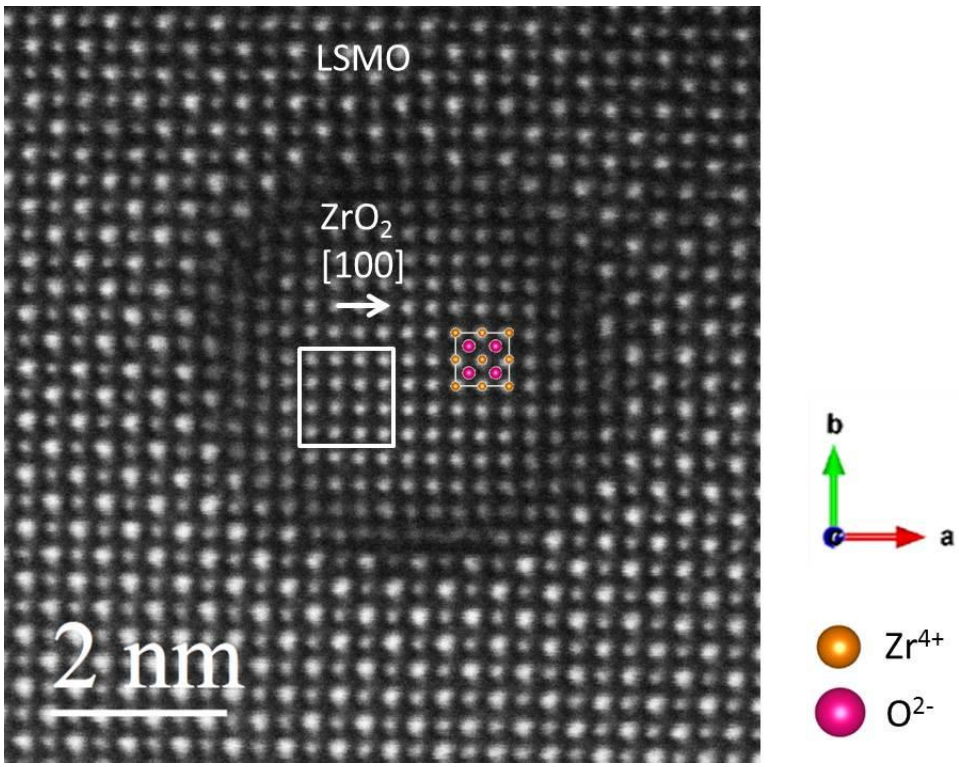

Figure 6.2 HAADF image of a plane-view 20 mol% ZrO_2-80 mol%LSMO sample. Inserted is the structure model of cubic ZrO_2 unit cell viewed along the [001] direction.

In my previous studies[122] and Chapter 3, I showed that ZrO_2 in the pillar region has tetragonal or cubic structure both of which having almost identical *a* lattice parameters. In my simulations I use the cubic structure as structural model[149].

STEM experiments were performed using an aberration-corrected JEOL ARM200CF microscope operated at 200 kV acceleration voltage. The microscope is equipped with a DCOR probe corrector (CEOS GmbH, Germany). The experimental convergence semi-angles were 20.4 mrad and 28 mrad. The JEOL HAADF detector was used to collect the HAADF signal and the JEOL BF detector as the ABF detector with the central part being blocked by a beam stopper. The corresponding collection angles are 75–310 mrad (HAADF) and 11–23 mrad (ABF) for the 20.4 mrad convergence semi-angle, and 87–361 mrad (HAADF) and 13–27 mrad (ABF) for the 28 mrad convergence semi-angle.

6.2.2 Simulation

The simulated results presented here were computed with the absorptive potential multislice algorithm as implemented in the STEMsim-software [150]. In this method, the thermal vibrations of the atoms are included in the calculation by an absorptive potential[151]. The size of the [001]-oriented cubic ZrO_2 (Fm-3m, a = 0.507 nm) supercell was 5×5 unit cells in the lateral directions with the *x*-direction parallel to the [100]-axis and the *y*-direction parallel to the [010]-axis, computed on a numerical grid of 50×50 pixels per

unit cell. All simulations were computed for an accelerating voltage of 200 kV. To get collection-angle-dependent results, I subdivided the calculated angular range (0–100 mrad) into 100 rings of 1 mrad width. The signals from the individual angular ranges were obtained by incoherently adding all signals in the corresponding rings. The sampling in reciprocal space is 0.99 mrad/pixel with an angular range between 0 and 123.75 mrad.

STEM images were simulated with a sampling in real space of 600×600 pixels per unit cell. This allowed precise determination of maxima/minima positions in simulated HAADF/ABF images. I found that for aberration-free probe, as expected due to symmetry there is no shift of maxima/minima positions along the direction perpendicular to the Laue center shift direction. Therefore, in order to save computing time, I calculated maxima/minima a position only from line scans of the STEM probe along the directions parallel to the shift direction of the Laue circle center.

For the line scan simulations, I used 600 pixels per line. As illustrated in Fig. 6.1b, the line scan extends between two Zr or O atoms along the [100] direction resulting in a sampling of 0.4225 pm/pixel. Each line starts from the center of adjacent Zr or O atoms along x direction [100] axis direction, passes through one Zr or O atomic column, and stops at the center of adjacent Zr or O atoms on the other side of the Zr or O atomic columns.

There are in general 3 options to model the specimen tilt, which are all implemented in the STEMsim package: (i) tilt the whole supercell (Fig. 6.3b), (ii) tilt the electron beam (Fig. 6.3c), and (iii) tilt via the propagator (Fig. 6.3d). Although option (i) resembles the experimental situation, it is not applied due to the increased computing time and complexity caused by varying slice potentials with specimen tilt. For small-angle tilts, there are no differences in the results when tilting the beam or tilting via propagator using an aberration-free probe. However, differences will become apparent in case of insufficient aberration correction or a nearly aberration-free probe as in modern aberration-corrected TEMs. Comparison of different spherical aberration values is shown in Fig. 6.4 with other aberration coefficients listed in Table 2.1. In our current study, despite of a small amount of residual aberrations in our experimental probe, I will limit our discussions to aberration-free probe using tilt via the propagator.

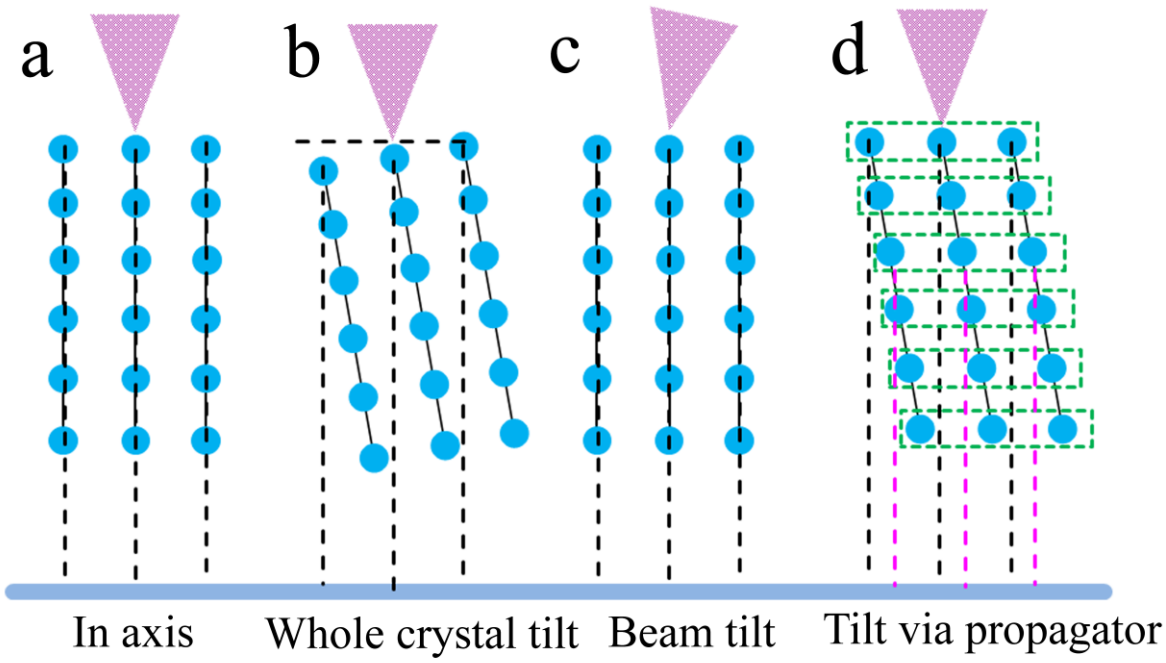

Figure 6.3 (a) Situation without specimen tilt. Illustrations of the three options to model the tilt between electron beam and specimen in STEMsim: (b) tilt of the whole crystal tilt, (c) tilt of the electron beam and (d) tilt via the propagator.

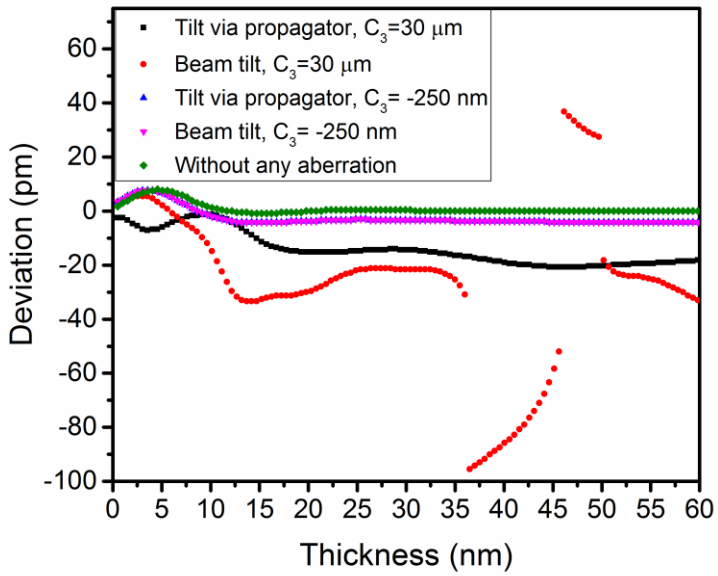

Figure 6.4 Comparison of deviations with different spherical aberration and the other aberration coefficients listed in Table 2.1.

6.2.3 Data processing

All experimental HAADF and ABF images were filtered using a Wiener filter (in reciprocal space) to reduce image noise [152]. The maxima/minima positions in acquired HAADF/ABF images were extracted by maximum/minimum finding and refined by

parabolic fitting using the ImageEval software package developed by Knut Müller-Caspary. All simulated STEM intensities are presented as fractional intensities, normalized to the incident intensity.

Image maxima/minima of simulations were determined by the same parabolic fitting as for the experimental data. In this chapter, I compare maxima positions in HAADF images and minima positions in ABF images and compare them with the true positions. Without tilt (Fig. 6.3a), both positions correspond to the projection of the atoms parallel to the electron propagating direction. On the other hand, in the tilted case it is not obvious whether real positions correspond e.g. to the atom positions in the top plane (black dash line in Fig. 6.3d) or in the central plane (magenta dash line in Fig. 6.3d). Considering the focal plane and limited depth of focus in aberration-corrected STEM imaging, I use the atom positions of the top plane as "true positions" for all specimen tilt situations.

6.3 Experimental results

Fig. 6.5 shows three groups of simultaneously acquired HAADF and ABF images of the ZrO_2 sample area marked in Fig. 6.2. Three different specimen tilt conditions were used, called "tilt 1" "tilt 2" and "tilt 3" in the following, as revealed by the diffraction patterns shown in Fig. 6.5a, 6.5d and 6.5g. Because of the simultaneous acquisition direct comparison of Figs. 6.5b and 6.5c, 6.5e and 6.5f, and 6.5h and 6.5i is possible. The position-averaged convergent beam electron diffraction (PACBED) patterns were acquired with the CCD camera through incoherent averaging of convergent beam electron diffraction patterns[153, 154] while the beam was scanned through the whole area shown in Fig. 6.2, including both LSMO and ZrO_2 regions. To improve the visibility the intensities in the diffraction patterns were color-coded.

For each specimen tilt, I acquired the HAADF and ABF images at two different convergence semi-angles (α) and corresponding different collection semi-angles (β) to make the collection semi-angle of ABF imaging approximately half the convergence semi-angle to convergence semi-angle. The angle values can be found in the experimental section and in Fig. 6.5. For the reasons discussed in section 6.5.2 (6^{th} point), I only selected the ones shown in the figures.

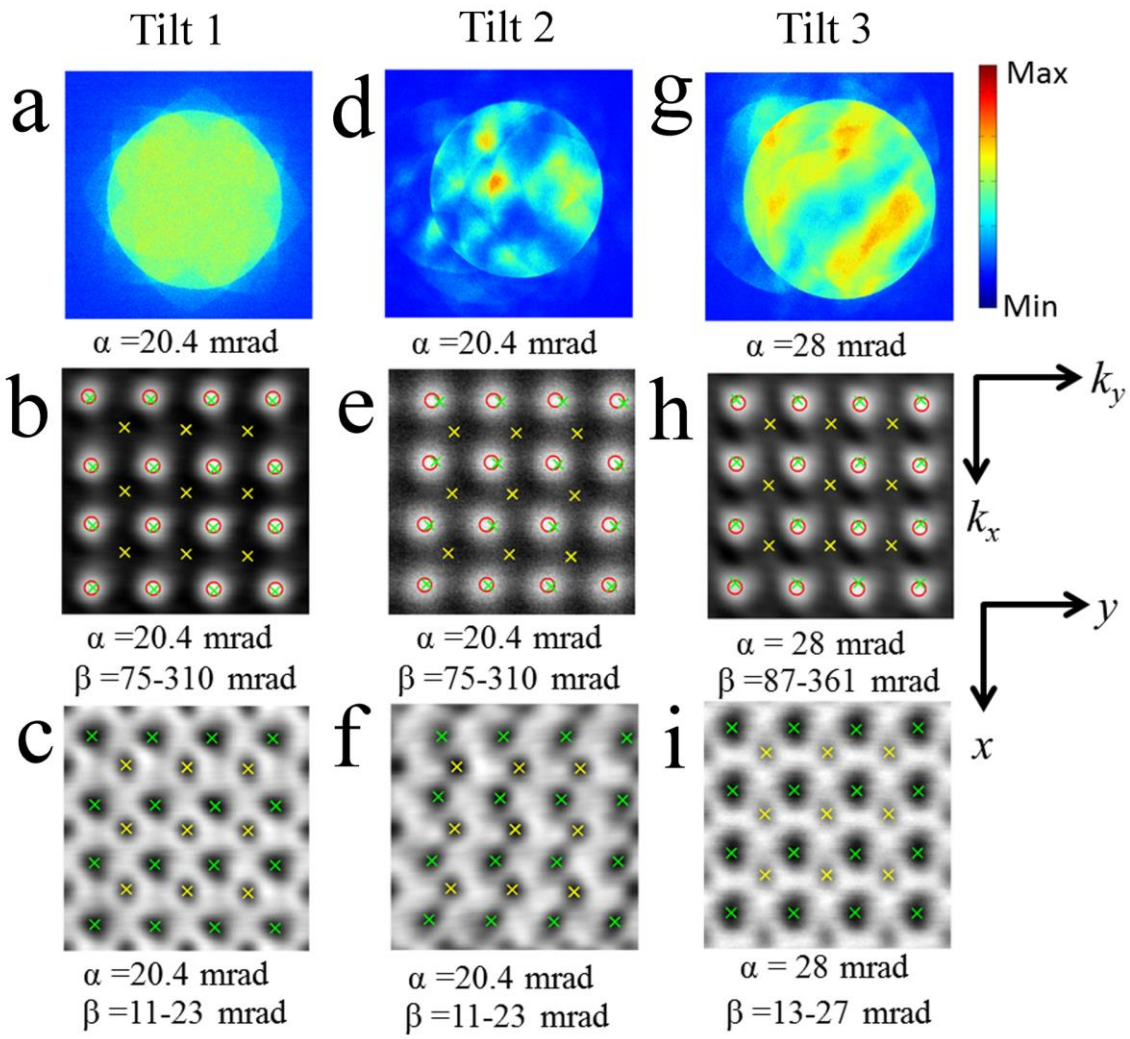

Figure 6.5 The PACBED patterns of the whole sample region shown in Fig. 1 under conditions of (a) tilt 1, (d) tilt 2 and (g) tilt 3. The HAADF images of the ZrO2 sample region inside the square box shown in Fig. 6.2 under the conditions of (b) tilt 1, (e) tilt 2 and (h) tilt 3. ABF images of the same sample region as the HAADF images under the conditions of (c) tilt 1, (f) tilt 2 and (i) tilt 3. The red circles in (b,e,h) indicate the fitted maxima corresponding to the Zr positions, the green crosses in (b-i) indicate the fitted minima in (c,f,i) corresponding to the Zr positions, and the yellow crosses in (b-i) indicate the fitted minima in (c,f,i) corresponding to the O positions.

The high symmetry of the diffraction pattern intensity of "tilt 1" (Fig. 6.5a) indicates that the specimen is in or at least very close to the [001] zone axis. The asymmetry of the diffraction pattern intensity of "tilt 2" (Fig. 6.5d) indicates a specimen tilt away from [001] axis, represented by a Laue center shift vector $(|k_x|, -|k_y|)$ with $|k_x| < |k_y|$. The diffraction pattern of "tilt 3" (Fig. 6.5g) indicates a specimen tilt away from the [001] axis represented by a Laue center shift vector $(-|k_x|, -|k_y|)$ with $|k_x| > |k_y|$.

In the HAADF images, maxima positions correspond to Zr atom column positions, while O atom column positions are invisible due to the low scattering cross-section. In the

ABF images, the minima positions with larger radius correspond to Zr atom column positions and the less dark minima positions with smaller diameter to O atom column positions. To show the relationship of maxima and minima positions of the same element, Zr, from simultaneously acquired HAADF and ABF images, I display both the fitted maxima positions corresponding to the Zr atom columns in HAADF images, labeled by red circles, and the fitted minima positions corresponding to the Zr atom columns in ABF images, labeled by green crosses.

The numerical data of the relative shift of maxima positions in HAADF images to the minima positions in ABF images for Zr are shown in Table 6.1. They show complexity but also with some apparent trends. For example, for "tilt 1", considered as "in zone axis orientation" from the diffraction pattern, non-negligible deviations are found. Thus, it seems that even very small specimen tilts, not visible from the diffraction pattern, lead to a detectable shift of minima/maxima in ABF and HAADF images. For "tilt 2", a parallel but opposite relationship can be found between the deviation direction and the shift direction the Laue circle center, i.e. $|\overline{\Delta \boldsymbol{x}}| < |\overline{\Delta \boldsymbol{y}}|$ and $|k_x| < |k_y|$.For "tilt3" it can be seen that the observed deviation direction directly correlates with the shift direction of the Laue circle center, i.e. $|\overline{\Delta \boldsymbol{x}}| > |\overline{\Delta \boldsymbol{y}}|$ and $|k_x| > |k_y|$.

Table 6.1 Relative shift of minima positions (Zr) from ABF images to maxima positions (Zr) from HAADF images. Here $\overline{\Delta \boldsymbol{x}}$ is the average relative shift along the *x*-direction, $\overline{\Delta \boldsymbol{y}}$ is the average relative shift along the *y*-direction and $\overline{\Delta \boldsymbol{d}}$ is the average relative shift vector length. And σ is the standard error.

Tilt	α (mrad)	$\overline{\Delta \boldsymbol{x}}$ (pm)	$\sigma_{\Delta x}$ (pm)	$\overline{\Delta \boldsymbol{y}}$ (pm)	$\sigma_{\Delta y}$ (pm)	$\overline{\Delta \boldsymbol{d}}$ (pm)	$\sigma_{\Delta d}$ (pm)
1 (~0)	20.4 (Fig. 6.5b)	7.5	2.7	2.2	3.3	8.7	1.6
2$(\lvert k_x\rvert, -\lvert k_y\rvert)$	20.4 (Fig. 6.5e)	4.6	3.8	20.3	7.6	21.2	7.4
3$(-\lvert k_x\rvert, -\lvert k_y\rvert)$	28(Fig. 6.5h)	-15.6	4.4	0.1	4.5	16.2	4.4

Moreover, in ABF images differences exist in the relative position of minima corresponding to O and minima corresponding to Zr. The fitted minima positions are displayed on the ABF images by green (Zr) and yellow (O) crosses. Taking the O positions in "tilt 1" as a reference, I obtain the relative shift of O minima positions, as shown in Table 6.2. However, I find a good match of the O minima position shift direction and the shift direction of the Laue circle center for both "tilt 2" and "tilt 3" between ABF and HAADF images. Details about how I get these data are as follows. To numerically show the shift of the minima positions corresponding to O, we firstly set the coordinates of the minima positions corresponding to the top left Zr atom columns to zero in Fig. 6.5c, f,

i. By doing this, we manually set the minima positions corresponding to Zr atom columns to be the same in all ABF images and assume them to be the rigid reference system, whose validity however needs verification by simulations. In a second step, the minima positions corresponding to O atom columns in Fig. 6.5c are taken as a reference what is more close to the zone axis as revealed by the PACBED pattern intensity symmetry. Thus the relative shifts of the minima positions (O) of the other images compared to Fig. 6.5c can be obtained by deducting their coordinates from those in Fig. 6.5c, as shown in Table 6.2. Images with an apparent sample drift are excluded from the analysis.

To understand these observed complexities, simulations are essential.

Table 6.2 Relative shift of minima positions (O) compared to "tilt 1" acquired with a 20.4 mrad convergence angle condition (Fig. 6.5e). Here $\overline{\Delta \boldsymbol{x}}$ is the average relative shift along the *x*-direction, $\overline{\Delta \boldsymbol{y}}$ is the average relative shift along the *y*-direction and $\overline{\Delta \boldsymbol{d}}$ is the average relative shift vector length, where σ is the standard error.

Tilt	α (mrad)	$\overline{\Delta \boldsymbol{x}}$ (pm)	$\sigma_{\Delta x}$ (pm)	$\overline{\Delta \boldsymbol{y}}$ (pm)	$\sigma_{\Delta y}$ (pm)	$\overline{\Delta \boldsymbol{d}}$ (pm)	$\sigma_{\Delta d}$ (pm)
1 (~0, reference)	20.4(Fig. 6.5c)	0	0	0	0	0	0
2($\lvert k_x \rvert, -\lvert k_y \rvert$)	20.4 (Fig. 6.5f)	0.5	0.1	-7.1	0.2	7.1	0.2
3 ($-\lvert k_x \rvert, -\lvert k_y \rvert$)	28(Fig. 6.5i)	-1.4	0.8	0.6	0.2	1.5	0.8

The detailed contrast and shape of minima positions in ABF images vary with specimen tilt and experimental imaging conditions. However, these are beyond the scope of this chapter.

6.4 Simulation results

6.4.1 Preliminary remarks

When interpreting the experimental results, I am assuming taking the maxima positions shown in HAADF images as the reference with all the relative shift measurements made with respect to their positions. These positions are assumed to be well defined due to the incoherent nature of STEM imaging. To verify these assumptions, however, image simulations are indispensable.

Before correlating the maxima/minima position shift observed in HAADF/ABF images with specimen tilt, the non-tilted situation at different convergence and collection semi-angles was calculated. The quantitative results show no shift of maxima/minima positions along either [100]- or [010]-direction in HAADF/ABF images. These results

demonstrate that these images are free from image delocalization which is very common in bright field images.

Results simulated with a specimen tilt of 5 mrad with a shift of the Laue circle center along the [100]-direction showed no atom position shift along the [010]-direction (the direction perpendicular to the tilting direction) whereas maxima/minima position shift along the [100]-direction are present in both HAADF and ABF images for both Zr and O with different shift length and thickness variation characteristics (e.g. Fig. 6.6a,b). The details will be explained in Chapter 6.4.2. The position shift along and opposite to the shift direction of the Laue circle center matches with the experimental data from tilt 2 (opposite to the shift direction) and tilt 3 (the same to the shift direction) situations. These results also confirm that a small specimen tilt in "tilt 1"-condition must have been present although invisible from the diffraction pattern.

By now, we can see that, for an aberration-free electron probe, the maxima/minima position shift can only show up in the presence of specimen tilt. In the following simulation, I start from the results obtained for convergence and collection semi-angles used in our experiments, applying 5 mrad specimen tilt, which is on the high side of typical mistilts. Then I investigate the convergence and collection angle dependence of the deviations separately, and finally, results for different tilt amounts are presented.

6.4.2 Correlating simulation with experimental results

Fig. 6.6 shows the deviations of HAADF and ABF atom positions from the true positions (deviation = 0) along the direction parallel to the shift direction of the Laue circle center. For the simulation of the ABF images, the same convergence and collection semi-angles were used as in the experiment, for HAADF images the same convergence semi-angle were used, but smaller collection semi-angles (71–100) mrad than in the experimental set-up to save computing time. The specimen tilt was set to 5 mrad.

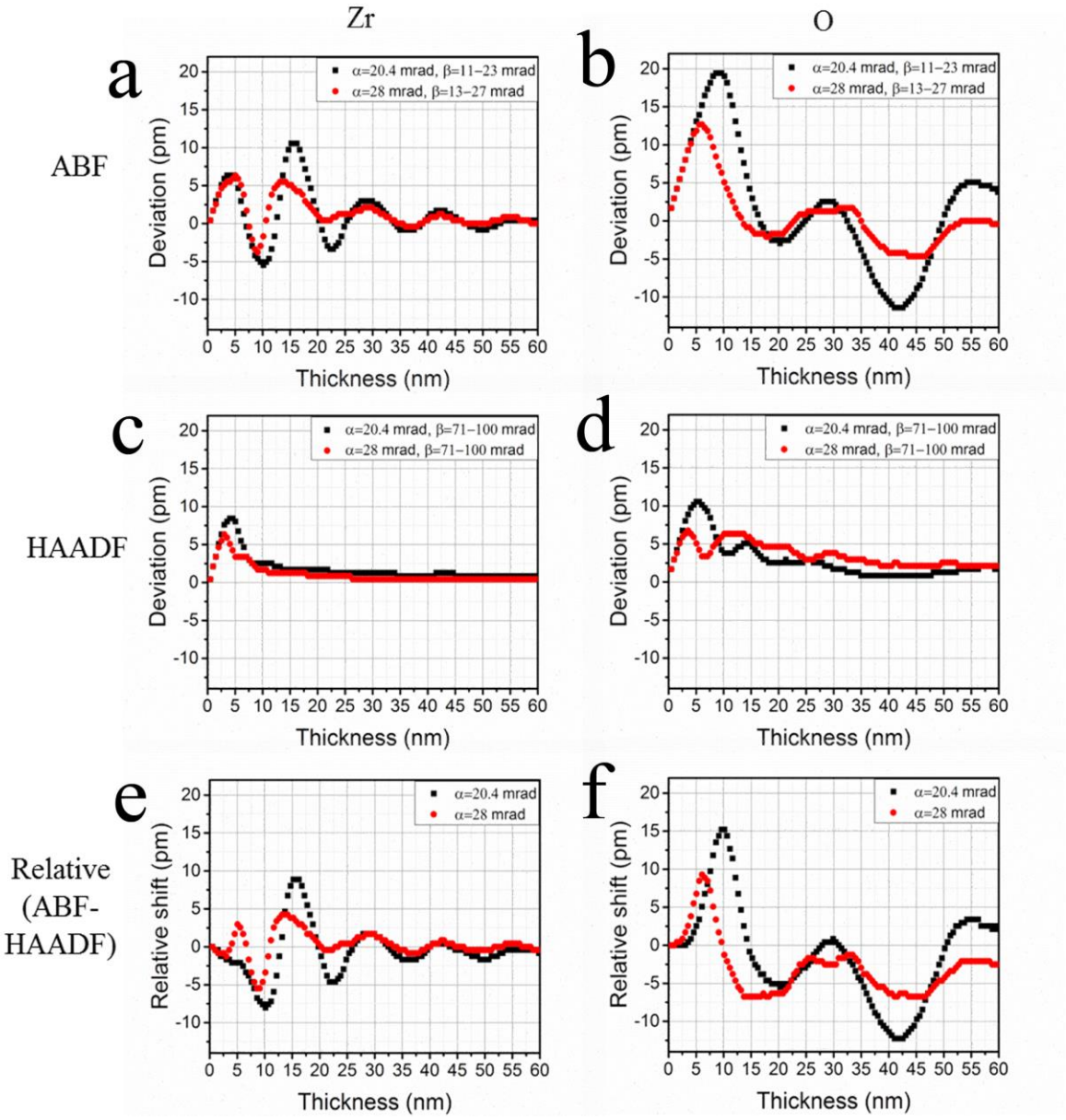

Figure 6.6 Simulated deviations of the minima positions of (a) Zr and (b) O in ABF imaging from true positions, simulated deviations of the maxima positions of (c) Zr and (d) O in HAADF imaging from true positions, and relative shift of the minima positions in ABF images to the maxima positions in HAADF images of Zr (e) and O (f) as a function of sample thickness.

As shown in Fig. 6.6a–d, firstly, deviations from true atomic positions exist for minima positions in ABF as well as maxima positions in HAADF images. The deviations extend to much thicker specimen regions for ABF imaging (Fig. 6.6a,b) than for HAADF imaging (Fig. 6.6c,d). This is probably because the thickness dependence of the 1s Bloch wave state, which is essential HAADF imaging[155], is weaker than the complex image formation in ABF imaging[43]. Independent of the imaging mode, deviations extend to thicker region for lighter element atom columns. This is mostly likely because of the weaker electron channeling of light element atom columns. Therefore, it is reasonable to choose heavy element atom columns in thicker specimen areas, e.g. above 15–20 nm for

Zr, as the rigid reference system. Still, deviations in ABF images are significant even at large thicknesses and do not allow accurate determination of absolute or relative atom positions. Such determination seems only possible at very small thicknesses (< 5 nm) where the specimen can be treated within the (weak) phase-object approximation [50] and thus deviations for both atom species are found to be similar. The difference between different convergence semi-angles becomes less as thickness increases and is most pronounced for Zr where no differences are detectable above 25 nm thickness, while in the case of O atomic columns the difference is still pronounced up to a thickness of 60 nm. This behavior is related with the decreasing fraction of tilt (5 mrad) versus amount of convergence. The oscillatory variation of deviations with thickness is quicker for Zr than for O, most likely owing to the smaller extinction length for the heavy element.

In the following, I study the convergence semi-angle and collection semi-angle dependence separately.

6.4.3 Convergence and collection angles

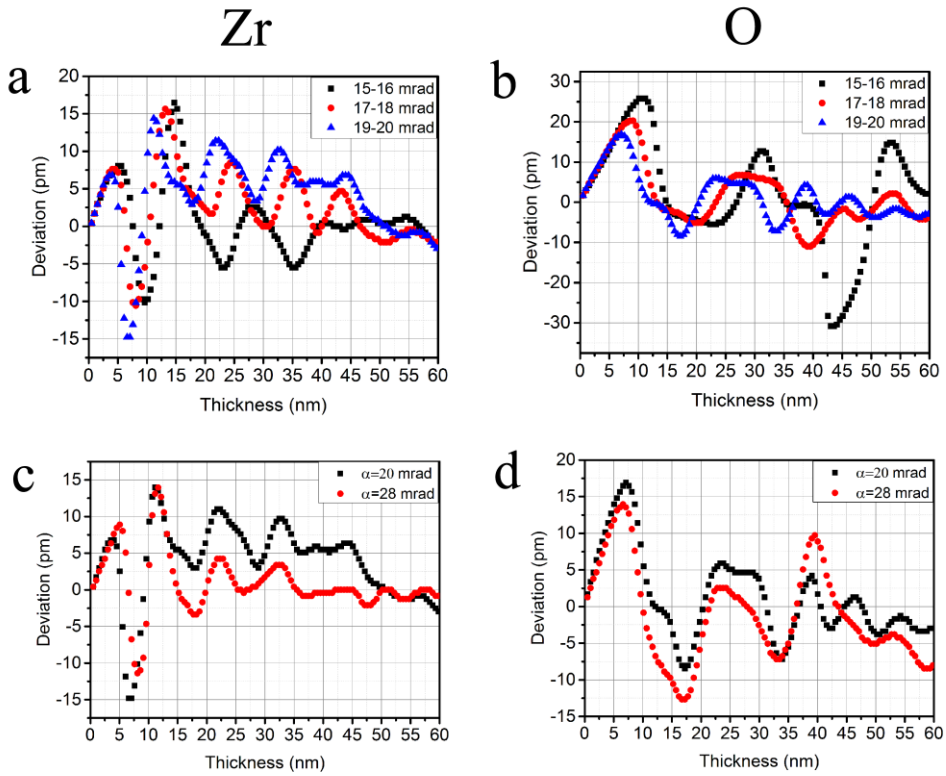

Figure 6.7 Collection angle dependence of the deviation in ABF imaging with 5 mrad orientation deviation along the shift direction of the Laue circle center for (a) Zr and (b) O using a convergence semi-angle of 20.4 mrad in the simulation. Convergence angle dependence of the deviation in ABF imaging with 5 mrad orientation deviation along the shift direction of the Laue circle center for (c) Zr and (d) O using a collection semi-angle of 19 to 20 mrad.

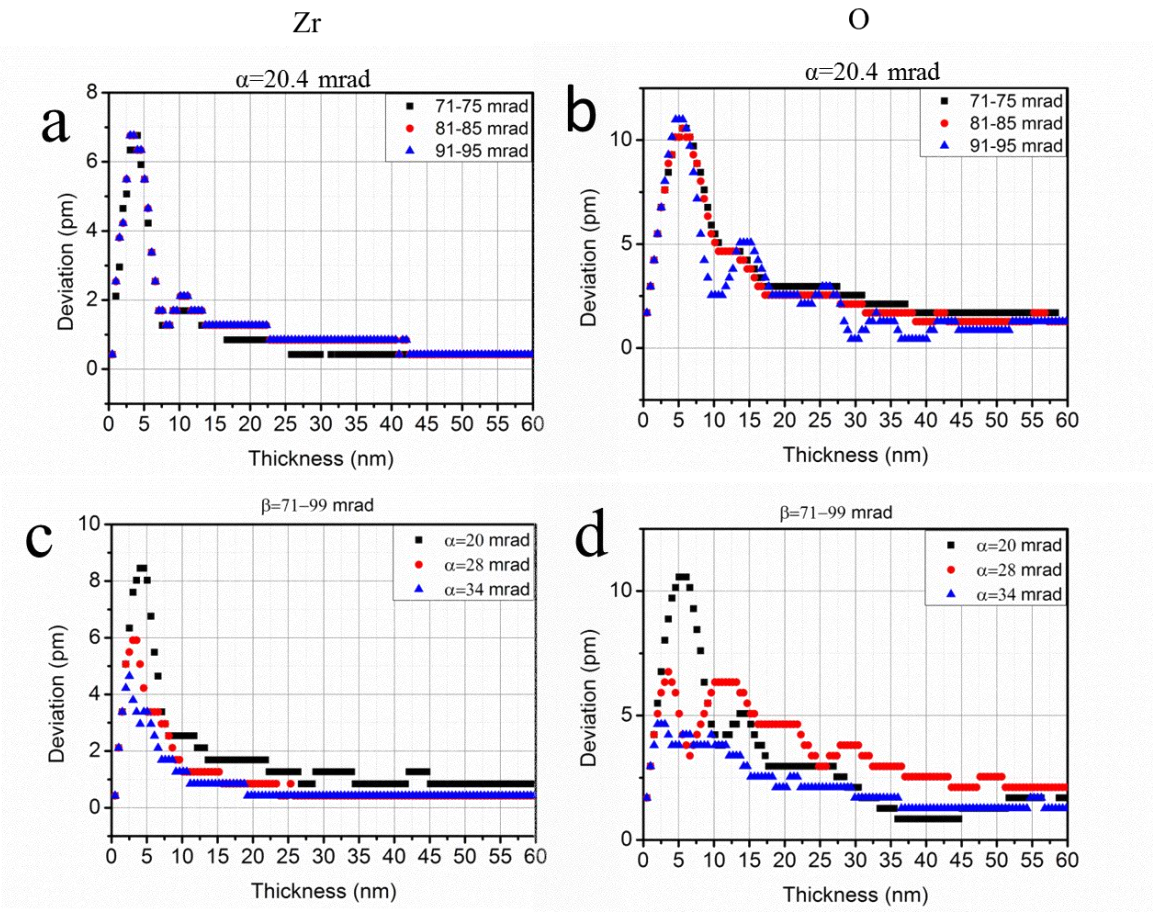

Figure 6.8 Collection angle dependence of the deviation in HAADF imaging with 5 mrad orientation deviation along the shift direction of the Laue circle center for (a) Zr and (b) O when the convergence semi-angle of 20.4 mrad was used in simulation. Convergence angle dependence of the deviation in HAADF imaging with 5 mrad orientation deviation along the shift direction of the Laue circle center for (c) Zr and (d) O when a collection semi-angle of 71 to 99 mrad was used in simulation.

In Fig. 6.6 data are shown where the ABF signal was calculated for the full range (11–23 mrad). I will now have a more detailed look how deviations vary across this range. Fig. 6.7 a,b shows the deviations in ABF images at 3 different collection angles (15, 17, and 19 mrad) integrated over 1 mrad width for Zr and O, respectively. The convergence semi-angle is 20.4 mrad. As shown in Fig. 6.7 a,b, a larger collection angle leads to a quicker variation of the oscillatory deviation with thickness. Moreover as noted above, Zr shows a quicker variation with thickness compared to O. It is interesting to compare Fig. 6.6 a,b, which is an integral over the entire angular range, with Fig. 6.7 a,b. The integrated signal shows significantly smaller deviations because signals from different collection angles tend to cancel each other. This effect is more significant for Zr.

To investigate the collection semi-angle's influence on the maxima position deviations in HAADF images, I separate the collection angle in 5 mrad step as shown in

Fig. 6.8a and b for Zr and O respectively. I intentionally select the collection semi-angle to be larger than three times the convergence semi-angle to make the main contributing signal thermal diffuse scattering [58]. Different from the minima position deviations in ABF images, the corresponding maxima position deviations in HAADF images are always positive, i.e. along the tilting direction, and less dependent on the collection angle (Fig. 6.8a,b). After an initial increase of the deviation with increasing thickness, the deviation values decrease monotonically with increasing thickness. There is only very limited influence of the deviations from the choice of collection semi-angle.

Comparisons for different convergence semi-angles (20.4 mrad and 28 mrad) at constant collection semi-angle are shown in Fig. 6.7c and 6.7d for Zr and O, respectively. The collection semi-angle is fixed to be 19 to 20 mrad. There are close similarities at these two convergence angles for both elements. More data from different convergence semi-angles and collection semi-angles can be found in Chapter 6.7.1 (Fig. 6.13), which also confirms this aspect. In general, larger convergence angles lead to smaller deviations because the specimen tilt becomes a smaller fraction of the probe-forming convergence angle as the latter is increased. These results indicate that the thickness dependence of the deviation is mainly due to variations of the collection angle, while the convergence angle modifies the deviations only slightly. For very thin samples the convergence angle almost does not influence the deviation. I observed that to get minimum contrast at atom column positions, a larger convergence semi-angle requires a larger inner collection semi-angle, especially for light elements.

The situation for HAADF imaging at different convergence semi-angles is presented in Fig. 6.8c,d. Generally speaking, a larger convergence angle results in smaller deviations of maxima position in HAADF imaging. The variations with thickness are more sensitive than those due to the collection angle. The first peak of the deviation moves towards the thinner region as the convergence angle increases.

6.4.4 Tilt amount

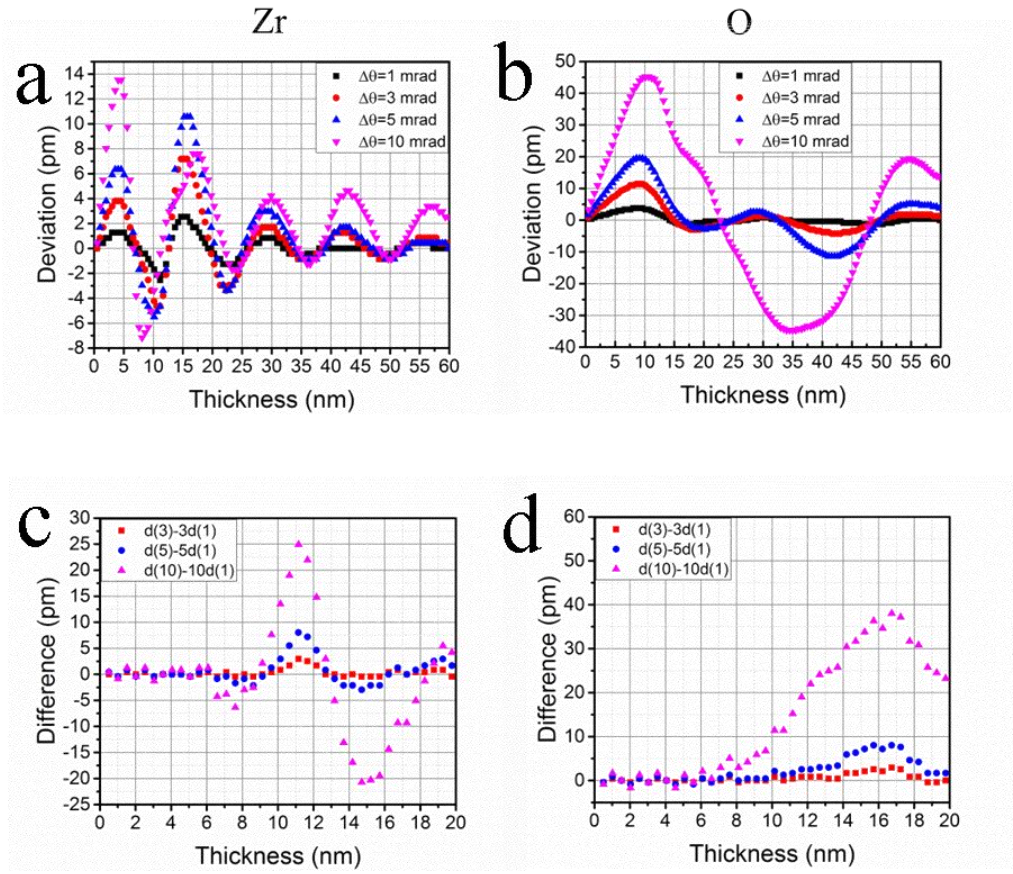

Figure 6.9 The deviation of the minima positions in ABF images of (a) Zr and (b) O for different tilting angles indicated by Δθ in the figures. The convergence semi-angle is 20.4 mrad and the collection semi-angle range is 11-23 mrad. (c,d) Comparison of the deviation from linearity at 3, 5, and 10 mrad tilt with 1 mrad tilt by looking at the differences between the larger angle tilts and the 1-mrad tilt multiplied by factors of 3, 5, and 10.

In general, with all the other conditions the same, larger specimen tilt gives larger deviation as shown in Fig. 6.9a (Zr) and 6.9b (O). The exceptions are those thicknesses at which the deviations are close to zero.

Fig. 6.9c, d show that the deviation of Zr and O atom columns is proportional to the tilt amount for thicknesses below about 6 nm for all the tilt amounts presented. Careful inspection of these two figures indicates a left shift of the thickness value, beyond which the linear relationship is lost, from smaller tilt amount to larger tilt amount. This is more visible for the light element O than the heavy element Zr. These observations can be correlated with the specimen tilt caused reduction of thickness below which the weak-phase object approximation is valid [50, 156].

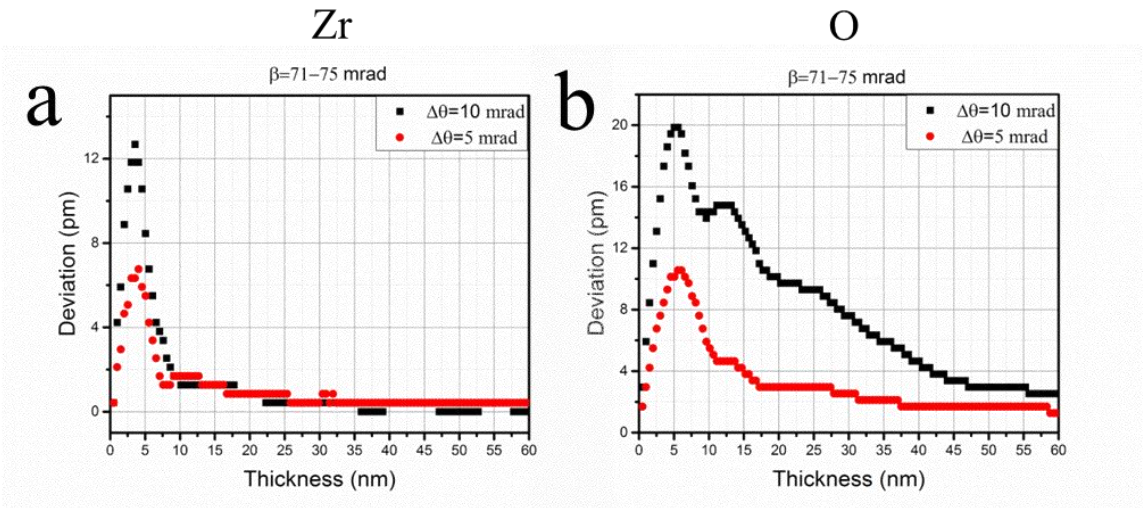

Figure 6.10 The deviation of maxima positions in HAADF images of (a) Zr and (b) O for different tilt angles indicated by Δθ in the figures. The convergence semi-angle is 20.4 mrad and the collection semi-angle is 71-75 mrad.

As HAADF imaging is not the emphasis of this current research, I will only briefly show the differences between different amounts of specimen tilt as for ABF imaging. As can be seen from Fig. 6.10, an increase of specimen tilt will increase the deviation, especially for the thin region and for the light element extending to a larger thickness range. While for heavier elements, the deviation at high thickness is quite small despite of the amount of specimen tilt.

6.5 Discussions

6.5.1 Influence on the angle measurement

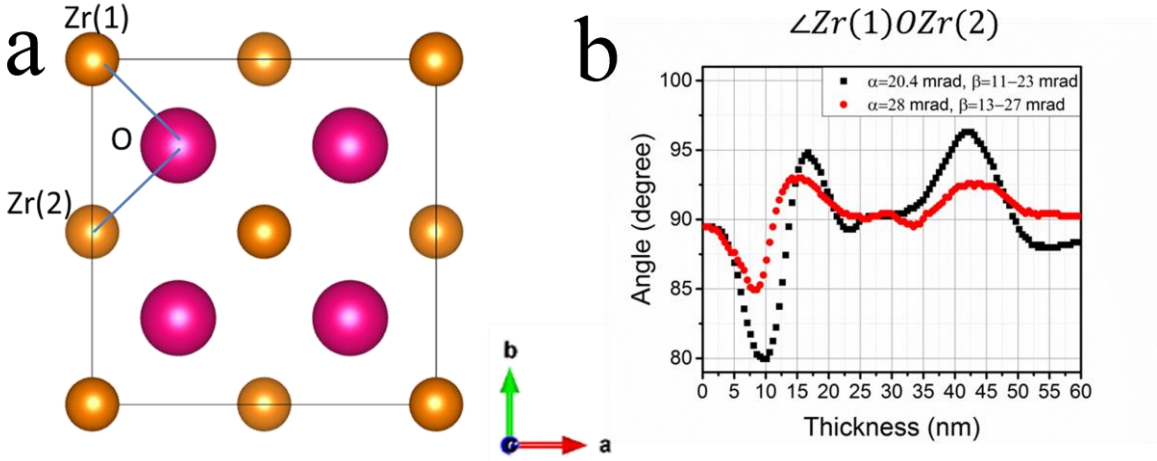

Figure 6.11 (a) Structure model of cubic ZrO_2 viewed along the [001] direction. (b) Projected angle between two neighboring Zr atoms and one O atom $\angle Zr(1)OZr(2)$ shown in (a) when the crystal is tilted by 5 mrad along the [100]-direction with the convergence semi-angles and collection semi-angles as indicated in the figure.

The case of measuring relative deviations between Zr and O positions, which is important for extracting information about the ligand coordination, is shown in Fig. 6.11. These results are from the simulated data with the same convergence semi-angles and collection semi-angles as in the experimental section at a specimen tilt of 5 mrad. In the true structure, the angle is 90 degree. However, the deviation causes the angle to vary between about 80 degree to 97 degree for 20.4 mrad convergence semi-angle, and between about 85 degree to 93 degree for 28 mrad convergence semi-angle as a function of thickness.

6.5.2 Summary of experimental and simulation results and suggestions to minimize errors

In order to minimize the quantitative error in the determination of the atom position by ABF imaging and to achieve a good match between experimental and simulated results a number of suggestions are listed in the following:

1 Align the specimen as close as possible to the targeted zone axis with assistance of techniques like PACBED[153]. This often allows alignment accuracy better than 1 mrad. However, this is often more difficult in thin specimen regions or in the case of large convergence angles, where the overlap of diffraction disks is large. Especially if one wants to determine atom positions with an accuracy of a few picometers, one should be aware of the fact that tilt deviations below 1 mrad can lead to errors larger than the required accuracy. In such cases, it is also not sufficient to use the HAADF maxima of heavy element columns in thicker specimen areas as a rigid reference system, because even then the deviations of the lighter element atom columns can still exceed the required accuracy.

2 For an aberration-free electron probe, a change of position and shape of maxima/minima can only show up when specimen tilt exists. Therefore, observation of a position mismatch between HAADF and ABF images for the same element is an indication of a small amount of tilt.

3 For the same element, the collection semi-angle and tilt angle determine the thickness dependence of the atom column position deviation. The larger the collection angles and the smaller the tilting angle, the more rapid will the deviations vary with thickness. For very thin specimen regions, the convergence angle does not modify the deviation, while larger tilt angles result in larger deviations. In thicker specimen regions, larger convergence angles give smaller deviation while larger tilt angle not necessarily gives larger or smaller deviation. Thus, selection of larger convergence semi-angles and corresponding larger collection semi-angles can give smaller error in determining the

relative positions or angles between different atom columns on average, but not for all thickness values.

4 For the same experimental conditions, the heavier the element, the smaller will be the overall deviation and the more rapid variations will occur with thickness.

5 To minimize deviations for small, unavoidable specimen tilt: For thin regions, use larger inner collection semi-angle; for thick regions, use a detector covering a larger angular range.

6 Change of convergence semi-angle, i.e. condenser aperture, can introduce a small amount of beam tilt. Therefore checking the diffraction pattern after changing condenser aperture is essential to avoid difficulties in correlating the deviations with diffraction patterns acquired with different condenser apertures.

6.6 Preliminary application – mis-orientation of LSMO on two sides of APBs

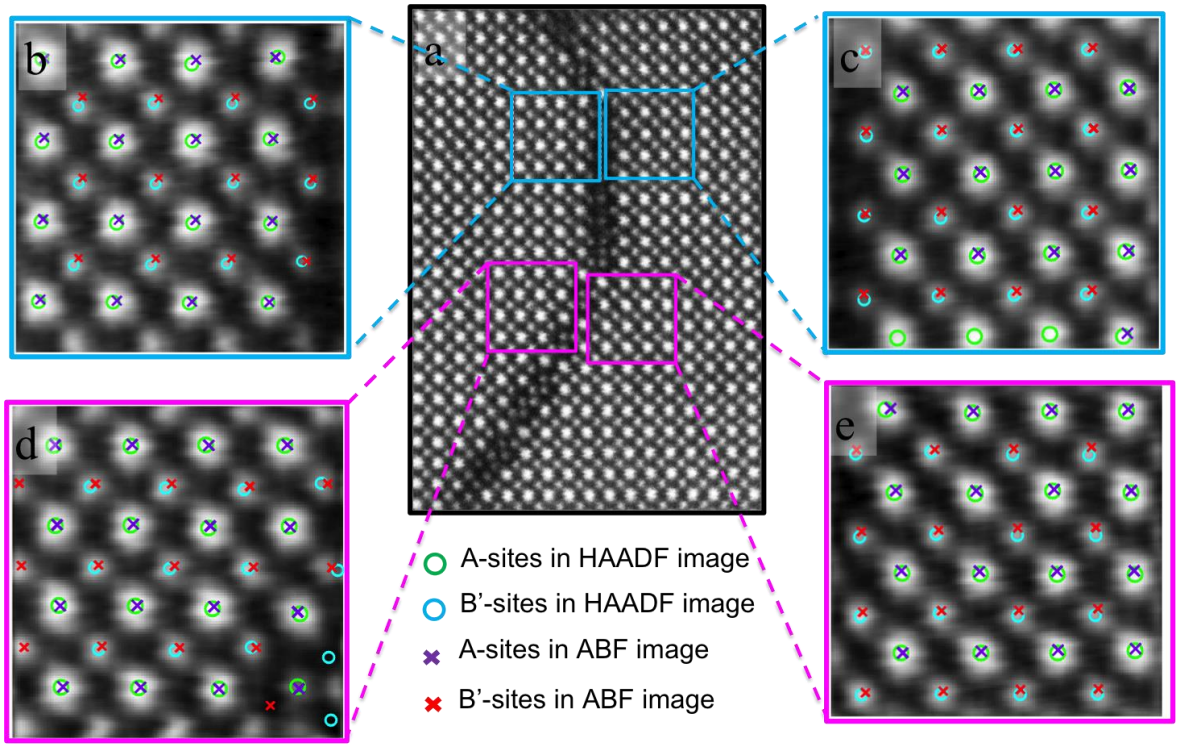

Figure 6.12 (a) HAADF image of a sample area including APB-1 and APB-2 presented in chapter 4. Replica of Fig. 4.5 with a larger LSMO area included. Cut of LSMO region on the (b) left side and (c) right side of APB-1, and (d) left side and (e) right side of APB-2. These cuts are overlapped with maxima and minima positions from simultaneously acquired HAADF and ABF images, similar to the process presented in Fig. 6.5.

From the results presented in this chapter, overlapping of the maxima and minima positions in HAADF and ABF images does not guarantee that the specimen is free from

relative tilt from the electron beam. However, mismatch of maxima and minima positions in HAADF and ABF images is a good indication for the existence of misalignment from the targeted zone axis. Moreover, the mismatch vector is parallel or antiparallel to the shift direction of the Laue circle center.

I applied the same analysis used for Fig. 6.5 and Table 6.1 to four regions of the simultaneously acquired HAADF and ABF images, which includes APB-1 and APB-2, as shown in Fig. 6.12. A relative shift of minima in ABF images from maxima in HAADF images was found to be the top right direction for the region on the left side of the APB-1 (Fig. 6.12b), the dominant right and slight up direction for the region on the left side of the APB-2 (Fig. 6.12d), and the right direction for the region on the right side of the APB-2 (Fig. 6.12e). These results indicate the possible existence of specimen tilt along these directions with different tilt amounts. The factors influencing the confidence of the existence of mis-orientation are the interface/strain effects on the atom column position determination in ABF imaging, which is still under investigation, as described in Chapter 6.8.2.

6.7 Appendix

6.7.1 More data about the convergence semi-angle's influence on ABF imaging

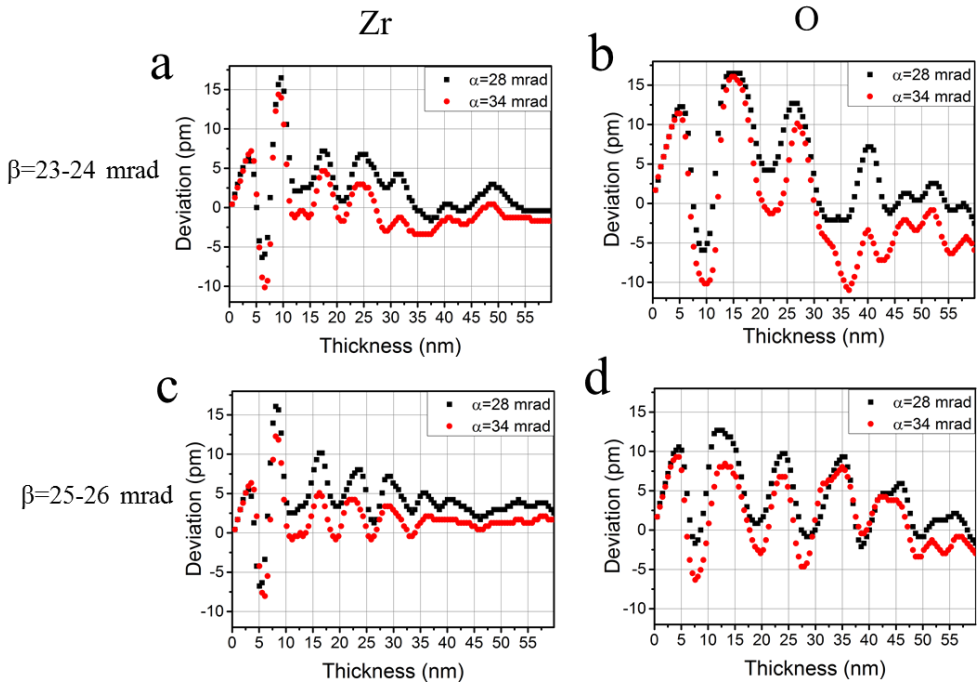

Figure 6.13 Further results about convergence angle dependence of deviation along the Laue circle center shift direction of 5 mrad for (a) and (c) Zr and (b) and (d) O when the collection semi-angle of 23 to 24 mrad and 25 to 26 mrad respectively were used in the simulations with convergence semi-angle indicated in the figures.

More simulated data on the convergence angle dependence of deviations in ABF imaging is presented in Fig. 6.13. These results confirm the conclusions obtained from Fig. 6.7c,d in Chapter 6.4.3 are also applicable to the other convergence and collection angles.

6.7.2 Quick view of the tilting effect

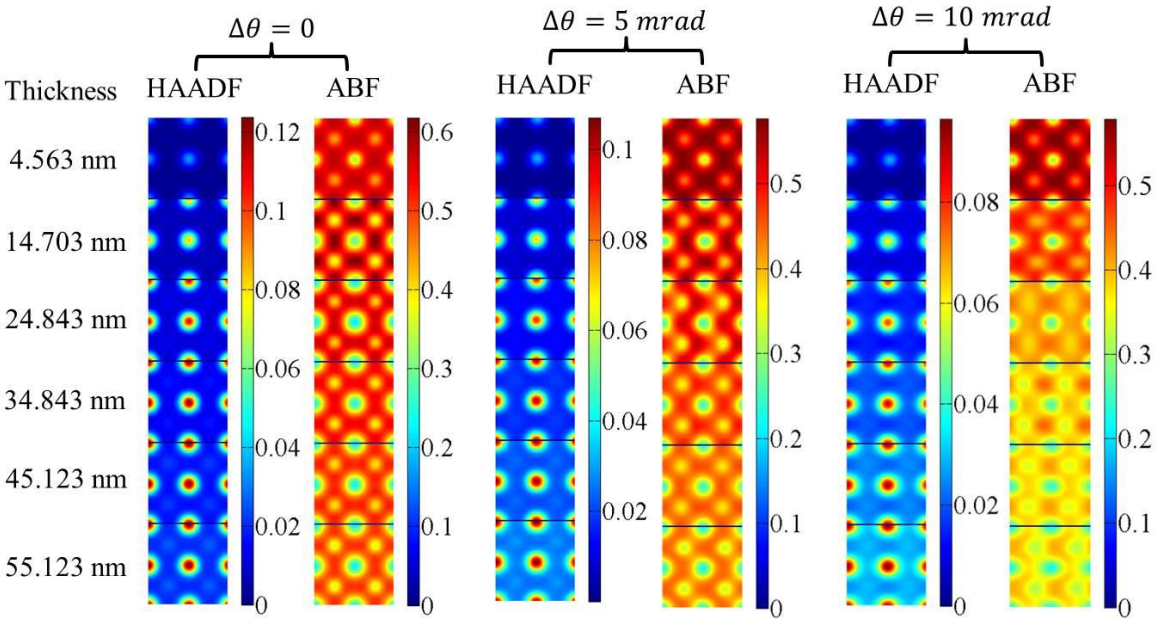

Figure 6.14 Visualization of the effect of sample tilt, where $\Delta\theta$ is the sample tilt with the shift vector of the Laue circle center parallel to the horizontal direction, on the variation of the maxima / minima positions in simulated HAADF (71-99 mrad)/ABF (12-20 mrad) images of cubic ZrO_2 (see structure in Fig. 6.1) for different thicknesses. The convergence semi-angle is 20.4 mrad.

As an illustration to show the effects of specimen tilt on ABF and HAADF images, I present the simulated results on ZrO_2 along the [001] direction in Fig. 6.14 with a convergence semi-angle of 20.4 mrad, a collection semi-angle of 12-20 mrad for ABF imaging and 71-99 mrad for HAADF imaging and a specimen tilt represented by a shift of the Laue circle center along [100]-direction for 0, 5 and 10 mrad, respectively, for 6 thickness values from 4.563 nm to 55.123 nm. For the STEM image simulations presented here, we calculated 40*40 pixels per unit cell. The images were obtained by scanning the virtual probe over a unit cell area and then interpolated by 15 pixel for both *x* and *y* directions to get smooth images. To include the effect from a finite source size which acts to blur the images, we used a Gaussian of half-width-at-half-maximum (HWHM) of 0.03 nm which was convoluted on all the ABF and HAADF images. The color bar shown in the figures represents the scale bar of the fractional intensity shown in the STEM images. Here, 'fractional intensity' means the image intensity normalized to the incident intensity. Both Zr and O are visible in ABF images as minima spots while only Zr is visible in

HAADF images as maxima spots. A few features can be observed which are described as follows:

1 The deviation of the minima positions corresponding to Zr atom columns in ABF images can be recognized by eye, especially at large specimen tilt, e.g. for a tilt angle of 10 mrad. The deviation vector is observed to be parallel to the shift vector of the Laue circle center. The shift of maxima positions corresponding to Zr atomic columns in HAADF images is visible only at low thickness and only along the shift vector of the Laue circle center.

2 The deviation vector of the minima positions corresponding to O atom columns in ABF images varies with tilt and thickness. On average, the shift is larger than that of the minima positions corresponding to Zr atom columns which make them more visible in the images. Moreover, the deviation increases with tilt angle with no visible deviation at zero tilt. Too large specimen tilt will cause a contrast inversion at the oxygen column positions, e.g. they become maxima positions instead of minima in the ABF images, which is excluded from our current discussion.

3 The contrast for both HAADF and ABF images is decreased at increasing tilting angles, more visible on ABF images, and the shape of the minima positions in the ABF images varies from round to elliptical, square and more complicated patterns in the ABF images with specimen tilt. Besides, the stretching of the atom shape, especially for the heavy atom is observed to be parallel to the tilting direction. No stretching is observed along the perpendicular direction. However, this stretching varies with thickness and tilt. This indicates that the stretching is thickness dependent and also possibly convergence and collection semi-angle dependent. This explains the phenomenon observed in the experimental part and no conflict was found between simulation and experimental results.

6.7.3 Factors influcing the precision of the simulated deviations

In the absorptive potential (AP) multislice method, the contribution of inelastic scattering from phonon scattering and plasmon generation is ignored which however has been discussed as main factors contributing to contrast reduction in high-resolution images. Although contrast and high angle electron scattering is not our emphasis in this paper, a comparison of the simulated results to those simulated with frozen lattice (FL) approximation is presented in Fig. 6.15 to make a cross-check of the presented data. The FL approximation simulations were preformed using 10 phonon configurations with Einstein approximation. The number of phonon configurations is limited to achieve realistic computing times for thick samples. It is conceivable that more sophisticated

phonon models or inclusion of other inelastic scattering processes may improve the close between simulations and experimental results. As shown in Fig. 6.15, the difference of the deviations simulated by AP multislice method and FL approximation method, in ABF imaging and HAADF imaging, is smaller at thinner region than at thicker region. And for the same angular range, heavier element, Zr has larger difference. These are because of increased inelastic scattering by increasing atomic number and thickness. The maximum difference is around 2 pm. This indicates that when a precision better than 2 pm is required, FL approximation instead of AP multislice method should be applied for simulation.

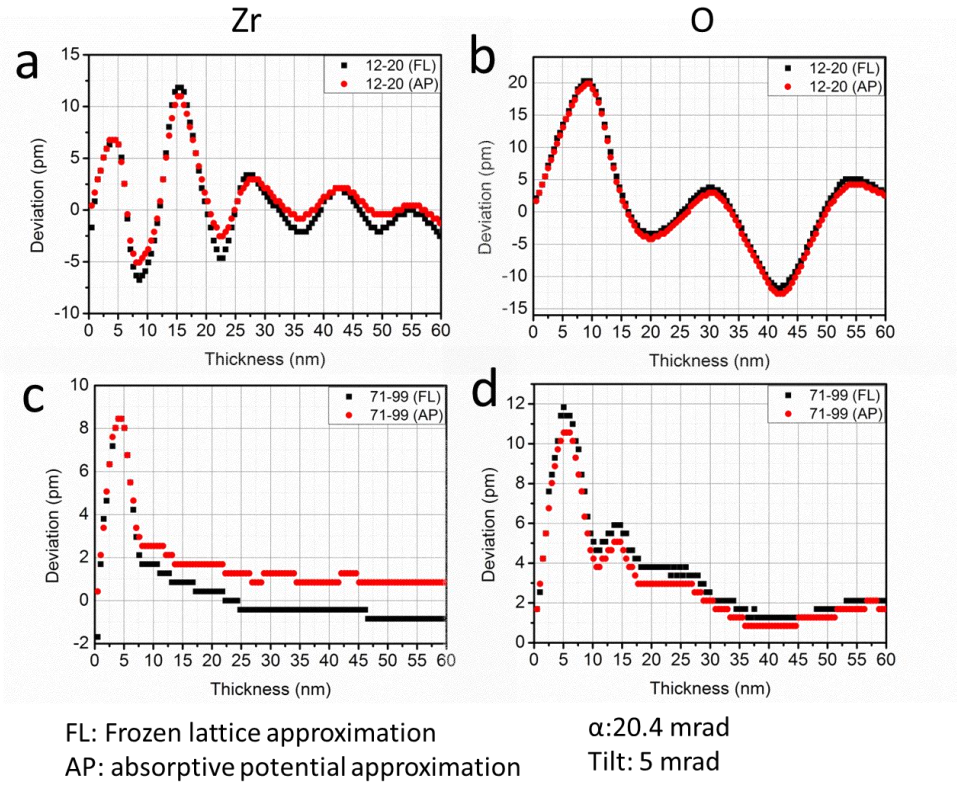

Figure 6.15 Comparison of the deviation values obtained from the FL approximation and AP multisclice method for (a, c) Zr and (b, d) O. (a, b) are for the minima position deviations in ABF imaging and (c, d) are for the maxima position deviations in HAADF imaging.

Besides, the thicker or the heavier the sample, the more signal can be scattered to higher angle and scattered back to the interested angular range. Therefore, higher overall angular range was required as thickness or atomic number increases. The angular range in reciprocal space can be calculated by $\frac{N}{2*n*a}$, where N is the number of pixels in reciprocal space along the direction with lattice parameter a. To investigate this factor's influence, I double the simulated angular range by setting the grid size to 100×100 per unit cell while keeping the other parameters as described before, and compare the simulated deviations with those simulated with the reciprocal space angular range used in this chapter. From

Fig. 6.16, we can see that, for the same element, difference relies more on the thickness dependence than on the angular range dependence, i.e. the thicker the specimen, the larger the deviation. The maximum difference is also around 2 pm.

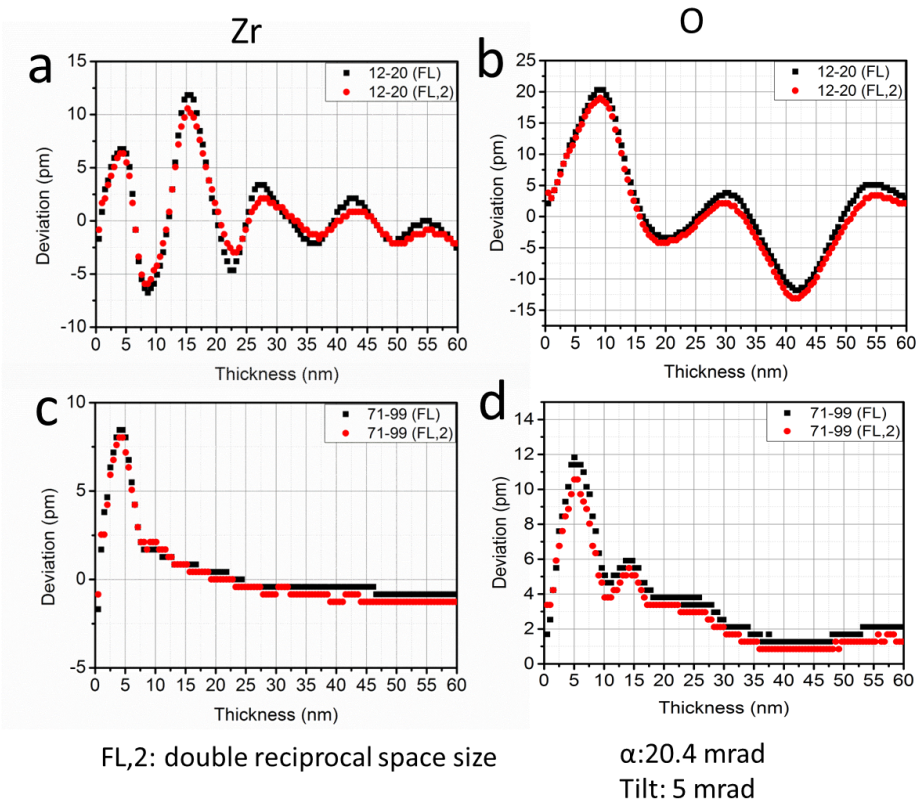

Figure 6.16 Comparison of the deviation values obtained from FL approximations with 0-123 mrad ('FL', the size of reciprocal space applied in this chapter) and 0-246 mrad ('FL,2', double the size of reciprocal space applied in this chapter) for (a, c) Zr and (b, d) O. (a, b) are for the minima position deviations in ABF imaging and (c, d) are for the maxima position deviations in HAADF imaging.

Moreover, the lower the collection angle, the higher the reciprocal space resolution is required to get more precise results. The reciprocal space resolution can be calculated by $\frac{1}{n*a}$, where n is the number of unit cells along the direction with a lattice parameter a. Therefore, I double the reciprocal spatial resolution by setting the supercell to 10×10 unit cells while keeping the other parameters as described in Chapter 6.2.2. As revealed in Fig. 6.17, the difference in case of deviation is smaller than 1 pm for the interested angular range.

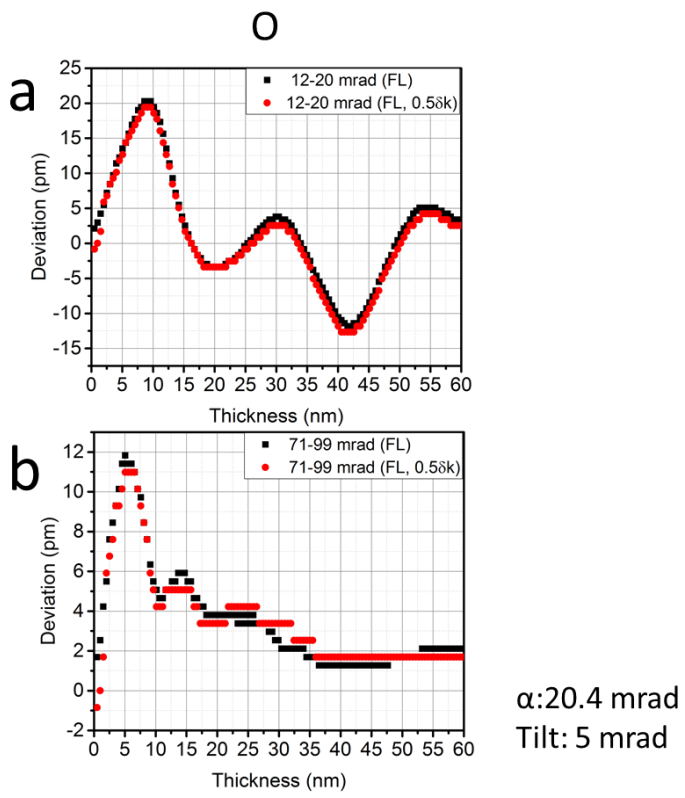

Figure 6.17 Comparison of the deviation values obtained from the FL approximations with 0.99 mrad/pixel ('FL', the spatial resolution of reciprocal space applied in this chapter) and 0.5 mrad/pixel mrad ('FL,0.5δk', half the spatial resolution of reciprocal space applied in this chapter by double the number of pixels per unit cell) for (a) ABF and (b) HAADF for O.

In Summary, the results presented in this part confirms these factors, AP multislice method or FL approximation, the reciprocal space angular range and the reciprocal space spatial resolution, won't influence the conclusions in this chapter when the precision required is larger than about 2 pm. Modification of these factors are essential when higher than 2 pm precision is required.

6.7.4 Diffraction pattern rotation

One assumption, not stated above, is that the normal vector of atomic planes in real space should have parallel relationship with the corresponding diffraction spots in reciprocal space. This is also the basic theory leading to the parallel or antiparallel direction relationships between the deviations in STEM imaging and the shift direction of the Laue circle center. Whereas practically in STEM imaging, this can be changed by the scanning rotation setting in either Digiscan or in TEM center of the JEOL TEM control center and the projection lenses after the specimen. To make valid comparisons between experimental and simulation results, a check of the rotation between image in real space and diffraction pattern in reciprocal space is essential.

To check the practical situation of our microscope, I firstly check if the software is designed to be smart enough to get the diffraction pattern (DP) rotates together with the scanning rotation setting. With scanning rotation value in TEM center set to 0, 10, 20, 30, 40, 50, 90 and 180 degree, no DP rotation was observed. Then I check if the parallel relationship between the normal vector of atomic planes and their corresponding planes is met, i.e. if the projection lenses bring extra rotation to the DPs. To do this, I work on the sample I used in the paper, which has a cubic structure, and therefore, the atomic arrangement in real space parallel to the normal vector of an atomic plane is also parallel to their diffraction spots. As shown in Fig. 6.18, there is 7 degree clockwise rotation between the atomic arrangement (dashed line in Fig. 6.18b) to the diffraction spots (solid line in Fig. 6.18a and 6.18b). That is to say, even there is no scanning rotation setting, to get the orientation relationship experimentally in this work, this rotation need to be calibrated.

For our experimental results presented above, a scanning rotation of about 4 degree clockwise is set, which reduces the rotation between image and DP to be about 3 degree, as shown in Fig. 6.19. This 3 degree is taken into consideration in this chapter.

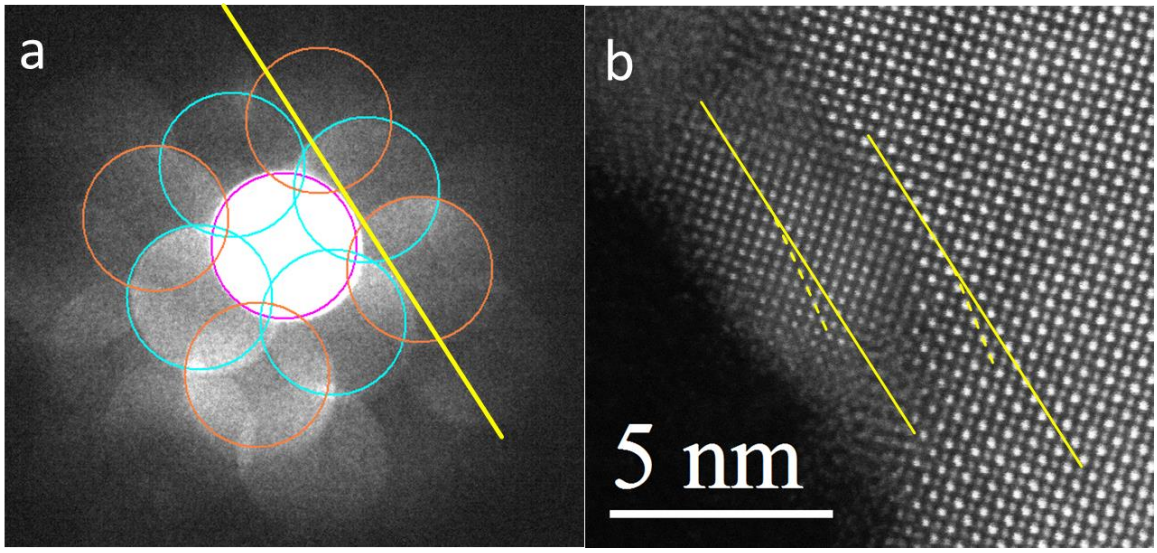

Figure 6.18 Condenser lens aperture is 10 um which gives a convergence semi-angle of 7.3 mrad. This smaller CL aperture compared to the experimentally applied value gives more separate diffraction disks and make the work easier. Diffraction spots marked by blue circles correspond to the adjacent Zr or La/Sr sites. This is labeled out in diffraction spots in DP by the yellow solid line which is the tangent to the symmetric two blue circles and yellow dashed line in HAADF STEM image. Moving the solid yellow line to the STEM image shows this mismatch of about 7 degree.

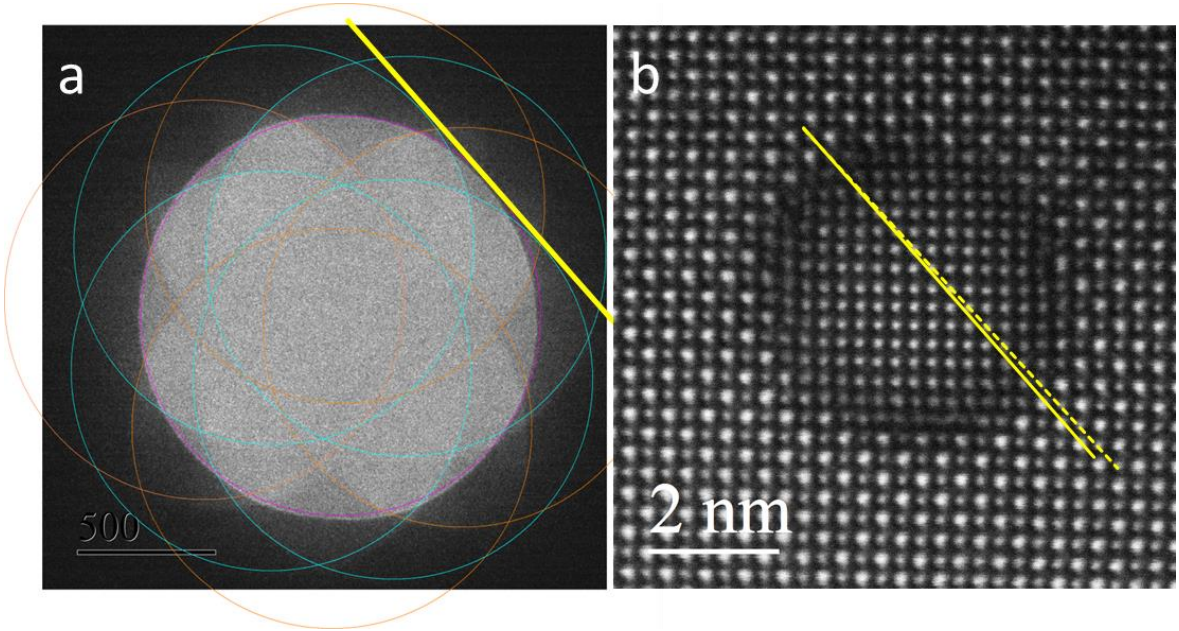

Figure 6.19 Condenser lens aperture is 40 um which gives a convergence semi-angle of 28 mrad. This larger CL aperture is the experimentally applied value and gives quite overlapping diffraction disks. Much care is needed to label out each diffraction spot. Diffraction spots marked by blue circles correspond to the adjacent Zr or La/Sr sites. This is labeled out in diffraction spots in DP by the yellow solid line which is tangent to the symmetric two blue circles and yellow dashed line in HAADF STEM image. Moving the solid yellow line to the STEM image shows this mismatch of about 3 degree.

6.7.5 Direction relationship between Laue center and diffraction pattern intensity gravity center when small tilt exists

As illustrated in Fig. 6.20 and Fig. 6.21, based on Ewald sphere, I can find that, small specimen tilt in real space will lead to the Laue circle center shifted along the same direction. Visually from the PACBED or DP, I can find the intensity gravity center shifted along the Laue circle center shift along the same direction. Moreover, within weak phase object approximation, i.e. very thin specimen below 5 nm depending on the exact element involved, the projected potential peak will be shifted along the direction of Laue circle center shift direction.

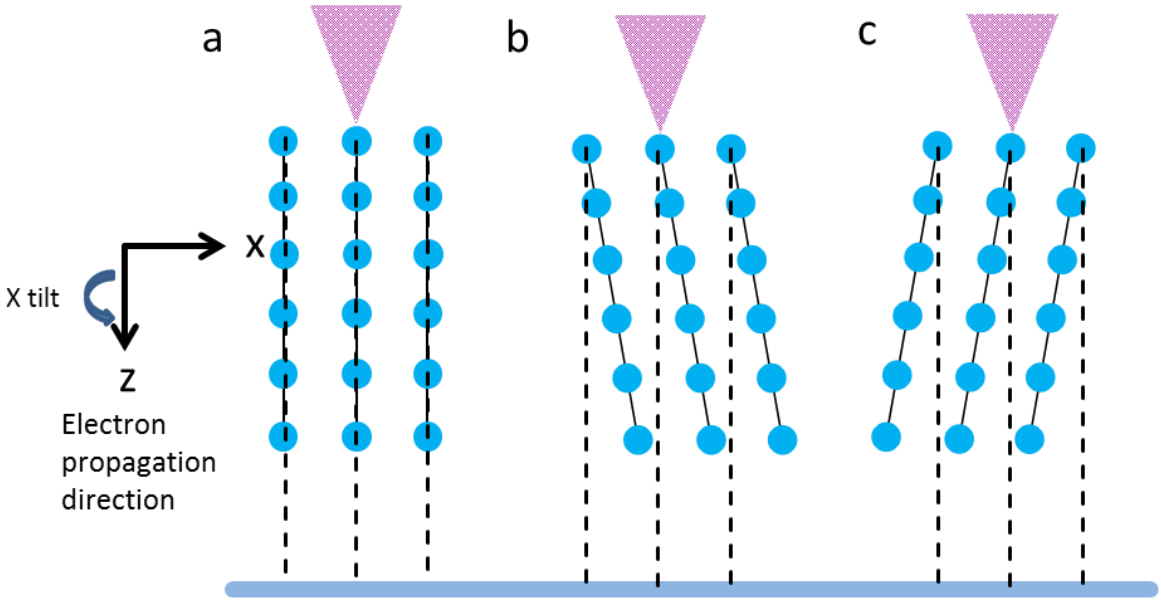

Figure 6.20 In STEMsim, (a) 0 mrad tilt, (b) positive amount of tilt parallel to the *x*-direction, and (c) negative amount of tilt parallel to the *x*-direction.

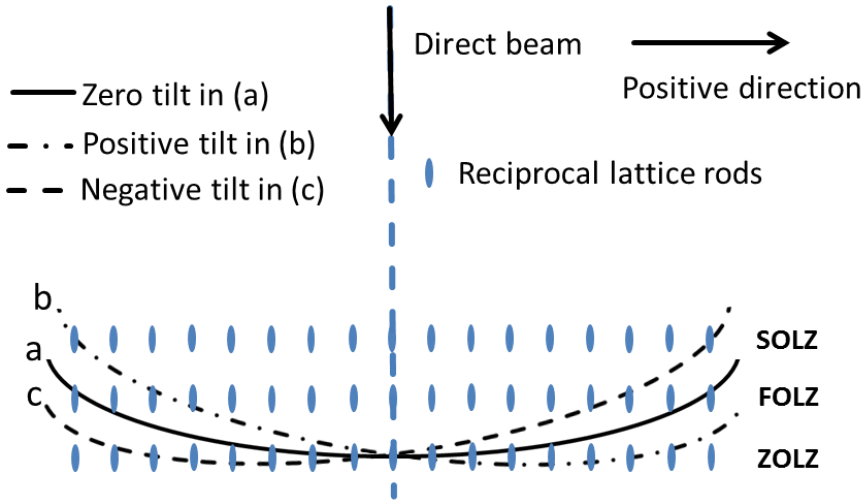

Figure 6.21 The corresponding Ewald sphere tilted to the tilt situations presented in Fig. 6.20. The ZOLZ is the zero order Laue zone, the FOLZ is the first order Laue zone, and the SOLZ is the second order Laue zone.

6.7.6 Weak-phase object approximation at thin specimen regions

The electron beam passing through the specimen in STEM imaging can be treated as a multiplication of the transmission function $t(\mathbf{x})$ with the probe function $\psi_{inc}(\boldsymbol{x})$, which includes the aperture function and the effects of the probe forming lens' aberrations. In this chapter, I ignore the lens' aberrations. Therefore, the electron wave function exit the specimen can be written as $\psi_t(\boldsymbol{x}) = t(\boldsymbol{x})\psi_{inc}(\boldsymbol{x})$. Very thin specimen can be treated with (weak) phase-object approximation, which means the electron beam passes through the specimen with only small deviation in their paths[50]. In the weak phase object (WPO) approximation, $t(\boldsymbol{x}) \sim \exp[i\sigma_e v_z(\boldsymbol{x})] \sim (1 + i\sigma_e v_z(\boldsymbol{x}) + \cdots)$ where σ_e is the interaction

constant ($\frac{2me\lambda}{h^2}$) and $v_z(\boldsymbol{x})$ is the projected atomic potential of the specimen in the beam propagation direction. Therefore, the final recorded image intensity is $I(\boldsymbol{x}) = (\int_{k_{min}}^{k_{max}} A(k) * FT\big(1 + i\sigma_e v_z(\boldsymbol{x})\big) * D(k))^2$. Here, $A(k)$ is the aperture function equal to 1 from zero to convergence semi-angle and $D(k)$ is the detector function equal to 1 from k_{min} to k_{max}. Therefore, in the bright-field region, the final image intensity $I(\boldsymbol{x}) \sim 1 - (\sigma_e v_z(\boldsymbol{x})^2$.

Therefore, the final image intensity in the bright field region will reach minimum values at the maximum peak positions of the projected atomic potential. The small angle tilt will lead to the projected atomic potential maximum peak shift of $\frac{1}{2} t * \Delta\, \theta$ with phase object approximation, where *t* is the specimen thickness and $\Delta\, \theta$ is the tilt angle. Within the phase object approximation, the shift length of the minima position in bright field images is expected to be $\frac{1}{2} t * \Delta\, \theta$. Check the simulated results, like for oxygen at 4 nm thick, within weak-phase object approximation, a tilt of 5 mrad should lead the projected atomic potential peak to be displaced by 10 pm (2nm * 5 mrad), which is quite close to the simulated data. Fig. 6.22 shows the quantitative information about the difference between simulated deviation length and the value calculated from $\frac{1}{2} t * \Delta\, \theta$ ($\Delta d_{simulated} - \Delta d_{WPO}$) with the thickness value from 0 to 20 nm. These results also explain the linear behavior of deviation with tilt amount for the same thickness at thin specimen regions shown in section 6.4.4.

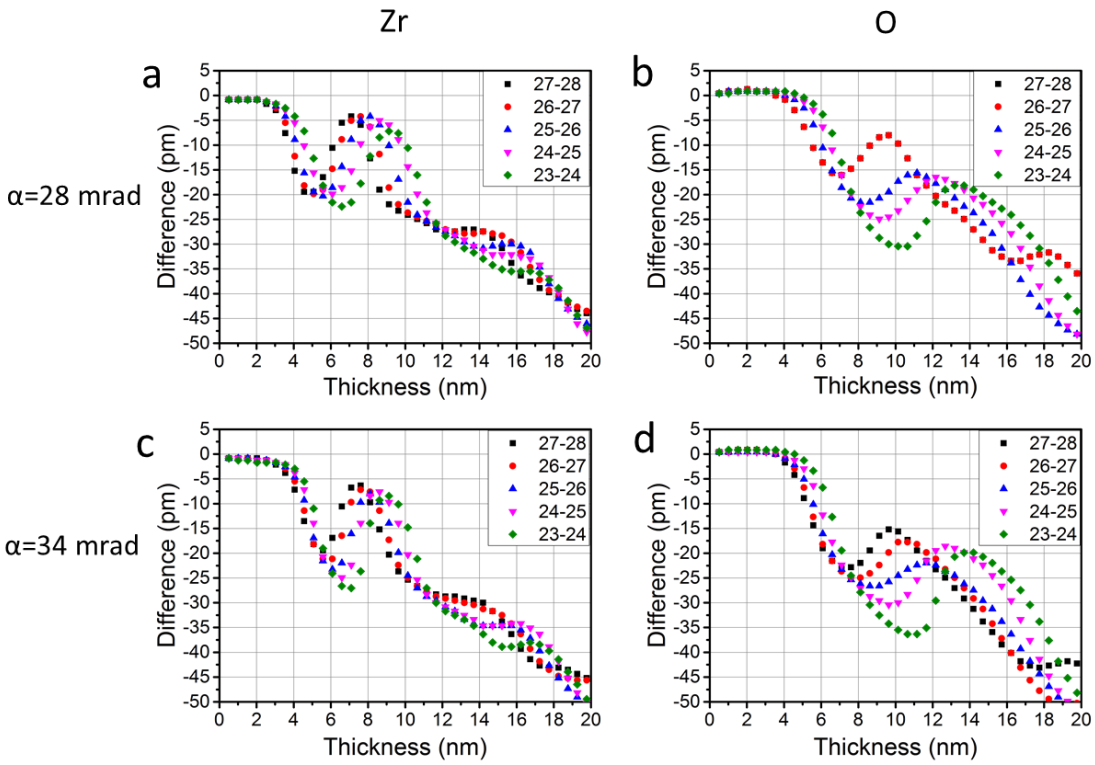

Figure 6.22 The difference between simulated deviation length and the value calculated from $\frac{1}{2}t * \Delta\,\theta$, i.e. $\Delta d_{simulated} - \Delta d_{WPO}$, with the thickness value from 0 to 20 nm for (a,c) Zr and (b, d) O. The convergence semiangles are indicated on the left and the collection semi-angles are indicated in the figures.

6.8 Outlook

In the view of the accuracy of the atom column position determination, two directions are suggested as near future work: probe aberration's influence and interface's influence.

6.8.1 Probe aberration's influences

In the simulations presented in this chapter, probe aberrations are all assumed to be zero. During the experiments, I tried to minimize all the aberration co-efficients, which however will never become all zero. Fig. 6.23 presents the phase map of the incident electron beam using experimentally measured aberration coefficients (as listed in Table 6.3) and the resulting relative deviations of O positions for different amount of Laue circle center shift. It shows that current small aberrations can increase the deviation amount with the scale of a few pm, especially for the thin specimen region. Besides, further simulations with C_1 of -5 nm (underfocus) and +5 nm (overfocus) with the other aberrations as listed in Table 6.3 yield that minor amount of under focus does not modify the deviation values while over focus does modify these values. Moreover, in section 6.2.2, I briefly show too

large aberrations can lead to quite large difference between beam tilt and tilt via propagation simulations

These results show that probe aberrations do have effect on the accuracy of the atom column position determination in ABF-STEM imaging, especially for the thin specimen region. The mechanism behind, like by contrast delocalization or contrast reversal, and different fold symmetry aberrations' influence, and the scale of influence has to be a future research topic.

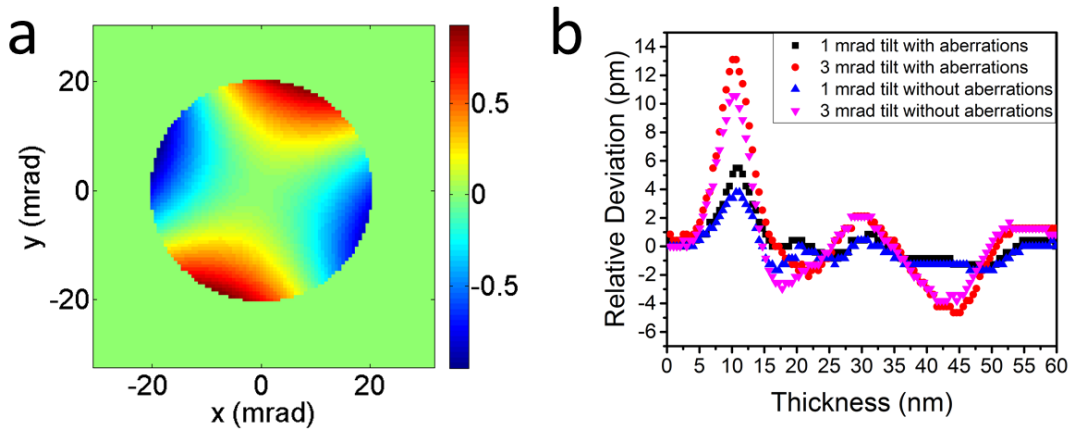

Figure 6.23 (a) Calculated incident electron wave phase map in reciprocal space with experimentally measured aberration coefficients listed in Table 6.3. (b) Comparison of the relative shift of O, between minima positions in ABF (collection semiangle of 11-23 mrad) imaging and maxima positions in HAADF (collection semiangle of 71-99 mrad) imaging, with and without experimental aberrations listed in Table 6.3 for different amounts of specimen tilt. For (a) and (b), the applied convergence semiangle is 20.4 mrad.

Table 6.3 Experimentally measured aberration coefficients values.

Aberration coefficients	Value	Angle (degree)
C_1/nm	0	Not applicable
A_1/nm	1.764	-109.4
A_2/nm	4.794	-17.6
B_2/nm	4.054	-23.2
C_3/nm	98.66	Not applicable
A_3/nm	89.17	-138
S_3/nm	12.96	-117.8
A_4/um	0.3397	125.2
D_4/um	0.4004	-61.8
B_4/um	0.1996	-154.3
C_5/mm	0.2444	Not applicable
A_5/um	32.41	157
R_5/um	3.046	-104.5
S_5/um	5.772	174.8

6.8.2 Interface's influences

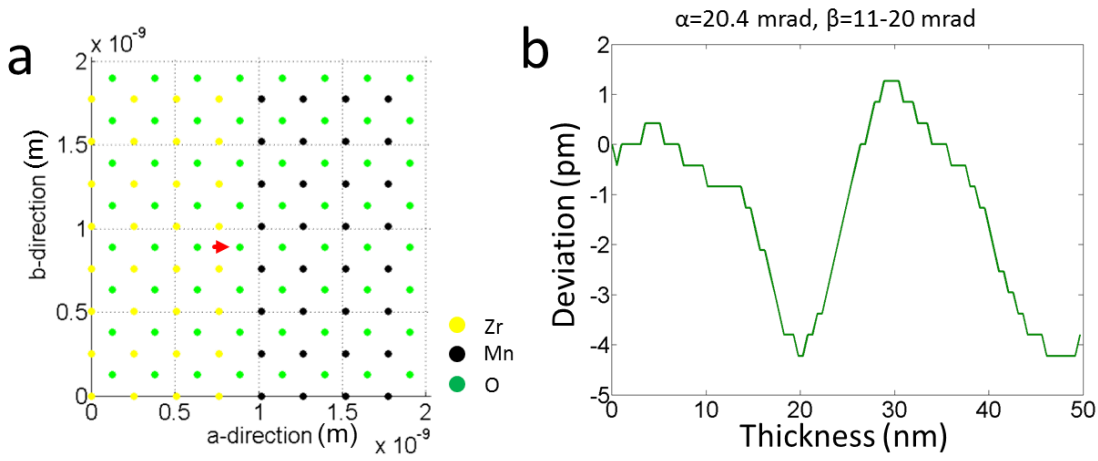

Figure 6.24 (a) Structure model of a ZrO_2-MnO_2 interface supercell. (b) Deviation of minima positions corresponding to the red arrow marked O (in (a)) in ABF images from their true positions. The convergence and collection semi-angles are indicated in the figure.

As mentioned in section 2.3.2, the low-angle scattering, which contributes to the ABF image intensity, is caused by the atom potential remote from the very core region. Differences among atoms of different *Z* of this low-angle scattering are less pronounced, which leads to less atomic number dependence of the ABF image intensity. From this scheme, we can see that low-angle scattering is sensitive to the atom potential distribution. For ABF-STEM imaging, I can imagine an asymmetric potential distribution around an atom could thus lead to minima positions deviate from their true positions. Interfaces, or I should extend it to any defect could cause an asymmetric potential distribution, and this yields a deviation of the minima position from the atom column's true position inside or very close to the interfaces. This is confirmed by the O position deviations from their true positions (Fig. 6.24b) inside the ZrO_2 and MnO_2, as marked by a red arrow in Fig. 6.24a, without any tilt or aberrations included. Again, the detailed mechanism and to what scale the interface's influence would be an interesting future research topic.

With these factors' influence on the accuracy of atom column position determination by ABF-STEM imaging discussed or to be studied, the purpose of this work is not trying to deny the possibility of quantitative determination of atom column position by ABF-STEM, but to emphasize the importance of accuracy and precision and to propose approaches to improve the accuracy and precision.

6.9 Conclusions

In this chapter, I investigated the reliability of the atom position determination in ABF-STEM imaging in an aberration-corrected STEM through a combination of

experimental and simulation results. Deviations from the true atom positions are observed in both experiments and simulations. The deviations are quantitatively studied for different collection semi-angles, convergence semi-angles and tilt amounts with an aberration-free probe. Suggestions on minimizing the errors in the atom position determination by ABF imaging are given based on our experimental experience and the simulated data. The deviations from the true atom positions caused by minor unavoidable specimen tilt are suggested to be taken into account when the researcher is pursuing better accuracy.

Besides, except the detector centering and detector sensitivity presented in chapter 2, more practical considerations, like simulation set-ups, diffraction pattern rotation and so on, which can influence the accuracy or precision of the presented data, are discussed in the appendix section.

Moreover, an outlook of the future work, concerning the probe aberration and interface/strain effects on atom column position determination is briefly introduced.

ACKNOWLEDGEMENTS

The authors thank Prof. H.-U. Habermeier for providing the ZrO_2-LSMO sample and Marion Kelsch for preparing the TEM plan-view sample, both Max Planck Institute for Solid State Research. The research leading to these results has received funding from the European Union Seventh Framework Programme [FP7/2007-2013] under grant agreement n°312483 (ESTEEM2) and from the Deutsche Forschungsgemeinschaft under Contracts RO2057/4-2 and MU3660/1-1.

Chapter 7 Contrast Investigation of Annular Bright-Field Imaging in Scanning Transmission Electron Microscopy of $LiFePO_4$

Abstract

In this chapter, I attempt to quantify the Li concentration in the battery material $LiFePO_4$ through image contrast simulations. It is found that for the maximum contrast variation with Li concentration and least variation with thickness, β_{in} and β_{out} are suggested to be set as $\frac{\alpha}{2}$ and larger than α. Deviation of defocus from 0 in a narrow range reduces the contrast, while further deviation of defocus to about −15 nm can increase the contrast sensitivity on the Li concentration. Focal series acquisition is thus suggested as a possibility for judging the Li concentration variation. Thickness information is important for the quantification of Li. Direct correlation with experimental results will need more theoretical investigations in this area.

People involved in this part research: Dan Zhou (1), Wilfried Sigle (1), Knut Müller-Caspary (2), Andreas Rosenauer (2), Peter A. van Aken (1).

(1) Max Planck Institute for Solid State Research, Stuttgart Center for Electron Microscopy, Heisenbergstraße 1, 70569, Stuttgart, Germany

(2) Institut für Festkörperphysik, Universität Bremen, Otto-Hahn-Allee 1, D-28359, Germany

7.1 Introduction

In this chapter, as an attempt of quantification Li concentration, I studied ABF imaging of light elements, for the case of lithium in $LiFePO_4$ (LFPO), in STEM by means of simulations using the STEMsim program.

7.2 Simulation set-up

The simulated results presented here were computed with the absorptive potential multislice algorithm as implemented in the STEMsim-software [150]. In this method, the thermal vibrations of the atoms are included in the calculation by randomly displacing atoms from their lattice sites using a Gaussian distribution function with the corresponding Debye–Waller factors for each atom species and its related absorptive potential. The size of the [010]-oriented orthombic $LiFePO_4$ (*Pnma*, a = 1.3240 nm, b=0.6006 nm, c=0.4694 nm) supercell was 2(a)×14(c) unit cells in the lateral directions with the x-direction parallel to the [100]-axis and the y-direction parallel to the [001]-axis, computed on a numerical grid of 100×50 pixels per unit cell. All simulations were computed for an accelerating voltage of 200 kV. To get collection-angle-dependent results, I subdivided the calculated angular range (0–100 mrad) into 100 rings of 1 mrad width. The signals from the individual angular ranges were obtained by incoherently adding all signals in the corresponding rings. The sampling in reciprocal space is 0.95 mrad/pixel (a axis), 0.38 mrad/pixel (c axis) with an angular range between 0 and 95.71 mrad (a axis) and 0 to 133.57 mrad (c axis).

To study the sensitivity of ABF on the lithium concentration, I intentionally create different concentrations of vacancies randomly distributed in the lithium atomic columns, as shown in Fig. 7.1. The parameters for the image simulations are set as shown in Fig. 7.2 except the sample thickness. To study the dynamics of ABF, the values of defocus and collection semi-angle (β_{in} and β_{out}) were varied. The maximum thickness was extended to 100 nm.

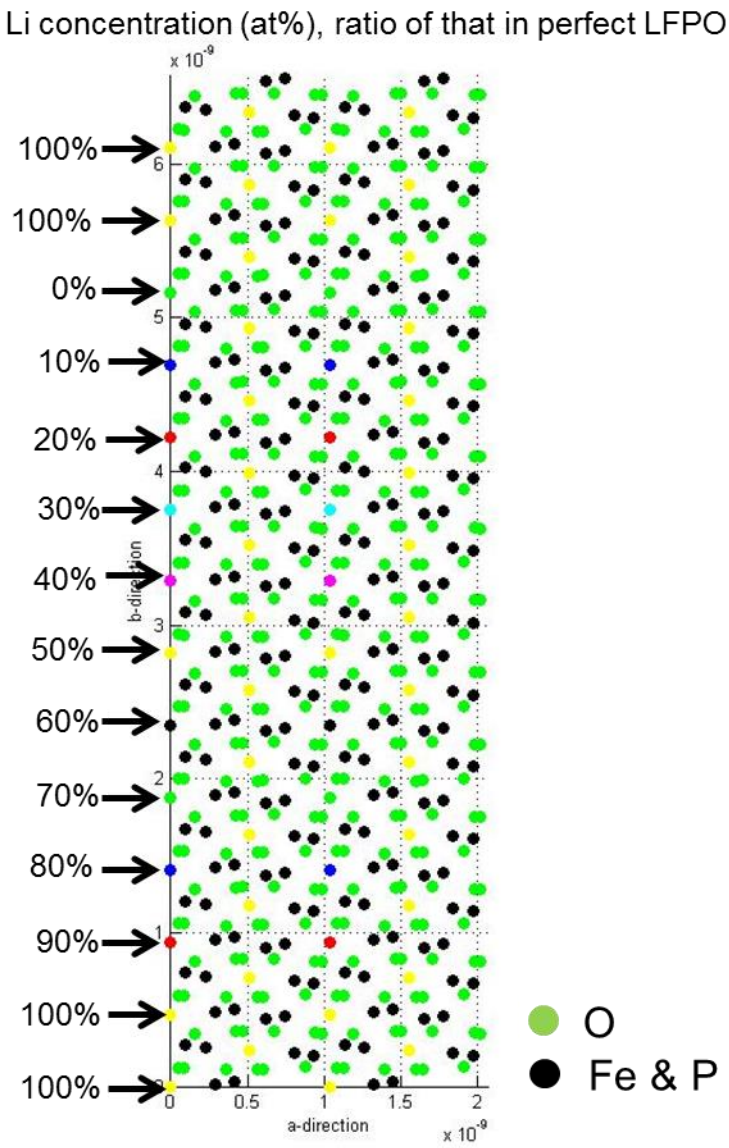

Figure 7.1 Set-up of the structure model of $LiFePO_4$ with different Li concentrations randomly distributed along the electron beam propagation direction. All other colors besides green (O) and black (Fe and P)in the structure model represent Li in different concentrations as indicated. The line scan is performed along the vertical direction at the center of the cell.

7.3 Results and Discussions

7.3.1 Preliminary remarks

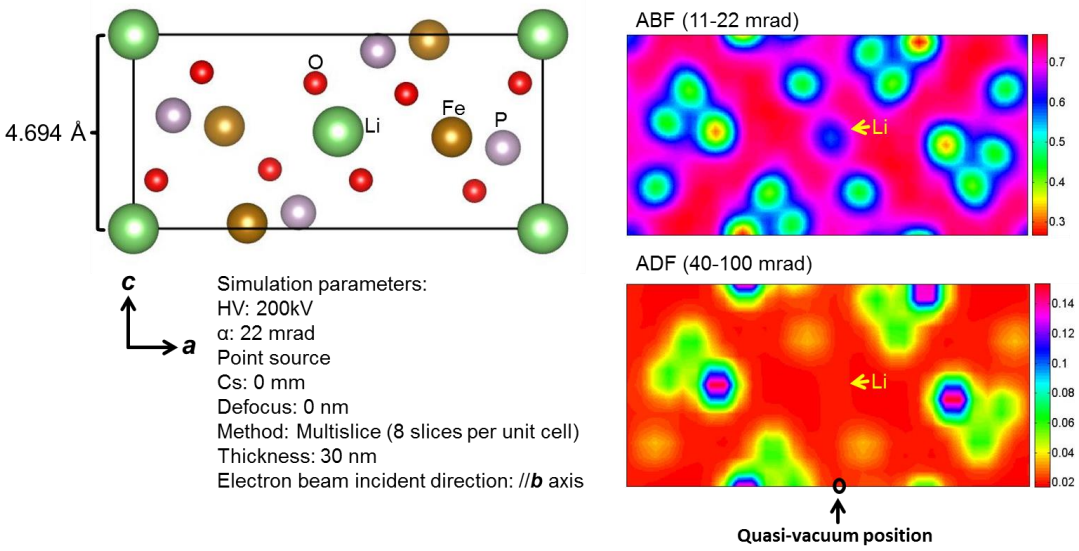

Figure 7.2 Simulation results on the visualization of lithium in $LiFePO_4$ with ADF and ABF imaging.

Fig. 7.2 presents the comparison of ADF and ABF imaging. It is obvious that Li is visible in ABF imaging while invisible in ADF imaging. For quantification I normalized the Li column image intensity with the intensity in a region remote from any atom column as marked in Fig. 7.2. The fractional intensity at this quasi-vacuum position (Fig. 7.3a) is relatively insensitive to the lithium concentration variation compared to the Li atomic column position for each thickness and each convergence and collection semi-angles set-up. Therefore, I calculate the contrast in the results part as follows:

$$Contrast = (I_{quasi\text{-}vacuum} - I_{Lithium}) / (I_{quasi\text{-}vacuum} + I_{Lithium})$$

For simplification, here ***I*** includes both coherent and incoherent signals.

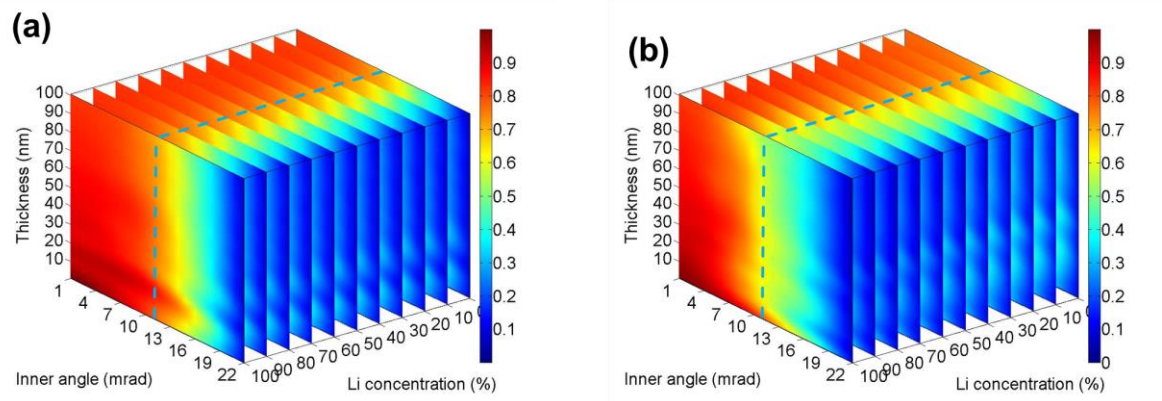

Figure 7.3 Comparison of the sensitivity of fractional intensity with varying lithium concentration between (a) quasi-vacuum position and (b) lithium position. Convergence semi-angle is 22 mrad and outer collection angle is also 22 mrad while the inner collection angle is as indicated in the inner angle axis. Note the independence of the fractional intensity on Li concentration in (a).

From Fig. 7.3 I find that the influence of thickness on the fractional intensities is smaller than those of collection semi-angle and Li concentrations. It looks like that the thickness does not influence the quantification of Li concentration. As an illustration, blue dashed lines are drawn to show the sensitivity of fractional intensity at the quasi-vacuum position (Fig. 7.3a) and Li position (Fig. 7.3b) for a collection semi-angle of 11-22 mrad and thickness of 100 nm. The fractional intensity at the quasi-vacuum position varies around 0.7, while that at the Li position varies from about 0.5 to about 0.7 when the Li concentration changes from 100% to 0%.

7.3.2 Effects of collection semi-angle

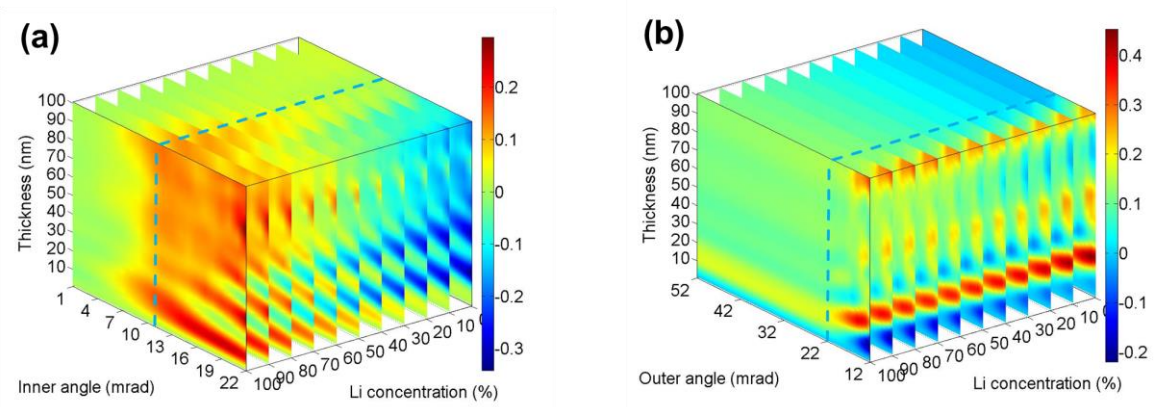

Figure 7.4 Contrast of lithium as a function of thickness (*z*-axis), lithium concentration (*x*-axis), and collection angle (*y*-axis). (a) Constant β_{out} (22 mrad) and (b) constant β_{in} (11 mrad).

In Fig. 7.4a data are shown where β_{out} was set constant and equal to the convergence semi-angle value, and β_{in} varies from 1 mrad to β_{out}. When β_{in} is around $\frac{\alpha}{2}$ (marked by blue dashed lines) maximum contrast difference as a function of Li concentration is achieved with least chance of contrast reversal and least variation with thickness

Based on this observation, I set β_{in} to be constant as $\frac{\alpha}{2}$ and β_{out} was allowed to vary from $\frac{\alpha}{2}$ to 52 mrad (Fig. 7.4b). When β_{out} is larger than the convergence semi-angle, the resulting signal includes the bright field and the low-angle dark-field signal. When β_{out} is around α (marked by blue dashed line) with constant β_{in}, it gives least thickness dependence and least chance of contrast reversal. Further increase of β_{out} over α will not alter the contrast significantly.

7.3.3 Effects of defocus

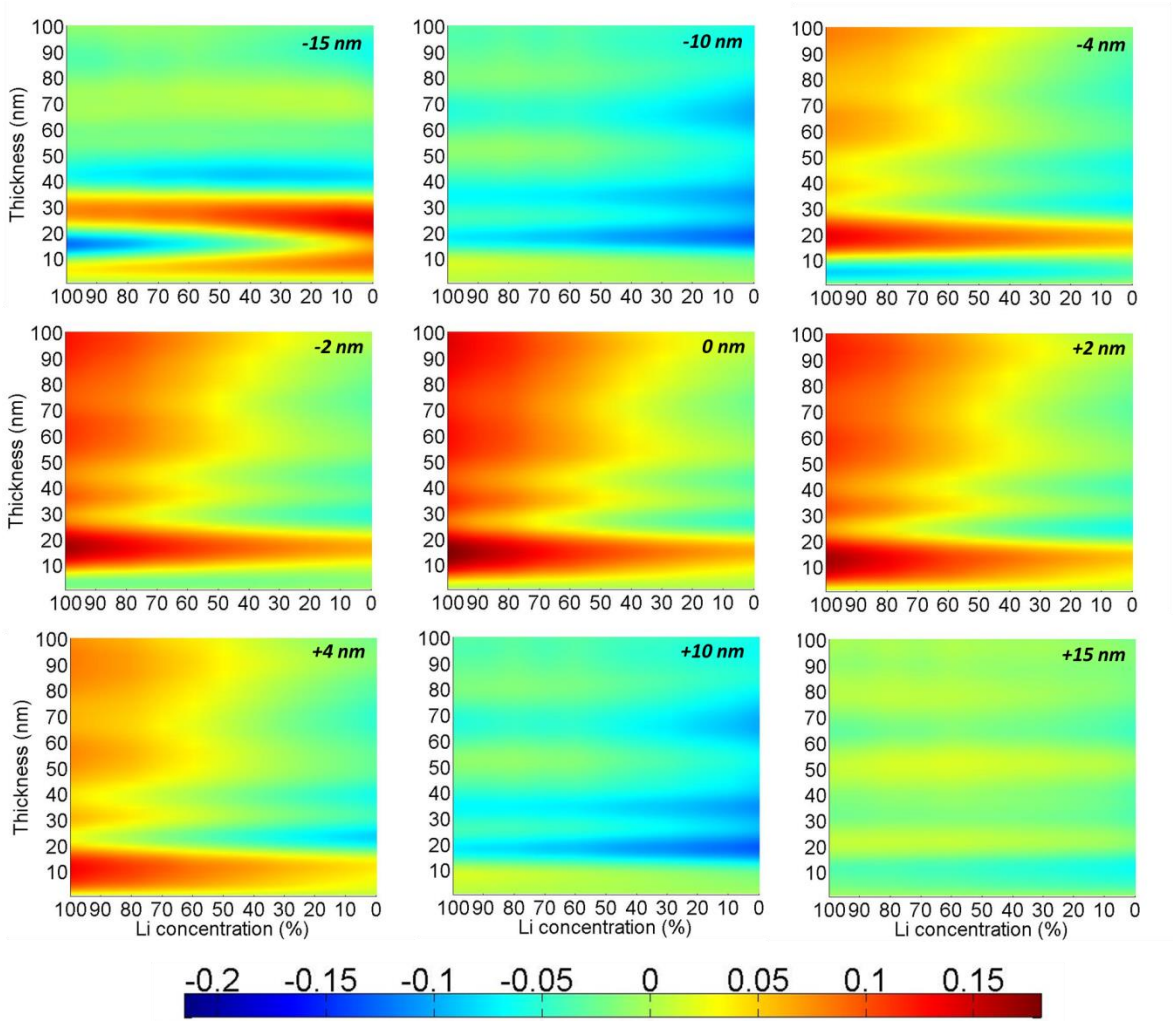

Figure 7.5 Contrast variation of lithium with thickness (*y*-axis), lithium concentration (*x*-axis) and defocus (labelled on the top right) with constant β_{in} (11 mrad), β_{out} (22 mrad), and C_s (0 mm).

The data for the defocus influence are presented in Fig. 7.5. Generally, the largest contrast shows up in a narrow defocus range approximately extending from -4 nm to +4 nm. As the defocus deviates from 0, the overall contrast decreases. In the positive defocus range, the contrast decreases as the Li concentration decreases for a fixed thickness value. It is therefore essential to get a precise thickness value for determining Li concentration from ABF images. From the map with defocus value −15 nm, the contrast increases as the Li concentration decreases for a certain thickness range. This indicates focal series might help to decide if delithiation happens or not.

7.4 Conclusions and future work

Here I presented theoretical ABF dynamics of lithium imaging with simulations. It is found that for the maximum contrast variation with Li concentration and least variation with thickness, β_{in} and β_{out} are suggested to be set as $\frac{\alpha}{2}$ and larger than α, respectively. Deviation of defocus from 0 in a narrow range reduces the contrast, while further deviation

of defocus to about −15 nm can increase the sensitivity to Li concentration change. Focal series acquisition is thus suggested as a possibility for judging the Li concentration variation. Thickness information is important for Li quantification.

As an outlook, more “real” conditions need to be simulated, including probe aberrations, the influence of structure distortions, the gradient of concentration change and so on, which however will more or less influence the final results.

Chapter 8 EELS Investigation of Size-dependent Delithiation Process in $LiFePO_4$

Abstract

In this chapter, the particle-size dependent delithiation process of $LiFePO_4$ with EELS is presented. From the core-loss region of the O-K edge pre-peak intensity and the Fe $L_{2,3}$ peak position, as well as from the low-loss region of the bulk plasmon peak position analysis, it is found that the sample with particle size of 25 nm delithiates homogeneously over the whole particle, and that of particle with sizes of 70 nm and 150 nm delithiates from the center to the edge and thus forms a $FePO_4$ core and a $LiFePO_4$ shell. The practical considerations, like radiation damage, delocalization, interface effects are discussed.

People involved in this part research: Dan Zhou, Wilfried, Sigle, Changbao Zhu, Joachim Maier, Peter A. van Aken

Max Planck Institute for Solid State Research, Heisenbergstraße 1, Stuttgart, Germany

8.1 Introduction

The mechanism of extraction (delithiation) and insertion (lithiation) of lithium (Li) in the battery material are still under debate. Models like core-shell[157], mosaic[158], domino-cascade[159] and so on are proposed based on the combined consideration of calculation and experimental data. Factors like the synthesis technique, reaction mechanism, morphology, shape, and particle size can influence the delithiation processes. Therefore a detailed study of the delithiation process is important. In TEM, the recent development of annular bright-field (ABF) scanning transmission electron microscopy (STEM) provides atomic-resolution information of the staging delithiation process in LFPO materials[39, 160, 161]. However, the restriction to special zone axes, along which pure Li columns are visible, and the crystalline quality often limit its application. More traditional and widely applied is EELS in either TEM or STEM mode.

In this chapter, experimental results from the core-loss region and the low-loss region of samples with LFPO nanocrystals with three different sizes (25, 70, and 150 nm) are presented and discussed.

8.2 Experimental section

In this work, partially delithiated (LFPO-$FePO_4$ (FPO)) powder samples were investigated. The details about sample preparation and delithiation treatment can be found in [162].

The as-prepared sample powder was dispersed in isopropanol and deposited on a holy carbon film. EELS analyses were performed with a parallel electron energy-loss spectrometer (Gatan ENFINA PEELS) fitted to a dedicated scanning transmission electron microscope (Vacuum Generator HB501UX) operating at 100 kV. The PEELS consists of a magnetic prism, quadrupole lenses, a scintillator, and a photodiode array for parallel recording of 1024 channels. The microscope is equipped with a cold field-emission electron source. The beam was focused to less than 1 nm diameter. The system had an energy resolution of 0.7 eV. The resulting EELS spectrum was recorded by a charge-coupled device (CCD) detector. The illumination angle was 10 mrad using a 40 µm objective aperture. The collection angle was 6.5 mrad using a 2 mm spectrometer entrance aperture.

For the core-loss region spectrum, point EELS spectra were measured to cover both O-K and Fe-L edges. Each single spectrum was acquired by integrating 10 frames of 1 second, which sums up to 10 seconds per spectrum. Non-simultaneous low-loss spectra

were also acquired by 10 frames with 0.1 s per frame to determine the sample thickness Too long acquisition time yield radiation damage of the sample and an alternation of the core-loss edges.

For the low-loss spectrum line profile acquisition, I used the shortest acquisition time allowed in the system, 0.005 s, for each pixel and maximize the counts by illuminating one point in the hole area and adjusting the extraction voltage to about 3.8 keV. For each spectrum line profile, 40 spectra were collected.

8.3 Results and discussions

The estimated mean free path under such an experimental set-up for LFPO is 106 nm and for FPO is 103 nm. This means that the analysis of samples with particle sizes of 25 nm and 70 nm will be little influenced by multiple scattering while the data of the sample with particle size of around 150 nm will suffer from the influence of multiple scattering.

8.3.1 The core-loss region

8.3.1.1 Delithiation related features at the O-K and Fe-L edge

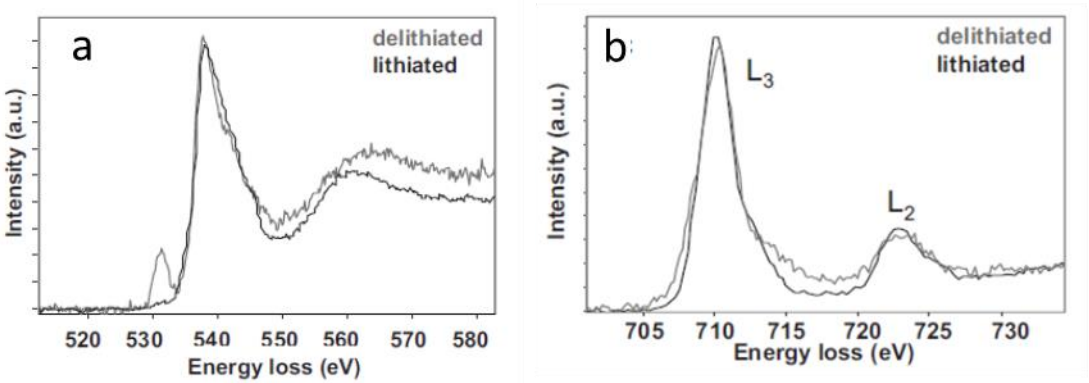

Figure 8.1 Reprint from [163]. (a) O-K and (b) Fe-$L_{2,3}$ core-loss EELS spectra from $LiFePO_4$ (black) and Li_xFePO_4 (x<<1) (gray) powders.

The fingerprints of delithiation in the core-loss region can be found from the O-K and Fe-$L_{2,3}$ near-edge structure, as shown in the Fig. 8.1 [163].

The O-K pre-edge peak, which is observed before the threshold of the main O-K edge, only appears when Li is removed[163-165], while the main peak, centered at about 538 eV always exists. This pre-edge peak appears in most transitional-metal oxides and is directly related to the hybridization of oxygen 2p and metal 3d bands. The pre-edge peak is interpreted as originating from transitions from O 1s states to empty O 2p components of metal 3d hybridized with O 2p states. In the presence of Li, the metal 3d bands are more

filled (Fe^{2+} in LFPO and Fe^{3+} in FPO) and thus less un-occupied states are available which leads to the reduced pre-edge peak intensity.

The Fe-$L_{2,3}$ edge consists of two strong white lines originating from transitions from spin-orbit-split 2p core levels into unoccupied 3d states. Roughly speaking, removing one lithium atom will remove one electron from the metal d band. This will increase the number of empty d levels and consequently increase the intensity of the pre-edge peak. However, this is not the full picture. Besides the emptying of one d level, the d band is also displaced farther to the conduction band[164]. The removal of Li from $LiFePO_4$ will change Fe from Fe^{2+} to Fe^{3+} and shift the Fe-$L_{2,3}$ peak to higher energy. As shown in Fig. 8.1b [163], the delithiated sample (mainly with Fe^{3+}) shows higher L_3 peak energy than the lithiated sample (mainly with Fe^{2+}).

Therefore, in this thesis, the pre-edge peak intensity and the peak position of Fe $L_{2,3}$ will be used for the delithiation process study.

8.3.1.2 Practical considerations

Energy calibration

Due to the lack of the possibility to acquire high-loss and low-loss spectra simultaneously, we take the O-K main peak at about 538 eV as reference and align all the spectra accordingly for the core-loss region. This peak's position is much less sensitive to compositional changes with delithiation process.

Influence of radiation damage

Despite the effort of minimizing radiation damage by multiple acquisitions with short acquisition time, radiation damage is not completely avoidable for this material under focused beam illumination. The loss of Li and O by electron beam radiation is not directly visible from the HAADF image. Since our analyzed objects have a thicker center and a thinner edge concluded form the particle shape, the ratio of radiation damaged to undamaged material would be higher for the thin region if the same amount of sample is influenced by radiation damage. Therefore, if the results give more FPO at the edge, I need to take care of the radiation damage influence on the qualitative conclusion. However, if the results is opposite, I only need to take care that quantitatively speaking, the difference between center region and edge region could be reduced by radiation damage.

8.3.1.3 Experimental results

Particle size ~25 nm

Unfortunately, due to the high sensitivity to radiation damage under electron beam illumination, core-loss spectra for particles with a size on the order of ~25 nm were not possible to be collected.

Particle size ~70 nm

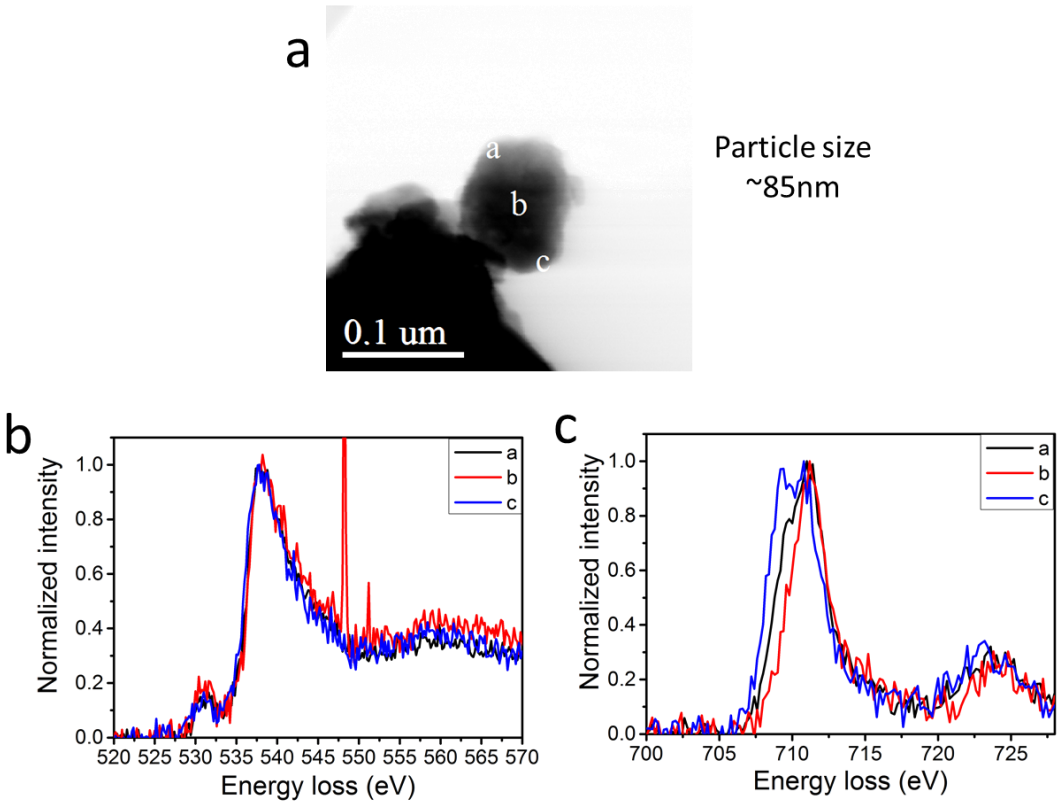

Figure 8.2 (a) BF STEM image of a particle with a particle size of about 85 nm. EELS spectra of (b) O-K and (c) Fe-$L_{2,3}$ edges from 3 sample areas marked in (a). The O-K edge is normalized to the main peak intensity and the Fe $L_{2,3}$ edges are normalized to the L_3 peak intensity.

As shown in Fig. 8.2, the O K pre-edge peak has a relative higher intensity at the center than at the edge and the Fe L_3 peak shows an obvious shift towards higher energy at the center region compared to the edge region. These two features together reveal that the particle center region is more delithiated than the edge leading to a higher valence state of Fe at the center. The presented particle has a diameter of about 85 nm. This result, i.e. more FPO at the center and more LFPO at the edge, was confirmed with particles with sizes of about 75 nm and 65 nm.

Particle size ~150 nm

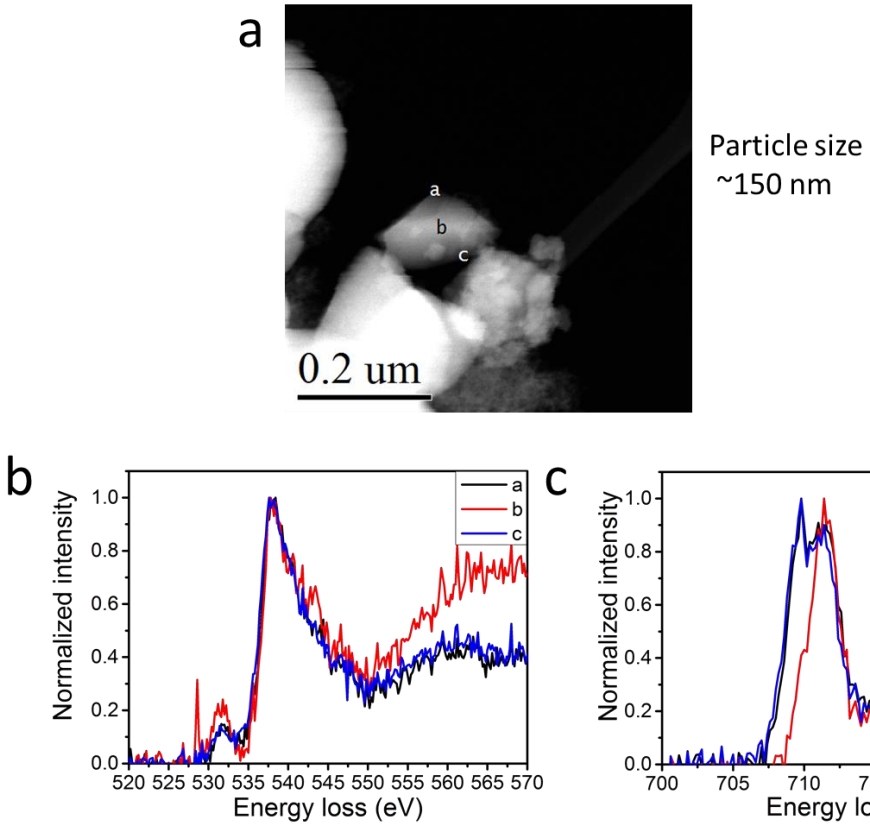

Figure 8.3 (a) HAADF STEM image of a particle with~150 nm diameter. EELS spectra of (b) O-K and (c) Fe-$L_{2,3}$ edges from 3 sample areas in the particle marked by "a", "b" and "c" in (a). The O-K edge is normalized to the main peak intensity and the Fe-$L_{2,3}$ edges are normalized to the L_3 peak intensity.

These large particles show the same trend as the particles with ~70 nm diameter, as shown in Fig. 8.3.

8.3.2 The low-loss region

8.3.2.1 Delithiation related features in the low-loss region

As reported before[163, 164, 166], the fingerprint of delithiation in the low-loss region relies on the intensity of the interband transition peak at around 5 eV and the position of the bulk plasmon peak at about 25 eV. As shown in Fig. 8.4, the interband transition originates from the transition of electrons at the top of the valence band which have mainly oxygen 2p character to the conduction band, which only appears in FPO. The bulk plasmon peak position is higher in FPO than in LFPO. Therefore, in principle, the intensity of the interband transition peak and the position of the bulk plasmon peak can be used to distinguish the delithiation status.

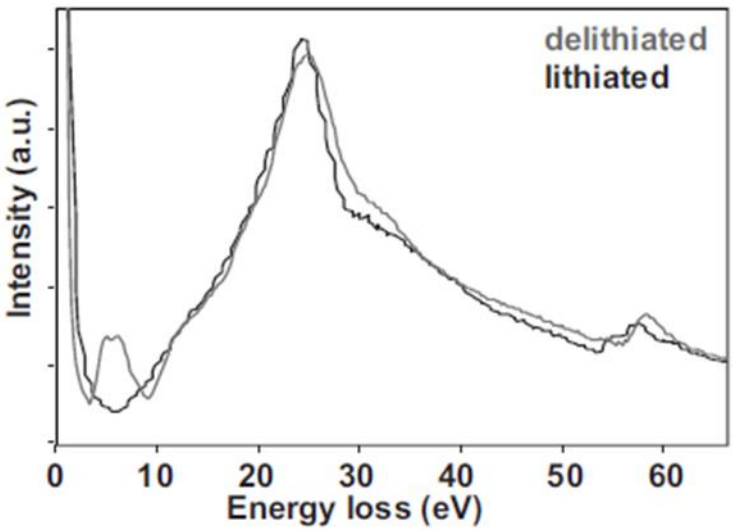

Figure 8.4 Reprint from [163]. Low-loss spectrum comparison of delithiated (FPO) and lithiated (LFPO) samples.

8.3.2.2 Practical considerations

Cherenkov loss and radiation damage

If the phase velocity *v* of an electron exceeds (for a particular frequency) the speed of light *c* in the material through which it is moving ($v > c/n$ where *n* is the refractive index of the medium[167]), the electron loses energy by emitting Cherenkov radiation at that frequencies which can cause extra peaks to be observed in the band-gap and interband region[76]. . At an accelerating voltage of 100 kV, v is ≈1.644× $10^8\ m\ s^{-1}$. The refractive index of LFPO is within the range of 1.66–1.7. The conditions for Cherenkov losses are therefore not fulfilled in this case since $v < c/n$. However, lowering accelerating voltage can increase specimen damage due to radiolysis. In addition, the threshold voltage for knock-on damage of Li is below 20 kV and goes to maximum at about that voltage and then decrease slowly towards higher energy (at high energy knock-on damage never will be zeo)[168]. This means that for available accelerating voltages 30-300kV, an increase of accelerating voltage will decrease the Li knock-on damage. Thus, increase of accelerating voltage will decrease the delithiation induced by electron-beam radiation.

Therefore, selection of 100 kV accelerating voltage and analysis of the low-loss region with short acquisition times is a good choice of balancing between radiation damage and signal.

Delocalization of inelastic scattering

As has been mentioned in Chapter 2, the delocalization of inelastic scattering is the main factor limiting the spatial resolution. Useful measures for the spatial resolution are

the diameters d_{80} and d_{50} of a disk which contain 80% and 50% of the intensity contributing to the signal at a given energy loss. As discussed by Erni and Browning[78], the classical approach derived by Egerton [169] and the quantum mechanical approach derived by Muller and Silcox [78] gives results in better agreement with experimental observations, especially for the energy-loss region over 5 eV. For simplicity, in this chapter, I use the classical approach from Egerton and plot the delocalization diameter as a function of energy loss (as shown in Fig. 8.5):

$$d_{50} = 0.8\lambda(\frac{E_0}{E})^{\frac{3}{4}}$$

where λ is the electron wavelength, E_0 is the incident electron energy and E is the energy loss .

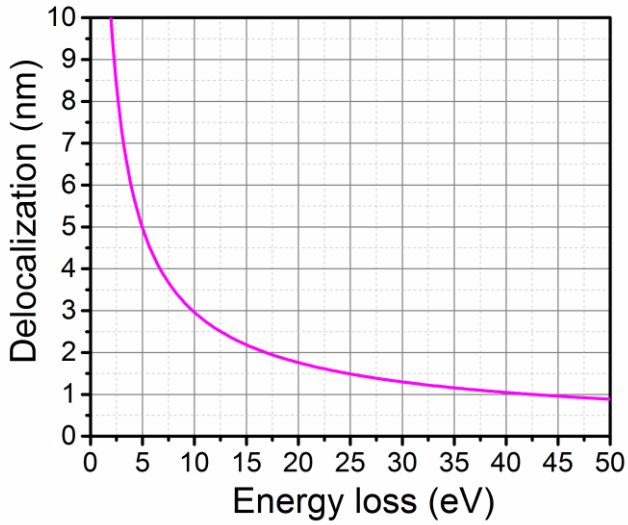

Figure 8.5 Delocalization (d_{50}) as a function of the energy loss calculated using the method of Egerton (2003) [169].

From Fig. 8.5 I find a delocalization of about 5 nm for the interband transition of FPO and of about 1.5 nm for the bulk plasmon. These values indicate that the signals observed using interband transition and bulk plasmon excitations actually come from larger regions than the size of the electron probe.

Interface/surface effects

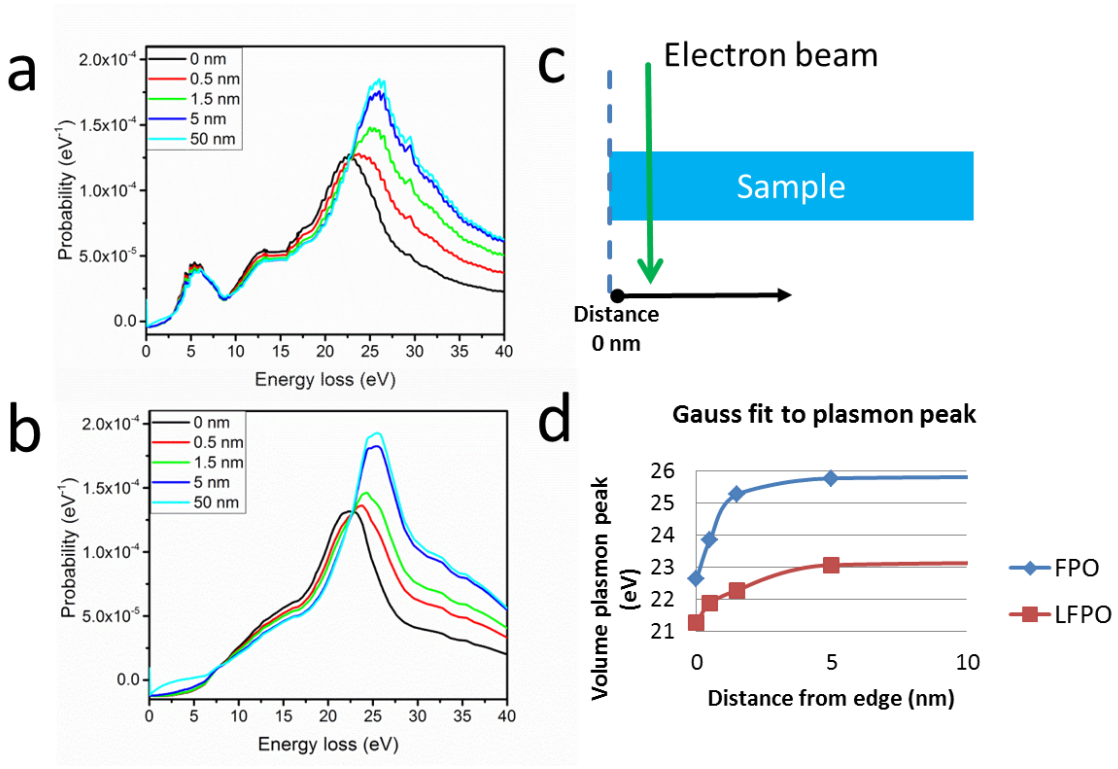

Figure 8.6 Calculated low-loss spectra of (a) FPO and (b) LFPO at different distances from the sample edge as indicated in the figures. (c) Illustration of the set-up for theoretical calculations. (d) Volume plasmon-peak positions for FPO and LFPO at different distances from the edge.

Fig. 8.6 shows EELS spectra calculated for FPO and LFPO as a function of distance from a free surface. The calculation is based on a formalism by Moreau et al.[93]. For this calculation dielectric functions were taken from literature[88]. The presence of the interface will lead to a shift of the bulk plasmon peak positions for both FPO and LFPO (Fig. 8.7d). It is clear that the plasmon peak shifts gradually to the bulk plasmon value which is reached at a distance of about 5 nm in both materials. FPO has a larger volume plasmon peak position at all positions. From these calculations it becomes clear that the plasmon peak position cannot be used for material identification at distances within 5 nm from the particle edge.

8.3.2.3 Experimental results

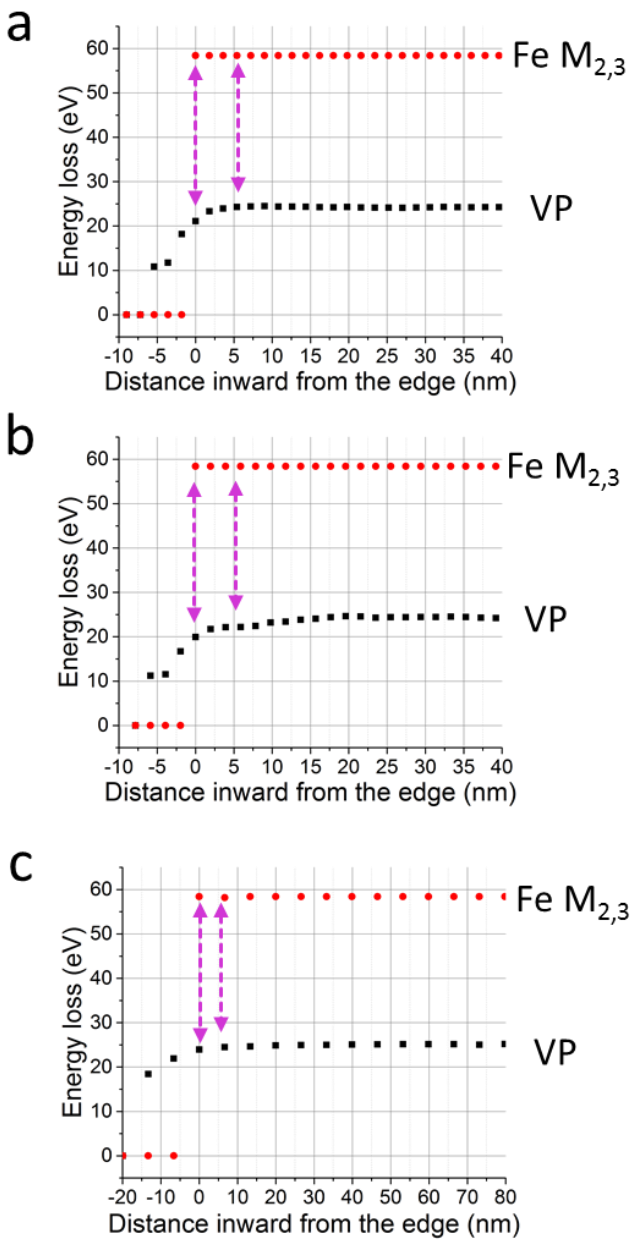

Figure 8.7 Volumn plasmon (VP) peak position and Fe-$M_{2,3}$ edge peak position of nanocrystals with size of (a) 25 nm (b) 70 nm (c) 150 nm. For the Fe-$M_{2,3}$ edge, '0' means it is not detected at this position. The two magenta lines are used to indicate (left) when the electron beam enters the material, i.e. Fe-$M_{2,3}$ edge shows up, and (right) when the delocalization effect can be neglected for correlating the plasmon peak shift with the LFPO/FPO phase change.

Even though the overlap of the Fe-$M_{2,3}$ edges (edge onset at 57 eV) and the Li-K edge (edge onset at 55 eV) makes the Li K edge impossible to be used as a fingerprint for delithiation, the reduced delocalization at this energy loss (compared to the plasmon loss) and the negligible influence by interface effects makes these edges suitable for a judgement whether the electron beam has entered the material or not.

The experimentally measured plasmon peak positions of samples with particle sizes of 25 nm, 70 nm, and 150 nm are presented in Fig. 8.7. The sample edge was set to 0 where the Fe-$M_{2,3}$ edge became visible and positive distance values correspond to the interior of the particle. Neglecting values less than 5 nm close to the surfaces (see Fig. 8.7) the bulk plasmon peak positions can be used to determine the delithiation status. It can be found that 25 nm nanoparticles form solid solution as observed from the non-changed plasmon peak position and 70 nm and 150 nm as FPO core with LFPO shell from the shift of the plasmon peak to higher value when approaching from surface to the center of the particle.

8.4 Conclusions and outlook

From the analysis of delithation-related fingerprints of EELS spectra in both core-loss and low-loss regions, the experimental observations show that 25 nm particles exist as solid solution whereas 70 nm and 150 nm large particles have an FPO core and an LFPO shell. Radiation damage and possible artefact peaks were discussed.

Chapter 9 Conclusion and Outlook

In this thesis, the application of methodology of aberration-corrected TEM to light elements in complex oxides has been presented covering simulations and experiments, imaging and analytical techniques, exploring new approaches and applying already well applied techniques, with the emphasis on ABF imaging.

Some practical considerations, such as alignment of all detectors centers and ways how to reduce sample drift, were presented in **Chapter 2** together with the description of basic methods and preliminary results.

In **Chapters 3–5**, I have presented atomic-scale studies of the structure, chemistry and bonding of the ZrO_2−LSMO pillar matrix system utilizing HAADF and ABF imaging along with EELS spectrum imaging and time-series image acquisition. I showed that ZrO_2 precipitates form at as low concentrations as 6 mol%. Precipitates mainly form pillars penetrating the entire LSMO film. Substantial interdiffusion is found at the LSMO−ZrO_2 interface with Mn replacing Zr in ZrO_2 (thus stabilizing the cubic or tetragonal phase) and Zr replacing Mn atoms in LSMO. Charge balancing requires formation of oxygen vacancies which are observed to segregate at the interface. Strain analyses show that the system has not reached elastic equilibrium yet. It is clear that LSMO as well as pillar regions are strained because of the misfit, however, also modified by the interdiffusion.

Besides, structure, composition and charge state of three APBs connecting ZrO_2 pillars in LSMO/ZrO_2 were analyzed. I observe a ladder-like structure of atomic columns within all APBs. All APBs are rich in Mn where the Mn valence is the same in the APB as in bulk LSMO. Lower HAADF contrast in APBs indicates lower occupancies of atomic sites within the APBs as compared to bulk LSMO. From combined HAADF and ABF imaging I obtain structure models with all positions of cation and anion atomic columns. The formation of APBs is supposed to be driven by strain relaxation and the availability of Mn atoms due to substitution of Mn atoms by Zr. From charge analysis I conclude that the APB structure is in accordance with minimization of electrostatic energy. Owing to their reduced occupancy numbers, the APBs might act as efficient ionic conductors. This could make such materials interesting as cathode materials in solid-oxide fuel cells.

Moreover, electron-beam-induced reconstructions of structure, composition and charge state of three APBs in LSMO/ZrO_2 were observed and analyzed. For all the APBs,

Mn segregation remains inside the boundaries but the Mn valence state gets reduced. During irradiation, atomic columns on the two sides of APBs of the LSMO matrix region move locally, accompanying the movement of B' sites inside the APBs. From combined HAADF and ABF imaging, I obtain structure models with all positions of cation and anion atomic columns. Moreover, despite the change of number of B'-sites inside the APBs, all APBs are confirmed to lose no heavy atoms, i.e. Mn, analyzed from the background subtracted HAADF signal ratio. The mechanism of electron-beam-induced reconstructions is supposed to be driven by the strengthened radiolysis at the interface region. Due to the loss of oxygen under electron beam irradiation and therefore rupture of bonds between oxygen and heavy atoms, the structures went from order to disorder, and to order again by local area atomic column movement to reach a new stabilized status.

In the $La_{(1-y)}Sr_yMnO_3$ system, the magnetic properties are directly related to the y value. Therefore, I believe that our results are relevant for the underlying mechanisms of electron transport and magnetism in this material system, like the observed anomalous transport properties and localization transition.

In **Chapters 6–8,** I first investigated the reliability of quantitative ABF imaging in terms of atomic position determination with experimental and simulation results. Starting from the experimental observations of simultaneously acquired HAADF and ABF images on ZrO_2 revealed the minima/maxima position sensitivity to specimen tilts. The deviations were studied systematically by simulation for different collection semi-angles, convergence semi-angles and tilt amounts with an aberration-free probe. Suggestions on the atom position determination by ABF imaging are given based on our experimental experience and the simulated data. The incorporation of probe aberrations needs to be taken into account in the future to get quantitative match of the deviation value between experiments and simulations.

Then I presented theoretical studies of Li ABF image contrast as a function of thickness, Li concentration, and scattering angles. It is found that for the maximum contrast variation with Li concentration and least variation with thickness, β_{in} and β_{out} should be set as $\frac{\alpha}{2}$ and larger than α. Deviation of defocus from 0 in a narrow range reduces the contrast, while further deviation of defocus to about −15 nm can increase the contrast of Li concentration change. Focal series acquisition is thus suggested as a possibility for judging the Li concentration variation. Thickness information is important for Li quantification. As an outlook, "real" conditions, i.e. more detailed consideration of a non-zero-C_s electron probe, and strain caused by delithiation will be taken into account in

future simulations. Moreover, the practical material environment won't be like the structure model presented here. This includes the presence of structure distortions and concentration fluctuations.

Finally, EELS fingerprints related with the delithiation process in both core-loss and low-loss regions were presented and led to the following conclusions: In a sample with particle size of 25 nm Li is solved as a solid solution in LFPO. For larger particle sizes (70 nm and 150 nm) I found an FPO core and an LFPO shell. Besides, radiation damage and possible artefact peaks were discussed. As an outlook for future work, the delocalization increases with increasing accelerating voltage of the microscope. The increase of the high voltage will also reduce the radiation damage for Li materials. Despite the fact that current results match with the low-loss comparison, the possibility to get a more localized low-loss spectrum and thus the possibility to remove multiple scattering and local area energy value calibration with dual-EELS capability will improve the precision and give more quantitative information.

List of Tables

Table 2.1 The experimentally measured aberration coefficients (except C_3, C_C, and $E–E_0$).

Table 4.1 Atomic-column arrangement within APB-1. The direction from left to right corresponds to [1-10] and the direction from top to bottom to [-1-10].

Table 4.2 Atomic-column arrangement within APB-2. The direction from left to right corresponds to [1-10] and the direction from top to bottom to [-1-10].

Table 4.3 Atomic-column arrangement within APB-3. The direction from left to right corresponds to [1-10] and the direction from top to bottom to [-1-10].

Table 4.4 Atom-column arrangement within APB-3. The direction from left to right corresponds to [-1-10] and the direction from top to bottom to [1-10].

Table 4.5 Charge sequence across the APB walls. For APB-1, the direction from left to right corresponds to [1-10] and the direction from top to bottom to [-1-10]. For APB-2 and APB-3, the direction from left to right corresponds to [1-30] and the direction from top to bottom to [-3-10].

Table 5.1 Charge sequence across the APB walls. For APB-1, the direction from left to right corresponds to [1-10] and the direction from top to bottom to [-1-10]. For APB-2 and APB-3, the direction from left to right corresponds to [1-30] and the direction from top to bottom to [-3-10].

Table 6.1 Relative shift of minima positions (Zr) from ABF images to maxima positions (Zr) from HAADF images. Here $\overline{\Delta \boldsymbol{x}}$ is the average relative shift along the *x*-direction, $\overline{\Delta \boldsymbol{y}}$ is the average relative shift along the *y*-direction and $\overline{\Delta \boldsymbol{d}}$ is the average relative shift vector length. And σ is the standard error.

Table 6.2 Relative shift of minima positions (O) compared to “tilt 1” acquired with a 20.4 mrad convergence angle condition (Fig. 6.5e). Here $\overline{\Delta \boldsymbol{x}}$ is the average relative shift along the *x*-direction, $\overline{\Delta \boldsymbol{y}}$ is the average relative shift along the *y*-direction and $\overline{\Delta \boldsymbol{d}}$ is the average relative shift vector length, where σ is the standard error.

Table 6.3 Experimentally measured aberration coefficients values.

List of Figures

Figure 1.1 Calculated probe size with parameters (a) 200kV, 1.4 mm chromatic aberration, 1.2 mm spherical aberration, 0.4 eV energy spread; (b) 200 kV, 1.4 mm chromatic aberration, -500 nm spherical aberration, 0.4 eV energy spread.

Figure 2.1 Phase plate of the electron probe in the back focal plane when C_3 is (a) 100 nm and (e) 1.2 mm. Electron probe intensity in the incident plane when C_3 is 100 nm and the convergence semi-angle is (b) 5 mrad, (c) 10 mrad, and (d) 30 mrad. Electron probe intensity in the incident plane when C_3 is 1.2 mm and the convergence semi-angle is (f) 5 mrad, (g) 10 mrad, and (h) 30 mrad.

Figure 2.2 Schematic illustration of ABF imaging and HAADF imaging in STEM.

Figure 2.3 Overview of $LiFePO_4$ TEM specimen prepared by FIB. Left: HAADF image taken with collection semi-angle of 90–370 mrad. Right: Thickness map using an EELS collection semi-angle of 60 mrad. The thickness scale is in units of the mean free path of 101.4 nm.

Figure 2.4 (a,c) HAADF images acquired using collection semiangles of 90–370 mrad. (b,d) ABF images using collection semi-angles of 11–22 mrad. (a) and (b) were simultaneously acquired from a sample region below 50 nm thickness, (c) and (d) were simultaneously acquired from a sample region of about 100 nm thickness. The convergence semiangle was 22 mrad and the probe size was about 0.08 nm.

Figure 2.5 (a) Structure model of $LiFePO_4$ viewed along the [010] axis. Simulated (b) ABF (11–22 mrad) and (c) HAADF (90–370 mrad) image intensity of each atomic column as function of thickness. The convergence semi-angle is 22 mrad and HT is 200 kV.

Figure 2.6 (a) Scanning image of the detector (with inserted beam stopper) showing variations in detector sensitivity. (b) Beam stopper (centered on 3 mm aperture) and BF apertures on pre-GIF Gatan XP1000 CCD.

Figure 2.7 Schematic illustration of the JEOL HAADF detector.

Figure 2.8 Pre-GIF CCD image of the 150 µm CL aperture at a camera length of 2 cm (a) with HAADF detector inserted (b) with HAADF detector retracted. (c,d) Superposition of all the images. In (d) the projected hole is shown in magenta color and the real hole of the beam-sensitive area in turquoise color for comparison.

Figure 2.9 Detector sensitivity (a) JEOL BF detector with only beam stopper inserted (b) JEOL BF detector with 3 mm BF aperture inserted (ABF mode) (c) JEOL HAADF detector (d) Gatan ADF detector. In all cases a probe size 10 c and a 30 µm CL aperture were used.

Figure 3.1 (a) Annular dark-field (ADF) image of a plan-view 70 mol%LSMO-30 mol%ZrO_2 sample. (b) HREM image of the side-view specimen with 30 mol% ZrO_2. (c) Three-color EELS spectrum image of the area shown in (a) with Zr-$L_{2,3}$ in orange, Mn-$L_{2,3}$ in blue and La-$M_{4,5}$ in green. (d) A schematic view of the sample.

Figure 3.2 HAADF image of ZrO_2 pillar overlapping with the LSMO matrix.

Figure 3.3 (a) HAADF image showing a matrix region with possible existence of small pillars, as indicated by the yellow frame. (b) Line profile of the intensity of the magenta line area in (a). Yellow arrows indicate reduced contrast in the yellow square area in (a), whereas blue arrows represent the contrast of LSMO.

Figure 3.4 (a, d) HAADF images of a plan-view 70 mol%LSMO-30 mol%ZrO_2 sample. Fourier filtered images using (b, e) {100} reflections and (c, f) {010} reflections.

Figure 3.5 Structure model of tetragonal LSMO (a) and tetragonal ZrO_2 (b) viewing along [001] direction.

Figure 3.6 Strain field images of the area shown in Fig. 3.4 a and d. (a) ε_{xx} and (b) ε_{yy} of Fig. 3.4a showing strain relaxed for the pillar-matrix interface with paired dislocations. (c) ε_{xx} and (d) ε_{yy} of Fig. 3.4d showing that compressive strain extends into the matrix on the side where misfit dislocations are missing (Fig. 3.4d, bottom right). This is not visible in the perpendicular direction because the misfit dislocations are paired (Fig. 3.4c).

Figure 3.7 (a) ADF image of the LSMO matrix area in a plan-view 70 mol%LSMO-30 mol%ZrO_2 sample. EELS spectrum image of (b) La-$M_{4,5}$ (integration window 821–868 eV), (c) Sr-$L_{2,3}$ (1935–2066 eV), (d) Mn-$L_{2,3}$ (627–678 eV), (e) Zr-$L_{2,3}$ (2218–2404 eV), and (f) O-K (520–578 eV).

Figure 3.8 (a) ADF image of a plan-view 70 mol%LSMO-30 mol%ZrO_2 sample. EELS spectrum line profile of areal density of (b) La-$M_{4,5}$ and Sr-$L_{2,3}$, and (c) Mn-$L_{2,3}$ and Zr-$L_{2,3}$ of the line drawn with identical integration windows to Fig. 3.7. The areal densities are normalized to the maximum value for each element.

Figure 3.9 (a) ADF image of a plan-view 70 mol%LSMO-30 mol%ZrO_2 sample at the pillar-matrix interface (matrix, left of the dotted line; pillar, right of the dotted line).

Atomic-resolution EELS spectrum image of areal density of (b) La-$M_{4,5}$, (c) Sr-$L_{2,3}$, (d) Mn-$L_{2,3}$, (e) Zr-$L_{2,3}$, and (f) O-K with identical integration windows to Fig. 3.7 of the pillar-matrix interface area shown in (a). The integrated line profiles of images (a) to (f) are shown in (g) to (l) respectively. The integrated areal density was normalized to the maximum value in each profile. The *x*-axis in (g) to (l) is the location axis as shown in (a), and the *y*-axis is the normalized intensity.

Figure 3.10 (a) Nonlinear Gaussian least square fitting on background subtracted Mn-L_3 edge of the two spectra from pillar and matrix region of the plan-view 70 mol%LSMO-30 mol%ZrO_2 sample; (b) same as Fig. 3.9a, clockwise rotated by 90^o; (c) Mn-L_3 peak positions obtained from Gaussian fitting of the background subtracted Mn-L_3 spectrum image recorded from the area in (b).

Figure 3.11 HREM image of the side-view sample of the LSMO specimen with 6 mol% ZrO_2. It already shows the formation of pillar.

Figure 4.1 (a) HAADF image of a plan-view 70 mol% LSMO-30 mol% ZrO_2 sample showing three ZrO_2 pillars connected by boundaries. (b) Magnified image of part of the boundary region shown in (a). (c) Temperature-colour view of the magenta frame region in (b) showing APB-1. (d) Temperature-colour view of the yellow frame region in (b) showing APB-2. (e) HAADF image of a plan-view 80 mol% LSMO-20 mol% ZrO_2 sample showing three ZrO_2 pillars connected by APB-3. (f) Temperature-colour view of the blue frame region in (e) showing APB-3.

Figure 4.2 (a) Side-view and (b) plan-view of the structure model of tetragonal LSMO.

Figure 4.3 HAADF image of the area from which the EELS-SI shown in Fig. 4.4 was taken (magenta rectangle).

Figure 4.4 (a) ADF image of the sample area including APB-1 and APB-2 in a plan-view 80 mol% LSMO-20 mol% ZrO_2 sample. EELS spectrum image of (b) La-$M_{4,5}$, (c) O-K, and (d) Mn-$L_{2,3}$. Background-subtracted (e) O-K and (f) Mn-$L_{2,3}$ EELS spectra from the APB region and the LSMO matrix region.

Figure 4.5 Simultaneously acquired HAADF image (a) and ABF image (b) of a region including APB-1 and APB-2 of the plan-view 80 mol% LSMO-20 mol% ZrO2 sample. Line profiles along the blue line in (c) the HAADF image and (d) the ABF image and along the magenta line in (e) the HAADF image and (f) the ABF image. The line profiles are integrated along the vertical direction over 5 pixels.

Figure 4.6 Simultaneously acquired HAADF image (a) and ABF image (b) of a region including APB-3 of a plan-view 80 mol% LSMO-20 mol% ZrO_2 sample. Line profiles along the magenta lines in the HAADF image (c) and the ABF image (d) and along the blue lines in the HAADF image (e) and the ABF image (f). The line profiles are integrated along the direction vertical to the line over 5 pixels.

Figure 4.7 (a) HAADF image of a sample region including APB-1 and APB-2, replica of Fig. 4.1a. Fourier-filtered images using 100 reflections (b) and 010 reflections (c) of the sample region in (a). (d) HAADF image of a sample region including APB-3, replica of Fig. 4.1e. Fourier-filtered images using 100 reflections (e) and 010 reflections (f) of the sample region in (d). Arrows in (a) and (d) represent the phase shift direction of the labelled side with respect to the other side of the APBs.

Figure 4.8 Illustration of the formation process of APB-1. (a) Starting structure model of LSMO viewing along <001> direction. (b) Phase shift of $\frac{1}{4}d_{110}$along {110} planes from (a). (c) Final structure model of APB-1 with atomic reconstructions from (b).

Figure 4.9 Illustration of the formation process of APB-2. (a) Starting structure model of LSMO viewing along <001> direction. (b) Phase shift of $\frac{1}{4}d_{110}$ along {310} planes from (a). (c) Final structure model of APB-2 with atomic reconstructions from (b).

Figure 4.10 Illustration of the formation process of APB-3. (a) Starting structure model of LSMO viewing along <001> direction. (b) Phase shift of $\frac{1}{2}d_{110}$along {310} planes from (a). (c) Final structure model of APB-3 atomic reconstructions from (b).

Figure 4.11 Illustration of the plane components in boundary planes in sequence of (a) APB-2 and (b) APB-3.

Figure 5.1 HAADF image of a plan-view 80 mol% LSMO-20 mol% ZrO_2 sample showing APB-1 and APB-2 (a) before and (b) after electron-beam-induced reconstructions, and APB-3 (c) before and (d) after electron-beam-induced reconstructions.

Figure 5.2 Lower magnification HAADF images of the area shown in (a) Fig. 5.1a and (b) Fig. 5.1b, respectively.

Figure 5.3 (a) ADF image of the APB-1 area in Fig. 5.1b in a plan-view 80 mol% LSMO-20 mol% ZrO_2 sample. EELS spectrum image of (b) O-K, (c) La-$M_{4,5}$, and (d) Mn-$L_{2,3}$. (e) Mn-L_3 peak positions obtained from Gaussian fitting of the background-subtracted Mn-L_3 spectrum image.

Figure 5.4 (a) ADF image of the APB-2 area in Fig. 5.1b in a plan-view 80 mol% LSMO-20 mol% ZrO_2 sample. EELS spectrum image of (b) O-K, (c) La-$M_{4,5}$, and (d) Mn-$L_{2,3}$. (e) Overlay of EELS spectrum image of La-$M_{4,5}$ in green and Mn-$L_{2,3}$ in red. (f) Mn-L_3 peak positions obtained from Gaussian fitting of the background subtracted Mn-L_3 spectrum image.

Figure 5.5 (a) HAADF image of the APB-3 area in a plan-view 80 mol% LSMO-20 mol% ZrO_2 sample, same as presented in Fig. 5.1d but rotated counterclockwise for about 45 degree. (b) ADF image of the sample area labeled by the yellow frame in (a). EELS spectrum image of (c) O-K, (d) La-$M_{4,5}$, and (e) Mn-$L_{2,3}$. (f) Overlay of EELS spectrum image of La-$M_{4,5}$ in green and Mn-$L_{2,3}$ in red. (g) Mn-L_3 peak positions obtained from Gaussian fitting of the background subtracted Mn-L_3 spectrum image.

Figure 5.6 Comparison of (a) O-K and (b) Mn-$L_{2,3}$ near-edge fine structures from the APB region before electron beam modification (labeled by "APB before"), the APB region after electron beam modification (labeled by "APB") and the LSMO matrix region near the APB walls after electron beam modification (labeled by "LSMO").

Figure 5.7 (a) Starting structure model of APB-1, as derived in chapter 4. Possible structure of APB-1 after electron beam modifications (b) non-presence and (c) presence of oxygen columns between B'-sites inside the APB. Simultaneously acquired (d) HAADF image and (e) ABF image of a region including APB-1 after electron beam illumination of the plan-view 80 mol% LSMO-20 mol% ZrO_2 sample. Line profiles along the blue line in (f) the HAADF image and (g) the ABF image. The line profiles are integrated along the horizontal direction for 3 pixels. The magenta lines are drawn to help identifying the APB walls and thus confirm the structure of APB-1 after electron-beam-modification, as shown in Fig. 5.8.

Figure 5.8 Lower-magnification HAADF image of APB-1including the sample area shown in Fig. 5.7d and 5.7e before (a) and after (b) electron-beam-induced reconstructions. The magenta lines cross the same atomic columns as the magenta lines in Fig. 5.7.

Figure 5.9 (a) Starting structure model of APB-2, as derived in Chapter 4. (b) Structure model of APB-2 after electron beam modifications.

Figure 5.10 (a) Starting structure model of APB-3, as derived in chapter 4. Possible structure of APB-3 after electron beam modifications (b) non-presence and (c) presence of oxygen columns between B'-sites along the <110> direction inside the APB. Simultaneously acquired (d) HAADF image and (e) ABF image of a region including

APB-3 after electron beam illumination of the plan-view 80 mol% LSMO-20 mol% ZrO_2 sample. Line profiles are shown along the magenta line in (f) the HAADF image and (g) the ABF image and along the blue line in (h) the HAADF image and (i) the ABF image. The line profiles are integrated along the vertical direction for 3 pixels.

Figure 5.11 Mn occupancy of APB-3 measured from the time-series HAADF images during reconstructions.

Figure 5.12 Illustration of the plane components in boundary planes in sequence of (a) APB-2 and (b) APB-3.

Figure 6.1 Structure models of cubic ZrO_2 viewed along (a) the [811] direction and (b) the [001] axis.

Figure 6.2 HAADF image of a plane-view 20 mol% ZrO_2-80 mol%LSMO sample. Inserted is the structure model of cubic ZrO_2 unit cell viewed along the [001] direction.

Figure 6.3 (a) Situation without specimen tilt. Illustrations of the three options to model the tilt between electron beam and specimen in STEMsim: (b) tilt of the whole crystal tilt, (c) tilt of the electron beam and (d) tilt via the propagator.

Figure 6.4 Comparison of deviations with different spherical aberration and the other aberration coefficients listed in Table 2.1.

Figure 6.5 The PACBED patterns of the whole sample region shown in Fig. 1 under conditions of (a) tilt 1, (d) tilt 2 and (g) tilt 3. The HAADF images of the ZrO2 sample region inside the square box shown in Fig. 6.2 under the conditions of (b) tilt 1, (e) tilt 2 and (h) tilt 3. ABF images of the same sample region as the HAADF images under the conditions of (c) tilt 1, (f) tilt 2 and (i) tilt 3. The red circles in (b,e,h) indicate the fitted maxima corresponding to the Zr positions, the green crosses in (b-i) indicate the fitted minima in (c,f,i) corresponding to the Zr positions, and the yellow crosses in (b-i) indicate the fitted minima in (c,f,i) corresponding to the O positions.

Figure 6.6 Simulated deviations of the minima positions of (a) Zr and (b) O in ABF imaging from true positions, simulated deviations of the maxima positions of (c) Zr and (d) O in HAADF imaging from true positions, and relative shift of the minima positions in ABF images to the maxima positions in HAADF images of Zr (e) and O (f) as a function of sample thickness.

Figure 6.7 Collection angle dependence of the deviation in ABF imaging with 5 mrad orientation deviation along the shift direction of the Laue circle center for (a) Zr and (b) O

using a convergence semi-angle of 20.4 mrad in the simulation. Convergence angle dependence of the deviation in ABF imaging with 5 mrad orientation deviation along the shift direction of the Laue circle center for (c) Zr and (d) O using a collection semi-angle of 19 to 20 mrad.

Figure 6.8 Collection angle dependence of the deviation in HAADF imaging with 5 mrad orientation deviation along the shift direction of the Laue circle center for (a) Zr and (b) O when the convergence semi-angle of 20.4 mrad was used in simulation. Convergence angle dependence of the deviation in HAADF imaging with 5 mrad orientation deviation along the shift direction of the Laue circle center for (c) Zr and (d) O when a collection semi-angle of 71 to 99 mrad was used in simulation.

Figure 6.9 The deviation of the minima positions in ABF images of (a) Zr and (b) O for different tilting angles indicated by Δθ in the figures. The convergence semi-angle is 20.4 mrad and the collection semi-angle range is 11-23 mrad. (c,d) Comparison of the deviation from linearity at 3, 5, and 10 mrad tilt with 1 mrad tilt by looking at the differences between the larger angle tilts and the 1-mrad tilt multiplied by factors of 3, 5, and 10.

Figure 6.10 The deviation of maxima positions in HAADF images of (a) Zr and (b) O for different tilt angles indicated by Δθ in the figures. The convergence semi-angle is 20.4 mrad and the collection semi-angle is 71-75 mrad.

Figure 6.11 (a) Structure model of cubic ZrO_2 viewed along the [001] direction. (b) Projected angle between two neighboring Zr atoms and one O atom $\angle Zr(1)OZr(2)$ shown in (a) when the crystal is tilted by 5 mrad along the [100]-direction with the convergence semi-angles and collection semi-angles as indicated in the figure.

Figure 6.12 (a) HAADF image of a sample area including APB-1 and APB-2 presented in chapter 4. Replica of Fig. 4.5 with a larger LSMO area included. Cut of LSMO region on the (b) left side and (c) right side of APB-1, and (d) left side and (e) right side of APB-2. These cuts are overlapped with maxima and minima positions from simultaneously acquired HAADF and ABF images, similar to the process presented in Fig. 6.5.

Figure 6.13 Further results about convergence angle dependence of deviation along the Laue circle center shift direction of 5 mrad for (a) and (c) Zr and (b) and (d) O when the collection semi-angle of 23 to 24 mrad and 25 to 26 mrad respectively were used in the simulations with convergence semi-angle indicated in the figures.

Figure 6.14 Visualization of the effect of sample tilt, where $\Delta\theta$ is the sample tilt with the shift vector of the Laue circle center parallel to the horizontal direction, on the variation of

the maxima / minima positions in simulated HAADF (71-99 mrad)/ABF (12-20 mrad) images of cubic ZrO_2 (see structure in Fig. 6.1) for different thicknesses. The convergence semi-angle is 20.4 mrad.

Figure 6.15 Comparison of the deviation values obtained from the FL approximation and AP multisclice method for (a, c) Zr and (b, d) O. (a, b) are for the minima position deviations in ABF imaging and (c, d) are for the maxima position deviations in HAADF imaging.

Figure 6.16 Comparison of the deviation values obtained from FL approximations with 0-123 mrad ('FL', the size of reciprocal space applied in this chapter) and 0-246 mrad ('FL,2', double the size of reciprocal space applied in this chapter) for (a, c) Zr and (b, d) O. (a, b) are for the minima position deviations in ABF imaging and (c, d) are for the maxima position deviations in HAADF imaging.

Figure 6.17 Comparison of the deviation values obtained from the FL approximations with 0.99 mrad/pixel ('FL', the spatial resolution of reciprocal space applied in this chapter) and 0.5 mrad/pixel mrad ('FL,0.5δk', half the spatial resolution of reciprocal space applied in this chapter by double the number of pixels per unit cell) for (a) ABF and (b) HAADF for O.

Figure 6.18 Condenser lens aperture is 10 um which gives a convergence semi-angle of 7.3 mrad. This smaller CL aperture compared to the experimentally applied value gives more separate diffraction disks and make the work easier. Diffraction spots marked by blue circles correspond to the adjacent Zr or La/Sr sites. This is labeled out in diffraction spots in DP by the yellow solid line which is the tangent to the symmetric two blue circles and yellow dashed line in HAADF STEM image. Moving the solid yellow line to the STEM image shows this mismatch of about 7 degree.

Figure 6.19 Condenser lens aperture is 40 um which gives a convergence semi-angle of 28 mrad. This larger CL aperture is the experimentally applied value and gives quite overlapping diffraction disks. Much care is needed to label out each diffraction spot. Diffraction spots marked by blue circles correspond to the adjacent Zr or La/Sr sites. This is labeled out in diffraction spots in DP by the yellow solid line which is tangent to the symmetric two blue circles and yellow dashed line in HAADF STEM image. Moving the solid yellow line to the STEM image shows this mismatch of about 3 degree.

Figure 6.20 In STEMsim, (a) 0 mrad tilt, (b) positive amount of tilt parallel to the *x*-direction, and (c) negative amount of tilt parallel to the *x*-direction.

Figure 6.21 The corresponding Ewald sphere tilted to the tilt situations presented in Fig. 6.20. The ZOLZ is the zero order Laue zone, the FOLZ is the first order Laue zone, and the SOLZ is the second order Laue zone.

Figure 6.22 The difference between simulated deviation length and the value calculated from $\frac{1}{2}t * \Delta\,\theta$, i.e. $\Delta d_{simulated} - \Delta d_{WPO}$, with the thickness value from 0 to 20 nm for (a,c) Zr and (b, d) O. The convergence semiangles are indicated on the left and the collection semi-angles are indicated in the figures.

Figure 6.23 (a) Calculated incident electron wave phase map in reciprocal space with experimentally measured aberration coefficients listed in Table 6.3. (b) Comparison of the relative shift of O, between minima positions in ABF (collection semiangle of 11-23 mrad) imaging and maxima positions in HAADF (collection semiangle of 71-99 mrad) imaging, with and without experimental aberrations listed in Table 6.3 for different amounts of specimen tilt. For (a) and (b), the applied convergence semiangle is 20.4 mrad.

Figure 6.24 (a) Structure model of a ZrO_2-MnO_2 interface supercell. (b) Deviation of minima positions corresponding to the red arrow marked O (in (a)) in ABF images from their true positions. The convergence and collection semi-angles are indicated in the figure.

Figure 7.1 Set-up of the structure model of $LiFePO_4$ with different Li concentrations randomly distributed along the electron beam propagation direction. All other colors besides green (O) and black (Fe and P)in the structure model represent Li in different concentrations as indicated. The line scan is performed along the vertical direction at the center of the cell.

Figure 7.2 Simulation results on the visualization of lithium in $LiFePO_4$ with ADF and ABF imaging.

Figure 7.3 Comparison of the sensitivity of fractional intensity with varying lithium concentration between (a) quasi-vacuum position and (b) lithium position. Convergence semi-angle is 22 mrad and outer collection angle is also 22 mrad while the inner collection angle is as indicated in the inner angle axis. Note the independence of the fractional intensity on Li concentration in (a).

Figure 7.4 Contrast of lithium as a function of thickness (*z*-axis), lithium concentration (*x*-axis), and collection angle (*y*-axis). (a) Constant β_{out} (22 mrad) and (b) constant β_{in} (11 mrad).

Figure 7.5 Contrast variation of lithium with thickness (*y*-axis), lithium concentration (*x*-axis) and defocus (labelled on the top right) with constant β_{in} (11 mrad), β_{out} (22 mrad), and C_s (0 mm).

Figure 8.1 Reprint from [163]. (a) O-K and (b) Fe-$L_{2,3}$ core-loss EELS spectra from $LiFePO_4$ (black) and Li_xFePO_4 (x<<1) (gray) powders.

Figure 8.2 (a) BF STEM image of a particle with a particle size of about 85 nm. EELS spectra of (b) O-K and (c) Fe-$L_{2,3}$ edges from 3 sample areas marked in (a). The O-K edge is normalized to the main peak intensity and the Fe $L_{2,3}$ edges are normalized to the L_3 peak intensity.

Figure 8.3 (a) HAADF STEM image of a particle with~150 nm diameter. EELS spectra of (b) O-K and (c) Fe-$L_{2,3}$ edges from 3 sample areas in the particle marked by "a", "b" and "c" in (a). The O-K edge is normalized to the main peak intensity and the Fe-$L_{2,3}$ edges are normalized to the L_3 peak intensity.

Figure 8.4 Reprint from [163]. Low-loss spectrum comparison of delithiated (FPO) and lithiated (LFPO) samples.

Figure 8.5 Delocalization (d_{50}) as a function of the energy loss calculated using the method of Egerton (2003) [169].

Figure 8.6 Calculated low-loss spectra of (a) FPO and (b) LFPO at different distances from the sample edge as indicated in the figures. (c) Illustration of the set-up for theoretical calculations. (d) Volume plasmon-peak positions for FPO and LFPO at different distances from the edge.

Figure 8.7 Volumn plasmon (VP) peak position and Fe-$M_{2,3}$ edge peak position of nanocrystals with size of (a) 25 nm (b) 70 nm (c) 150 nm. For the Fe-$M_{2,3}$ edge, '0' means it is not detected at this position. The two magenta lines are used to indicate (left) when the electron beam enters the material, i.e. Fe-$M_{2,3}$ edge shows up, and (right) when the delocalization effect can be neglected for correlating the plasmon peak shift with the LFPO/FPO phase change.

Curriculum vitae

Personal details

Name: Dan Zhou

Date of birth: 04. October 1986

Place of birth: Jiangsu, China

Marital status: Single

Nationality: China

Education:

Ph. D student in Physics (Feb. 2012 – present)

Stuttgart Center for **E**lectron **M**icroscopy (StEM)

Max Planck Institute for Intelligent Systems (Feb. 2012 – Mar. 2015), and then Max Planck Institute for Solid State Research (Apr. 2015 – present)

Stuttgart, Germany

Supervisor: Prof. Dr. Peter A. van Aken, Dr. Wilfried Sigle

M. Sc. Research in Physics (Sep. 2009 **–** Dec. 2011)

School of Physics, Trinity College Dublin (The University of Dublin), Dublin, Ireland

Supervisor: Prof. Dr. Hongzhou Zhang

B. Sc. (Honors) in Physics (Sep. 2004 **–** Jun. 2008)

Department of Applied Physics, School of Science, Beijing University of Aeronautics & Astronautics, Beijing, P.R. China

Honors and Awards

1. Microscopy & Microanalysis (M&M) 2015 Best Poster Award 1st place in Physical Science, August 2-6, 2015, Portland, OR, USA
2. International Federation of Societies for Microscopy (IFSM) School Young Scientist Award, Pre-school of 18th IMC, September 6-7, 2014, Prague, Czech Republic
3. Microscopy & Microanalysis (M&M) 2014 Presidential Scholar award , August 3-7, 2014, Hartford, CT, USA

4. European Materials Research Society Young Scientist Award, 2014 E-MRS Spring Meeting, May 26-30, Lille, France
5. The Excellent Graduation Dissertation of Beijing University of Aeronautics & Astronautics 2008

Research Grants

1. 2015.1.1-2015.12.31

   Max Planck Institute for Intelligent System Grassroots project: Quantitative information extraction from annular bright field (ABF) scanning transmission electron microscopy (STEM) images

   Amount: €15,000

   Researchers: ***Dan Zhou*** (StEM -- IS Stuttgart), Wilfried Sigle (StEM -- IS Stuttgart), Michael Hirsch (Empirical Interference -- IS Tübingen), Peter A. van Aken (StEM -- IS Stuttgart)

   *This project stopped on 1st April 2015 due to the transfer of StEM group from Max Planck Institute for Intelligent Systems to Max Planck Institute for Solid State Research. Therefore, the actual funded money is €5000.

2. 2014.1.1-2014.12.31

   Max Planck Institute for Intelligent System Grassroots project: Quantitative information extraction from annular bright field (ABF) scanning transmission electron microscopy (STEM) images

   Amount: €20,000

   Researchers: ***Dan Zhou*** (StEM -- IS Stuttgart), Wilfried Sigle (StEM -- IS Stuttgart), Stefan Harmeling (Empirical Interference -- IS Tübingen), Peter A. van Aken (StEM -- IS Stuttgart)

Workshops attended

1. StEM Ringberg Workshop, July 15-17, 2015, Ringberg Castle, Lake Tegernsee, Bavaria, Germany
2. The International Workshop on Advanced and In-situ Microscopes of Functional Nanomaterials and Devices (IAM Nano), July 8-10, 2015, Hotel Riverside, Hamburg, Germany

3. StEM Ringberg Workshop, July 2-4, 2014, Ringberg Castle, Lake Tegernsee, Bavaria, Germany
4. European Workshop on Spatially-resolved electron spectroscopy & Three country workshop meeting on EELS & EFTEM, April 23-25, 2014, Graz, Austria
5. European School on Advanced TEM Sample Preparation Workshop, December 2-6, 2013, Stuttgart, Germany
6. Quantitative Electron Microscopy 3rd edition, May, 2013, Saint-Aygulf, France
7. International Workshop on Computational Methods in Transmission Electron Microscopy, January 23-26, 2013, Ringberg Castle, Lake Tegernsee, Bavaria, Germany
8. SuperSTEM 5th summer school 2012, Manchester, UK
9. StEM Workshop on Advanced Transmission Electron Microscopy Techniques, July 11-13, 2012, Ringberg Castle, Lake Tegernsee, Bavaria, Germany
10. EMAT winter workshop on transmission electron microscopy, January, 2011, EELS group, Antwerp, Belgium

Scholarships

1. International Microscopy Congress (IMC) European Scholarship (€400), 18th International Microscopy Congress, September 7-12, 2014, Prague, Czech Republic
2. Deutsche Gesellschaft Für Elektronenmikroskopie (DGE, German Society for Electron Microscopy) Travel Scholarship (€700) for attending 18th International Microscopy Congress, September 7-12, 2014, Prague, Czech Republic
3. Graduate assistantships (conference fee waivers) from Symposium E, Defect induced effect in Nanomaterials, of 2014 E-MRS Spring Meeting, May 26-30, Lille, France
4. Scholarship from European Microscopy Society (EMS) of €250 for attending Microscopy Conference (MC), August 25-30, 2013, Regensburg, Germany
5. Student travel bursary award for €500 from Microscopy Society of Ireland enabling attending EMAT Winter Workshop on Transmission Electron Microscopy, January, 2011

Publications

Articles:

1. ***D.Zhou***, K. Müller-Caspary, W. Sigle, F. F. Krause, A. Rosenauer, P. A. van Aken, Sample tilt effects on atom column position determination in ABF-STEM imaging, Ultramicroscopy 160, 110-117, 2016.

2. ***D. Zhou,*** W. Sigle, M. Kelsch, H. U. Habermeier, P.A. van Aken, Linking atomic structure and local chemistry at manganese-segregated antiphase boundaries in ZrO_2-$La_{2/3}Sr_{1/3}MnO_3$ thin films, Advanced Materials Interfaces 2, 1500377, 2015.

3. ***D. Zhou***, W. Sigle, E. Okunishi, Y. Wang, M. Kelsch, H. Habermeier, P.A. van Aken, Interfacial chemistry and atomic arrangement of ZrO_2-$La_{2/3}Sr_{1/3}MnO_3$ pillar-matrix structures, APL Materials, 12/2014, 2(12), 127301.

4. ***D.Zhou***, X. Su, M. Boese, R. Wang, H. Zhang, $Ni(OH)_2$@$Co(OH)_2$ hollow nanohexagons: controllable systhesis, facet selected competitive growth and capacitance property, Nano Energy 5, 52-59, 2014.

5. T. Tao, Y. Chen, ***D. Zhou***, H. Zhang, S. Liu, R. Amal, N. Sharma, A. Glushenkov, Expanding the Applications of the Ilmenite Mineral to the Preparation of Nanostructures: TiO2 Nanorods and their Photocatalytic Properties in the Degradation of Oxalic Acid, Chemistry-A European Journal 19(3), 1091–1096, 2013.

6. G. Behan, ***D. Zhou***, M. Boese, R. Wang, H. Zhang, An investigation of nickel cobalt oxide nanorings using transmission electron, scanning electron and helium ion microscopy, Journal of Nanoscience and Nanotechnology, 12(2), 1094-1098, 2012

7. ***D. Zhou***, M. Boese, R. Wang, H. Zhang, Synthesis and self-assembly of ultrathin NixFe1-x(OH)2 nanodiscs via a wet-chemistry method, Journal of Nanoscience and Nanotechnology, 11(12), 11028-11031, 2011

8. D. Fox, A. O'Neill, ***D. Zhou***, M. Boese, J. Coleman, H. Zhang, Nitrogen assisted etching og graphene layers in a scanning electron microscope, Applied Physics Letters 98 (24), 243117, 2011.

9. T. Tao, A. Glushenkov, Q. Chen, H. Hu, ***D. Zhou***, H. Zhang, M. Boese, S. Liu, R. Amal, Y. Chen, Porous TiO_2 with a controllable bimodal pore size distribution from natural ilmenite, CrystEngComm 13 (5), 1322-1327, 2011

10. T. Tao, A. Glushenkov, C. Zhang, H. Zhang, ***D. Zhou***, Z. Guo, H. Liu, Q. Chen, H. Hu, Y. Chen, MoO_3 nanoparticles dispersed uniformly in carbon matrix: a high capacity composite anode for Li-ion batteries, Journal of Materials Chemistry 21 (25), 9350-9355, 2011

Proceedings

1. ***D. Zhou,*** W. Sigle, M. Kelsch, H. U. Habermeier, P.A. van Aken, Manganese segregation at antiphase boundaries connecting ZrO2 pillars in ZrO_2-$La_{2/3}Sr_{1/3}MnO_3$ pillar-matrix structures, Microscopy & Microanalysis (M&M), 08/2015, 21(S3), 2067-2068.
2. Y. Wang, W. Sigle, ***D. Zhou***, F. Baiutti, G. Logvenov, G. Gregori, G. Gregori, J. Maier, P. A. van Aken, Atomic-scale quantitative and analytical STEM investigation of Sr-δ-doped La_2CuO_4 multilayers, Microscopy & Microanalysis (M&M), 08/2015, 21(S3), 2071-2072.
3. ***D. Zhou,*** W. Sigle, Y. Wang, M. Kelsch, Y. Gao, H.U. Habermeier, P.A. van Aken, Chemical and defect analysis in a ZrO_2/LSMO pillar-matrix system, Microscopy and Microanalysis, 08/2014, 20(S3), 1040-1041.
4. ***D. Zhou***, R. Wang, M. Boese, H. Zhang, Synthesis and self-assembly of ultrathin ß-nickel hydroxide nanodisks via a wet-chemistry method, Nanoelectronics Conference (INEC), 2010 3rd International, 1264-1265, 2010.

Oral presentations

Invited

1. ***D. Zhou***, Atomic-resolution TEM studies of pillar-matrix structures in ZrO_2-$La_{2/3}Sr_{1/3}MnO_3$ films, Invited talk in Prof. Lin Gu's Group, April 28, 2015, Institute of Physics, Chinese Academy of Sciences, Beijing, China
2. ***D. Zhou***, W. Sigle, Y, Wang, H. U. Habermeier, P.A. van Aken (invited, presenting author), Interfacial chemistry and atomic arrangement of ZrO_2/LSMO pillar-matrix structures, Electronic Materials and Applications (EMA) 2015, January 21-23, 2015, Orlando, Florida, USA

Contributed

1. ***D. Zhou,*** W. Sigle, M. Kelsch, H.U. Habermeier, P.A. van Aken, Chemistry and structure of antiphase boundaries connecting ZrO_2 pillars in ZrO_2-$La_{2/3}Sr_{1/3}MnO_3$ pillar-matrix structures, European Congress and Exhibition on Advanced Materials and Processes (EUROMAT), September 20-24, 2015, Warsaw, Poland

2. Y. Wang, W. Sigle, ***D. Zhou***, F. Baiutti, G. Logvenov, G. Gregori, G. Gregori, J. Maier, P. A. van Aken, Atomic-scale quantitative and analytical STEM investigation of Sr-δ-doped La_2CuO_4 multilayers, Microscopy & Microanalysis (M&M), August 2-6, 2015, Portland, OR, USA

3. ***D. Zhou,*** W. Sigle, Y. Wang, M. Kelsch, H.U. Habermeier, P.A. van Aken, Chemical and defect analysis in a ZrO_2/LSMO pillar-matrix system, Microscopy & Microanalysis (M&M), August 3-7, 2014, Hartford, CT, USA

4. ***D. Zhou***, Atomic-resolution TEM studies of pillar-matrix structures in ZrO_2-$La_{2/3}Sr_{1/3}MnO_3$ films, July 2-4, 2014, StEM Workshop at Ringberg Castle, Lake Tegernsee, Bavaria, Germany

5. ***D. Zhou***, Y. Wang, W. Sigle, M. Kelsch, Y. Gao, H.U. Habermeier, P. A. van Aken, Elemental and strain analysis of a $La_{2/3}Sr_{1/3}MnO_3/ZrO_2$ system, E-MRS 2014 Spring Meeting, May 26-30, 2014, Congress Center, Lille, France

6. ***D. Zhou***, Imaging light atoms with aberration corrected transmission electron microscopy – delithiation process study of $LiFePO_4$, StEM Workshop on Advanced Transmission Electron Microscopy Techniques, July 11-13, 2012, Ringberg Castle, Lake Tegernsee, Bavaria, Germany

7. D. Fox, Y. Chen, ***D. Zhou***, C. Faulkner, H. Zhang, Ultra high quality TEM lamella preparation by helium ion microscopy, Microscopy Society of Ireland Annual Symposium, August 24-26, 2011, CRANN, Dublin, Ireland

8. ***D. Zhou***, C. Dickinson, R. Wang, H. Zhang, Facet-selective growth of Ni/Co monoxide hexagonal nanorings, Microscopy Society of Ireland Annual Symposium, August 24-26, 2011, CRANN, Dublin, Ireland

9. ***D. Zhou***, G. Behan, M. Boese, H. Zhang, Sythesis and chracterization of Ni-Co nanostructures, Joint Microscopical Society of Ireland and Northern Ireland Biomedical Engineering Society Annual Symposium, August 25-27, 2010, Belfast, Northern Ireland, UK

Poster presentations

1. ***D. Zhou***, W. Sigle, M. Kelsch, H. U. Habermeier, P.A. van Aken, Atomic arrangment at antiphase boundaries connecting ZrO_2 pillars in ZrO_2-$La_{2/3}Sr_{1/3}MnO_3$ pillar-matrix structures, Microscopy Conference (MC), September 6-11, 2015, Göttingen, Germany
2. ***D. Zhou***, K. Müller-Caspary, W. Sigle, F. F. Krause, A. Rosenauer, P. A. van Aken, Effects of small sample tilt on atom column position determination in ABF-STEM imaging, Microscopy Conference (MC), September 6-11, 2015, Göttingen, Germany
3. ***D. Zhou,*** W. Sigle, M. Kelsch, H. U. Habermeier, P.A. van Aken, Manganese segregation at antiphase boundaries connecting ZrO2 pillars in ZrO_2-$La_{2/3}Sr_{1/3}MnO_3$ pillar-matrix structures, Microscopy & Microanalysis (M&M), August 2-6, 2015, Portland, OR, USA
4. ***D. Zhou***, W. Sigle, Y. Wang, M. Kelsch, H.U. Habermeier, P.A. van Aken, Chemical and defect analysis in a ZrO_2/LSMO pillar-matrix system, 18^{th} International Microscopy Congress (IMC), September 7-12, 2014, Prague, Czech, Republic
5. ***D. Zhou***, W. Sigle, K. Müller, A. Rosenauer, C. Zhu, M. Kelsch, J. Maier, P.A. van Aken, Contrast investigation of annular bright-field imaging in scanning transmission electron microscopy of $LiFePO_4$, 18^{th} International Microscopy Congress (IMC), September 7-12, 2014, Prague, Czech, Republic
6. ***D. Zhou***, W.Sigle, A. Rosenauer, P.A. van Aken, Study of annular bright-field imaging of light elements in scanning transmission electron microscopy by computer simulation: case study of lithium in $LiFePO_4$, Microscopy Conference (MC) 2013, August 25-30, 2013, University of Regensburg, Regensburg, Germany
7. ***D. Zhou***, D. Fox, H. Zhang, EELS characterization of Si TEM lamella sample processed by helium ion microscopy, Microscopy Society of Ireland Annual Symposium, August 24-26, 2011, CRANN, Dublin, Ireland
8. ***D. Zhou***, G. Behan, M. Boese, M. Finneran, C. Faukner, D. Fox, H. Zhang, Synthesis and characterization of hexagonal Ni-Co nanorings, nanoweek, CRANN, 2010, Dublin, Ireland

Bibliography

1. M. Knoll, E. R., Beitrag zur geometrischen Elektronenoptik. **1932,** *12*, 607-661.
2. Haider, M.; Uhlemann, S.; Schwan, E.; Rose, H.; Kabius, B.; Urban, K., Electron microscopy image enhanced. *Nature* **1998,** *392* (6678), 768-769.
3. Dellby, N.; Krivanek, O. L.; Nellist, P. D.; Batson, P. E.; Lupini, A. R., Progress in aberration-corrected scanning transmission electron microscopy. *J Electron Microsc* **2001,** *50* (3), 177-185.
4. Jia, C. L.; Houben, L.; Thust, A.; Barthel, J., On the benefit of the negative-spherical-aberration imaging technique for quantitative HRTEM. *Ultramicroscopy* **2010,** *110* (5), 500-505.
5. Lentzen, M.; Jahnen, B.; Jia, C. L.; Thust, A.; Tillmann, K.; Urban, K., High-resolution imaging with an aberration-corrected transmission electron microscope. *Ultramicroscopy* **2002,** *92* (3-4), 233-242.
6. Allen, L. J.; Findlay, S. D.; Lupini, A. R.; Oxley, M. P.; Pennycook, S. J., Atomic-resolution electron energy loss spectroscopy imaging in aberration corrected scanning transmission electron microscopy. *Phys Rev Lett* **2003,** *91* (10).
7. Tanaka, N.; Yamasaki, J.; Kawai, T.; Pan, H. Y., The first observation of carbon nanotubes by spherical aberration corrected high-resolution transmission electron microscopy. *Nanotechnology* **2004,** *15* (12), 1779-1784.
8. Ward, E. P. W.; Arslan, I.; Midgley, P. A.; Bleloch, A.; Thomas, J. M., Direct visualisation, by aberration-corrected electron microscopy, of the crystallisation of bimetallic nanoparticle catalysts. *Chem Commun* **2005,** (46), 5805-5807.
9. Evans, J. E.; Hetherington, C.; Kirkland, A.; Chang, L. Y.; Stahlberg, H.; Browning, N., Low-dose aberration corrected cryo-electron microscopy of organic specimens. *Ultramicroscopy* **2008,** *108* (12), 1636-1644.
10. Kirkland, A. I.; Nellist, P. D.; Chang, L. Y.; Haigh, S. J., Aberration-Corrected Imaging in Conventional Transmission Electron Microscopy and Scanning Transmission Electron Microscopy. *Advances in Imaging and Electron Physics, Vol 153* **2008,** *153*, 283-325.
11. Urban, K. W., Studying atomic structures by aberration-corrected transmission electron microscopy. *Science* **2008,** *321* (5888), 506-510.

12. Hansen, T. W.; Wagner, J. B.; Dunin-Borkowski, R. E., Aberration corrected and monochromated environmental transmission electron microscopy: challenges and prospects for materials science. *Mater Sci Tech-Lond* **2010,** *26* (11), 1338-1344.
13. Stephen J. Pennycook, P. D. N., *Scanning transmission electron microscopy, imaging and analysis*. Springer: 2011.
14. Brydson, R., *Aberration-corrected analytical transmission electron microscopy*. Wiley: 2011.
15. Sasaki, T.; Sawada, H.; Okunishi, E.; Hosokawa, F.; Kaneyama, T.; Kondo, Y.; Kimoto, K.; Suenaga, K., Evaluation of probe size in STEM imaging at 30 and 60 kV. *Micron* **2012,** *43* (4), 551-556.
16. Haider, M.; Uhlemann, S.; Zach, J., Upper limits for the residual aberrations of a high-resolution aberration-corrected STEM. *Ultramicroscopy* **2000,** *81* (3-4), 163-175.
17. David B. Williams, C. B. C., *Transmission electron microscopy, a textbook for material science*. 2nd ed.; Springer: 2009.
18. Voronin, Y. M.; Mokhnatk.Av; Khaitlin.Ry, Reconstruction of Electron-Microscopic Images, According to Focal Series Method. *Izv an Sssr Fiz+* **1974,** *38* (7), 1382-&.
19. Klingstedt, M.; Sundberg, M.; Eriksson, L.; Haigh, S.; Kirkland, A.; Gruner, D.; De Backer, A.; Van Aert, S.; Terasaki, O., Exit wave reconstruction from focal series of HRTEM images, single crystal XRD and total energy studies on SbxWO3+y (x similar to 0.11). *Z Kristallogr* **2012,** *227* (6), 341-349.
20. Buist, A. H.; Miedema, M. A. O.; Vandenbos, A., Parameters in exit wave reconstruction from focal series in TEM. *Electron Microscopy 1994, Vol 1* **1994**, 469-470.
21. Buist, A. H.; vandenBos, A.; Miedema, M. A. O., Optimal experimental design for exit wave reconstruction from focal series in TEM. *Ultramicroscopy* **1996,** *64* (1-4), 137-152.
22. Thust, A.; Rosenfeld, R., State of the art of focal-series reconstruction in HRTEM. *Electron Microscopy 1998, Vol 1* **1998**, 119-120.
23. Kubel, C.; Thust, A., TrueImage - A sofhvare package for focal-series reconstruction in BRTEM. *Nato Sci Ser Ii-Math* **2006,** *211*, 373-392.
24. Lichte, H., Electron Holography Approaching Atomic Resolution. *Ultramicroscopy* **1986,** *20* (3), 293-304.
25. Jia, C. L.; Lentzen, M.; Urban, K., Atomic-resolution imaging of oxygen in perovskite ceramics. *Science* **2003,** *299* (5608), 870-873.

26. Krumeich, F.; Muller, E.; Wepf, R. A., Phase-contrast imaging in aberration-corrected scanning transmission electron microscopy. *Micron* **2013,** *49*, 1-14.
27. Sader, K.; Brown, A.; Brydson, R.; Bleloch, A., Quantitative analysis of image contrast in phase contrast STEM for low dose imaging. *Ultramicroscopy* **2010,** *110* (10), 1324-1331.
28. Ohtsuka, M.; Yamazaki, T.; Kotaka, Y.; Hashimoto, I.; Watanabe, K., Imaging of light and heavy atomic columns by spherical aberration corrected middle-angle bright-field STEM. *Ultramicroscopy* **2012,** *120*, 48-55.
29. Kotaka, Y., Direct visualization method of the atomic structure of light and heavy atoms with double-detector Cs-corrected scanning transmission electron microscopy *Appl Phys Lett* **2012**.
30. Shibata, N.; Findlay, S. D.; Kohno, Y.; Sawada, H.; Kondo, Y.; Ikuhara, Y., Differential phase-contrast microscopy at atomic resolution. *Nature Physics* **2012,** *8* (8), 611-615.
31. Findlay, S. D.; Shibata, N.; Sawada, H.; Okunishi, E.; Kondo, Y.; Yamamoto, T.; Ikuhara, Y., Robust atomic resolution imaging of light elements using scanning transmission electron microscopy. *Appl Phys Lett* **2009,** *95* (19).
32. Okunishi, E.; Ishikawa, I.; Sawada, H.; Hosokawa, F.; Hori, M.; Kondo, Y., Visualization of Light Elements at Ultrahigh Resolution by STEM Annular Bright Field Microscopy. *Microsc Microanal* **2009,** *15*, 164-165.
33. Shibata, N.; Kohno, Y.; Findlay, S. D.; Sawada, H.; Kondo, Y.; Ikuhara, Y., New area detector for atomic-resolution scanning transmission electron microscopy. *J Electron Microsc* **2010,** *59* (6), 473-479.
34. Yang, H.; Pennycook, T. J.; Nellist, P. D., Efficient phase contrast imaging in STEM using a pixelated detector. Part II: Optimisation of imaging conditions. *Ultramicroscopy* **2015,** *151*, 232-239.
35. Pennycook, T. J.; Lupini, A. R.; Yang, H.; Murfitt, M. F.; Jones, L.; Nellist, P. D., Efficient phase contrast imaging in STEM using a pixelated detector. Part 1: Experimental demonstration at atomic resolution. *Ultramicroscopy* **2015,** *151*, 160-167.
36. Ishikawa, R.; Okunishi, E.; Sawada, H.; Kondo, Y.; Hosokawa, F.; Abe, E., Direct imaging of hydrogen-atom columns in a crystal by annular bright-field electron microscopy. *Nat Mater* **2011,** *10* (4), 278-281.
37. Huang, R.; Ikuhara, Y., STEM characterization for lithium-ion battery cathode materials. *Curr Opin Solid St M* **2012,** *16* (1), 31-38.

38. Gu, L.; Zhu, C. B.; Li, H.; Yu, Y.; Li, C. L.; Tsukimoto, S.; Maier, J.; Ikuhara, Y., Direct Observation of Lithium Staging in Partially Delithiated LiFePO(4) at Atomic Resolution. *J Am Chem Soc* **2011,** *133* (13), 4661-4663.

39. Suo, L. M.; Han, W. Z.; Lu, X.; Gu, L.; Hu, Y. S.; Li, H.; Chen, D. F.; Chen, L. Q.; Tsukimoto, S.; Ikuhara, Y., Highly ordered staging structural interface between LiFePO4 and FePO4. *Phys Chem Chem Phys* **2012,** *14* (16), 5363-5367.

40. Zhang, Q. H.; Wang, L. J.; Wei, X. K.; Yu, R. C.; Gu, L.; Hirata, A.; Chen, M. W.; Jin, C. Q.; Yao, Y.; Wang, Y. G.; Duan, X. F., Direct observation of interlocked domain walls in hexagonal RMnO(3) (R = Tm, Lu). *Phys Rev B* **2012,** *85* (2).

41. Findlay, S. D.; Azuma, S.; Shibata, N.; Okunishi, E.; Ikuhara, Y., Direct oxygen imaging within a ceramic interface, with some observations upon the dark contrast at the grain boundary. *Ultramicroscopy* **2011,** *111* (4), 285-289.

42. Findlay, S. D.; Saito, T.; Shibata, N.; Sato, Y.; Matsuda, J.; Asano, K.; Akiba, E.; Hirayama, T.; Ikuhara, Y., Direct Imaging of Hydrogen within a Crystalline Environment. *Appl Phys Express* **2010,** *3* (11).

43. Findlay, S. D.; Shibata, N.; Sawada, H.; Okunishi, E.; Kondo, Y.; Ikuhara, Y., Dynamics of annular bright field imaging in scanning transmission electron microscopy. *Ultramicroscopy* **2010,** *110* (7), 903-923.

44. Huang, R.; Ding, H. C.; Liang, W. I.; Gao, Y. C.; Tang, X. D.; He, Q.; Duan, C. G.; Zhu, Z. Q.; Chu, J. H.; Fisher, C. A. J.; Hirayama, T.; Ikuhara, Y.; Chu, Y. H., Atomic-Scale Visualization of Polarization Pinning and Relaxation at Coherent BiFeO3/LaAlO3 Interfaces. *Adv Funct Mater* **2014,** *24* (6), 793-799.

45. Hwang, H. Y.; Iwasa, Y.; Kawasaki, M.; Keimer, B.; Nagaosa, N.; Tokura, Y., Emergent phenomena at oxide interfaces. *Nat Mater* **2012,** *11* (2), 103-113.

46. Chakhalian, J.; Millis, A. J.; Rondinelli, J., Whither the oxide interface. *Nat Mater* **2012,** *11* (2), 92-94.

47. Zubko, P.; Gariglio, S.; Gabay, M.; Ghosez, P.; Triscone, J. M., Interface Physics in Complex Oxide Heterostructures. *Annu Rev Conden Ma P* **2011,** *2*, 141-165.

48. Stemmer, S.; Allen, S. J., Two-Dimensional Electron Gases at Complex Oxide Interfaces. *Annu Rev Mater Res* **2014,** *44*, 151-171.

49. CEOS, Instruction mannual DCOR 01, Stuttgart. In *Spherical aberration corrector for transmission electron microscopes JEOL ARM 200F/2200FS/2100F*, 2015.

50. Kirkland, E. J., Advanced computing in electron microscope. 2 ed.; 2010.

51. Haider, M.; Muller, H.; Uhlemann, S.; Zach, J.; Loebau, U.; Hoeschen, R., Prerequisites for a C-c/C-s-corrected ultrahigh-resolution TEM. *Ultramicroscopy* **2008,** *108* (3), 167-178.

52. Krivanek, O. L.; Dellby, N.; Lupini, A. R., Towards sub-angstrom electron beams. *Ultramicroscopy* **1999,** *78* (1-4), 1-11.

53. Uhlemann, S.; Haider, M., Residual wave aberrations in the first spherical aberration corrected transmission electron microscope. *Ultramicroscopy* **1998,** *72* (3-4), 109-119.

54. Typke, D.; Dierksen, K., Determination of Image Aberrations in High-Resolution Electron-Microscopy Using Diffractogram and Cross-Correlation Methods. *Optik* **1995,** *99* (4), 155-166.

55. Hawkes, P. W. a. K., E, *Principles of electron optics*. Academic press: London, 1989.

56. Brydson, R., *Aberration-corrected analytical transmission electron microscopy*. RMS-Wiley: Chichester, West Sussex, U.K., 2011; p xv, 280 p.

57. H. Rose, C. K., On the reciprocity of TEM and STEM. *Microsc Microanal* **2005,** *11* (Supplement S02), 2.

58. Spence, J. C. H., *High-resolution electron microscopy*. 3rd ed.; 2009.

59. Crewe, A. V.; Wall, J., A Scanning Microscope with 5 a Resolution. *J Mol Biol* **1970,** *48* (3), 375-&.

60. Pennycook, S. J., Z-Contrast Stem for Materials Science. *Ultramicroscopy* **1989,** *30* (1-2), 58-69.

61. Pennycook, S. J.; Jesson, D. E., High-Resolution Z-Contrast Imaging of Crystals. *Ultramicroscopy* **1991,** *37* (1-4), 14-38.

62. Jones, L.; Nellist, P. D., Identifying and Correcting Scan Noise and Drift in the Scanning Transmission Electron Microscope. *Microsc Microanal* **2013,** *19* (4), 1050-1060.

63. Mitchell, D. R. G., Determination of mean free path for energy loss and surface oxide film thickness using convergent beam electron diffraction and thickness mapping: a case study using Si and P91 steel. *J Microsc-Oxford* **2006,** *224*, 187-196.

64. Malis, T.; Cheng, S. C.; Egerton, R. F., Eels Log-Ratio Technique for Specimen-Thickness Measurement in the Tem. *J Electron Micr Tech* **1988,** *8* (2), 193-200.

65. Andreas Rosenauer, K. M., Marco Schowalter, Tim Grib, Thorsten Mehrtens *Quantitative intensity in HR(ST)EM images*; Institut für Festkörperphysik,Universität Bremen, D 28359 Bremen, Germany: 2013.

66. LeBeau, J. M.; Findlay, S. D.; Allen, L. J.; Stemmer, S., Quantitative atomic resolution scanning transmission electron microscopy. *Phys Rev Lett* **2008,** *100* (20).
67. Findlay, S. D.; LeBeau, J. M., Detector non-uniformity in scanning transmission electron microscopy. *Ultramicroscopy* **2013,** *124*, 52-60.
68. LeBeau, J. M.; Stemmer, S., Experimental quantification of annular dark-field images in scanning transmission electron microscopy. *Ultramicroscopy* **2008,** *108* (12), 1653-1658.
69. Egerton, R. F., *Electron energy-loss spectroscopy in the electron microscopy*. 3rd ed.; Springer: 2011.
70. Dorneich, A. D.; French, R. H.; Mullejans, H.; Loughin, S.; Ruhle, M., Quantitative analysis of valence electron energy-loss spectra of aluminium nitride. *J Microsc-Oxford* **1998,** *191*, 286-296.
71. Mohr, M.; Maultzsch, J.; Dobardzic, E.; Reich, S.; Milosevic, I.; Damnjanovic, M.; Bosak, A.; Krisch, M.; Thomsen, C., Phonon dispersion of graphite by inelastic x-ray scattering. *Phys Rev B* **2007,** *76* (3).
72. Egoavil, R.; Gauquelin, N.; Martinez, G. T.; Van Aert, S.; Van Tendeloo, G.; Verbeeck, J., Atomic resolution mapping of phonon excitations in STEM-EELS experiments. *Ultramicroscopy* **2014,** *147*, 1-7.
73. Krivanek, O. L.; Lovejoy, T. C.; Murfitt, M. F.; Skone, G.; Batson, P. E.; Dellby, N., Towards sub-10 meV energy resolution STEM-EELS. *Electron Microscopy and Analysis Group Conference 2013 (Emag2013)* **2014,** *522*.
74. Zabala, N.; Rivacoba, A.; de Abajo, F. J. G.; Pattantyus, A., Cherenkov radiation effects in EELS for nanoporous alumina membranes. *Surf Sci* **2003,** *532*, 461-467.
75. de Abajo, F. J. G.; Pattantyus-Abraham, A. G.; Zabala, N.; Rivacoba, A.; Wolf, M. O.; Echenique, P. M., Cherenkov effect as a probe of photonic nanostructures. *Phys Rev Lett* **2003,** *91* (14).
76. Egerton, R. F., Electron Energy-Loss Spectroscopy in the Electron Microscope. 3 ed.; 2011.
77. Keast, V. J.; Scott, A. J.; Brydson, R.; Williams, D. B.; Bruley, J., Electron energy-loss near-edge structure - a tool for the investigation of electronic structure on the nanometre scale. *Journal of Microscopy* **2001,** *203*, 135-175.
78. Erni, R.; Browning, N. D., Valence electron energy-loss spectroscopy in monochromated scanning transmission electron microscopy. *Ultramicroscopy* **2005,** *104* (3-4), 176-192.

79. Liu, H. J.; Chen, L. Y.; He, Q.; Liang, C. W.; Chen, Y. Z.; Chien, Y. S.; Hsieh, Y. H.; Lin, S. J.; Arenholz, E.; Luo, C. W.; Chueh, Y. L.; Chen, Y. C.; Chu, Y. H., Epitaxial Photostriction-Magnetostriction Coupled Self-Assembled Nanostructures. *Acs Nano* **2012,** *6* (8), 6952-6959.
80. Imai, A.; Cheng, X.; Xin, H. L. L.; Eliseev, E. A.; Morozovska, A. N.; Kalinin, S. V.; Takahashi, R.; Lippmaa, M.; Matsumoto, Y.; Nagarajan, V., Epitaxial Bi5Ti3FeO15-CoFe2O4 Pillar-Matrix Multiferroic Nanostructures. *Acs Nano* **2013,** *7* (12), 11079-11086.
81. Zheng, H.; Zhan, Q.; Zavaliche, F.; Sherburne, M.; Straub, F.; Cruz, M. P.; Chen, L. Q.; Dahmen, U.; Ramesh, R., Controlling self-assembled perovskite-spinel nanostructures. *Nano Lett* **2006,** *6* (7), 1401-1407.
82. Moshnyaga, V.; Damaschke, B.; Shapoval, O.; Belenchuk, A.; Faupel, J.; Lebedev, O. I.; Verbeeck, J.; Van Tendeloo, G.; Mucksch, M.; Tsurkan, V.; Tidecks, R.; Samwer, K., Structural phase transition at the percolation threshold in epitaxial (La0.7Ca0.3MnO3)(1-X):(MgO)(X) nanocomposite films. *Nat Mater* **2003,** *2* (4), 247-252.
83. Mannhart, J.; Schlom, D. G., Oxide Interfaces-An Opportunity for Electronics. *Science* **2010,** *327* (5973), 1607-1611.
84. Chen, A. P.; Bi, Z. X.; Hazariwala, H.; Zhang, X. H.; Su, Q.; Chen, L.; Jia, Q. X.; MacManus-Driscoll, J. L.; Wang, H. Y., Microstructure, magnetic, and low-field magnetotransport properties of self-assembled (La0.7Sr0.3MnO3)(0.5):(CeO2)(0.5) vertically aligned nanocomposite thin films. *Nanotechnology* **2011,** *22* (31).
85. Goyal, A.; Kang, S.; Leonard, K. J.; Martin, P. M.; Gapud, A. A.; Varela, M.; Paranthaman, M.; Ijaduola, A. O.; Specht, E. D.; Thompson, J. R.; Christen, D. K.; Pennycook, S. J.; List, F. A., Irradiation-free, columnar defects comprised of self-assembled nanodots and nanorods resulting in strongly enhanced flux-pinning in YBa2Cu3O7-delta films. *Supercond Sci Tech* **2005,** *18* (11), 1533-1538.
86. Sinclair, J. W.; Zuev, Y. L.; Cantoni, C.; Wee, S. H.; Varanasi, C.; Thompson, J. R.; Christen, D. K., Matching field effects at tesla-level magnetic fields in critical current density in high-T-c superconductors containing self-assembled columnar defects. *Supercond Sci Tech* **2012,** *25* (11).
87. Yang, R. G.; Chen, G.; Dresselhaus, M. S., Thermal conductivity of simple and tubular nanowire composites in the longitudinal direction. *Phys Rev B* **2005,** *72* (12).
88. Robert, R.; Romer, S.; Reller, A.; Weidenkaff, A., Nanostructured complex cobalt oxides as potential materials for solar thermoelectric power generators. *Adv Eng Mater* **2005,** *7* (5), 303-308.

89. Gao, Y. Z.; Cao, G. X.; Zhang, J. C.; Habermeier, H. U., Intrinsic and precipitate-induced quantum corrections to conductivity in La2/3Sr1/3MnO3 thin films. *Phys Rev B* **2012,** *85* (19).

90. Gao, Y. Z.; Zhang, J. C.; Cao, G. X.; Mi, X. F.; Habermeier, H. U., Magnetic field dependence of weak localization in La2/3Sr1/3MnO3 thin films with nonmagnetic nano-scaled precipitates. *Solid State Commun* **2013,** *154*, 46-50.

91. Gao, Y. Z.; Zhang, J. C.; Fu, X. W.; Cao, G. X.; Habermeier, H. U., Tuning the magnetic anisotropy in LSMO manganite films through non-magnetic nanoparticles. *Prog Nat Sci-Mater* **2013,** *23* (2), 127-132.

92. Haussler, D.; Houben, L.; Essig, S.; Kurttepeli, M.; Dimroth, F.; Dunin-Borkowski, R. E.; Jager, W., Aberration-corrected transmission electron microscopy analyses of GaAs/Si interfaces in wafer-bonded multi-junction solar cells. *Ultramicroscopy* **2013,** *134*, 55-61.

93. Muller, D. A.; Kourkoutis, L. F.; Murfitt, M.; Song, J. H.; Hwang, H. Y.; Silcox, J.; Dellby, N.; Krivanek, O. L., Atomic-scale chemical imaging of composition and bonding by aberration-corrected microscopy. *Science* **2008,** *319* (5866), 1073-1076.

94. Lazar, S.; Shao, Y.; Gunawan, L.; Nechache, R.; Pignolet, A.; Botton, G. A., Imaging, Core-Loss, and Low-Loss Electron-Energy-Loss Spectroscopy Mapping in Aberration-Corrected STEM. *Microsc Microanal* **2010,** *16* (4), 416-424.

95. Idrobo, J. C.; Walkosz, W.; Klie, R. F.; Ogut, S., Identification of light elements in silicon nitride by aberration-corrected scanning transmission electron microscopy. *Ultramicroscopy* **2012,** *123*, 74-79.

96. Hatt, A. J.; Spaldin, N. A., Structural phases of strained LaAlO3 driven by octahedral tilt instabilities. *Phys Rev B* **2010,** *82* (19).

97. Trukhanov, S. V.; Troyanchuk, I. O.; Bobrikov, I. A.; Simkin, V. G.; Balagurov, A. M., Crystal Structure Phase Separation in Anion-Deficient La-0.70 Sr-0.30 MnO3 (-) (delta) Manganite System. *J Surf Invest-X-Ray+* **2007,** *1* (6), 705-710.

98. Kallel, N.; Ihzaz, N.; Kallel, S.; Hagaza, A.; Oumezzine, M., Research on charge-ordering state in La0.5Sr0.5MnO2.88 and La0.5Sr0.5Mn0.5Ti0.5O3 systems. *J Magn Magn Mater* **2009,** *321* (15), 2285-2289.

99. Ding, H. P.; Virkar, A. V.; Liu, F., Defect configuration and phase stability of cubic versus tetragonal yttria-stabilized zirconia. *Solid State Ionics* **2012,** *215*, 16-23.

100. Bayer, G., Stabilization of Cubic Zro2 by Mno and Partial Substitution of Ti, Nb, or Ta for Zr. *J Am Ceram Soc* **1970,** *53* (5), 294-&.

101. Smallman, R. E.; Bishop, R. J., *Modern Physical Metallurgy and Materials Engineering* 6. ed.; Butterworth-Heinemann Oxford, 1999.
102. Igawa, N.; Ishii, Y., Crystal structure of metastable tetragonal zirconia up to 1473 K. *J Am Ceram Soc* **2001,** *84* (5), 1169-1171.
103. Kang, S. W.; Park, H. J.; Kim, T.; Dann, T.; Kryliouk, O.; Anderson, T., The influence of interdiffusion on strain energy in the GaN-sapphire system. *Phys Status Solidi C* **2005,** *2* (7), 2420-2423.
104. Tan, H. Y.; Verbeeck, J.; Abakumov, A.; Van Tendeloo, G., Oxidation state and chemical shift investigation in transition metal oxides by EELS. *Ultramicroscopy* **2012,** *116*, 24-33.
105. Garvie, L. A. J.; Craven, A. J.; Brydson, R., Use of Electron-Energy-Loss near-Edge Fine-Structure in the Study of Minerals. *Am Mineral* **1994,** *79* (5-6), 411-425.
106. Saravanakumar, S.; Kamalaveni, J.; Rani, M. P.; Saravanan, R., Solubility of Mn stabilized cubic zirconia nanostructures. *J Mater Sci-Mater El* **2014,** *25* (2), 837-843.
107. Appel, C. C., Zirconia Stabilized by Y and Mn: A Microstructural Characterization. *Ionics* **1995,** *1* (5-6), 406-413.
108. Lajavardi, M.; Kenney, D. J.; Lin, S. H., Time-resolved phase transitions of the nanocrystalline cubic to submicron monoclinic phase in Mn2O3-ZrO2. *J Chin Chem Soc-Taip* **2000,** *47* (5), 1055-1063.
109. Kawada, T.; Sakai, N.; Yokokawa, H.; Dokiya, M., Electrical-Properties of Transition-Metal-Doped Ysz. *Solid State Ionics* **1992,** *53*, 418-425.
110. Kim, M. S.; Yang, J. B.; Cai, Q.; James, W. J.; Yelon, W. B.; Parris, P. E.; Malik, S. K., Structural, magnetic, and transport properties of Zr-substituted La0.7Sr0.3MnO3. *J Appl Phys* **2007,** *102* (1).
111. Roy, S.; Ali, N., Charge transport and colossal magnetoresistance phenomenon in La1-xZrxMnO3. *J Appl Phys* **2001,** *89* (11), 7425-7427.
112. Alharbi, A. A.; Alkahtani, M.; Al-Dossary, O., The Role of Oxygen Vacancies on Magnetic Properties of LSMO. *Aip Conf Proc* **2011,** *1370*.
113. Picozzi, S.; Ma, C.; Yang, Z.; Bertacco, R.; Cantoni, M.; Cattoni, A.; Petti, D.; Brivio, S.; Ciccacci, F., Oxygen vacancies and induced changes in the electronic and magnetic structures of La0.66Sr0.33MnO3: A combined ab initio and photoemission study. *Phys Rev B* **2007,** *75* (9).
114. Majumdar, S.; van Dijken, S., Pulsed laser deposition of La1-xSrxMnO3: thin-film properties and spintronic applications. *J Phys D Appl Phys* **2014,** *47* (3).

115. Evgeny Y. Tsymbal, E. R. A. D., Chang-Beom Eom, and Ramamoorthy Ramesh, *Multifunctional Oxide Heterostructures*. Oxford University Press: 2012.

116. Jin, K. J.; Lu, H. B.; Zhao, K.; Ge, C.; He, M.; Yang, G. Z., Novel Multifunctional Properties Induced by Interface Effects in Perovskite Oxide Heterostructures. *Adv Mater* **2009,** *21* (45), 4636-4640.

117. Salje, E.; Zhang, H. L., Domain boundary engineering. *Phase Transit* **2009,** *82* (6), 452-469.

118. Salje, E. K. H., Domain boundary engineering - recent progress and many open questions. *Phase Transit* **2013,** *86* (1), 2-14.

119. Ohtomo, A.; Muller, D. A.; Grazul, J. L.; Hwang, H. Y., Artificial charge-modulation in atomic-scale perovskite titanate superlattices. *Nature* **2002,** *419* (6905), 378-380.

120. Tokura, Y.; Tomioka, Y., Colossal magnetoresistive manganites. *J Magn Magn Mater* **1999,** *200* (1-3), 1-23.

121. Huijben, M.; Martin, L. W.; Chu, Y. H.; Holcomb, M. B.; Yu, P.; Rijnders, G.; Blank, D. H. A.; Ramesh, R., Critical thickness and orbital ordering in ultrathin La0.7Sr0.3MnO3 films. *Phys Rev B* **2008,** *78* (9).

122. Zhou, D.; Sigle, W.; Okunishi, E.; Wang, Y.; Kelsch, M.; Habermeier, H. U.; van Aken, P. A., Materials News: Interfacial chemistry and atomic arrangement of ZrO2-La2/3Sr1/3MnO3 pillar-matrix structures. *APL Materials* **2014,** *2* (12).

123. Klenov, D. O.; Stemmer, S., Contributions to the contrast in experimental high-angle annular dark-field images. *Ultramicroscopy* **2006,** *106* (10), 889-901.

124. Peng, B.; Locascio, M.; Zapol, P.; Li, S. Y.; Mielke, S. L.; Schatz, G. C.; Espinosa, H. D., Measurements of near-ultimate strength for multiwalled carbon nanotubes and irradiation-induced crosslinking improvements. *Nat Nanotechnol* **2008,** *3* (10), 626-631.

125. Kis, A.; Csanyi, G.; Salvetat, J. P.; Lee, T. N.; Couteau, E.; Kulik, A. J.; Benoit, W.; Brugger, J.; Forro, L., Reinforcement of single-walled carbon nanotube bundles by intertube bridging. *Nat Mater* **2004,** *3* (3), 153-157.

126. Gomez-Navarro, C.; De Pablo, P. J.; Gomez-Herrero, J.; Biel, B.; Garcia-Vidal, F. J.; Rubio, A.; Flores, F., Tuning the conductance of single-walled carbon nanotubes by ion irradiation in the Anderson localization regime. *Nat Mater* **2005,** *4* (7), 534-539.

127. Lee, H.; Miyamoto, Y.; Yu, J. J., Possible origins of defect-induced magnetic ordering in carbon-irradiated graphite. *Phys Rev B* **2009,** *79* (12).

128. Esquinazi, P.; Spemann, D.; Hohne, R.; Setzer, A.; Han, K. H.; Butz, T., Induced magnetic ordering by proton irradiation in graphite. *Phys Rev Lett* **2003,** *91* (22).

129. Makarova, T. L.; Shelankov, A. L.; Serenkov, I. T.; Sakharov, V. I., Magnetism in graphite induced by irradiation of hydrogen or helium ions - A comparative study. *Phys Status Solidi B* **2010,** *247* (11-12), 2988-2991.

130. Fox, D.; O'Neill, A.; Zhou, D.; Boese, M.; Coleman, J. N.; Zhang, H. Z., Nitrogen assisted etching of graphene layers in a scanning electron microscope. *Appl Phys Lett* **2011,** *98* (24).

131. Lee, J.; Zhou, W.; Pennycook, S. J.; Idrobo, J. C.; Pantelides, S. T., Direct visualization of reversible dynamics in a Si-6 cluster embedded in a graphene pore. *Nat Commun* **2013,** *4*.

132. Lin, Y. C.; Dumcencon, D. O.; Huang, Y. S.; Suenaga, K., Atomic mechanism of the semiconducting-to-metallic phase transition in single-layered MoS2. *Nat Nanotechnol* **2014,** *9* (5), 391-396.

133. Zhou, D.; Sigle, W.; Kelsch, M.; Habermeier, H.-U.; van Aken, P. A., Linking Atomic Structure and Local Chemistry at Manganese-Segregated Antiphase Boundaries in ZrO2–La2/3Sr1/3MnO3 Thin Films. *Adv Mater Interfaces* **2015,** *Early view*.

134. Zhou, D. S., Wilfried; Kelsch, Marion; Habermeier, Hanns-Ulrich; van Aken, Peter A., Manganese Segregation at Antiphase Boundaries Connecting ZrO2 Pillars in ZrO2 −La2/3 Sr1/3 MnO 3 Pillar−Matrix Structures *Microsc Microanal* **2015,** *21(Supplement S3)*, 2.

135. Degroot, F. M. F.; Grioni, M.; Fuggle, J. C.; Ghijsen, J.; Sawatzky, G. A.; Petersen, H., Oxygen 1s X-Ray-Absorption Edges of Transition-Metal Oxides. *Phys Rev B* **1989,** *40* (8), 5715-5723.

136. Lafuerza, S.; Subias, G.; Garcia, J.; Di Matteo, S.; Blasco, J.; Cuartero, V.; Natoli, C. R., Origin of the pre-peak features in the oxygen K-edge x-ray absorption spectra of LaFeO3 and LaMnO3 studied by Ga substitution of the transition metal ion. *J Phys-Condens Mat* **2011,** *23* (32).

137. Marris, H.; Deboudt, K.; Flament, P.; Grobety, B.; Giere, R., Fe and Mn Oxidation States by TEM-EELS in Fine-Particle Emissions from a Fe-Mn Alloy Making Plant. *Environ Sci Technol* **2013,** *47* (19), 10832-10840.

138. Wang, Z. L.; Yin, J. S.; Jiang, Y. D., EELS analysis of cation valence states and oxygen vacancies in magnetic oxides. *Micron* **2000,** *31* (5), 571-580.

139. Wang, Y. Q.; Maclaren, I.; Duan, X. F., EELS analysis of manganese valence states in rare-earth manganites (La1-xYx)(0.5)(Ca1-ySry)(0.5)MnO3. *Mat Sci Eng a-Struct* **2001,** *318* (1-2), 259-263.

140. Su, D. S., Electron beam induced changes in transition metal oxides. *Anal Bioanal Chem* **2002,** *374* (4), 732-735.

141. Garvie, L. A. J.; Craven, A. J., Electron-Beam-Induced Reduction of Mn4+ in Manganese Oxides as Revealed by Parallel Eels. *Ultramicroscopy* **1994,** *54* (1), 83-92.

142. Yao, L. D.; Majumdar, S.; Akaslompolo, L.; Inkinen, S.; Qin, Q. H.; van Dijken, S., Electron-Beam-Induced Perovskite-BrownmilleritePerovskite Structural Phase Transitions in Epitaxial La-2 3 Sr-1/3 MnO3 Films. *Adv Mater* **2014,** *26* (18), 2789-2793.

143. Egerton, R. F.; Li, P.; Malac, M., Radiation damage in the TEM and SEM. *Micron* **2004,** *35* (6), 399-409.

144. Gazquez, J.; Bose, S.; Sharma, M.; Torija, M. A.; Pennycook, S. J.; Leighton, C.; Varela, M., Lattice mismatch accommodation via oxygen vacancy ordering in epitaxial La0.5Sr0.5CoO3-delta thin films. *APL Materials* **2013,** *1* (1).

145. Donner, W.; Chen, C. L.; Liu, M.; Jacobson, A. J.; Lee, Y. L.; Gadre, M.; Morgan, D., Epitaxial Strain-Induced Chemical Ordering in La0.5Sr0.5CoO3-delta Films on SrTiO3. *Chem Mater* **2011,** *23* (4), 984-988.

146. S. D. Findlay, a N. Shibata,1,2 H. Sawada,3 E. Okunishi,3 Y. Kondo,3 T. Yamamoto,1,4; and Y. Ikuhara1, 5, Robust atomic resolution imaging of light elements using scanning transmission electron microscopy. *Appl Phys Lett* **2009**.

147. Xiaoqing He1, L. G., Changbao Zhu3, Yan Yu3, Chilin Li3, Yong-Sheng Hu1, Hong Li1, Susumu Tsukimoto2, Joachim Maier3, Yuichi Ikuhara2 4 5, and Xiaofeng Dua, Direct Imaging of Lithium Ions Using Aberration-Corrected Annular-Bright-Field Scanning Transmission Electron Microscopy and Associated Contrast Mech. *Material express* **2011**.

148. Maccagnano-Zacher, S. E.; Mkhoyan, K. A.; Kirkland, E. J.; Silcox, J., Effects of tilt on high-resolution ADF-STEM imaging. *Ultramicroscopy* **2008,** *108* (8), 718-726.

149. Xia, X.; Oldman, R.; Catlow, R., Computational Modeling Study of Bulk and Surface of Yttria-Stabilized Cubic Zirconia. *Chem Mater* **2009,** *21* (15), 3576-3585.

150. Rosenauer, A.; Schowalter, M., STEMSIM-a New Software Tool for Simulation of STEM HAADF Z-Contrast Imaging. *Springer Proc Phys* **2008,** *120*, 169-172.

151. Rosenauer, A., A local absorptive potential multislice approximation to calculate intensity contributions from thermal diffuse scattering in conventional TEM. *Microsc Microanal* **2007,** *13* (Suppl 3), 2.

152. Rosenauer, A.; Kaiser, S.; Reisinger, T.; Zweck, J.; Gebhardt, W.; Gerthsen, D., Digital analysis of high resolution transmission electron microscopy lattice images. *Optik* **1996,** *102* (2), 63-69.

153. LeBeau, J. M.; Findlay, S. D.; Allen, L. J.; Stemmer, S., Position averaged convergent beam electron diffraction: Theory and applications. *Ultramicroscopy* **2010,** *110* (2), 118-125.
154. LeBeau, J. M.; Findlay, S. D.; Allen, L. J.; Stemmer, S., Position Averaged Convergent Beam Electron Diffraction. *Microsc Microanal* **2009,** *15*, 494-495.
155. Peng, Y. P.; Nellist, P. D.; Pennycook, S. J., HAADF-STEM imaging with sub-angstrom probes: a full Bloch wave analysis. *J Electron Microsc* **2004,** *53* (3), 257-266.
156. Vulovic, M.; Voortman, L. M.; van Vliet, L. J.; Rieger, B., When to use the projection assumption and the weak-phase object approximation in phase contrast cryo-EM. *Ultramicroscopy* **2014,** *136*, 61-66.
157. Padhi, A. K.; Nanjundaswamy, K. S.; Goodenough, J. B., Phospho-olivines as positive-electrode materials for rechargeable lithium batteries. *J Electrochem Soc* **1997,** *144* (4), 1188-1194.
158. Andersson, A. S.; Thomas, J. O., The source of first-cycle capacity loss in LiFePO4. *J Power Sources* **2001,** *97-8*, 498-502.
159. Delmas, C.; Maccario, M.; Croguennec, L.; Le Cras, F.; Weill, F., Lithium deintercalation in LiFePO(4) nanoparticles via a domino-cascade model. *Nat Mater* **2008,** *7* (8), 665-671.
160. He, X. Q.; Gu, L.; Zhu, C. B.; Yu, Y.; Li, C. L.; Hu, Y. S.; Li, H.; Tsukimoto, S.; Maier, J.; Ikuhara, Y.; Duan, X. F., Direct Imaging of Lithium Ions Using Aberration-Corrected Annular-Bright-Field Scanning Transmission Electron Microscopy and Associated Contrast Mechanisms. *Mater Express* **2011,** *1* (1), 43-50.
161. Gu, L.; Zhu, C. B.; Li, H.; Yu, Y.; Li, C. L.; Tsukimoto, S.; Maier, J.; Ikuhara, Y., Direct Observation of Lithium Staging in Partially Delithiated LiFePO4 at Atomic Resolution. *J Am Chem Soc* **2011,** *133* (13), 4661-4663.
162. Zhu, C. B.; Gu, L.; Suo, L. M.; Popovic, J.; Li, H.; Ikuhara, Y.; Maier, J., Size-Dependent Staging and Phase Transition in LiFePO4/FePO4. *Adv Funct Mater* **2014,** *24* (3), 312-318.
163. Sigle, W.; Amin, R.; Weichert, K.; van Aken, P. A.; Maier, J., Delithiation Study of LiFePO4 Crystals Using Electron Energy-Loss Spectroscopy. *Electrochem Solid St* **2009,** *12* (8), A151-A154.
164. Kinyanjui, M. K.; Axmann, P.; Wohlfahrt-Mehrens, M.; Moreau, P.; Boucher, F.; Kaiser, U., Origin of valence and core excitations in LiFePO(4) and FePO(4). *J Phys-Condens Mat* **2010,** *22* (27).

165. Kinyanjui, M. K.; Axmann, P.; Wohlfahrt-Mehrens, M.; Moreau, P.; Boucher, F.; Kaiser, U., Origin of valence and core excitations in LiFePO4 and FePO4. *J Phys-Condens Mat* **2010,** *22* (27).

166. Moreau, P.; Mauchamp, V.; Pailloux, F.; Boucher, F., Fast determination of phases in LixFePO4 using low losses in electron energy-loss spectroscopy. *Appl Phys Lett* **2009,** *94* (12).

167. John W. Anthony, R. A. B., Kenneth W. Bladh, and Monte C. Nichols, *Handbook of Mineralogy*. Mineral Data Publishing: 2000; Vol. IV.

168. Wang, F.; Graetz, J.; Moreno, M. S.; Ma, C.; Wu, L. J.; Volkov, V.; Zhu, Y. M., Chemical Distribution and Bonding of Lithium in Intercalated Graphite: Identification with Optimized Electron Energy Loss Spectroscopy. *Acs Nano* **2011,** *5* (2), 1190-1197.

169. Egerton, R. F., New techniques in electron energy-loss spectroscopy and energy-filtered imaging. *Micron* **2003,** *34* (3-5), 127-139.